AN INVESTIGATION OF THE TENSILE, COMPRESSIVE AND INTERFACIAL PROPERTIES OF CARBON FIBRES USING LASER RAMAN SPECTROSCOPY

NIKOLAOS MELANITIS

A thesis presented for the degree of Doctor of Philosophy

QUEEN MARY AND WESTFIELD COLLEGE
DEPARTMENT OF MATERIALS

UNIVERSITY OF LONDON

1991

ABSTRACT

Laser Raman Spectroscopy (LRS) has been employed to characterise the structure of carbon fibres, the effect of surface treatment and the response of the material to externally applied loads. The strain sensitivity provided a unique relationship between the applied strain and the Raman frequency for each type of fibre, termed as the Raman Frequency Gauge Factor.

After examining a wide range of fibres, of various Young's moduli and various manufacturing routes, it was concluded that both tensile and compressive properties of carbon fibres can be improved by controlling the fibre morphology during manufacture. This morphological control seems to achieve its objectives by reducing the skin-core effect in the fibre structure. The result of such an alteration can be detected in tension by the increase of the initial fibre modulus and in compression, by the absence of premature catastrophic type of failure. Nevertheless, non-linear stress-strain phenomena seem to be a permanent feature of all carbon fibres and the significant modulus softening in compression appears to determine the limits of the fibre compressive strength.

The load transfer mechanism at the carbon fibre/epoxy resin interface has been subsequently investigated during the fibre fragmentation process in a single fibre model composite. The fibre strain distribution along the fibre fragments has been derived through the Raman spectrum of the fibre and its Raman Frequency Gauge Factor. In turn, the interfacial shear stress distribution has been evaluated using a simple balance of forces model. The maximum shear stress, allowed to develop at the fibre/matrix interface, has been considered as a reasonable estimate of its interfacial strength. It was concluded that both the fibre surface treatment and the use of a lower modulus filament can increase the system's interfacial strength, reduce debonding propagation and withhold the interfacial yielding in the vicinity of the fibre discontinuities.

To my parents

Μανωλη και Ξενη Μελανιτη

ACKNOWLEDGEMENTS

I express my gratidude to my supervisor, Dr Costas Galiotis, for his tireless guidance, advice and encouragement throughout the course of this project.

I am indebted to my colleague Phil Tetlow for his assistance, numerous discussions and friendship; I also express my appreciation to my friends and colleagues Cosmas Vlattas, Hamid Jahankhani and Brian Smith for their useful remarks and helpful ideas.

Many thanks are due to Mike Pitkethly (RAE), Ron Robinson and Steve Smith (Courtaulds Grafil) and Craig Davies (QMW) for their fruitful cooperation, their helpful suggestions and recommendations.

Finally, I am indebted to the Ministry of Defense (RAE) and the Science and Engineering Research Council (SERC) for their financial support.

CONTENTS

LIST OF FIGURES

CHAPTER 2. *(pages 81 to 97)*

LIST OF TABLES

CHAPTER 5. *(pages 226 to 236)*

NOMENCLATURE

A list of symbols and abbreviations most frequently used in this thesis are displayed below.

α_ε Strain dependence of the Raman frequency, or Raman Frequency Gauge Factor (abbr.RFGF).

α_σ Stress dependence of the Raman frequency.

A Total debonded length along a fibre fragment embedded in resin.

A_L Debonded length on the left-hand side of a fibre fragment.

A_R Debonded length on the right-hand side of a fibre fragment.

BSU Basic structural unit (crystallite) of carbon fibres.

B Interfacial shear stress take-up length along a fragment.

CCD Charge-coupled-device (the photon detection system).

CB Cantilever beam.

C Well bonded length along a fibre fragment.

D-line The line of the carbon fibre Raman spectrum appearing at 1360cm^{-1}

D'-line The line of the carbon fibre Raman spectrum appearing at 1620cm^{-1}

d Diameter.

δ_{max} Maximum deflection at the free end of the cantilever beam.

E Young's modulus (subscript "f" for fibre, "m" for matrix).

ε	Strain (subscript "f" for fibre, "m" for matrix).
ϕ	Angle orientation of carbon fibre crystallites.
$\mathbb{F}$	Matrix representation of the potential energy.
FGL	Fragmentation gauge length.
$\mathbb{G}$	The Wilson matrix representation of the kinetic energy.
Γ	Irreducible representation of a molecular symmetry.
G-line	The line of the carbon fibre Raman spectrum appearing at $1580cm^{-1}$
G'-line	The line of the carbon fibre Raman spectrum appearing at $2700cm^{-1}$
G''-line	The line of the carbon fibre Raman spectrum appearing at $2950cm^{-1}$
HHBW	Half-height-bandwidth.
I_D/I_G	"Disorder" ratio, or intensity ratio between the D and the G-lines of the carbon fibre Raman spectrum.
ISS	Intefacial shear stress.
IFSS	Interfacial shear strength.
L_a	Crystallite length.
L_c	Crystallite thickness.
LRS	Laser Raman spectroscopy.
l_{av}	Average fragment length at the end of the fragmentation test
L_{cr}	Fibre critical length at the end of the fragmentation test.
ν_f	Fibre Poisson ratio.

ν_m Matrix Poisson ratio.

PAN Polyacrylonitrile.

PMMA Polymethylmethacrylate.

Q Normal vibrational mode.

RGFG Raman Frequency Gauge Factor (symbol: α_ε).

R/r Ratio denoting the matrix cylinder of radius R surrounding a fibre of radius r.

RGL Raman gauge length (the region of the FGL scanned by the Laser Raman probe).

σ_x Stress along the x-axis.

σ_r Radial stress.

σ_ϑ Tangential stress.

σ_{rx} Shear stress.

$\sigma_f(x)$ Fibre axial stress distribution.

τ_{rx},τ Interfacial shear stress (abbr. ISS).

$\tau(x)$ ISS distribution along the x-axis.

τ_m^* Shear yield stress of the matrix.

V_f,V_m Volume fraction of the fibre and the matrix, respectively.

GENERAL INTRODUCTION

The purpose of this thesis was to study the structure of carbon fibres, the response of this material to externally applied deformations and, finally, the mechanisms of adhesion of carbon fibres to polymeric matrices. The major experimental tool employed in all sections of this investigation was Laser Raman Spectroscopy (LRS). It was, therefore, considered necessary to commence this programme of research by introducing the structural aspects of carbon fibres and the principles of Laser Raman Spectroscopy. Hence, this is the subject of Chapter 1.

A concise presentation of each topic was attempted in structuring this thesis. Therefore, each Chapter comprises a literature survey, a description of the specific experimental details, a display of the results and a discussion of the findings. A synoptic evaluation of the whole project can be found in the final Chapter.

In particular, Chapter 2 deals with the characterisation of carbon fibres through their Raman spectrum. Each Raman band of the spectrum is assigned to a certain feature of the carbon fibre structure. A range of fibres are studied and classified with respect to their spectroscopic properties and their quoted mechanical properties.

In Chapter 3, the effect of applied tensile strain on the Raman spectrum of carbon fibres is investigated. The strain sensitivity of the Raman bands firstly confirms the anharmonic nature of the material force constants and secondly probes the degree of crystallinity of the fibre structure. Furthermore, it can reveal the existence of radial anisotropy, or, "skin-core" effects. The strain dependence of the Raman frequency bands also provides a calibration curve of the frequency as a function of the applied strain, which is characteristic for each type of fibre.

The compressional behaviour of carbon fibres is examined in Chapter 4. Using a cantilever beam technique to apply well defined compressive load on single filaments, the compressive strain dependence of the carbon fibre Raman spectrum is obtained. The findings of Chapter 3 are employed to explain the modes of compressive failure. The reduced strain sensitivity of the carbon fibre Raman spectrum in compression is interpreted as a reduction in the fibre stiffness. By considering the tensile and compressive behaviour of carbon fibres in a continuous fashion, non-linear

phenomena in the mechanical response of carbon fibres can be investigated.

Chapters 2 to 4, deal exclusively with the characterisation of the carbon fibre structure and the response of this structure to external deformations, as detected by Laser Raman Spectroscopy. One of the most important findings, the unique relationship between the Raman frequency and applied strain, can be subsequently utilised to measure the micro-deformations in fibres embedded in a matrix material and, hence, study the load transfer mechanisms at the fibre/matrix interface. This is the subject of Chapter 5.

A detailed review of the load transfer theories precedes the Raman interfacial studies. Subsequently, the single fibre "fragmentation test" is chosen as the loading configuration in the experimental undertaking. The effect of the fibre surface treatment and the fibre modulus are incorporated in the study by a suitable selection of fibre/epoxy resin systems for examination. The strain distribution in the embedded fibre and its fragments is monitored throughout the fragmentation process. In turn, a simple balance of forces model is employed to evaluate the Interfacial Shear Stress (ISS) distribution along the fibre and its fragments. Furthermore, the Interfacial Shear Strength (IFSS) of the fibre/epoxy resin interfacial bond is estimated. In addition, fibre/matrix debonding phenomena as well as effects of interfacial yielding in the vicinity of the fibre fracture are also examined.

An overall evaluation of the results of this investigation, the methods used for the carbon fibre characterisation and the examination of the fibre/matrix interface are attempted in Chapter 6. Suggestions for improvements in the study of carbon fibre properties and developments in the techniques used are, finally, included in the closing remarks. ▮

CHAPTER 1

THE MATERIAL AND THE METHOD

1.1. About the material : carbon and carbon fibres.

Carbon fibres are today the strategical components of a material generation which tends to replace the old guard of metals in applications such as, aerospace, machinery, sporting goods, cryogenics, medical science, etc. Superior specific stiffness and strength, essential requirements for strong and light structural applications, exceptional thermal stability, necessary for high temperature applications, are some of the mechanical and physical properties of carbon fibres that have established them as an outstanding reinforcing component in polymer, as well as in metal and ceramic matrix composites **[Hull 1981, Donnet 1984]**. The exponentially increasing world industrial demand for carbon fibres through the 1980's to the 1990's and the relative stability of the production cost **[Fitzer 1985, Dresselhaus 1988]**, have set out positive economic preconditions for extensive Research and Development on carbon fibres.

1.1.1. *The nature of carbon.*

The fundamental step in the study of the outstanding properties of carbon fibres, lies in the nature of the carbon atom, the interatomic bonds and the nuclear configurations, when the carbon atom is bonded to other atoms. Briefly, there are three possible configurations of the four free electrons of carbon **[Jenkins 1976]**:

(a) the tetrahedral sp^3 state, where all 4 electrons are absorbed into 4 tetrahedrical hybrid orbitals with the carbon nucleus at the centre. An example of such a hybridisation with bond energy 83 kcal/mole and interatomic distance of 1.54 Å, can be found in the ethane (H_3C-CH_3).

(b) the trigonal sp^2 state, where 3 electrons are absorbed in a symmetric hybridised orbital system and one electron is free, available for formation of a subsidiary bond π-type. An example of such a bond with bond energy 147 kcal/mole and interatomic distance of 1.35 Å, can be found in the ethylene ($H_2C=CH_2$).

(c) the diagonal sp state, where two electrons are absorbed in a molecular orbital system and two are free to form two subsidiary π bonds, as in the acetylene (HC≡CH), with further increase in bond energy and reduction in interatomic distance **[Jenkins 1976]**.

Carbon exists in nature in two allotropic crystalline forms; as graphite and as diamond. Graphite consists of layers of carbon atoms in the sp^2 state forming the characteristic structure shown in figure 1.1. The in-basal plane bonds are strong and stiff, creating a material able to withstand thermal degradation up to 3300°C. The interplanar bonds are weak Van der Waals type of low shear resistance. The graphitic nature of carbon fibres will be discussed in a following paragraph. Diamond consists of carbon atoms in the sp^3 state creating interatomic bonds equally stiff and strong. It withstands temperatures up to 1800°C, beyond which it reverts to graphite, due to the higher stability (energetically) of the sp^2 state above that temperature **[Jenkins 1976]**.

1.1.2. *The structure of graphite.*

The structure of graphite has been known for almost 70 years **[Fitzer 1985]**. The bond strength between atoms controls directly the lattice elasticity of a material. The elastic constant C_{11} along the a-axis of the graphite crystal (fig.1.1) has been calculated to be about 1060 GPa **[Kelly 1981, Dresselhaus 1988]**. The weak bonding between neighbouring layers, as well as in the shear (interplanar) direction, accounts for the lower stiffness along the c-axis of the graphite lattice. This is also evident in the lower values of the corresponding elastic constants, C_{33}=36.5 GPa and C_{44}=4.5 GPa **[Kelly 1981]**. Defects within the graphitic lattice, stacking faults which alter the interlayer distances, and disclinations (fig.1.2) can, on the one hand, decrease the tensile strength but, on the other hand, can improve the shear resistance of graphitic materials **[Fitzer 1985]**.

1.1.3. *Carbon fibre production.*

In carbon fibre industry, there are two major categories of raw materials for fibre production: polymers and petroleum products **[Diefendorf 1985]**. Polymers are spun to fibres using industrial synthetic fibre processes, and subsequently the polymeric fibres are converted to carbon fibres by careful pyrolysis. The polymeric precursors mainly are: polyacrylonitrile ("PAN" $-[CH_2-CH-(CN)_n$), cellulose $(C_6H_{10}O_5)_n$ and rayon;

the petroleum products used for carbon fibre production are pitch, coal tar and other petroleum fractions. The selection of the raw material can affect the manufacturing procedures (methods and temperatures), the carbon fibre yield fraction and the structural properties of the product carbon fibre **[Gill 1972, Donnet 1984]**. Synoptically, the multi-versatile and complicated process for the carbon fibre production **[Gill 1972, Diefendorf 1985]** is schematically illustrated in figure 1.3.

Polyacrylonitrile (PAN) is recognised as the most important polymeric precursor for carbon fibre production **[Donnet 1984]**. That is because the PAN fibre precursor, which has been produced after wet or dry spinning of the bulk polymer **[Fitzer 1985]**, has high degree of molecular orientation and gives greater yield of carbon fibre **[Donnet 1984]**. The fibre precursor is subjected to thermal stabilisation, which is an oxidative treatment in air between 200°C and 300°C, in order to increase the melting point of the material, improve the cross-linking of the polymer chains and make the fibre suitable for carbonisation without changing its form. While still in the stabilisation stage, the fibres are stretched in tension so that the orientation of the polymer chains to the fibre axis is maintained and improved **[Dresselhaus 1988]**. The chemical mechanism of the PAN fibre oxidisation during the stabilisation stage has been thoroughly studied in literature **[Gill 1972, Jenkins 1976, Donnet 1984]**.

Carbonisation is the pyrolysis of the stabilised PAN fibre in an inert atmosphere. In this stage most of the non carbon elements in the PAN structure are removed in forms of H_2O, HCN, NH_3, CO, CO_2, N_2 etc. Most volatiles are extracted below 1000°C and only the nitrogen content remains as high as 6%. The carbon fibre yield at this stage is about 50% of the mass of the original PAN **[Gill 1972, Donnet 1984]**. The polymeric chains have been transformed into a graphite "turbostratic" structure, term which describes the disturbed (turbulent) arrangement of the stratified (stuck in layers) graphite planes **[Watt 1973]**. Characteristic examples of such an structure will be given in the next section.

Further increase of the heat treatment temperature does not alter significantly the fibre weight. It only assists into improving the orientation of the stratified graphite planes, the crystallites or crystalline units, and to the growth of their dimensions **[Donnet 1984, Dresselhaus 1988]**. Heat treatment temperatures over 1500°C are known as graphitisation temperatures, just because, beyond this stage, the structure of the produced carbon fibre exhibits strong graphitic nature and increased

three dimensional crystallinity. The Young's modulus of the carbon fibre has been found to be directly related to the final heat treatment temperature during graphitisation **[Donnet 1984, Fitzer 1988a]**. Additional techniques, such as hot stretching of PAN based carbon fibres, can be also employed during the graphitisation stage, to yield fibres with even higher Young's modulus and improved crystallite orientation **[Fitzer 1988b]**.

1.1.4. *Structure of carbon fibres.*

A complete carbon fibre characterisation has to deal with aspects of both the internal and the surface structure of the fibre. The information required to describe the carbon fibre microstructure is related to:

(i) the degree of crystallinity,
(ii) the size and morphology of the crystalline units,
(iii) the orientation of the crystalline units,
(iv) the orientation of non-crystalline areas, if present,
(v) the interconnection of the microstructural units,
(vi) the degree of homogeneity throughout the fibre.

To complete the characterisation, additional surface properties must be considered **[Jaffe 1981]**; these include surface composition (nature, quantity, distribution of surface structural units), surface energy properties, specific area (roughness, accessible microporosity), flaws, dislocations and their distribution.

Various experimental techniques are available for the study of the carbon fibre structure. They include optical microscopy, Transmission Electron Microscopy (TEM) **[Guigon 1984, FitzGerald 1988]**, Scanning Electron Microscopy (SEM) **[Donnet 1973, Sharp 1973]** wide and small angle X-ray diffraction **[Johnson 1988, Fourdeux 1973]**, mechanical testing **[Cooper 1971, Fitzer 1988b]**, Infra-Red spectroscopy **[Ishitani 1985]** and Laser Raman Spectroscopy (LRS) **[Tuinstra 1970 a&b, Fitzer 1988, Dresselhaus 1988]**. The latter is the main method employed in the present investigation.

(a).Carbon fibre structure models.

As only PAN-based carbon fibres are dealt with in this thesis, the attention in reviewing the fibre structural aspects will be focused mainly

on this material. It is widely known that the carbon fibre structure is related to the final heat temperature at which the precursor is subsequently processed **[Gill 1972, Dresselhaus 1988]**. Therefore, the modelling of the carbon fibre structure becomes quite complicated, as it requires a separate approach to each type of fibre, according to its heat treatment temperature.

According to one of the earliest models **[Ruland 1967]** (fig.1.4), developed initially for the structure of rayon-based carbon fibres and extended, later, to all fibre types **[Fourdeux 1973]**, the carbon fibre basic structural unit is a ribbon-shaped graphitic layer which is present already in 1000°C heat treated fibres. The ribbons, with arbitrarily defined plane boundaries, have a width of about 60 Å and a length of several thousand Å. A number of ribbons run together to form microfibrils, which have a preferred orientation with respect to the fibre axis. The microfibrils are wrinkled and imperfections in packing create voids in their boundaries (typically 20 Å thick to 200 Å long).

In a parallel investigation **[Johnson 1969]**, the proposed carbon fibre model possesses a two-phase microstructure of crystallites and voids. Both crystallites (which comprise turbostratic graphite layer planes) and pores or voids, have a preferred orientation with the fibre axis. The dimension of crystallites vary upon the processing temperature. Typical values for 1300°C carbon fibres are 10 Å for L_c and 20 Å for L_a and for 2500°C carbon fibres 100 Å and 60 Å, respectively. The tetragonal idealized crystallites are stack end-to end (fig.1.5), with subgrain tilt or twist boundaries between them and separated by sharp-edged needle-like voids **[Johnson 1969]**.

The above model was subsequently modified **[Cooper 1971]** on the basis of observations that the voids are planar and lie between the graphite layer planes, or crystallites **[Heninckx 1968]**. These crystallites are quite large and can be followed for some distance throughout the structure, although they are kinked and distorted in such a way as to give the effect of a large number of smaller crystallites (fig.1.6).

More recently, a 3-dimensional model was developed **[Bennet 1976]**, resulting from X-ray diffraction and TEM observations of high modulus PAN-based fibres, which modifies the initial tetragonal idealised crystallite unit into a tube-like folding of graphite layers (fig.1.7).

In a similar approach, based on TEM observations, the suggested model **[Guigon 1984]** consists of staples of graphite layer-planes forming a tube-like structure. The basic structural unit (BSU, fig.1.8) is defined by

the parameters L_c (thickness), L_a (length), and r_t (curvature of BSU). The basic structural units are crumpled along the fibre axis like sheets of paper. Such crumpling results in irregular pores elongated parallel to the fibre axis. This model is applied to both high temperature (HT) and high tensile strength fibres (HTT), as shown in figure 1.9a and b. From the transverse section of the model the folding and crumpling of layers can be observed, producing a "skin-core" effect as the BSU layers flatten towards the outer surface.

The "skin-core" effect has also been detected in other investigations **[Hawthorne 1975, Chen 1983]**. Observations of a three dimensional phase structure in high modulus fibres **[Johnson 1973]**, led to the development of a structural model for a high modulus carbon fibre (fig.1.10), which takes into account the radial anisotropy **[Barnet 1974]**. According to this model, a high modulus fibre includes at least two phases consisting of turbostratic graphite ribbons interspersed with inclusions of three dimensional graphite, when the heat treatment process is above 2000°C. Both phases contain microvoids, microcracks and other lattice faults. The orientation of the material is less in the central part of the fibre ("core") while more perfect ribbons are located outside ("sheath"), with a mixed region in between. Although the surface is the most highly oriented part of the fibre, it still contains exposed edge-planes as well as basal planes.

(b). Surface treatment on carbon fibres.

It is not only the intrinsic properties of carbon fibres themselves that are significantly affected by the structural configuration of the material, but also the surface properties. The surface structure dominates the material's mechanical and adhesive properties and, through that, the performance of composite materials in which carbon fibres are the reinforcing filaments **[Donnet 1984, Kalnin 1985]**. The adhesion promoting surface treatment is based on the finding that oxidation of carbon fibres, while changing the initially hydrophobic surface of carbonaceous materials to hydrophylic, also increases the adhesive strength to polymeric materials **[Amon 1948]**. This treatment (usually a manufacturer's secret) may be oxidative (which is widely established and easier to perform), or non oxidative (such as recent developments of whiskerisation and surface

coating) **[Donnet 1984]**. The surface treatment may be carried out in **[Kalnin 1985]**:

(1) gas or liquid phase,

(2) low or elevated temperatures,

(3) by chemical, physical or other means which may bring about changes to the carbon fibre weight.

The techniques used and the way they affect the surface properties of carbon fibres have been described in various studies **[Rand 1977, Bahl 1984]**. The primary aim of the fibre surface treatment is the improvement of the interfacial properties of the fibre composites, by strengthening the fibre/resin bond. Three major mechanisms appear to contribute to the fibre/resin bond **[Rand 1977]**:

(a) absorption (either chemical or physical) of resin molecules onto the surface complexes,

(b) physical absorption onto the basal planes,

(c) mechanical "keying" effect, when the resin penetrates pits and channels on the roughened surface brought about during oxidation.

The carbon fibre surface treatment has been found to affect the intrinsic mechanical properties of carbon fibres, such as the Young's modulus and strength **[Bahl 1984]**, as well as the composite properties, such as the interlaminar shear strength (ILSS) **[Donnet 1984, Megerdigian 1987]**, the tensile and compressive strength, and the shear modulus **[Megerdigian 1987]**. The mechanical aspects of adhesion and its reinforcing role on the fibre/matrix interface will be further discussed in Chapter 5.

1.2. About the Method : Raman Spectroscopy.

In this project, Laser Raman Spectroscopy (LRS) is employed as the main experimental tool for the characterisation of the carbon fibre surface and subsequently for monitoring of deformations in fibres and composites, at a microscopic level. Therefore, a brief review of the background and the principals of LRS, as well as the basic aspects of molecular vibrations should be considered in order to introduce the terminology used in this specific spectroscopic approach.

1.2.1. *The Raman effect.*

The interaction of light (as a form of electromagnetic radiation) with matter can take place in a number of ways. Light can be transmitted through, reflected by, absorbed by and/or scattered by a material. When a beam of monochromatic radiation meets a substance, the scattered beam of light includes mainly an elastic portion (with frequency or energy equal to that of the incident beam), the so called Rayleigh Scattering. However, it also includes an inelastic fraction, estimated to be as low as one millionth of the elastic fraction **[Guillory 1977]**, the so called Raman Scattering. The latter comprises distinct frequencies or amounts of energy below and above that of the incident beam. This phenomenon is called the Raman effect **[Raman 1928]**.

A comprehensive modelling of the Raman effect is given by the quantum theory of radiation. Radiation of frequency ν_1 consists of a stream of photons having energy $E_1 = h \cdot \nu_1$, where h is Planck's constant. Photons can be imagined to undergo a collision with molecules and then to be scattered. If the collision is perfectly elastic, no change of frequency will occur in the backscattered radiation. However, when the collision is inelastic, a small amount of energy is exchanged between photons and molecule and the backscattered radiation has energy $E_2 = h \cdot \nu_2$. The difference $\Delta E = h \cdot (\nu_1 - \nu_2) = h \cdot \nu_{12}$ represents the gain (if $\Delta E > 0$) or the loss (if $\Delta E < 0$) of energy by the molecules **[Banwell 1983]**. Radiation with a frequency lower than that of the incident beam is referred to as "Stokes" radiation, while that with a higher frequency is called "anti-Stokes" radiation (fig.1.11) **[Szymanski 1967]**. The frequency change ν_{12} is called the Raman Shift, its

magnitude is referred to as the Raman Frequency and the set of Raman frequencies of the scattering species constitutes its Raman Spectrum. It is found that Raman Shifts correspond to vibrational and rotational transitions of the scattering molecule **[Szymanski 1967]**.

There are two distinct approaches in the fundamental study of the Raman Scattering. The classical one is based on the fact that light scattering phenomena may be given a classical explanation, in terms of the electromagnetic radiation produced by electric and magnetic multipoles of the material. These multipoles are induced in the scattering system by the electric and magnetic fields of the incident beam **[Long 1977]**. The quantum mechanical approach is based on a wave-mechanical analysis and especially on the wave-mechanical quantity known as transition moment. This quantity characterises the transition between two energy states of the scattering species **[Woodward 1972]**. A brief description of the two treatments is given below.

(a). Classical theory of Raman scattering.

The change of frequency of the backscattered light in the Raman effect does not involve absorption as with Infra-red spectroscopy. In the Raman effect we are concerned with the dipole moment π , which is induced to the molecule by the electric field of the incident light. Consisting as it does of positively charged nuclei in a "cloud" of negative electrons, a molecule is electrically polarisable. An applied electric field **E** will therefore induce in it, a dipole moment π which is related to the electric field of the light through the electric polarisability of the molecule **[Woodward 1972, Guillory 1977]**:

$$\pi = \alpha \cdot \mathbf{E} \qquad (1.1)$$

where π and **E** are vectors and α is the tensor of polarisability with nine coefficients α_{ij} , i,j = x,y,z in a Cartesian system of coordinates. The electric polarisability of a molecule as a function of all its normal vibrational modes Q (discussed further in the next paragraph), can be expanded in Taylor Series:

$$\alpha = \alpha_0 + \sum_{kk} \left(\frac{\partial \alpha}{\partial Q}\right)_0 \cdot Q_k \qquad (1.2)$$

where α_0 is the polarisability of the molecule in equilibrium and $(\partial\alpha/\partial Q_k)_0$ is the derived polarisability corresponding to the k_{th} normal vibrational mode. The induced dipole moment can now be expressed:

$$\pi = \alpha \cdot \mathbf{E} = \alpha_0 \cdot \mathbf{E} + \sum_{kk} \left\{ \left(\frac{\partial \alpha}{\partial Q}\right)_0 \cdot Q_k \right\} \cdot \mathbf{E} \qquad (1.3)$$

where the $\alpha_0 \cdot \mathbf{E}$ part represents the Rayleigh scattering and each of the summands describe the contribution of each normal mode to the Raman spectrum **[Woodward 1972]**.

(b). Quantum theory of Raman scattering.

In quantum-mechanical terms, if a transition from an initial state *m* to a final state *n* , is induced by incident radiation of a certain circular frequency, the transition moment amplitude associated with this change is given by the equation **[Long 1977]**:

$$P_{nm} = \int (\psi^{(n)} \cdot \pi \cdot \psi^{(m)}) d\tau = \mathbf{E} \cdot \int (\psi^{(n)} \cdot \alpha \cdot \psi^{(m)}) d\tau \qquad (1.4)$$

where $\psi^{(m)}$ and $\psi^{(n)}$ are the time-depended wave functions for the initial and the final states. The integral is all over the coordinate space. Using the expanded in Taylor's Series form for the polarisability tensor (eq.1.2), the transition moment amplitude can be expressed as :

$$P_{nm} = \mathbf{E} \cdot \alpha_0 \cdot \int \psi^{(n)} \cdot \psi^{(m)} d\tau + \mathbf{E} \cdot \sum \left(\left(\frac{\partial \alpha}{\partial Q_k}\right)_0 \cdot \int \psi^{(n)} \cdot Q_k \cdot \psi^{(m)} d\tau \right) \qquad (1.5)$$

where, again, as in the classical treatment, the first term corresponds to the Rayleigh scattering and each summand of the second term represents the contribution of each normal mode to the Raman spectrum **[Woodward 1972]**.

In both classical and quantum-mechanical treatments, the restricted selection rule which governs whether a particular normal vibrational mode shall be permitted or forbidden in Raman scattering, depends upon the factor $(\partial\alpha/\partial Q_k)_0$ **[Guillory 1977]**. If this factor vanishes the mode will be forbidden. Specifically, the rule states that only these normal modes can be active in Raman scattering, which satisfy the condition $(\partial\alpha_{ij}/\partial Q_k)\neq 0$, for at least one of the components of the molecular polarisability (i,j = x,y or z). A physical interpretation of this rule can be visualised by means of the polarisability ellipsoid of the molecule **[Guillory 1977]**. If the molecular displacement in the vibrating species induce change in its polarisability (and the shape of the polarisability ellipsoid - fig.1.12) then the specific vibrational mode is Raman active. If no change occurs in the polarisability shape then the vibrational mode is Raman inactive (fig.1.12).

The derivation of the restricted selection rules depends on two special approximate assumptions. The first is that the molecular vibrations are simple-harmonic and the second is that the higher order terms, of the expanded in Taylor Series polarisability tensor, are negligible. Relaxation of any of these assumptions - as in real molecules and crystals - means a change of the nature of the potential energy and, hence, also in the wave equation and its solutions.

1.2.2. *Molecular vibrations.*

When a molecule or crystal, containing N atoms, vibrates, the displacements of its atoms can be represented in terms of the internal coordinates q_1, q_2,..., q_N **[Burns 1977]**. They correspond to bond stretching, angle deformation, out of plane bending and torsion. In fact, not all the 3N degrees of freedom of the system are internal vibrations. Excluding the translational and the rotational motions there are 3N-6 (3N-5 for linear molecules) degrees of internal freedom. By taking this into account, another set of coordinates can be introduced - the fundamental or normal coordinates Q - to describe the vibrational modes of the system. A

characteristic fundamental frequency is associated with each of these normal vibrational modes. A normal vibrational mode can alternatively be defined as a state in which the center of gravity of the molecule does not move when all atoms move with the same frequency and in phase. Except in case of degeneracy (where two or more vibrational states have the same energy), each normal mode is independent of the others, in that anyone can occur without affecting the rest **[Woodward 1972]**. Both the potential energy V and the kinetic energy T of the system are expressed in terms of these coordinates **[Woodward 1972, Guillory 1977]**:

$$V = 1/2 \cdot \sum \lambda_k Q_k^2 \qquad (1.6)$$

$$T = 1/2 \cdot \sum (\dot{Q}_k)^2 \qquad (1.7)$$

where k = 1, 2, ...,3N-6 , $\dot{Q}_k = dQ_k/dt$, $\lambda = 4\pi\nu_k^2$ and ν_k the frequency associated with the vibrational mode Q_k. Now the classical equation of motion and the Hamiltonian of the system (total energy) can be expressed **[Woodward 1972, Guillory 1977]**:

$$\frac{d}{dt}(\partial T/ \partial \dot{Q}_k) + (\partial V/ \partial Q_k) = 0 \qquad (1.8)$$

$$H = T + V = 1/2 \sum (\dot{Q}_k)^2 + 1/2 \sum \lambda_k Q_k^2 \qquad (1.9)$$

The study of the molecular vibrations of a system using the classical mechanical approach is a quite complicated procedure. At first it requires the definition of the internal coordinates of the system and the exclusion of the rotational and transitional motions for the molecular system to derive the normal coordinates. Subsequently, the molecular symmetry and the intermolecular force-field (the force constants) should also be considered before assembling the secular equation of the system. The latter is derived from the equation of motion (eq.1.8). The final form of the secular equation is **[Woodward 1972]**:

$$| F - \lambda . G^{-1} | = 0 \qquad (1.10)$$

where $\mathbb{G}$ (Wilson matrix) is a matrix representation of the kinetic energy, $\mathbb{F}$ is a matrix representation of the potential energy, which depends on the force-field and λ is the eigenvalue vector for the determinant **[Woodward 1972]**. Even at this stage, the attempt to solve the secular determinant is an extremely difficult undertaking. This is due to the fact that the degree of the polynomial, which is obtained from the expansion of the secular determinant, is equal to the number of normal modes characterising the system. However, for any molecule possessing a degree of symmetry, a valuable simplification of the vibrational problem can be achieved by taking this symmetry fully into account, as discussed below.

(a). Molecular symmetry.

Molecules and crystals possess a high degree of symmetry. A symmetry operation on a molecule is any interchange of the atom positions, which results in no change in the appearance of the molecule before and after the operation. Point symmetry operations are those for which one point of the system is kept fixed. The symmetry operations can be inversions, rotations and reflections **[Woodward 1972, Long 1977, Burns 1977]**. The full set of symmetry operations applicable to a molecular model is said to constitute a mathematical point group. Point group theory is of a particular value in the study of the molecular vibrations of complex molecules **[Burns 1977]**.

The application of the point group theory to classify the symmetry in a molecule or crystal leads, eventually, to a simplified form of the determinant of the secular equation of motion (eq.1.10). The resulting determinant comprises only diagonal terms in a form of matrices of 1x1, 2x2 and 3x3 dimensions. When each vibrational mode is independently described by one of these matrices, this representation of the secular equation is called the irreducible representation Γ **[Woodward 1972]**. Matrix blocks of (1x1) correspond to non-degenerate vibrations and are denoted with the letters A and B. Vibrational modes with two-fold degeneracy are denoted with the letter E and are represented by (2x2) matrices in the irreducible representation Γ. If the molecule has a centre of symmetry, then the subscripts *g* and *u* are attached to the letters A,B, and E to indicate whether the vibrations are symmetric or antisymmetric, with respect to inversion at the centre of symmetry. In addition, the subscripts 1,2 are used to distinguish the symmetry of the vibrational mode about a rotational axis of the molecule **[Turrell 1972]**.

(b). Application of group theory on graphite.

Pristine graphite has symmetry consistent with the D_{6h}^4 space group **[Tuinstra 1970a, Dresselhaus 1977]**. The Schoenflies notation for graphite's space group reveals the following details for its symmetry properties **[Tuinstra 1970a, Nemanich 1979]**. The crystal belongs to the D_{6h} point group (fig.1.13), which means that the unit cell has 6 two-fold axes (hexagonal crystal system) perpendicular to the C_6 axis of highest order and a plane of symmetry (σ_h) perpendicular to the same axis **[Janssen 1973]**. Twenty four symmetry operations can be applied to the crystal belonging to 12 vibrational modes (six independent). The direct sum of the irreducible representation for graphite is **[Tuinstra 1970a, Dresselhaus 1977, Nemanich 1977]**:

$$\Gamma = 2B_{2g} + 2E_{2g} + A_{2u} + E_{1u} \qquad (1.12)$$

The acoustic ones are A_{2u} and E_{1u}, the E modes involve motions within the layer planes, whereas the A and B modes are characterised by atomic displacements normal to the planes. A schematic representation of the above displayed vibrational modes is given in figure 1.14. The frequency values corresponding to each vibrational mode $\nu(Q)$, can be calculated if the force constants for the graphitic force-field are known **[Al-Jishi 1982, Lespade 1982]**, or measured using techniques like Infra-Red **[Nemanich 1977]** and Raman Spectroscopy **[Tuinstra 1970a, Dresselhaus 1977, Nemanich 1979]**. ▮

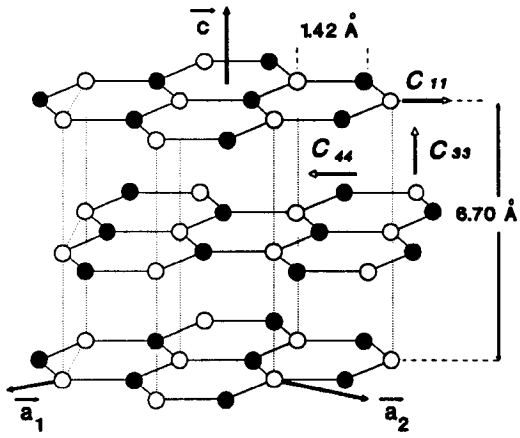

Fig.1.1 The characteristic structure of the graphite crystal.

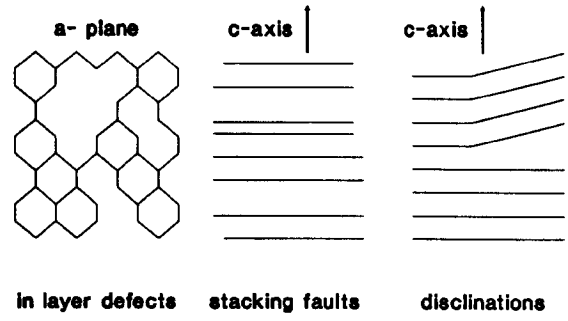

Fig.1.2 Defects in the graphite lattice.

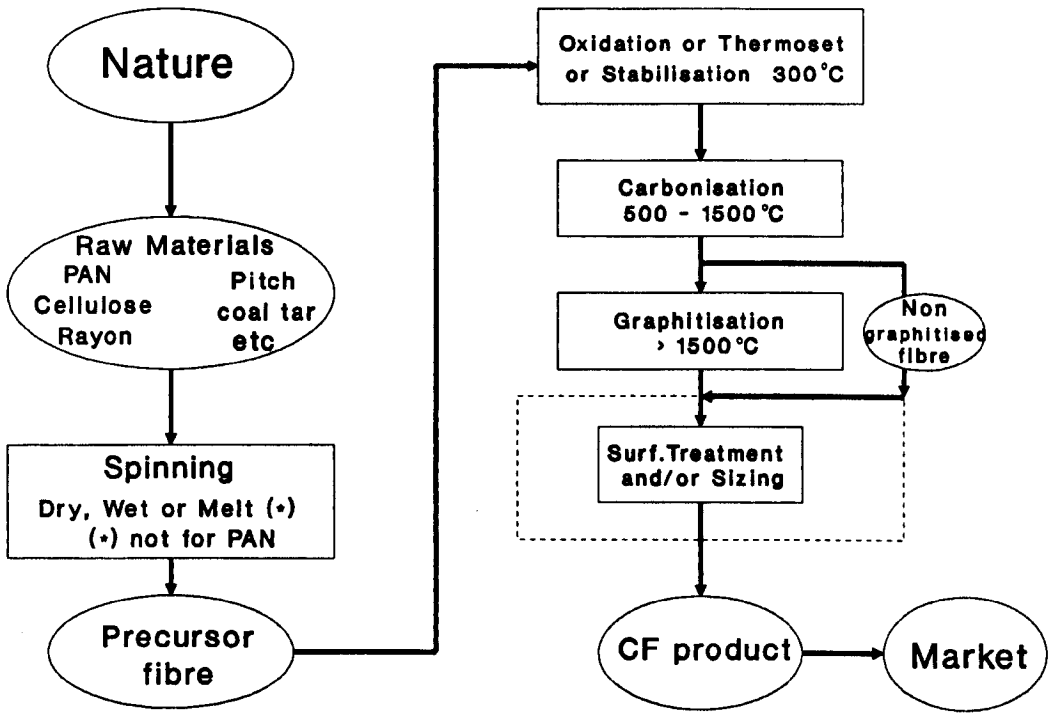

Fig.1.3 The carbon fibre production line.

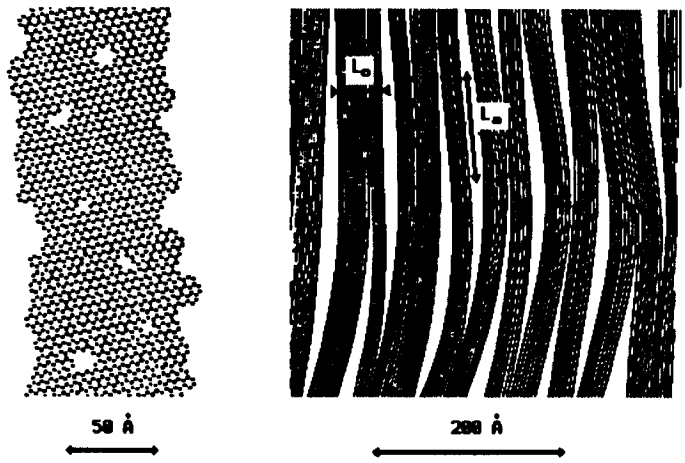

Fig.1.4 Ruland's model of the carbon fibre structure **[Ruland 1967, Fourdeux 1973].**

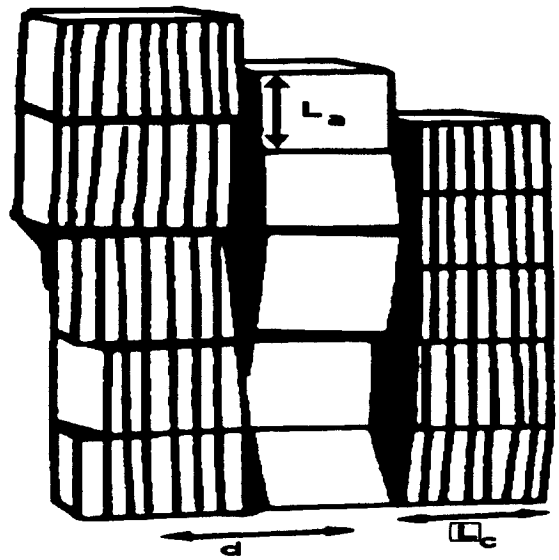

Fig.1.5 Johnson's initial model of the carbon fibre structure **[Johnson 1969].**

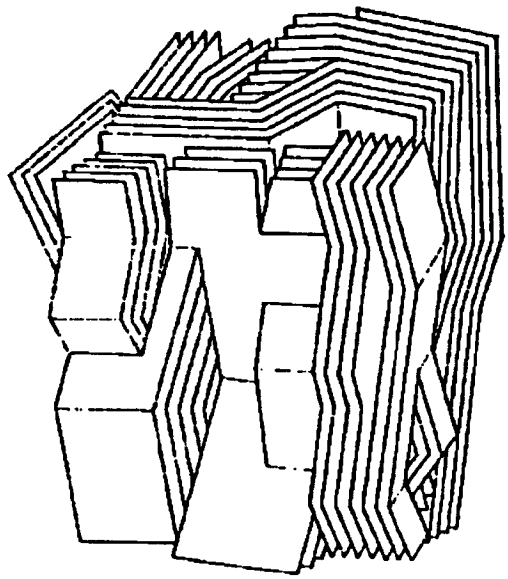

Fig.1.6 Cooper's modification of Johnson's model of the carbon fibre structure **[Cooper 1971]**.

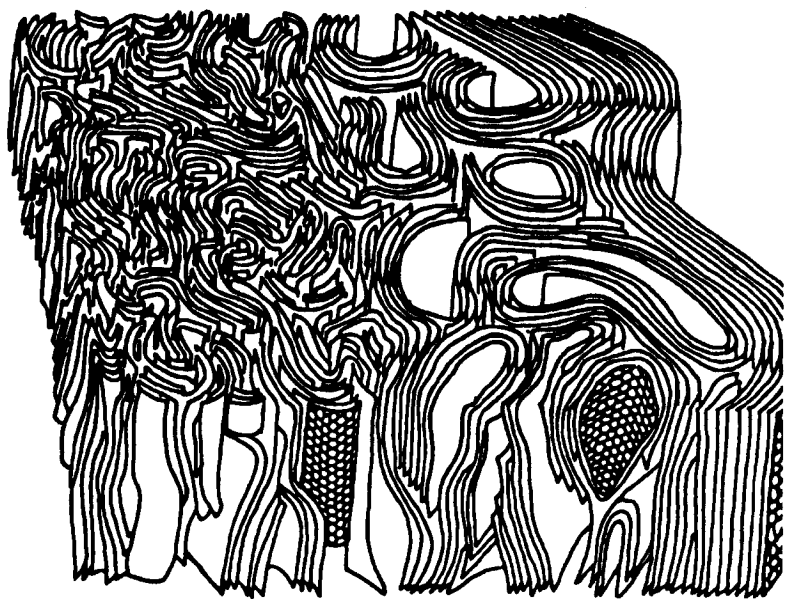

Fig.1.7 A three dimensional model of the carbon fibre structure **[Bennet 1976]**.

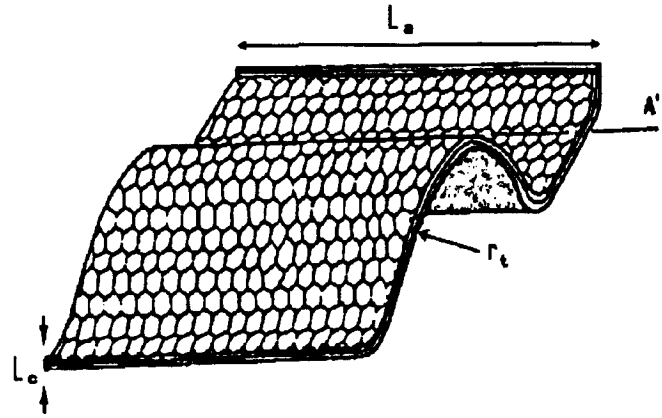

Fig.1.8 The basic structural unit (BSU) and its geometrical parameters **[Guigon 1984].**

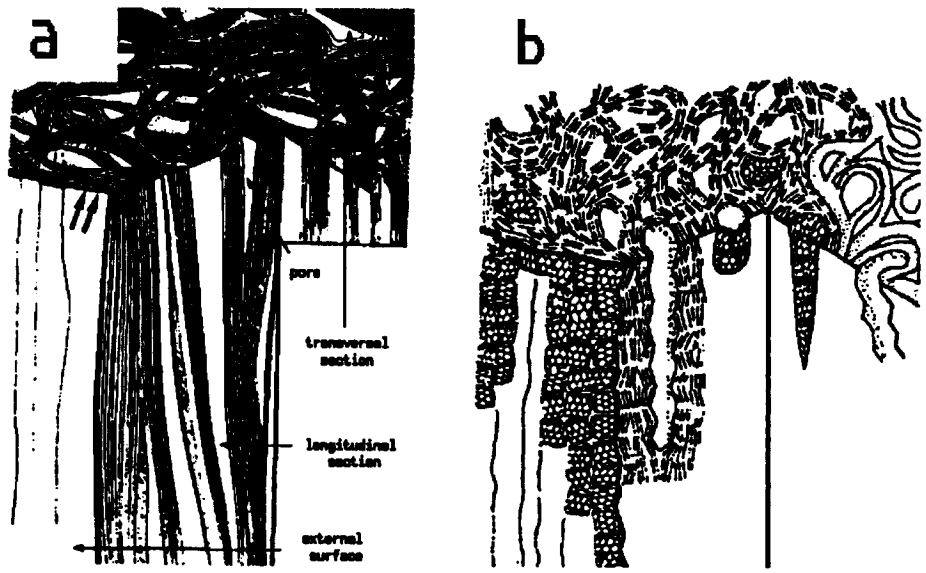

Fig.1.9 Guigon's model of structure of **(a)** high modulus and **(b)** high strength carbon fibres **[Guigon 1984].**

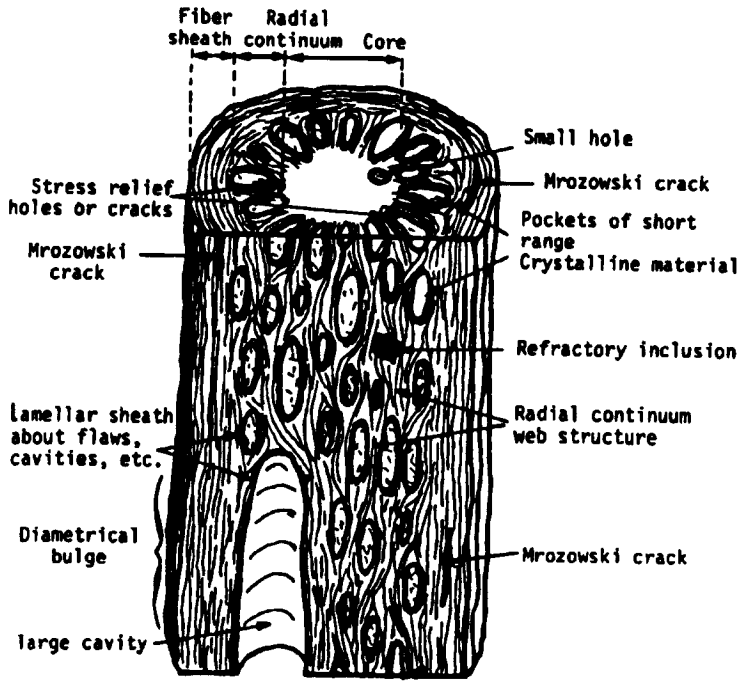

Fig.1.10 Barnet's three dimensional model of the carbon fibre structure **[Barnet 1974, Kalnin 1985].**

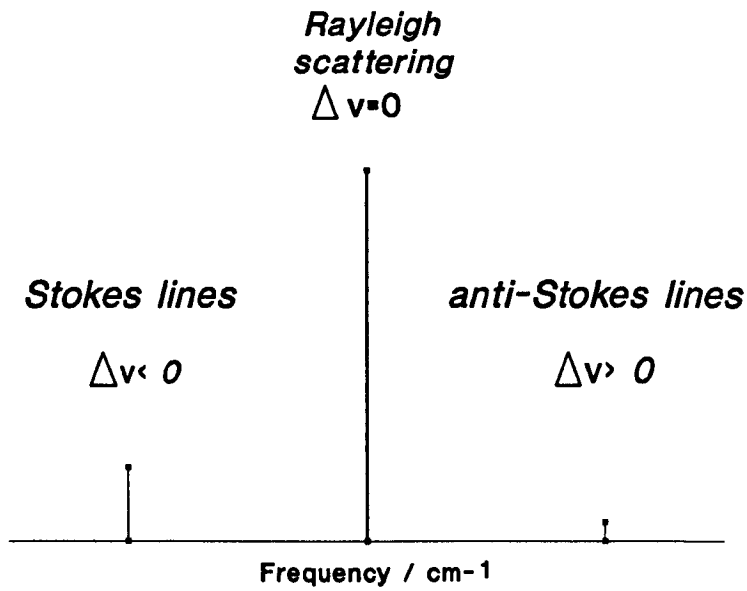

Fig.1.11 The Stokes and anti-Stokes lines in the Raman spectrum.

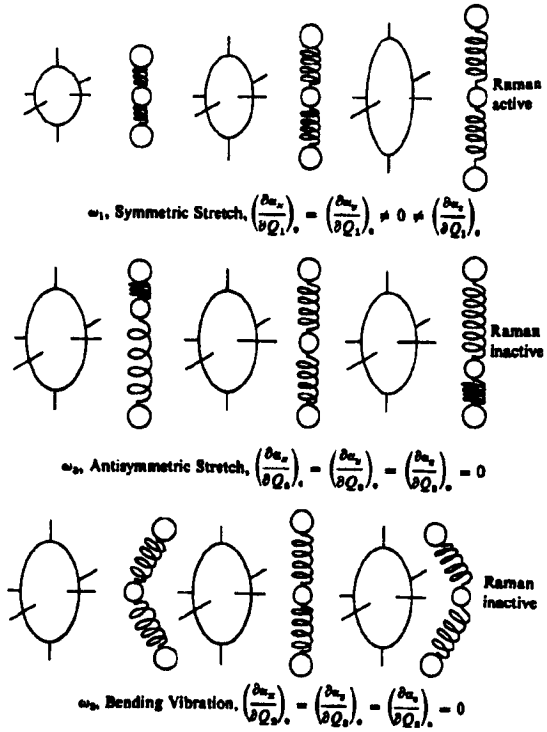

Fig.1.12 The change in polarisability (and the polarisability ellipsoid) and the Raman activity of a vibrational mode **[Guillory 1977]**.

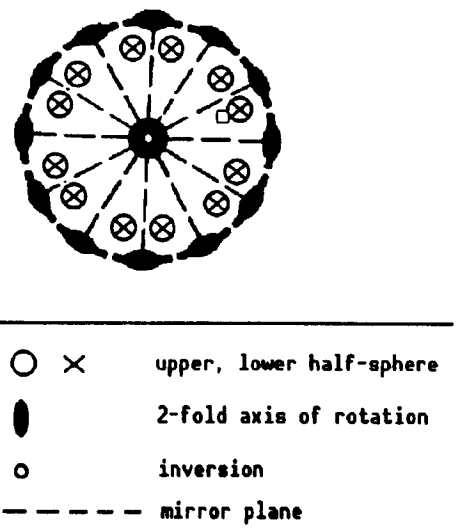

Fig.1.13 Geometric representation of the crystallographic point group D_{6h} **[Janssen 1973]**.

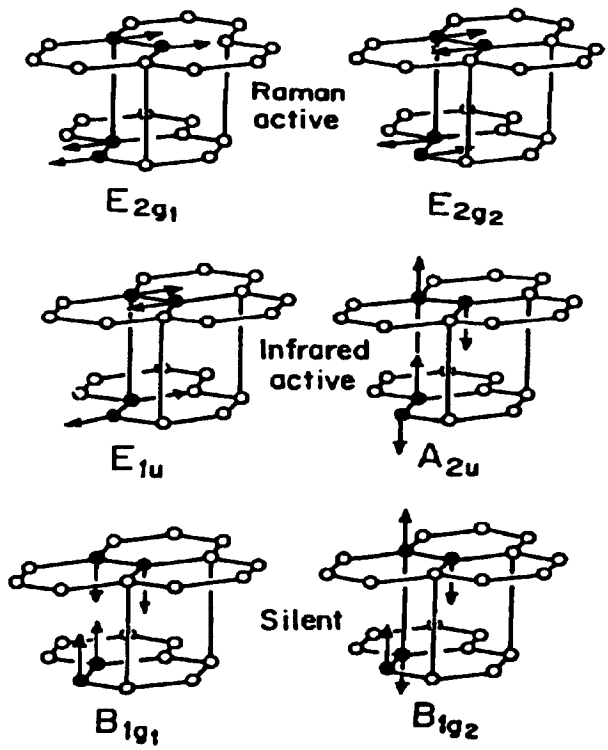

Fig.1.14 Schematic representation of the vibrational modes of the graphite crystal **[Nemanich 1977a, Dresselhaus 1988]**.

CHAPTER 2

CHARACTERISATION OF CARBON FIBRES USING LRS

2.1. Introduction and literature review.

The potential of Laser Raman Spectroscopy (LRS) as a non-destructive technique for material characterisation is now widely recognised **[Summerscales 1987]**. The invention of laser revived the interest in the Raman effect, due to the advantages of the highly collimated, intense, coherent and monochromatic radiation, over other sources of light **[Beesley 1971]**. In addition, its recent application for strain measurements in fibres **[Galiotis 1985, 1988a, Robinson 1987]** and composites **[Galiotis 1988b]** at microscopic level, has further enhanced the usefulness of Laser Raman spectroscopy as a non-destructive method.

Raman Spectroscopy on graphite, carbons and carbon fibres is inseparably related to the study of the graphite structure. The lattice dynamics of graphite have been extensively investigated in the past **[Yoshimori 1956]** and various force constant models have been developed **[Dresselhaus 1977, Nicholshon 1977]**. The determination of a force constant model and subsequently the phonon dispersion relations of graphite **[Maeda 1979, Al-Jishi 1982]** have allowed the distribution of the lattice frequencies to be theoretically calculated **[Al-Jishi 1982, Lespade 1982a]**. The experimental Raman studies on graphite and carbons reviewed below, cover a frequency range from 0 to 3300 cm^{-1}. The frequency range up to 1650 cm^{-1} has been denoted as the "first-order region" and from 1650 cm^{-1} to 3300 cm^{-1}, as the "second-order region". These terms refer to the fundamental and overtone/combination frequencies of the scattering species, respectively **[Turrell 1972]**.

2.1.1. *First-order region Raman spectrum.*

The "graphitic" band.

The most prominent feature in the Raman spectrum of graphite and carbons is the Raman band appearing at about 1580 cm^{-1} **[Tuinstra 1970a&b]**. This line, has been unanimously assigned to the double degenerate vibrational mode E_{2g} of graphite (fig.1.14) **[Tuinstra 1970 a&b, Nakamizo 1974]**. This vibrational mode is the only one allowed by the Raman selection rules, in the single graphite crystal and corresponds to a sharp

and intense line in the Raman spectrum **[Tuinstra 1970a, Nemanich 1979]**. It has been found to become less intense and broader for polycrystalline materials, as can be "smeared out" by adjacent growing bands in the Raman spectrum of non-graphitised carbons **[Nemanich 1979]**.

The "disorder" band.

Another less prominent band appears at about 1360 cm^{-1} and is attributed to the breakdown of the lattice symmetry of the graphite unit cell. Although the presence of this band is, generally, attributed to a higher level of disorder in the polycrystalline structure, conflicting views have been expressed concerning its origin. The development of this line has been related to (i) the increase in the amount of "disorganised" graphite and (ii) the decrease of the graphite crystal size **[Tuinstra 1970 a&b]**. Through this analysis, it has been assigned to the A_{1g} vibrational mode (the "breathing" vibration in the graphite plane shown in figure 2.1) of the D_{3h} space symmetry possessed by "finite" crystallites only **[Tuinstra 1970 a&b]**. The intensity ratio between this and the 1580 cm^{-1} bands, was found to be proportional to $1/L_a$, where L_a is the length of the graphite crystallite unit in the carbon fibre structure **[Tuinstra 1970a]**.

However, other researchers **[Nakamizo 1974]** have attributed the appearance of the 1360 cm^{-1} band to the growth of polycondensed aromatic planes in disordered carbons, as found from the Raman study of other carbonaceous materials. Using the phonon dispersion curves and lattice dynamics analysis, the presence of the 1360 cm^{-1} line was explained as being due to the high phonon density of states at two points of the Brillouin zone **[Tsu 1978]**, following a distortion in the crystal structure. This would suggest a breakdown of the usual selection rules which determine Raman activity **[Chieu 1982]**.

All of the above approaches have considered the "disorder" induced line at 1360 cm^{-1} to be an in-plane vibration. A different approach was based on the observation of the scattering angular dependence of the intensity of all Raman bands on Graphon carbon black **[Menarch 1984]**. Here, the 1360 cm^{-1} line was found to be the less sensitive of all bands and was associated with the non-planar zones of microstructure distortion. The theoretical support for such an assessment was given by the modelling of

disordered carbons in terms of the C_{6v}^4 space group symmetry and C_{3v} layer site symmetry possessed by that material **[Menarch 1984]**.

Raman studies on the edge planes of graphite fibres (fig.2.2) have recently been undertaken **[Katagiri 1984, 1988]**. According to these investigations, the 1360 cm^{-1} line is due to vibrations arising from edge planes that penetrate the surface in less graphitised materials, where the D_{6h} group symmetry is not maintained. This type of discontinuity can be regarded as a kind of imperfection, the nature of which controls also the broadness of that "disorder" induced band **[Katagiri 1984, 1988]**.

The origin of the 1360 cm^{-1} line, according to a quite different approach, was attributed to the sp^3 configuration of the carbon atoms in the disordered carbons, similar to the one observed in diamond-like structures **[Fitzer 1987, 1988 c&d]**. The diamond Raman spectrum has, indeed, a strong feature at 1332 cm^{-1}. In the case of carbon fibres, it has been claimed **[Fitzer 1988d]** that the diamond line has a frequency shift to higher values, at 1360 cm^{-1}, due to smaller bond length of the carbon atoms in that peculiar sp^3 hybridisation. However, x-ray analysis has failed to show any evidence for the existence of such a structure **[Fitzer 1988d]**.

The "graphitic shoulder".

A third, even less intense peak in the Raman spectrum of carbon fibres appears at about 1620 cm^{-1}. This peak is strongly related to the 1360 cm^{-1} band, being another disorder induced feature **[Katagiri 1988]**. It was initially thought to be the counterpart of the double degenerate E_{2g} mode, which for disordered carbons, splits into two bands, at 1590 cm^{-1} and at 1627 cm^{-1}, respectively **[Tsu 1978]**.

However, more careful observations showed that the behaviour of this line is closely related to the "disorder" induced 1360 cm^{-1} band, with their intensities being inversely proportional to the degree of graphitisation and linearly related to the decrease of the crystallite size L_a **[Chieu 1982]**. Further work has demonstrated that this feature corresponds to a maximum in the vibrational density of states **[Chieu 1982]** and becomes attenuated as long range two dimensional ordering is established and three dimensional ordering develops **[Chieu 1982]**. Finally the edge plane concept has also been employed to explain the origin of the 1620 cm^{-1} line **[Katagiri 1984]**.

Other bands.

Another first-order region line reported is the 48 cm^{-1} low frequency E_{2g2} which is only obtained using special techniques as it is so close to the laser line **[Nemanich 1979]**. Extra Raman features have been reported, but not clearly identified in the region 1100 - 1300 cm^{-1} **[Nemanich 1979]**. This type of Raman activity has been theoretically predicted in lattice dynamics models of graphite **[Lespade 1982a, Yoshimori 1956]**. Finally, in a study of the Raman spectrum of pitch fibres through various stages of their structural composition, a quite strong feature was present at about 1240 cm^{-1} and was attributed to a C-H bending vibration, during low graphitisation stages **[Sasaki 1984]**.

2.1.2. *Second-order region Raman spectrum.*

The second-order region Raman spectrum has been explained in terms of a two-phonon analysis **[Loudon 1964]**. If the two-phonon state is formed from two phonons of equal energy, in the same branch of the phonon dispersion curves, the resulting state is called an overtone. When the state represents the sum or difference of two phonons of unequal energy is then termed a combination **[Turrell 1972, Nemanich 1979]**.

The stronger band in this region is the line appearing at about 2700 cm^{-1} for both crystalline graphite and microcrystalline carbons **[Nemanich 1979]**. This is a sharp and intense band, though it broadens with increasing disorder **[Chieu 1982]**. The frequencies reported for this band vary considerably from 2700 cm^{-1} **[Menarch 1984, Nemanich 1979]** to 2730 cm^{-1} **[Chieu 1982, 1983]**. This is due to an unresolved "shoulder" feature at 2700 cm^{-1} at the leading edge of the main 2730 cm^{-1} **[Chieu 1983]** in highly graphitised carbons **[Lespade 1984]**. The 2700 cm^{-1} feature dominates the region in the spectrum of most carbon fibres. This line has been considered as the overtone (2x1360) of the 1360 cm^{-1} disorder induced mode **[Nemanich 1979, Chieu 1982]**.

Another feature in this region, which is sharp only in highly crystalline graphites and fibres is the 3250 cm^{-1} line. It is considered to be the second-order counterpart of the 1620 cm^{-1} line (2x1620) **[Nemanich 1979, Chieu 1982]**.

The Raman band at 2950 cm^{-1} seems to be another "disorder" induced feature, which does not appear in single graphite crystals and becomes more observable as the crystallite size L_a decreases **[Nemanich 1979, Chieu 1982]**. This second-order region feature is assigned to a combination vibrational mode, as the sum of the 1360 cm^{-1} band with either the 1620 cm^{-1} line **[Nemanich 1979]**, or with the 1580 cm^{-1}line **[Wright 1976]**.

As it has already become apparent, not all the features in the second-order region have been well-understood. The 2450 cm^{-1} is one of them; it appears small and sharp in highly crystalline fibres but broader for polycrystalline carbons, following the same trend as most of the features in the second-order region **[Nemanich 1979]**. Only a few references exist in literature on the nature of this line. However, according to one study **[Nemanich 1979]**, this band may be related to possible Raman activity of the region between 1100 and 1300 cm^{-1} **[Lespade 1982a, Sasaki 1984]**.

2.1.3. *Polarisation, temperature and wavelength dependence of the Raman spectrum.*

Polarisation effects in the Raman spectrum of graphite and carbon fibres are not extensively reported in the literature. Initially, polarisation effects were not detected **[Tuinstra 1970a]**. In recent Raman studies of the graphite edge planes **[Katagiri 1984, 1988]**, the polarisation configuration was found to affect the intensity of each Raman line itself, as well as the relative intensities between different Raman lines of the same spectrum.

The temperature dependence of the Raman frequencies of carbon materials is also rarely reported in the literature. Work on graphite particles **[Lespade 1982b]** has shown that a frequency shift of the E_{2g} vibrational mode from 1581 cm^{-1} to 1573 cm^{-1} can be observed, with a four-fold increase of the laser power. On the other hand, no shift was observed when the particles were embedded in a transparent and thermally conductive matrix. In another investigation on highly oriented pyrolytic graphite (HOPG), the linear dependence of the 1580 cm^{-1} and the 2700 cm^{-1} lines with temperature was determined to be about -2.8×10^{-2} cm^{-1}/degree and -5.6×10^{-2} cm^{-1}/degree, respectively **[Ebril 1981]**. On the other hand, an increase in the frequency of the E_{2g} mode of HOPG was reported on

cooling **[Nemanich 1977b]**.

A detailed study of the temperature dependence of the 1360 cm^{-1}, the 1580 cm^{-1} and the 2720 cm^{-1} lines of disordered carbons **[Fischbach 1986]**, provided numerical evidence for the effect. All values reported ranged between -0.9×10^{-2} and -2.7×10^{-2} cm^{-1}/degree over a temperature range of 300 K. The stronger dependence was found for the 1580 cm^{-1} line, followed of that of the 2720 cm^{-1} band. The temperature dependence of the 1360 cm^{-1} line was found to be half that of the 2720 cm^{-1} band. No temperature effects on the line bandwidths have been observed **[Lespade 1982b, Fischbach 1986]**. The negative temperature dependence of the Raman frequencies of carbons has been attributed to the complicated interatomic motions and the influence of negative off-diagonal terms in the anharmonic Hamiltonian of the system **[Nemanich 1977b]**, which simply implies that changes in temperature alter the interatomic lengths and, therefore, the force constants of the lattice.

In a recent study on laser heating effects on the Raman spectrum of carbon fibres **[Ager 1990]**, the largest frequency negative shift observed on the 1580 cm^{-1} band of a high modulus fibre was about 13 cm^{-1} at a laser power of 30mW on the sample. Above this laser power level the fibre was physically damaged. The negative shift became more pronounced as the fibre modulus decreased. The position of the 1360 cm^{-1} line, as well as, the intensity ratio between the two major bands in the first-order region were also affected. It was concluded that laser heating effects are significantly larger in fibres with smaller longitudinal thermal conductivity.

A systematic study of the effect of the excitation wavelength on the Raman bands of carbons yielded interesting information about the nature and origin of the Raman lines **[Vidano 1981]**. According to this survey, the bands located at 1360, 2720, and 2950 cm^{-1}, for an excitation wavelength λ of 488 nm, shifted to lower frequencies as λ increased to 647.1 nm. The 1580 and 1620 cm^{-1} bands did not not change. Over this wavelength range, the 1360 cm^{-1} line shifted about 35 cm^{-1} whereas the 2720 cm^{-1} band shifted by approximately twice this amount. This behaviour is consistent with the assignment of the 2720 cm^{-1} line as the overtone of the line at 1360 cm^{-1} and the 2950 cm^{-1} band as the combination mode of the 1360 cm^{-1} with either the 1620 cm^{-1} or the 1580 cm^{-1} band **[Nemanich 1979, Chieu 1982]**. It is possible that the band shifting with wavelength might be related to probing

the structure at different depths below the surface. The penetration depth δ of the laser beam in a material is linearly dependent upon the light wavelength:

$$\delta = \lambda/(4\pi n\kappa) \qquad (2.1)$$

where λ is wavelength, n the refractive index and κ the extinction coefficient of the crystal. Therefore, the optical depth at 647.1 nm is expected to be 30% higher than that at 488 nm radiation **[Vidano 1981]**.

To cope with the problem arising from the small shifts of the Raman bands with temperature or wavelength a letter notation for the most important Raman lines has been introduced **[Vidano 1981]**. This notation ascribes the 1360 cm^{-1} band as the D-line, the 1580 cm^{-1} band as the G-line an the remaining 1620, 2720 and 2950 cm^{-1} bands as D′, G′ and G′′, respectively. This terminology will be widely used in the forthcoming paragraphs.

2.2. Experimental.

2.2.1. *The Raman setup and data acquisition.*

The Raman setup is schematically displayed in figure 2.3. Its various components are denoted in this figure by the letters A, B, C etc, and they are described below. The laser source (figure 2.3, A) is an Argon-ion laser Lexel Model 85 (water-cooled) of maximum power 2.5 W. It is equipped with power control and wavelength tunability covering the range of 458 nm to 514.5 nm (green line). The latter is the excitation wavelength used in this investigation. The laser light is directed through a set of optical mirrors (B) and a plasma line filter (C) to a Nikon Raman microscope (D), through which the laser beam is focused on the specimen. The specimen is positioned on an X-Y-Z translation stage (E), beneath the microscope. Using a long working distance Olympus objective (x50), the beam is converged to a 2 μm focal spot. The focusing is controlled and monitored by a CCTV camera (F).

The 180° backscattered light is collected by the microscope objective and redirected through a spatial filter (G) to the entrance slit of a SPEX-1877 triple monochromator (H) (the dispersing system), specially tailored to provide low stray light and flat, undistorted focal plane, ideal for sensitive light imaging. The spectrometer (H) is supplied with a spectrograph stage with 3 gratings, for low, medium and high resolution and spectral coverage of 5300 cm^{-1}, 1320 cm^{-1}, and 870 cm^{-1}, respectively (for the green line). The total spectral range is from 185 nm to 1000 nm (54000 cm^{-1} to 10000 cm^{-1}), with wavelength accuracy of + 0.5 nm and resettability of + 0.2 nm.

A CCD (charge-coupled-device) nitrogen-cooled camera produced by Wright Instruments and employed as the photon detection system, is attached to the other end of the spectrometer (I). The Raman signal is delivered to the imaging area of the CCD camera (600x400 pixels), where it is converted to an electrical signal. In turn, this is transmitted to a PC-AT computer (J) for recording and subsequent analysis. The great advantage of this system in comparison with the photomultiplier used in the past, is a 30 times reduction of the required Raman spectrum acquisition time.

The whole Raman setup is mounted on an anti-vibrational optical table (K) (Photon Control) powered by a nitrogen bottled gas supply.

The analysed backscattered laser light is dispersed on the microchip of the CCD camera forming a characteristic image pattern, shown in figure 2.4. The horizontal axis corresponds to the frequency or wavelength axis, while the vertical one is the intensity (number of photons detected) axis. Image analysis of this pattern results in the intensity versus frequency plot of figure 2.4, which is the established way of spectral representation. The spectrometer/CCD camera resolution at the high and low resolution gratings are 0.020 nm and 0.125 nm per pixel, respectively. In wavenumber terms this is translated into 0.66 cm^{-1} and 4 cm^{-1} per pixel, respectively (when the spectrometer is centered at 560 nm).

2.2.2. *Spectrum analysis.*

The collected Raman signal is processed using a dedicated software package supplied by Wright Instruments. A representative hardcopy output of a typical spectrum and its analysis is shown in figure 2.5. The filename under which the raw data is recorded is displayed at the top of the screen. In the graphics window the intensity of the spectral features (number of photons detected) is plotted as a function of the frequency. The line fitted to the raw data consists of:
(a) the background estimate, which has a quadratic form :

$$Q= a_0 + a_1 \cdot x + a_2 \cdot x^2 \qquad (2.2a)$$

The quadratic coefficients a_0, a_1 and a_2 correspond to the intercept of the intensity axis when x=0, the slope of the background and its degree of curvature, respectively. Their values are plotted in the table below the graphics window (fig.2.5),
(b) the Lorentzian distribution function of the first frequency peak:

$$L=a_0 \cdot [a_2^2/((x-a_1)^2 + a_2^2)] \qquad (2.2b)$$

where a_0 expresses the intensity of the peak, a_1 the centered value of the distribution and $2 \cdot a_2$ the half-height-bandwidth (HHBW) of the Lorentzian distribution. Regression of the spectral data, using a Gaussian distribution, is also available. Up to 9 curves, including the background, can be calculated for one spectrum and the overall summation is fitted to

the raw data.

In complicated spectra, where one or more of the features have been well characterised independently, one of the coefficients a_1, a_2 can be fixed to a certain value, to facilitate the characterisation for the rest of the spectral features. This technique is mainly applied in cases of neighbouring bands, where the trailing edge of one overlaps with the leading edge of the other. As an example, it can be used to resolve the carbon fibre Raman signal from a composite fibre/resin spectrum. However, when strong resin Raman activity swamps the fibre frequency bands, additional physical filtering of the signal becomes necessary to remove "unwanted" components.

In general, the Raman characterisation of a fibre follows a certain experimental procedure. Initially, the backscattered laser beam is analysed by the low resolution grating of the spectrometer (dispersion : 0.125 nm per pixel of the CCD chip). This allows a wide frequency band of the fibre spectrum to be obtained in one exposure, so that the relative intensities between the spectral lines can be compared. The Raman spectrum obtained by the low resolution grating is always plotted as a function of the wavelength (nm); since the wavenumber (cm^{-1}) is inversely proportional to the wavelength (nm), a wide spectral coverage of the Raman spectrum exhibits strong non-linearities if it is plotted as a function of frequency (or wavenumber, cm^{-1}).

Every pronounced frequency band of the spectrum is subsequently analysed using the high resolution grating of the spectrometer (dispersion : 0.020 nm per pixel of the CCD chip). This allows close examination of interacting Raman bands, as well as accurate measurement of the bandwidths of various frequency peaks. When using the high resolution grating, the wavenumber (cm^{-1}) scaling of the x-axis is quite accurate. The whole procedure described above is demonstrated in figure 2.6, for the Raman spectrum of a high modulus carbon fibre.

2.2.3. *Materials.*

Almost all carbon fibres examined were supplied by Courtaulds Grafil plc. They can be classified into three general categories with respect to their diameter and the route of their manufacture.

The first group, consists of the 7 microns technology fibres. It includes a high modulus fibre HM, both in the untreated (HMU) and in the standard treated form (HMS), an intermediate modulus fibre IMS, which is a laboratory fibre produced for the purposes of this study, and, finally, a low modulus commercial fibre of five different treatments, XA0, XA1, XA2, XA3, and XA4, where the number 0,1,...4, indicates the "amount" of treatment as coded by the manufacturer. Treatment "1" is the standard treatment for this fibre (XA1=XAS).

The second group includes four 5 microns technology fibres, three of which are laboratory fibres and one, the IM 43-750 (or IM43, or IMD), is a commercial product. Their modulus ranges from between 305 GPa to 405 GPa. The commercial brand (305 GPa), in particular, has been supplied in 6 different surface treatments, denoted by the letters A(0% treatment), B(5%), C(20%), D(50%), E(100%) and F(200%). The IMA corresponds to the untreated fibre, whereas the IMD characterises the standard (optimum) treatment.

In both groups of fibres, the lowest modulus fibre has been produced at low graphitisation temperatures (about 1300°C for a 230 GPa modulus fibre **[Dresselhaus 1988]**). This exhibits the smallest crystallite dimensions (L_a and L_c), as well as the widest angles of crystallite orientation, ϕ, measured with reference to the fibre axis. To produce higher modulus fibres the graphitisation (heat treatment) temperature is increased (over 2000°C for a modulus above 400 GPa **[Dresselhaus 1988]**), resulting in a fibre product with a larger crystallite size, and improved orientation. These established principles and procedures **[Jenkins 1976, Donnet 1984]** are applied in the production of these two groups of fibres. However, no specific information on the heat treatment temperatures is available. The differences between two fibres that exhibit similar Young's modulus but belong to a different group, are related to morphological variations in the crystallite size and the preferred orientation. These have been achieved by modifications in the classic manufacturing technology. Specific details have not been fully published by the manufacturer. It is believed that the "modifications in the classic manufacturing technology" involve different amounts of prestretching applied to the precursor fibre, at different stages of the stabilisation and the carbonisation procedures. The controlled alteration of parameters such as heat treatment temperature and prestretching of the precursor fibre can yield carbon fibres with similar modulus but different morphological

characteristics **[Crasto 1990]**.

A third group of fibres was specifically produced to study this morphological transition. All three of them possess similar Young's modulus, but exhibit a significantly different surface morphology. The notation "neutral morphology" is assigned to the fibre (LF-neut) with structural characteristics identical to the 5 microns technology fibre; the term "negative morphology" refers to the fibre (LF-neg) with surface features resembling the 7 microns technology fibre. This fibre possesses the highest degree of surface crystallinity of all three fibres (i.e. the largest crystallite dimensions and the highest degree of orientation). Finally, the classification "positive morphology" is given to the fibre (LF-pos) which exhibits the lowest degree of crystallinity out of all three fibres in this group. The manufacturer quoted diameter and mechanical properties of all the carbon fibres employed in the following Raman studies are displayed in Table 2.1.

2.2.4. *Other experimental details.*

To obtain the Raman spectrum of a carbon fibre the specimen is mounted on microscope slides and positioned on the translational experimental stage (fig.2.3 -(E)). The fibre is aligned with its axis parallel to the polarisation direction of the incident beam (fig.2.7a). The laser beam (usually ~1 mW on the sample) is subsequently focused on the surface of the filament. A typical exposure time required for a spectrum acquisition is 30 seconds.

The effect of the laser power on the Raman spectrum of carbon fibres is studied by increasing the power of the probing laser beam from 0.5 mW to 8 mW, at discrete steps.

For the Raman study of the fibre cross-section single filaments are embedded in a thermoplastic matrix (Cerafix), mildly ground and polished in the plane normal to the fibre axis **[Tetlow 1990]**. The laser beam is focused in approximately the middle of the fibre cross-section (fig.2.7b) and the Raman spectrum of the region can be obtained in both the high and the low resolution mode.

2.3. Results.

The full spectrum and the main spectral lines of all carbon fibres have been examined in detail. The intensities, real and relative, the position of the Raman lines and the bandwidth of all these lines have been measured and classified. The effect of the laser power upon the above has also been examined. Furthermore, the Laser Raman characterisation technique has been employed to assess the structural effects of the surface treatment on the carbon fibre surface layers. Finally, the Raman spectrum of the carbon fibre cross-section has been obtained, in an attempt to probe the carbon fibre core. It should be noted that the penetrating depth of the laser beam is estimated about 50 nm [**Tuinstra 1970a**]. It must be realised, therefore, that the information contained in the Raman spectrum of a carbon fibre is primarily obtained from a surface layer of about 50 nm thickness, that is less than 1% of the fibre diameter.

2.3.1. *The first and second-order Raman spectrum.*

The first and second-order Raman spectrum of 10 carbon fibres (of standard treatment), is presented in this section. All spectra have been obtained after 30 seconds exposure of the sample under ~1 mW of laser power. The laser light was always polarised parallel to the fibre axis and this polarisation was mostly preserved in the backscattered light.

(a) The first and second-order Raman spectrum of the 7 microns diameter carbon fibres.

With respect to the 7 μm series, the spectra of the HMS, IMS and XAS carbon fibres are presented in figure 2.8. The size of each plot has been normalised to the maximum intensity feature, for comparison purposes.

The low modulus XAS (7 μm) fibre Raman spectrum (fig.2.8a) exhibits only two distinct broad bands in the first-order region, while Raman activity can hardly be detected in the second-order region. The two pronounced features are located at about 553.5 nm and 560.5 nm in the spectrum (fig.2.8a). Taking into account that the laser line (and the

Rayleigh scattering) is located at 514.5 nm (the excitation wavelength) these shifts from the laser line correspond to about 1370 cm^{-1} (514.5^{-1} - 553.5^{-1}) and about 1600 cm^{-1} (514.5^{-1} - 560.5^{-1}), respectively. They correspond to the Raman bands denoted as D and G-lines (§ 2.1.1).

The intermediate modulus IMS (7 μm) fibre spectrum (fig.2.8b) shows a significant transformation, compared with the XAS spectrum. Both first-order features have clearly resolved and sharpened, whereas in the second-order region new lines have grown such as the G'-line (§ 2.1.2) at about 597.5 nm, which corresponds to about 2700 cm^{-1} shift from the laser line (fig.2.8b). The remaining second-order features are located at ~2450 cm^{-1} (on the left of the G'-line, fig.2.8b), at ~2950 cm^{-1} (on the right of the G'-line, denoted as G''-line) and at ~3240 cm^{-1} on the far right end of the spectrum.

In the high modulus HMS (7 μm) fibre spectrum (fig.2.8c) the major developments, compared with the IMS spectrum, are further growth and narrowing of the G-line, decrease of the high frequency "shoulder" of the G-band (that appears as a high frequency asymmetry in the same band for IMS), decay of the "disorder" induced D-line, and further enhancement of the second-order G'-line. The remaining second-order region bands remain small but have further sharpened.

(b) The first and second-order Raman spectrum of the 5 microns diameter carbon fibres.

The Raman spectra of the 5 microns fibres series provide a unique opportunity to study the developments in the fibre spectrum within a relatively short modulus range, from 305 GPa for the IMD (or IM43-750) fibre to 405 GPa for the LF58 fibre. The increment of modulus is about 35 GPa. As in the 7 μm series, the lowest modulus fibre of the group, the IM43-750, exhibits the broadest bands in its spectrum (fig.2.9a) from all fibres in this series (fig.2.9a to d). It shows a very poor Raman activity in the second-order region and if compared with the 7 μm series fibres, its spectral features are closer to the lowest modulus XAS fibre (230 GPa), rather than to its equivalent modulus 7 μm fibre IMS (305 GPa).

The 335 GPa modulus LF48 fibre possesses a drastically transformed Raman spectrum (fig.2.9b). All features in the second-order region have developed and both major bands in the first-order region have sharpened and

almost totally separated from each other. Further increase of the heat treatment temperature, to produce a higher modulus fibre, results in the enhancement of the G and the G'-line and the consistent reduction of the "disorder" induced D-line. This is demonstrated in the Raman spectra of the LF53 and LF58 fibres, shown in figures 2.9c and d.

(c) The first and the second-order Raman spectrum of the "morphology" carbon fibres.

The Raman spectrum of the LF-positive, is shown in figure 2.10a. The Raman lines observed in the examined so far, fibres, are also present in the spectrum of this fibre. The intensity of the disorder induced D-line is almost as high as the intensity of the graphitic G-line, but both lines are clearly resolved from each other. The increase in the surface crystallinity results in enhancement of the G and G'-lines and the relative reduction of the D-line, demonstrated in figure 2.10b for the LF-neutral fibre. This process is accelerated in the highly crystalline LF-negative fibre (fig.2.10c), the spectrum of which is in fact very similar to the one of the HMS fibre (fig.2.8c). These are the only two out of the 10 fibres of all series, for which the ratio of intensities I_D/I_G is less than or equal to 0.5 (Table 2.2).

The relative intensities of all lines in the first-order Raman spectrum, with respect to the intensity of the G-line, have been calculated for all fibres and they are presented in Table 2.2. The relative intensities of all lines in the second-order Raman spectrum, with respect to the intensity of the G-line, are displayed in Table 2.3.

2.3.2. *Closer examination of the major Raman lines.*

Comparison of the Raman spectral lines of different fibres can be undertaken using two different formats. The first, denoted as "normalised intensities" plot, presents the fibres' spectra with their intensities normalised over the intensity of the strongest feature. This presentation allows the comparison of bandwidths and asymmetries to the line under investigation. The second format, denoted as "real intensities" plot, displays the fibres' spectra superimposed, retaining their true

intensities. This format allows the evaluation of the amount of the scattering units that give rise to the specific line under observation.

The high resolution analysis of the carbon fibre Raman spectrum can reveal features not apparent in the wide spectrum range of figures 2.8 to 2.10. One of them is the high frequency asymmetry on the G-line. By plotting the Raman spectra of the three 7 μm fibres, in the region of 558 to 562 nm (1500 cm^{-1} to 1660 cm^{-1}) on the same normalised intensities graph, the significance of the disorder related D'-line at about 1620 cm^{-1} is fully shown (fig.2.11a). While in the high modulus HMS fibre the D'-line accounts only for ~10% of the intensity of the G-line, in the intermediate modulus fibre IMS, it rises to about 30% of the G-line. Furthermore, in the case of the low modulus fibre XAS, the D'-line is dominant in the fibre spectrum. The two bands (G and D') have merged in one broad feature, shifting the center of symmetry from 1580 cm^{-1} to ~1600 cm^{-1}. The real intensities plot of the same set of spectra, in figure 2.11b, reveals that not only the D'-line increases as the fibre modulus decreases (and the degree of crystallinity is reduced), but also the graphitic G-line diminishes dramatically.

The same findings are also demonstrated in the 5 μm fibre series. In the normalised intensities graph (fig.2.12a), the relative intensity of the D'-line, with respect to the intensity of the graphitic G-line, rises gradually from just above 0.2, on the 405 GPa LF58 fibre spectrum, to about 0.3, on the 335 GPa LF48 fibre spectrum. In a rather sudden transition, seen in the spectrum of the IM43 fibre (305 GPa), the "shoulder" D'-line has totally overwhelmed its graphitic partner, shifting the symmetry axis of the merged (G-D') feature at ~1600 cm^{-1}, also seen in the case of the XAS fibre. The analysis of the 1500 cm^{-1} to 1660 cm^{-1} region for the 5 μm fibres, is complemented by the real intensity plot of the Raman spectrum of these 4 fibres, in figure 2.12b. As with the 7 μm fibres, the broad line of the lowest modulus fibre is composed by the merging of the G-line, which is very weak in the low modulus fibre and the D'-line, which is particularly strong in these fibres.

The "morphology" fibres reconfirm the findings presented up to now. The higher the degree of the fibre crystallinity, the more intense the G-line and conversely, the weaker the D'-line of the carbon fibre Raman spectrum (fig.2.13 - real intensities plot).

High resolution spectra of the main second-order band, the G'-line at

~2700 cm^{-1}, reinforce the opinion that this feature develops in tandem to the graphitic G-line. The higher the fibre modulus and its surface crystallinity, the stronger the presence of this line in the second-order Raman spectrum of the carbon fibre and the sharper its linewidth. This is demonstrated in the real intensity comparative spectra of figure 2.14 for the 5 μm fibre series. Similar plots can be produced for the G'-line of the 7 μm fibres and the "morphology" fibres.

In Tables 2.2 and 2.3, all the parameters of the Raman spectrum of carbon fibres, such as the Raman frequency values, the half-height-bandwidth (HHBW) of each band and the relative intensity of each line with respect to the G-line, are presented. The accuracy of the frequency measurements depends on the spectrometer calibration precision which is estimated to be within 5 cm^{-1}. The differences between the Raman frequency values for different fibres can be estimated with a higher precision, in the order of ±1 cm^{-1}. The error in the measurement of the bandwidth is in the order of ±10%, mainly due to the slight differences in the size of the focal spot, on the fibre specimen. The scatter in the intensity ratios of Tables 2.2 and 2.3, is in the order of ±0.05, and is primarily attributed to local variations of the fibre structure.

2.3.3. *The effect of laser power on the Raman spectrum of carbon fibres.*

The D-line, the G-line, its "shoulder" D' and the second-order G'-line of three selected carbon fibres, the HMS (7 μm), the IM43 (5 μm) and the XAS (7 μm) fibres have been monitored by the high resolution Raman probe, under varying laser power from 0.5 mW to 8 mW.

The "disorder" induced D-line shifts linearly to lower frequencies with increasing laser power, at a rate of -0.35 cm^{-1}/mW, for the HMS fibre, -0.90 cm^{-1}/mW, for the IM43, and, -1.10 cm^{-1}/mW, for the XAS carbon fibre. No significant change in the fibres bandwidth is observed within the examined range of laser power, from 0.5 to 8 mW. This is in accordance with recently reported studies [Ager 1990], where a measurable increase in the bandwidth of this line was detected only at laser power over 30 mW on the sample.

The effect of laser power on the G-line of the carbon fibre Raman spectrum is negligible with respect to the bandwidth. On the other hand,

the frequency value of this line shifts linearly to lower wave numbers at a rate of -0.45 cm^{-1}/mW for the HMS fibre and, five times higher, -2.30 cm^{-1}/mW and -2.40 cm^{-1}/mW for the IM43 and the XAS fibre, respectively. Particularly in the HMS fibre spectrum, where the D' disorder line can be distinguished, the laser power dependence of this feature is calculated to be -0.40 cm^{-1}/mW.

The second-order Raman spectrum, the G'-line at about 2700 cm^{-1} also shifts linearly to lower frequency values, at a rate of -0.60 cm^{-1}/mW with increasing laser power, while its bandwidth remains unchanged. In Table 2.4, all results presented in this section are summarised. Finally, no change in the relative intensities of the main lines of the Raman spectrum was detected for the three fibres examined, after exposing the samples up to 8 mW laser power.

2.3.4. *The effect of fibre surface treatment on the Raman spectrum of carbon fibres.*

To study the effect of the surface treatment on the Raman spectrum of carbon fibres three types of fibres were examined. These were the high modulus HM (7 μm) fibre in both its untreated (HMU) and surface treated (HMS) forms, the intermediate modulus IM43 (5 μm) fibre in the untreated (IMA) and variously treated forms (B, C, D, etc) and the low modulus XA (7 μm) fibre in all its available surface treatments (Table 2.1).

The first and second-order Raman spectrum of the HMS fibre (fig.2.8c) is compared with the spectrum of the untreated fibre HMU, in figure 2.15. The intensity scale is normalised to the intensity of the prominent G-line. The following direct observations can be made. The "disorder" induced D-line rises from about 30% to 40% of the intensity of the G-line after the fibre surface treatment; the high frequency shoulder of the graphitic G-line, denoted as D'-line, becomes more pronounced in the spectrum of the treated fibre HMS; finally, the second-order G'-line intensity is reduced from about 75% to 60% of the intensity of the main graphitic G-line.

To elaborate further in the region of the graphitic G-line (fig.2.16), the high resolution real intensity Raman spectra of the HMS and the HMU fibres are superimposed within the range of 1500 cm^{-1} to 1660 cm^{-1}. It is worth noting here, that it is not only the "shoulder" D'-line that is enhanced by the fibre surface treatment, but at the same time, the Raman

scattering originating from the pristine graphitic units of the fibre surface (G-line) is also reduced.

A completely different result is obtained from the Raman spectra of variously surface treated IM43 and XA fibres. The first-order Raman spectra (real intensities) for all treatments of these two types of fibres have been superimposed in figures 2.17 and 2.18, respectively. It can be seen that the Raman spectrum of each of these fibres is not affected, by the degree of surface treatment.

2.3.5. *The Raman spectrum of the carbon fibre cross-section.*

Two 7 μm fibres, the HMS and the XAS, which correspond to the highest and the lowest modulus fibres of this fibre group, were selected for examination. The results of the Raman examination of the carbon fibre cross-section, compared with the results obtained from the fibre surface, are displayed below.

The first and second-order Raman spectra of the 7 μm HMS carbon fibre obtained from its cross-section and from the fibre surface are overlaid in figure 2.19a. The real intensity scaling has been retained, with just an offset added to the top spectrum. The dramatic rise of the "disorder" induced features D and D′ is accompanied by a sharp reduction of the intensity of the graphitic G-line and the G′-line. The characteristic "disorder" or "crystallinity" ratio I_D/I_G **[Tuinstra 1970 a&b]** is inverted from a value of 0.36 in the carbon fibre surface Raman spectrum, to a value 1.65 in the cross-sectional Raman spectrum. The enhancement of the 2950 cm^{-1} feature in the cross section spectrum is consistent with the assignment of this feature as a combination mode of the D and the D′-lines **[Nemanich 1979]**. The high resolution Raman spectrum near the G-line, presented in figure 2.19b, shows the significant growth of the D′ shoulder of the graphitic G-line at the cross-section of the HMS carbon fibre. It should be highlighted here, that at the fibre cross-section, the incident laser beam "sees" more graphite plane edges than basal planes **[Katagiri 1988]** and, therefore, a reduction in the Raman activity originated from the in-plane vibrational mode E_{2g}, corresponding to the G-line, is expected.

The first-order Raman spectrum of the low modulus XAS carbon fibre exhibits almost identical features regardless as to whether is originated

from the fibre skin or the core (fig.2.20a). No second-order features are anywhere present in the cross-sectional spectrum, which compares well with the lack of second-order features at the Raman spectrum of the surface. The intensity ratio $I_D/I_{G-D'}$ increases slightly from 0.80 in the surface spectrum to about ~1.0 in the cross-sectional Raman spectrum. Since the G-line is almost overshadowed by the D'-line in the XAS surface spectrum, the changes in the high resolution spectra of the G-D' lines (fig.2.20b) obtained from the surface and the cross-section are unobservable.

2.4. The Raman spectrum of carbon fibres and their structure.

The graphitic and the "disorder" features.

The Raman spectrum of a carbon fibre can describe the degree of crystallinity at the near-surface region of the fibre (~50 nm). The sharper the G-line (at 1580 cm^{-1}) and the G'-line (at 2700 cm^{-1}), the higher the surface crystallinity of the fibre and, in general, the fibre Young's modulus. The G-line is attributed to the E_{2g} vibrational mode of the graphite cell **[Tuinstra 1970a, Nemanich 1979]** (fig.1.14) and is the dominant feature in the spectrum of all fibres tested, with the exception of the low modulus XAS (7 μm) fibre and the intermediate IM43 (5 μm) fibre. In these two cases, the G-line has been literally overshadowed by the growth of the "disorder" induced D'-line at 1620 cm^{-1}, (figs.2.11, 2.12)

As mentioned earlier, the D' "shoulder" to the G-line, is related with the "disorder" induced D-line at 1355 cm^{-1}. In fact, the intensity ratio between the D' and D-lines ($I_{D'}/I_D$) is impressively stable for all fibres, between 0.2 and 0.3, as can be retrieved from Table 2.2. This implies that during carbonisation and graphitisation both these two features decay at the same rate.

The origin of the "disorder" features has been a point of controversy. Although the theoretical models, based on the phonon dispersion relationships, explain the presence of these lines through a distortion in the symmetry of the crystallite and a breakdown of the selection rules for Raman activity **[Chieu 1982, Lespade 1982]**, this may occur either due to the presence of finite crystallite size in non-graphitised carbon fibres **[Tuinstra 1970 a&b]**, or due to the presence of plane edges "facing" the laser Raman probe **[Katagiri 1988]**. The view that the "disorder" induced D-line and the "graphitic" G-line are related with the same structural configuration, can be also supported by the finding that the HHBW of these two bands follows a 1:1 relationship, as revealed in figure 2.21. The deviation of the IM43 and the XAS from this 1:1 trend is obviously attributed to the fact that the G-line for these fibres is merged with its "shoulder" feature (figs. 2.11,2.12). The second school of thought, attributing the appearance of the "disorder" features to the presence of aromatic polycarbonates in the carbon fibre surface **[Nakamizo 1974]** or even to the presence of a diamond-like structure with peculiar sp^3 hybridisation

[Fitzer 1988d], seems less convincing, since X-rays evidence has not confirmed the presence of such structural configurations **[Fitzer 1988d]**. Whichever is the source of these "disorder" features, their presence is an indication of how much "graphitic" is the morphology of the carbon fibre surface. Therefore, in the present investigation, the term "disorder" implies the perturbation of the smoothly stratified long graphite layers by finite size crystals or even discontinuities introduced by the graphite plane edges exposed in the fibre surface. The quality of the graphitic nature of the fibre can also be evaluated by the ratio of the intensities of the D and the G-lines, I_D/I_G, known as "disorder" ratio of intensities, or, "crystallinity" ratio.

Altering of the "disorder" ratio at the fibre's treated surface.

The "disorder" intensity ratio does not change only as the carbonisation and graphitisation temperatures rise to produce higher modulus fibres, but it changes also within the same fibre, depending on whether the fibre scattering region is its cross-section or its surface-treated sheath. In both cases, observable changes have been detected only on highly crystalline fibres, like the HMS. The change of that ratio with fibre surface treatment (fig.2.15) is satisfactorily interpreted as due to the removal of the mostly graphitised external layers from the high modulus fibre surface.

This finding is in agreement with previous claims that surface treatment on high modulus carbon fibres acts in a two-fold mechanism **[Drzal 1983 a&b]**; it removes weak boundary graphite layers from the fibre surface and adds chemical functional groups which can bond to matrices. The removal of the weakest in shear (and most highly orientated) graphite crystallites from the fibre surface is being considered as the most efficient surface treatment with respect to the adhesive properties of carbon fibres **[Kalnin 1985]**. The rise of the "disorder" induced D and D'-lines is explained by the fact that the removal of the highly graphitised surface layers reveals some of the less crystalline core structure of the high modulus fibre **[Guigon 1984, Chen 1983]**, and exposes more graphitic edge planes to the laser Raman probe. Similar effects have been observed on the Raman spectrum of Ar^+ etched highly oriented pyrolytic graphite (HOPG) **[Ishida 1986]**. The model developed in that study to explain

the enhancement of the "disorder" induced Raman lines, shown in the sketch of figure 2.22, may also be applicable in the case of surface treatment of the high modulus carbon fibres. Finally, the observation that the second-order G'-line decreases in intensity as a result of fibre surface treatment and the consequent reduction in the surface crystallinity, supports the view, that this line is closely related to the graphitic G-line, instead of being assigned as an overtone of the "disorder" D-line **[Nemanich 1979, Chieu 1982]**, as discussed later.

The contrast in the effect of surface treatment upon the Raman spectrum of the high modulus fibre (fig.2.15) on the one hand and the intermediate and low modulus on the other (fig.2.17, 2.18), can only be explained in terms of the skin-core model which has attracted considerable attention in literature **[Donnet 1984]**. Electron diffraction studies on PAN based carbon fibres **[Bennet 1978]** revealed that the crystallite width L_c and the angle orientation ϕ at the skin of heat-treated carbon fibres at 2500°C, are about 100 Å and 14° respectively, whereas at the fibre core, the same structural parameters have values of 33 Å and 24°. On the other hand, heat-treated carbon fibres at 1500°C, exhibited L_c=160 Å and ϕ=43° in both regions. No change was observed between surface and core of carbon fibres heat treated at 1000°C **[Donnet 1984]**. It seems, therefore, reasonable to claim, that any etching of the fibre outer regions caused by surface treatment, will not be detected in the Raman spectrum of the fibre, if no new structural parameters are revealed. The improvement of the adhesive properties of these types of fibres with surface treatment is then mainly promoted by the chemical alterations on the fibre surface **[Drzal 1983a]**.

Altering of the "disorder" ratio at the fibre cross-section.

The Raman spectroscopic data from carbon fibre cross-sections should be treated with caution before any conclusions are drawn with respect to the internal structure of carbon fibres. This is due to the fact that experimental evidence **[Tidjani 1986]** has shown that grinding can induce disorder to natural graphite. Furthermore, it has been shown that the graphite interlayer distance increases and the crystallite size reduces with severe grinding, while mild grinding does not alter significantly these parameters. The claim that polishing imperfections may be introduced

to graphite by grinding has been questioned **[Katagiri 1988]**, on the basis of findings of the dependence of the I_D/I_G ratio with respect to the polishing angle ϑ (fig.2.23). While the I_D/I_G ratio from the cleaved basal plane is as low as 0.05 for pyrolytic graphite, it increases to 0.2 by 0° polishing angle. If polishing could introduce structural imperfection, the I_D/I_G ratio should not show any polishing angular dependence, or, in other words, that ratio should be the same for all polishing angles **[Katagiri 1988]**. The fact that this ratio increases to 0.6 at 90° polishing angle reinforces the view that the change in the I_D/I_G ratio between the surface and the cross-section of the fibre is not an artifact of "disorder" introduced by specimen preparation.

The "disorder" ratio change between the surface and the cross-section spectra of high modulus fibres, should not be directly interpreted as a skin-core effect within the fibre, since the scattering units are at a different orientation to the incident beam in the two configurations (fig.2.7). However, the finding that, the IM43 (5 μm) and XA (7 μm) fibres spectra look hardly changed, either when they are obtained from the untreated surface, or the treated surface, or the fibre cross-section, indicates the existence of high degree of structural homogeneity throughout these fibres.

Special reference to the "poorly" crystalline fibres.

The case of the IM43 and the XAS fibres should be dealt with separately. To recall, the IM43 and the XAS are the lowest modulus fibres in the groups of the 5 μm and the 7 μm series, respectively. The Raman features of these two fibres deviate dramatically from the trend followed by the rest of the fibres due to the merger of the G and the D-lines (figs. 2.11, 2.12). A proof to this claim can be also produced from the plot of the half-height-bandwidth (HHBW) of these two bands, as a function of the "disorder" ratio I_D/I_G, for all fibres (fig.2.24a). The "disorder" induced D-line, for both the IM43 and the XAS fibres, is particularly broad and also deviates from the trend followed by the other fibres (fig.2.24b). But above all, these two fibres differ from the rest in that they have no second-order Raman features. Only a trace of the G'-line (at about 2700 cm^{-1}) is present, along with the weak and broad G''feature (at about 2950 cm^{-1}).

Since the Raman spectrum of carbon fibres is related to the structural features of the fibre surface, such as the crystallite symmetry, its size and its average orientation **[Tuinstra 1970 a&b]**, the distinctly different Raman spectrum of the IM43 and the XAS fibres indicates significant structural differences of these two fibres in comparison with the rest. It is noteworthy that these two fibres have been produced at the lowest carbonisation temperatures of all fibres in their series. There might be a critical heat treatment temperature level, below which, nitrogen groups present in the composition of the precursor **[Gill 1972, Jenkins 1976]**, have a significant vibrational contribution to the fibre Raman spectrum, particularly if they are present in a form of a heterocyclic compound **[Dollish 1974]**. A nitrogen content of ~3.0% has been measured in fibres carbonised at 1300°C **[Donnet 1984]**. The Raman spectrum of a PAN fibre, shown in figure 2.25, demonstrates a number of frequency lines that might still interfere in the spectrum of a low modulus (low heat treatment temperature) carbon fibre. In accordance to this approach the broad G''-band at about 2950 cm^{-1} is a remain of the strong high frequency line in the spectrum of the precursor PAN fibre (fig.2.24), assigned to a -C-H stretching vibrational mode of PAN **[Siesler 1980]**. If that is true, then it rules out the claim that the G''-line is an combination of the D with the D'-line **[Nemanich 1979]** and confirms the view that is attributed to H impurities in the carbon fibre structure **[Tsu 1978]**. However, such a claim has to be supported by spectroscopic evidence from the PAN fibre at various stages of oxidisation and stabilisation during carbon fibre production.

The ambiguous nature of the second-order G'-feature.

The most pronounced second-order line for all but the two above mentioned fibres, is the G'-line appearing at ~2700 cm^{-1}. The half-height-bandwidth of this line increases as the intensity ratio I_D/I_G increases (fig.2.24c). Although the presence of this line is related with the main graphitic G-line, and both these two bands grow together as the graphitisation temperature rises, is has been emphatically assigned as an overtone of the "disorder" induced D-line **[Nemanich 1979]**, due to its numerical coincidence (2700=2x1350) and its analogous sensitivity to the excitation wavelength **[Vidano 1981]**. However, the evolution of the G'-line follows closely the growth of the graphitic G-line (Table 2.3), while the

assumed as fundamental of the G', the D-band, tends to eliminate with the rise in the graphitisation temperature. The view that the G'-line is associated with the development of two-dimensional ordering in the fibre structure **[Lespade 1984]**, is a much more appropriate assignment for this band. In support to this interpretation, the HHBW of the G'-line is found to exhibit a 2:1 relationship with the HHBW of the G-line, rather than the D-line (Tables 2.2, 2.3 and figs. 2.26 a&b). It has been also found that this feature splits into two at even higher graphitisation temperatures, manifesting the introduction of three-dimensional ordering in the graphite lattice **[Lespade 1984]**. ▮

Table 2.1. Material properties (carbon fibres).

Fibre	Young's Modulus (GPa)	Diameter (μm)	Fibre treatment
HMS	390	7	0 (HMU), Standard (HMS)
IMS	305	7	Standard
XAS	230	7	0, 1 (Standard), 2, 3, 4
LF58	405	5	Standard
LF53	370	5	Standard
LF48	335	5	Standard
IM43	305	5	A(0),B,C,D(Standard),E,F
LF-neg	378	5	Standard
LF-neut	378	5	Standard
LF-pos	364	5	Standard

The Young's modulus quoted value has been produced by testing fibre tows up to 0.4% tensile strain.

Table 2.2. The first-order Raman spectrum of carbon fibres.

Fibre	D-line			G-line			D'-line		
	Frequency cm^{-1}	HHBW cm^{-1}	I_D/I_G	Frequency cm^{-1}	HHBW cm^{-1}	I_G/I_G	Frequency cm^{-1}	HHBW cm^{-1}	$I_{D'}/I_G$
HMS	1353	38	0.35	1579	32	1	1624	32	0.12
IMS	1354	52	0.85	1583	48	1	1622	30	0.30
XAS	1366	190	0.80	1599(*)	125(*)	1	-(*)	-	-
LF58	1352	50	0.60	1582	42	1	1622	32	0.22
LF53	1353	58	0.85	1584	58	1	1623	30	0.25
LF48	1353	65	0.95	1586	65	1	1622	30	0.27
IM43	1354	140	0.80	1595(*)	100	1	-(*)	-	-
LF-neg	1353	44	0.50	1581	35	1	1623	28	0.15
LF-neut	1353	46	0.70	1582	42	1	1622	28	0.19
LF-pos	1353	54	0.95	1584	56	1	1623	30	0.26

The intensities of all lines have been normalised to the intensity of the G-line, with the exception of the XAS and the IM43 fibres, for which the G and D' bands are merged and, therefore, the G-D' feature is the reference band.

Table 2.3. The second-order Raman spectrum of carbon fibres.

Fibre	G'-line			2450	cm^{-1}	line (*)	G''-line (*)			3240	cm^{-1}	line(*)
	Frequency cm^{-1}	HHBW cm^{-1}	$I_{G'}/I_G$	Frequency cm^{-1}	HHBW cm^{-1}	I_{2450}/I_G	Frequency cm^{-1}	HHBW cm^{-1}	$I_{G''}/I_G$	Frequency cm^{-1}	HHBW cm^{-1}	I_{3240}/I_G
HMS	2705	60	0.60	2450	100	0.03	2950	100	0.06	3240	50	0.03
IMS	2703	95	0.60		v.weak		2950	130	0.12	3240	100	0.03
XAS	-	-	-	-	-	-	-	-	-			
LF58	2703	82	0.70	2450	100	0.03	2950	100	0.07	3240	70	0.04
LF53	2702	95	0.60		v.weak		2950	130	0.12	3240	80	0.06
LF48	2700	115	0.60		v.weak		2950	160	0.15	3240	100	0.06
IM43		v.weak			v.weak		2950	300	0.10	-	-	
LF-neg	2705	62	0.80	2450	100	0.03	2950	100	0.08	3240	70	0.04
LF-neu	2704	75	0.70		v.weak		2950	130	0.11	3240	70	0.05
LF-pos	2702	105	0.60		v.weak		2950	160	0.15	3240	120	0.06

The intensities of all lines have been normalised to the intensity of the first-order G-line.
The spectral features of the star (*) denoted bands are only approximately estimated.

Table 2.4. The effect of laser power on the Raman spectrum of carbon fibres.

Frequency band	Laser power dependence (cm^{-1}/mW)		
	HMS	IMD	XAS
D line	-0.35	-0.90	-1.10
G line	-0.45	-2.30	-2.40
D' line	-0.40		
G' line	-0.60	-	-

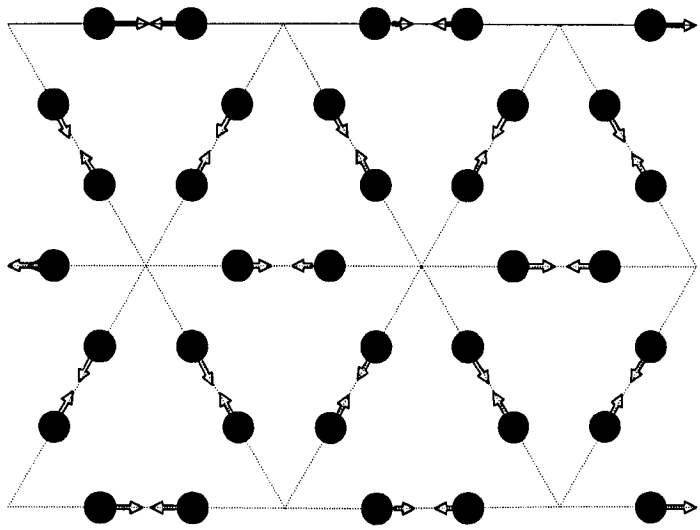

Fig.2.1 The "breathing" in-plane A_{1g} vibrational mode of the hexagonal cell, for finite-size graphite crystals **[Tuinstra 1970 a&b].**

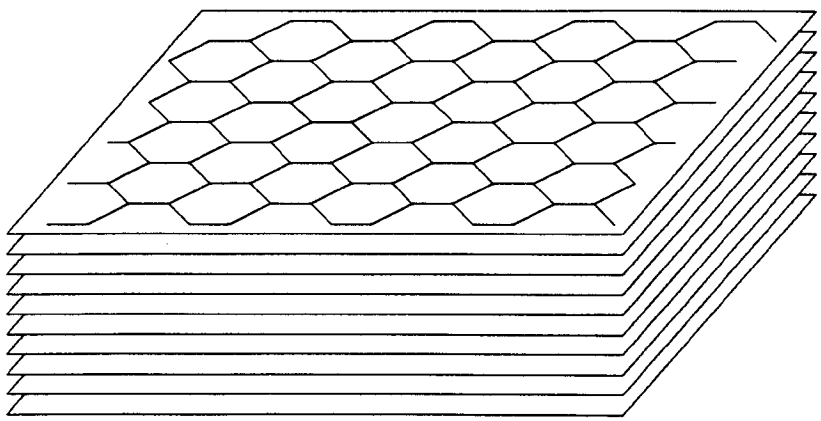

Fig.2.2 Schematic illustration of the graphite basal planes and their edges.

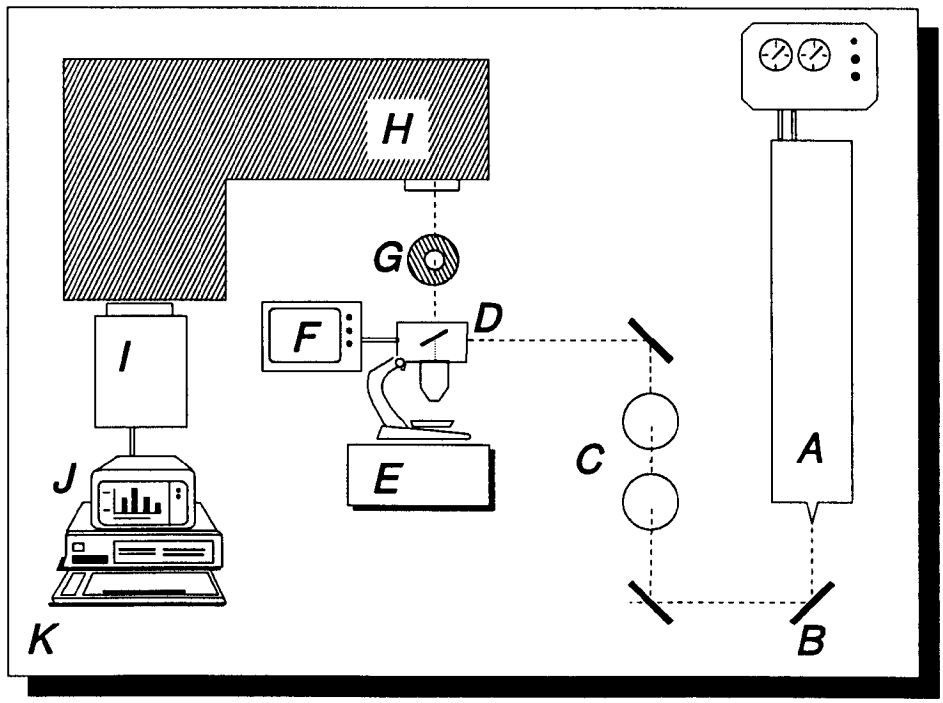

Fig.2.3 The Laser Raman setup.

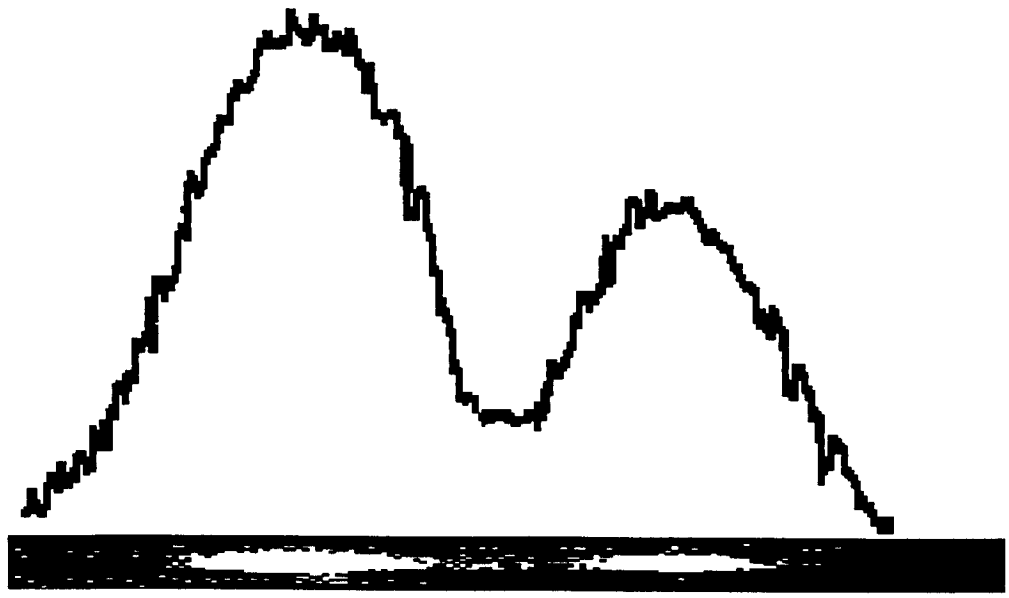

Fig.2.4 CCD image display of the Raman spectrum and image analysis (sectional plot) of the spectroscopic data.

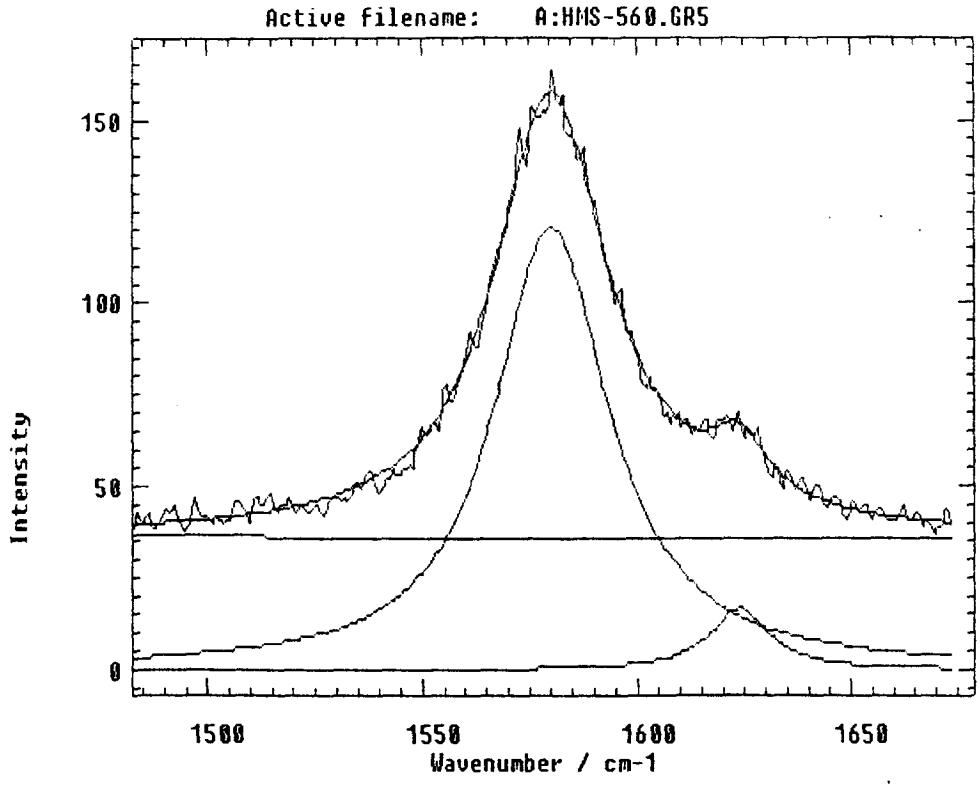


```
08/05/91 14:18:44          AT1 CCD imaging system                Fitting:73

                              Curve Fitting
Files:  Active......Input:A:HMS-560.GR5        ....Output:A:HMS-560.GR5
Fit:    Chi-squared value for last fit..................... 8.7373
        Background to peak weighting parameter............. 1.0000
        Effective peak weighting range (in peak widths).. 1.0000
Curves: Number to fit (max 9).............................3
        1.G/L/G.G...a0= 125.85    F/XF..a1=-.11153    F/XF..a2=0.34684E-04F/XF
        2.G/L/G.L...a0= 120.79    F/XF..a1= 1580.2    F/XF..a2= 16.145    F/XF
        3.G/L/G.L...a0= 16.599    F/XF..a1= 1624.0    F/XF..a2= 8.2473    F/XF
        4.G/L/G.G...a0=0.00000E+00F/XF..a1=0.00000E+00F/XF..a2=0.00000E+00F/XF
        5.G/L/G.G...a0=0.00000E+00F/XF..a1=0.00000E+00F/XF..a2=0.00000E+00F/XF
        6.G/L/G.G...a0=0.00000E+00F/XF..a1=0.00000E+00F/XF..a2=0.00000E+00F/XF
        7.G/L/G.G...a0=0.00000E+00F/XF..a1=0.00000E+00F/XF..a2=0.00000E+00F/XF
        8.G/L/G.G...a0=0.00000E+00F/XF..a1=0.00000E+00F/XF..a2=0.00000E+00F/XF
        9.G/L/G.G...a0=0.00000E+00F/XF..a1=0.00000E+00F/XF..a2=0.00000E+00F/XF
        G=a0+a1*x+a2*x^2 G=a0EXP[-((x-a1)/a2)^2] L=a0*(a2^2)/((x-a1)^2+a2^2)
        F=Fit a parameter X=fiX a parameter
Press:  F1 to Draw curve, F2 to fit to data,
        F3 to put into active file buffer, F4 to find background + n-1 peaks.
                                  MESSAGES
```

Fig.2.5 Hardcopy output of a typical spectrum and its analysis.

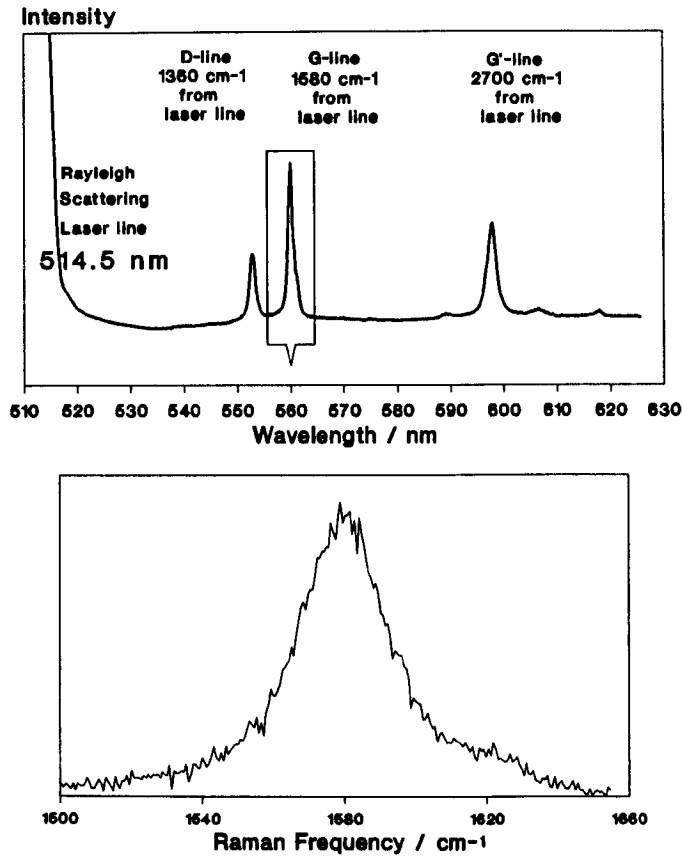

Fig.2.6 The Raman spectrum of the HMS fibre, including the Rayleigh line (top). The region of the G-line can be examined closer, using the high resolution diffraction grating.

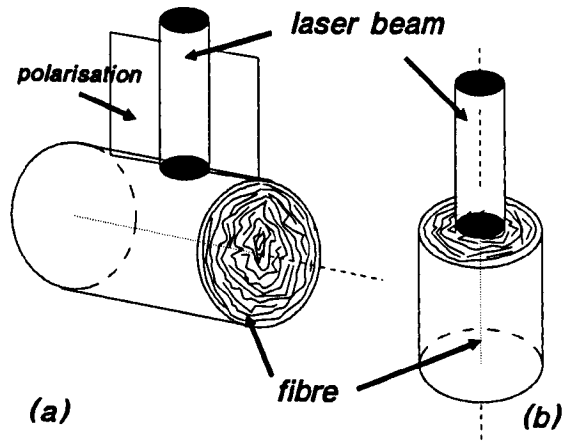

Fig.2.7 Raman probing from **(a)** the fibre surface and **(b)** the fibre cross-section.

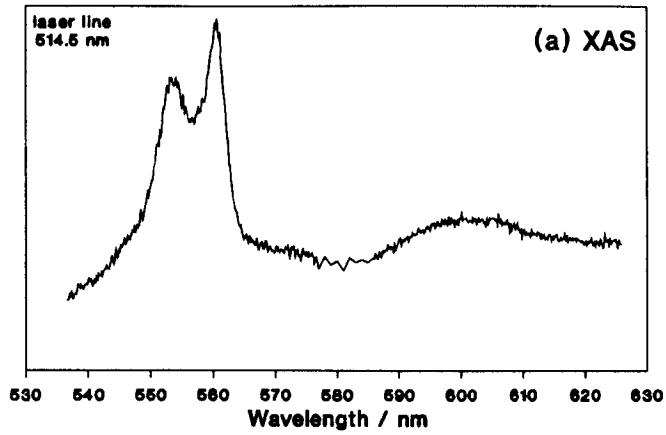

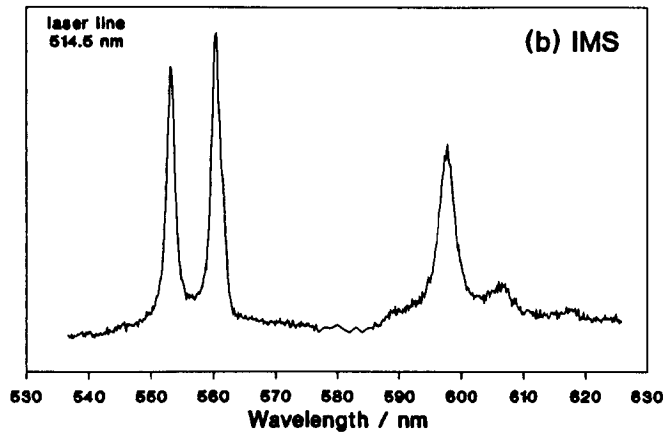

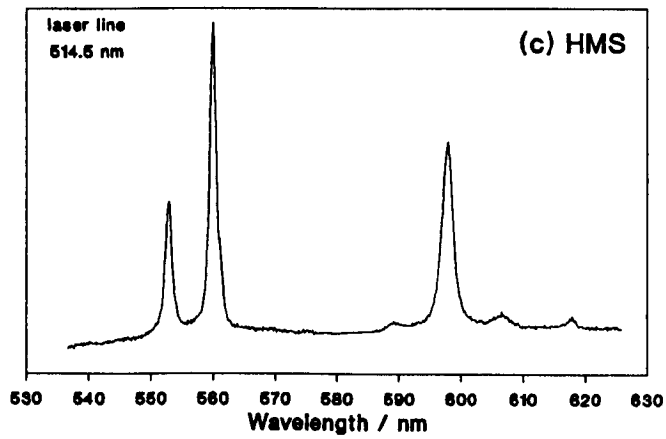

Fig.2.8 The Raman spectrum of the 7 μm fibres:
(a) XAS, **(b)** IMS and **(c)** HMS.

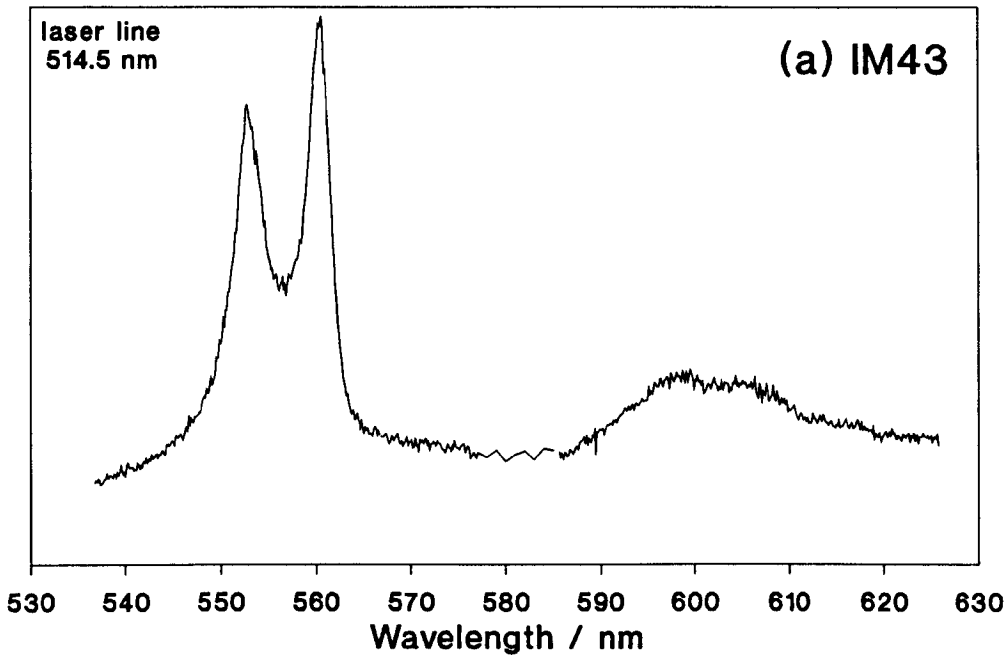

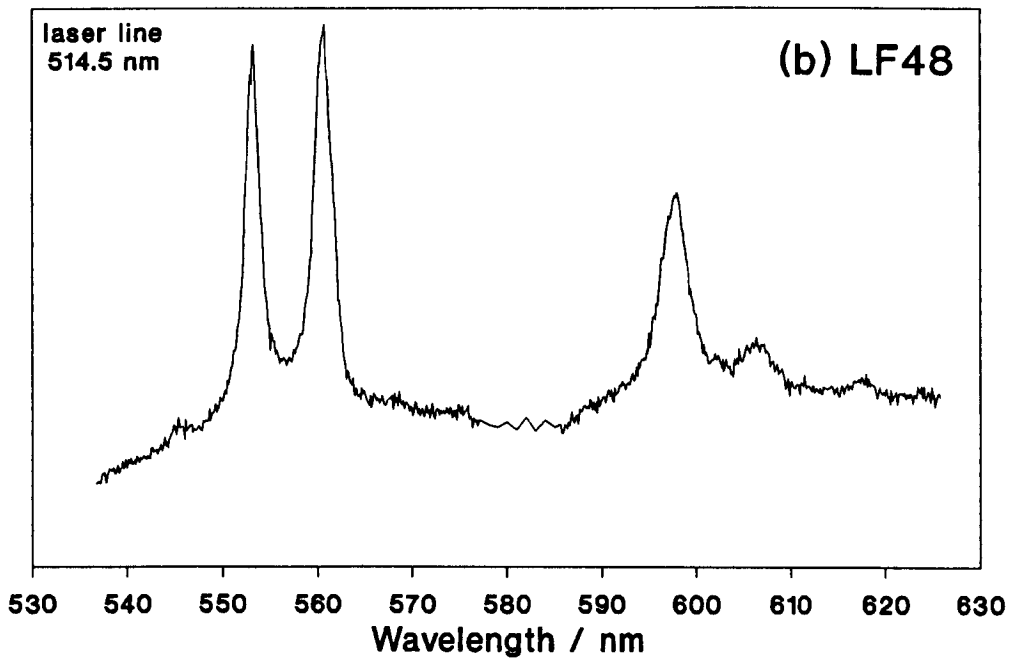

Fig.2.9 The Raman spectrum of the 5 μm fibres:
(a) the IM43, **(b)** LF48 (cont.)

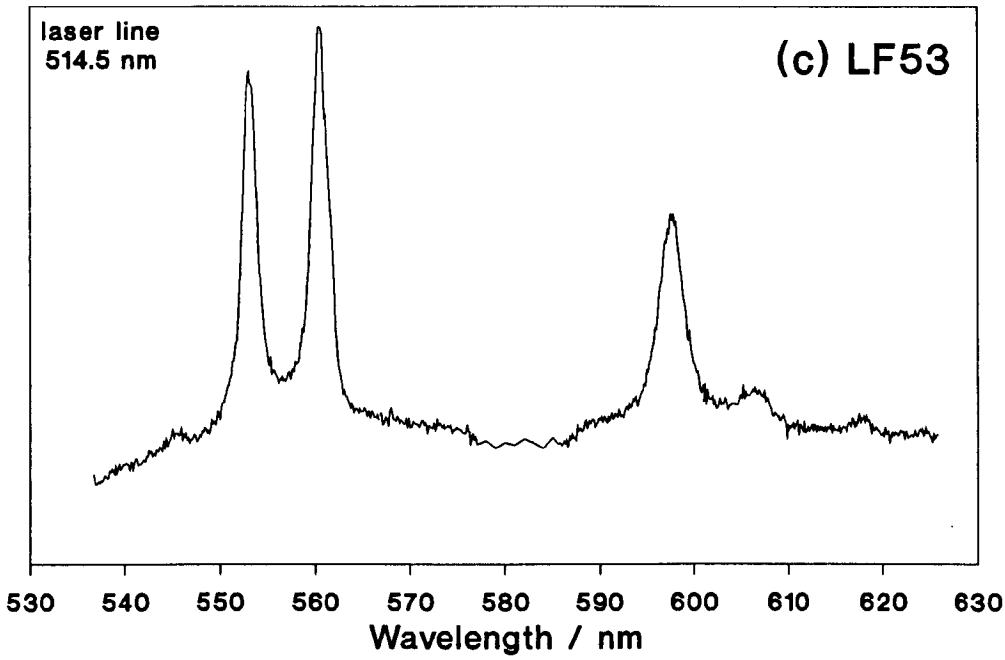

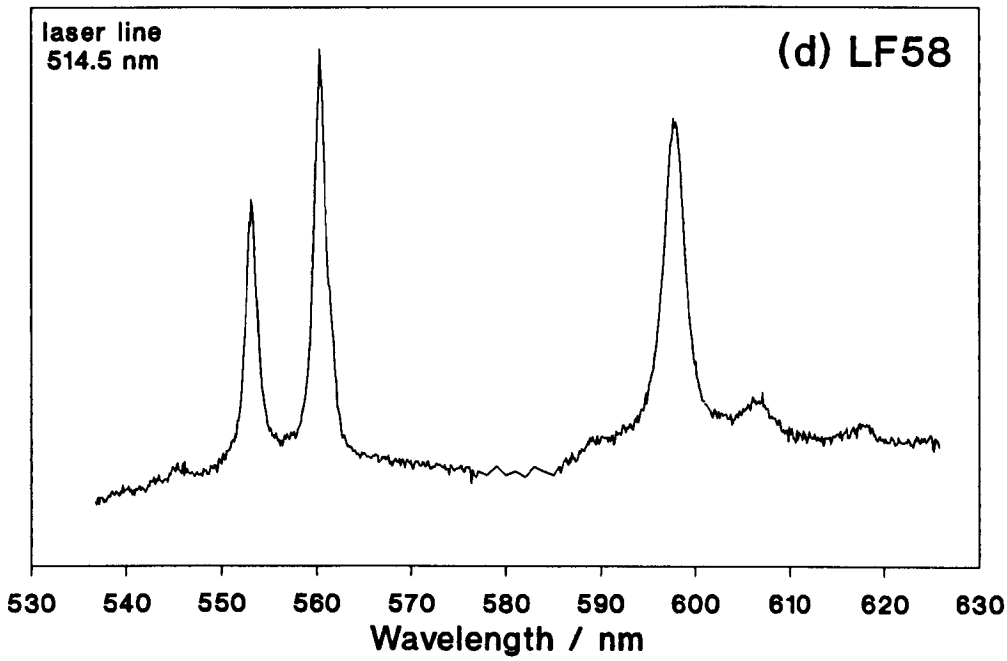

Fig.2.9 (cont.) The Raman spectrum of the 5 μm fibres: (c) LF53, and (d) LF58.

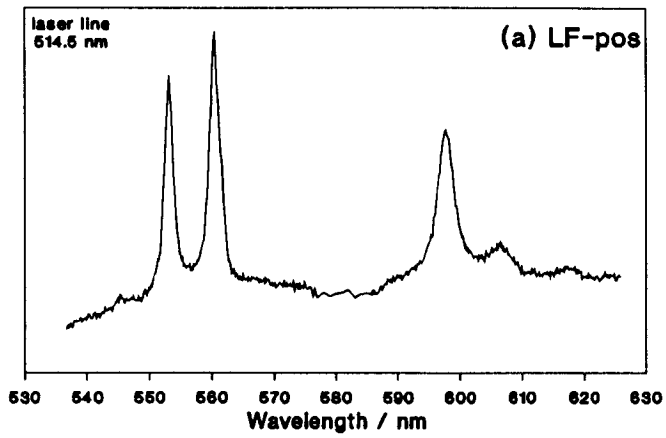

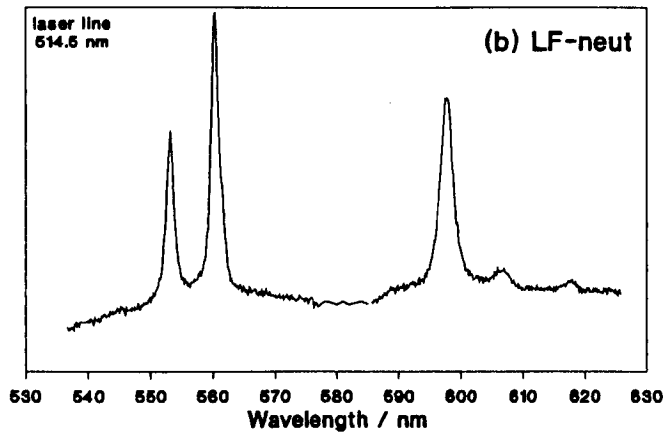

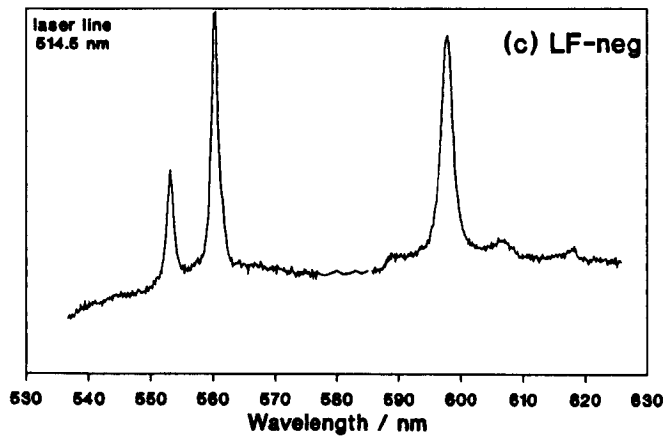

Fig.2.10 The Raman spectrum of the "morphology" fibres: **(a)** LF-positive, **(b)** LF-neutral, and **(c)** LF-negative.

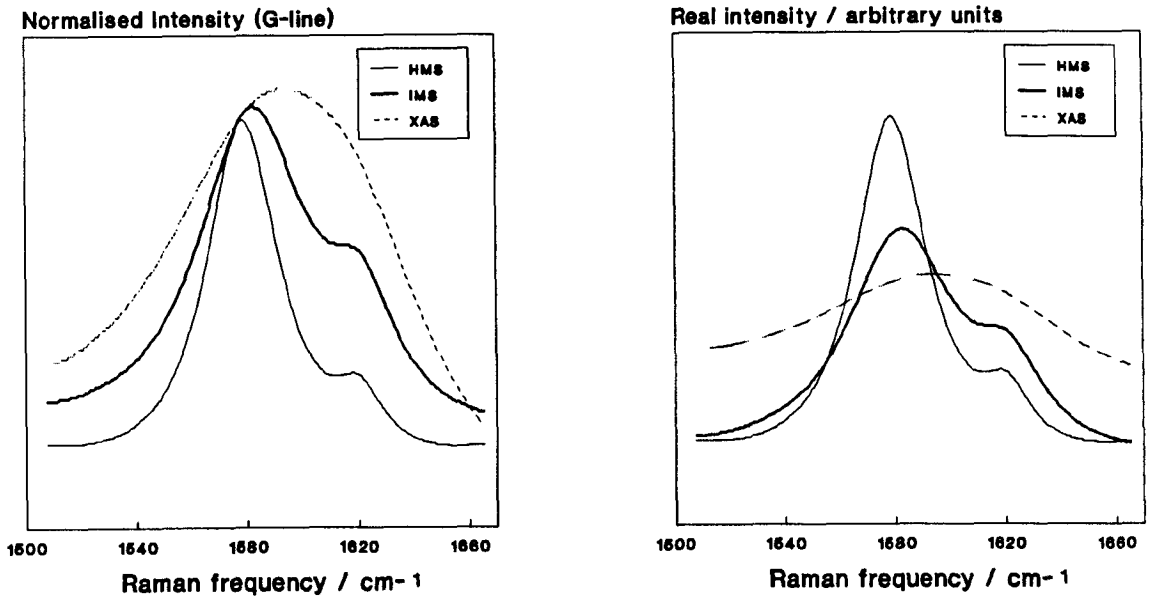

Fig.2.11 **(a)** The G-line of the three 7 μm fibres (normalised intensities) **(b)** The G-line of the 7 μm fibres (real intensities).

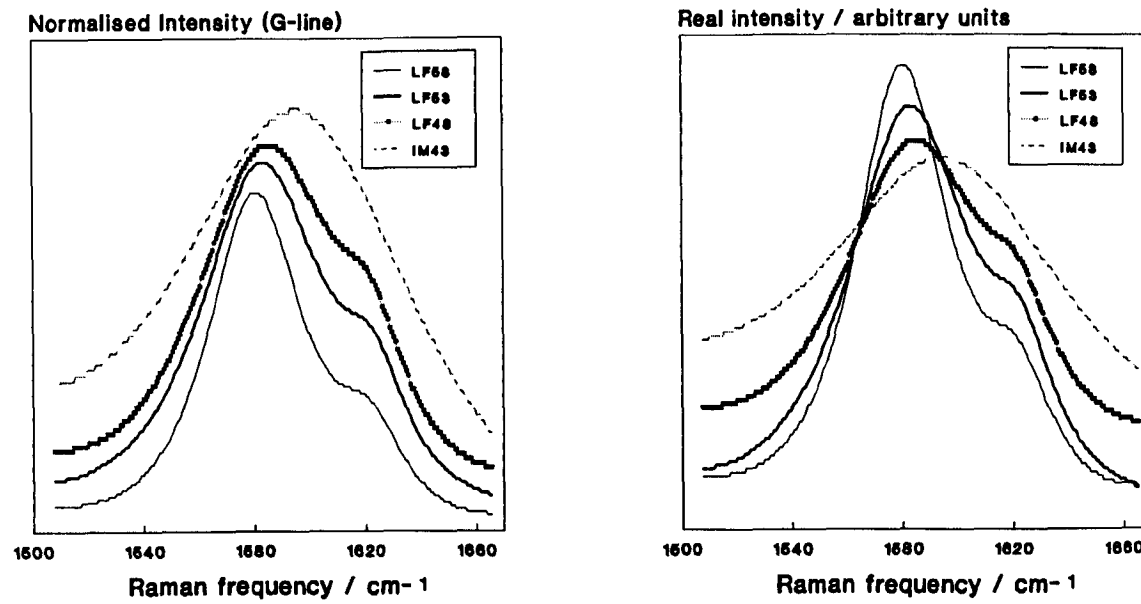

Fig.2.12 **(a)** The G-line of the four 5 μm fibres (normalised intensities) **(b)** The G-line of the 5 μm fibres (real intensities).

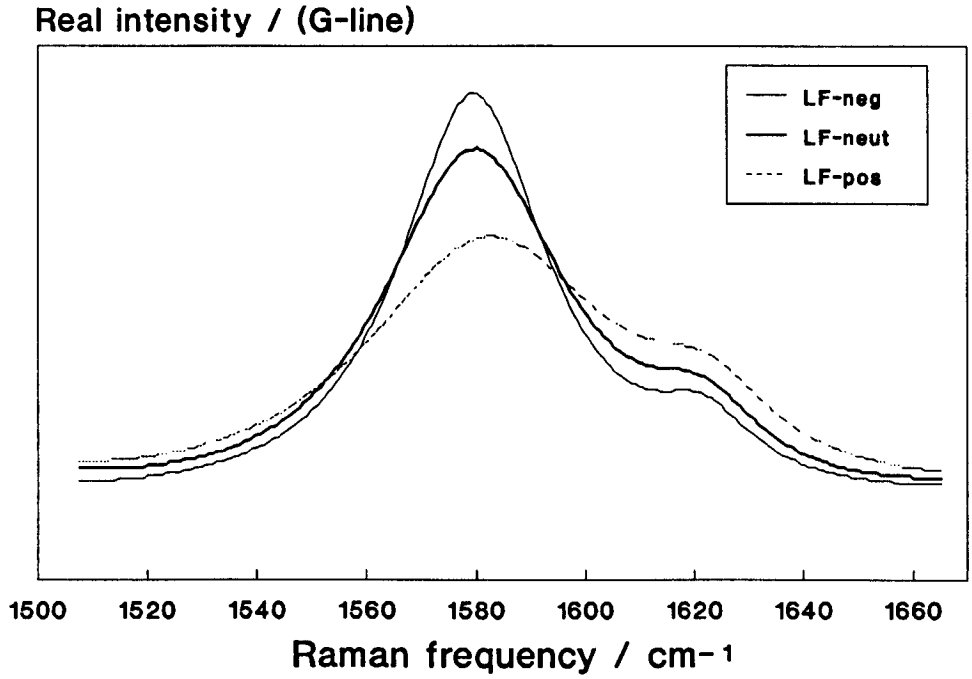

Fig.2.13 The G-line of the "morphology" fibres (real intensities).

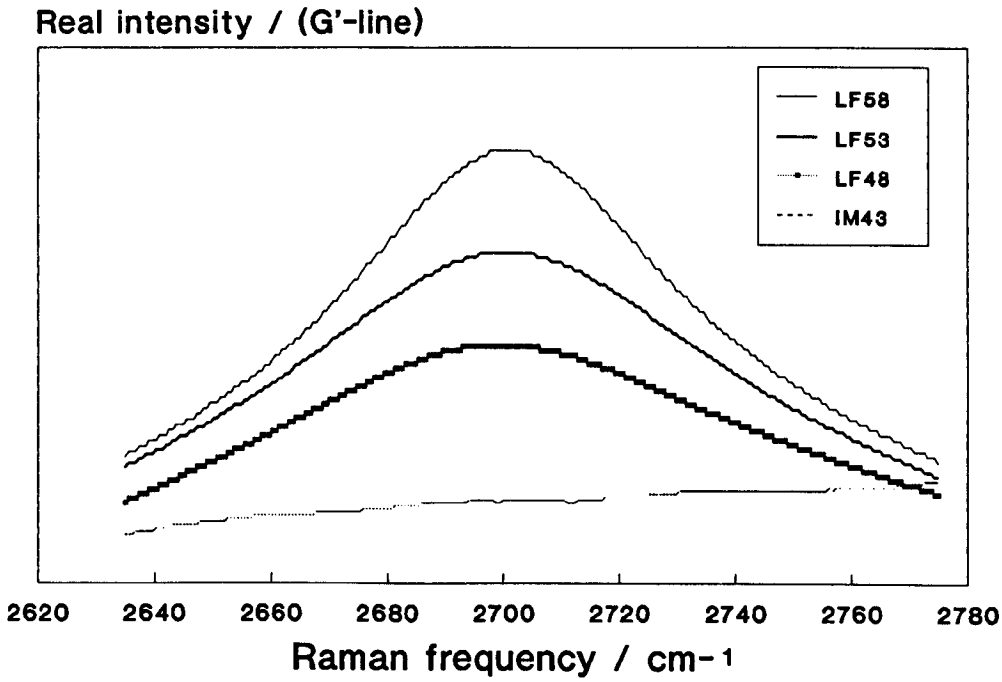

Fig.2.14 The G' line of the 5 μm fibres (real intensities).

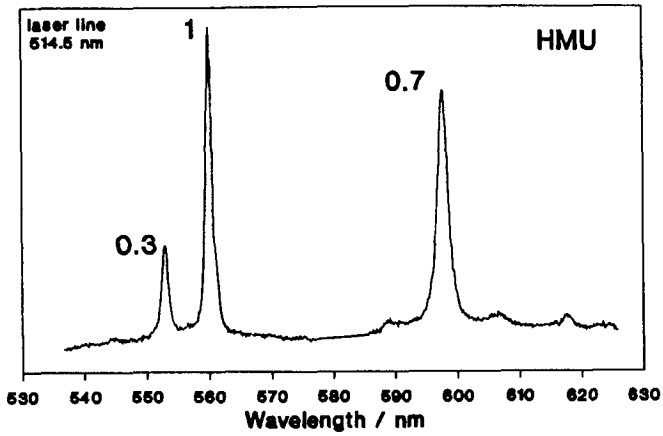

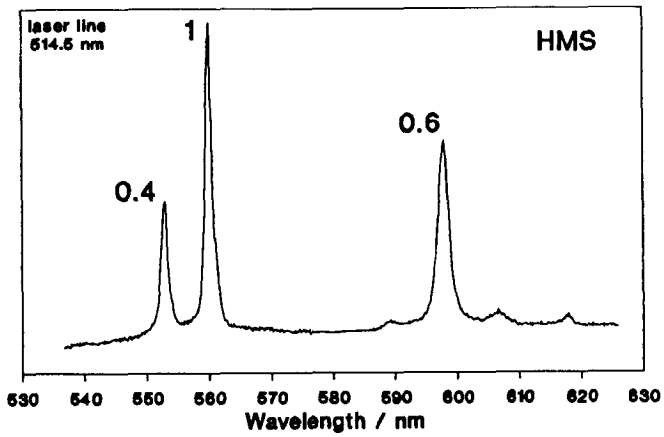

Fig.2.15 Comparison of the Raman spectrum of the treated (HMS) and the untreated (HMU) high modulus fibre.

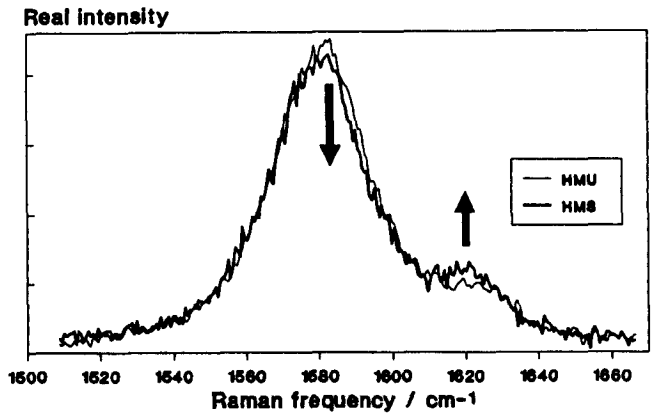

Fig.2.16 Real intensity high resolution spectra of the G-line of the HMS and the HMU fibre.

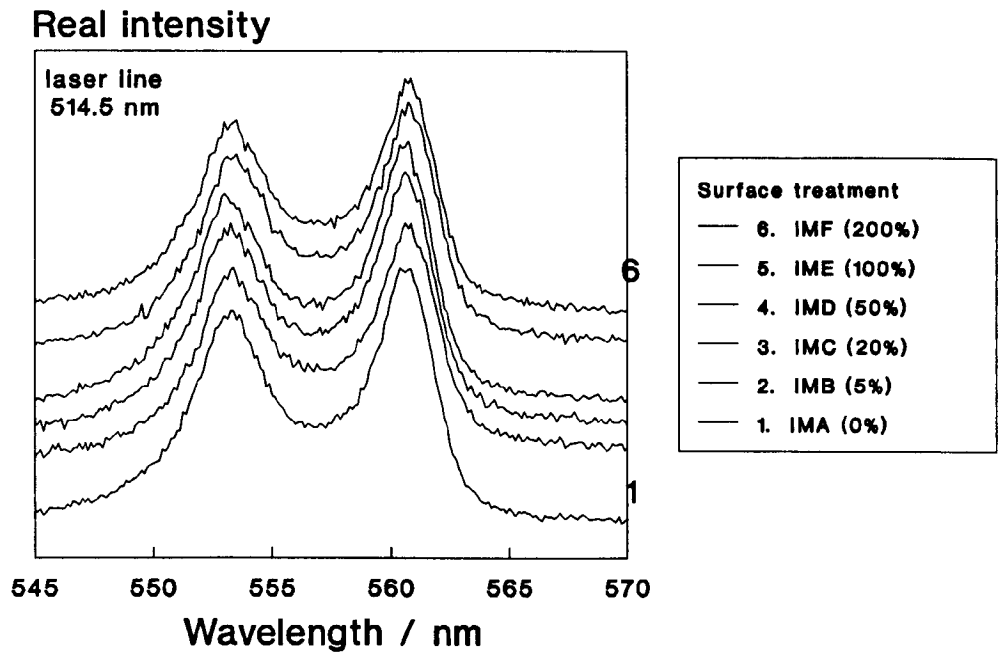

Fig.2.17 The first-order Raman spectrum of the IM43 fibre for various degrees of surface treatment.

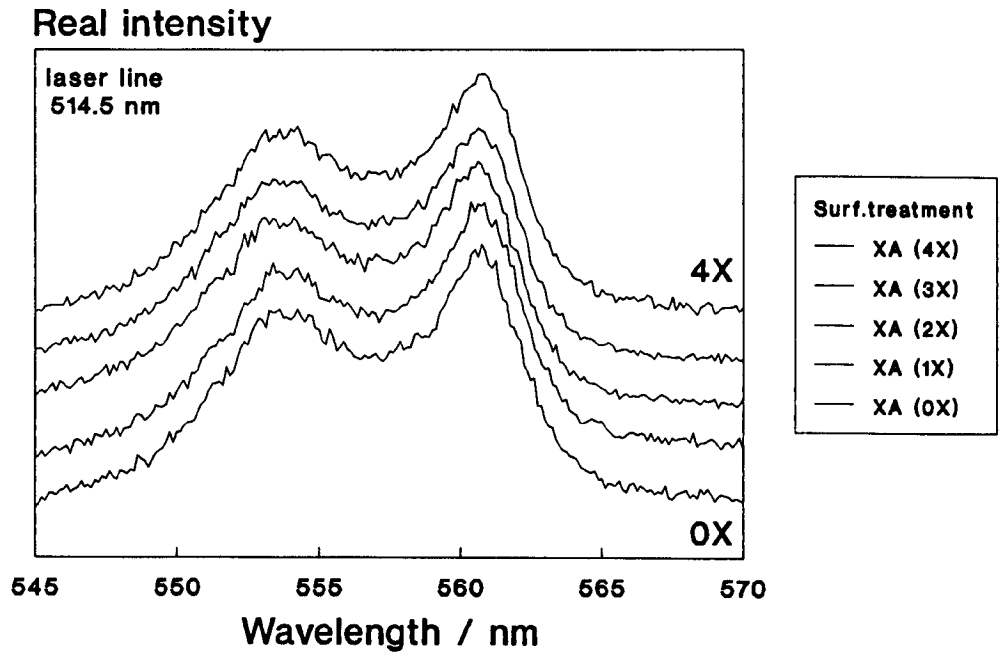

Fig.2.18 The first-order Raman spectrum of the XA fibre for various degrees of surface treatment.

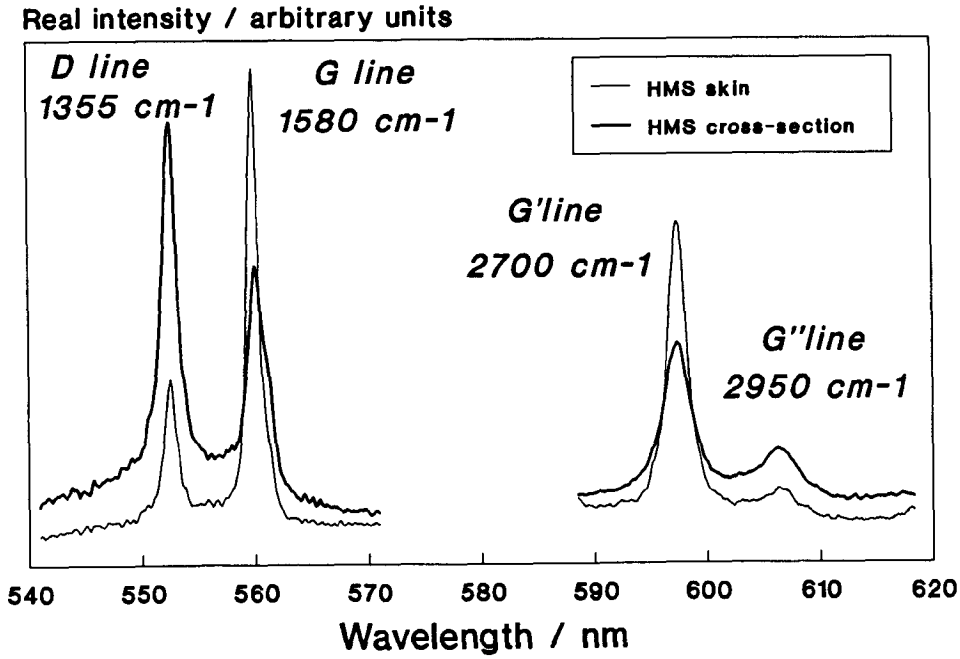

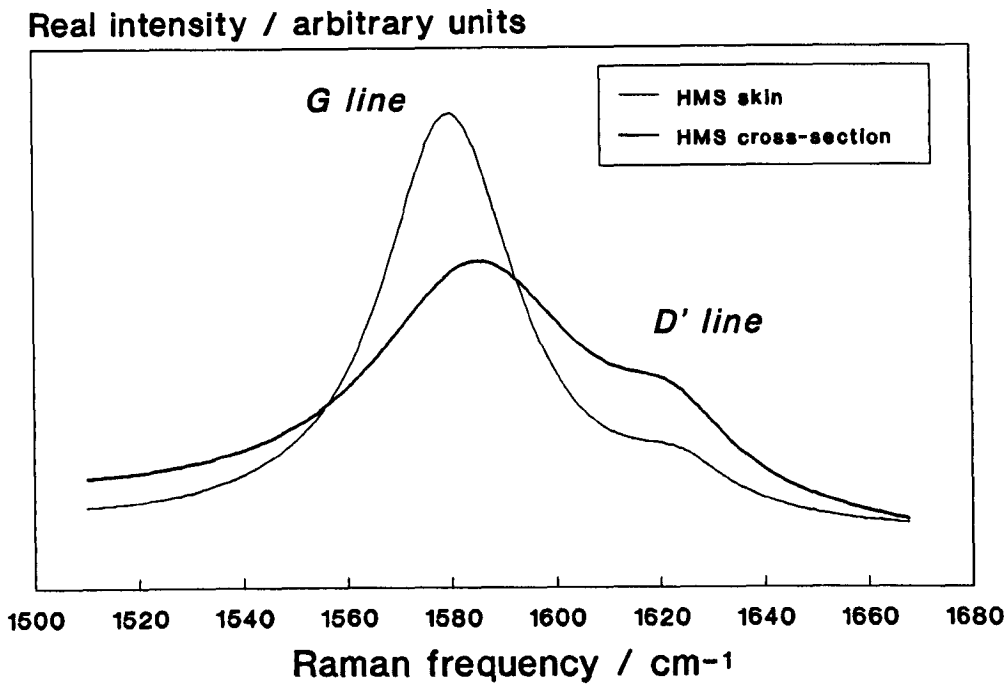

Fig.2.19 **(a)** The first-order Raman spectrum taken from the surface and the cross-section of the HMS fibre (real intensities).

(b) High resolution spectrum (G-line) taken from the surface and the cross-section of the HMS fibre (normalised intensities).

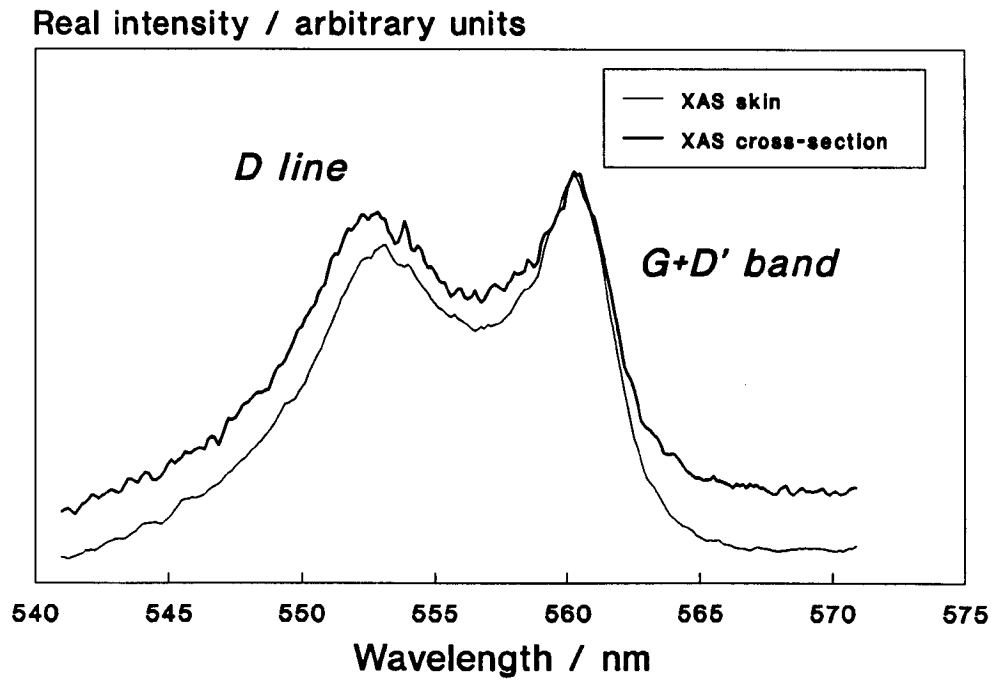

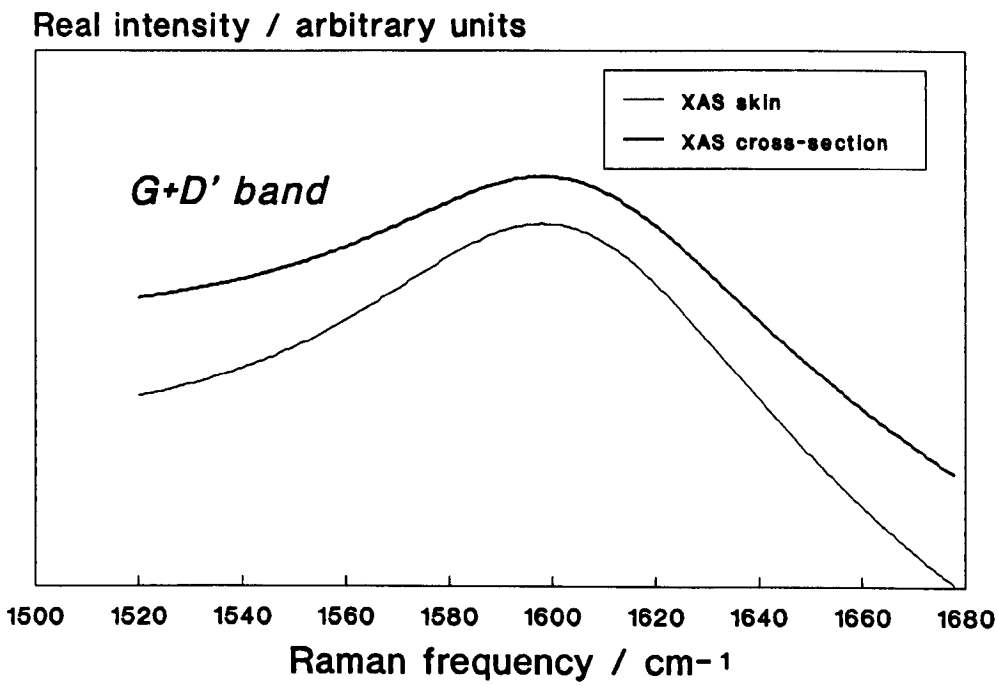

Fig.2.20 (a) The first-order Raman spectrum taken from the surface and the cross-section of the XAS fibre (real intensities).

(b) High resolution spectrum (G-D' band) taken from the surface and cross-section of the XAS fibre (normalised intensities).

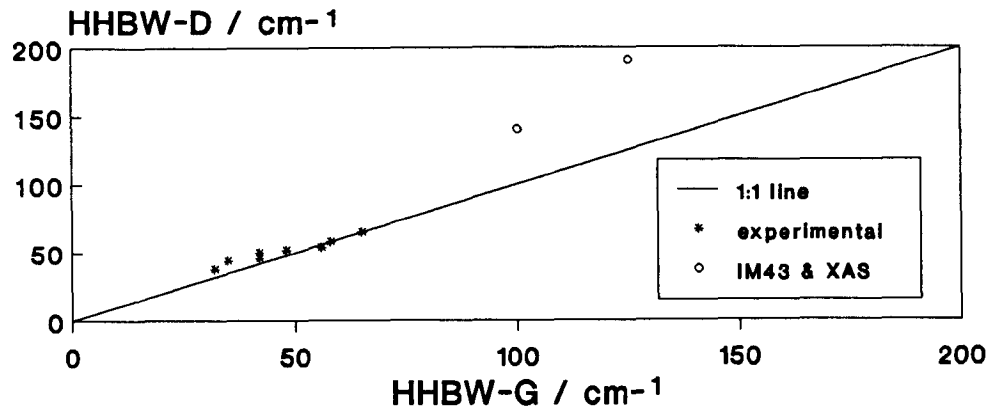

Fig.2.21 The half-height-bandwidth (HHBW) of the D-line as a function of the HHBW of the G-line, of the carbon fibre Raman spectrum.

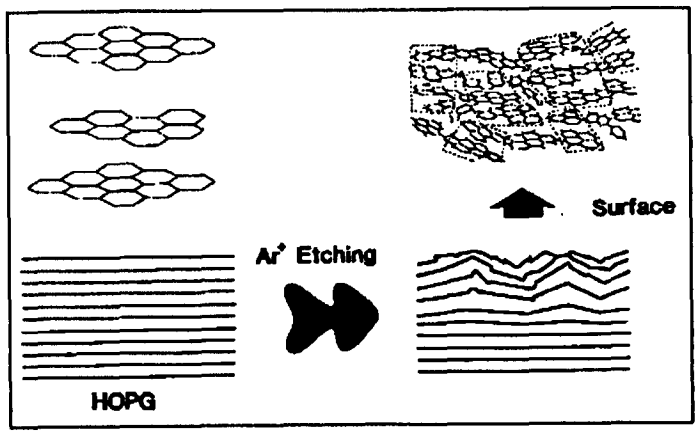

Fig.2.22 The proposed mechanism of surface Ar^+ etching of HOPG, [Ishida 1986].

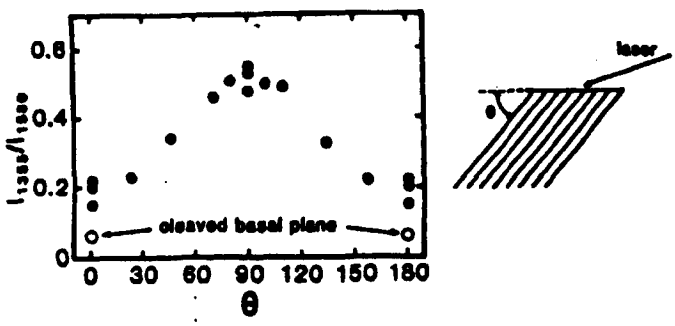

Fig.2.23 Angular dependence of the ratio I_D/I_G, brought about by preferential polishing [Katagiri 1988].

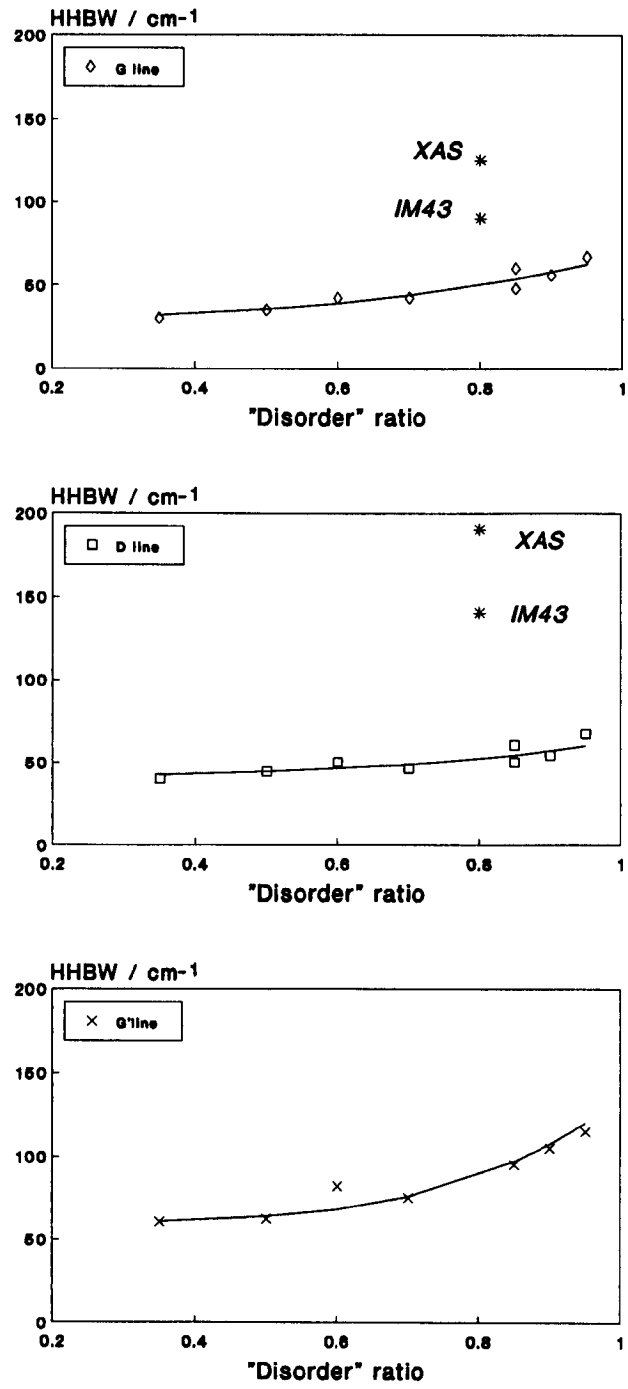

Fig.2.24 The half height bandwidth (HHBW) as a function of the intensity ratio I_D/I_G for the: **(a)** G-line, **(b)** D-line and **(c)** the G'-line.

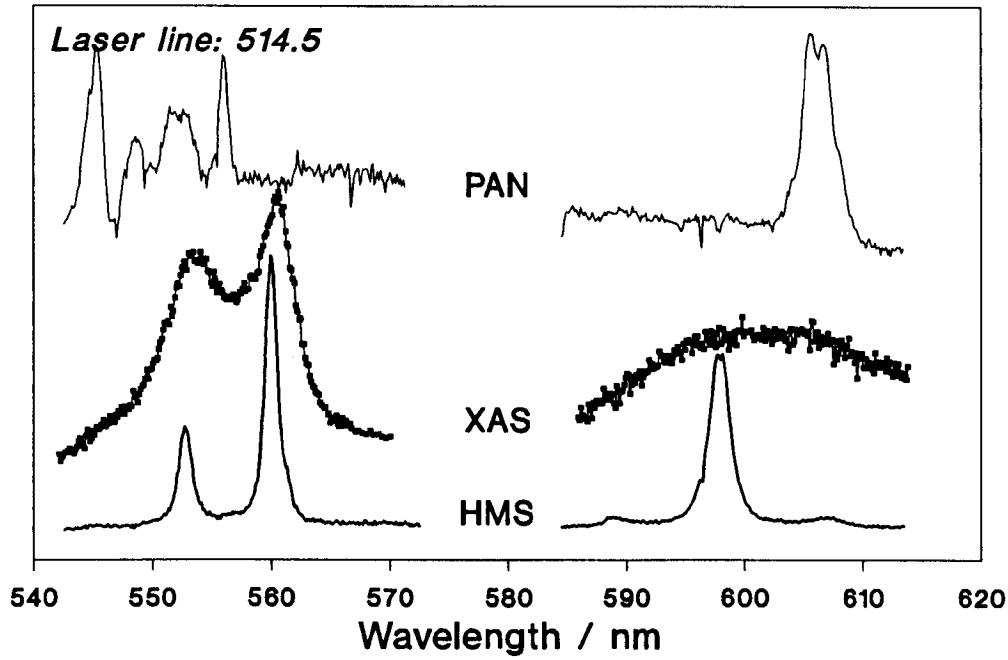

Fig.2.25 The Raman spectrum of the precursor PAN fibre, compared with the spectra of the HMS and the XAS carbon fibres.

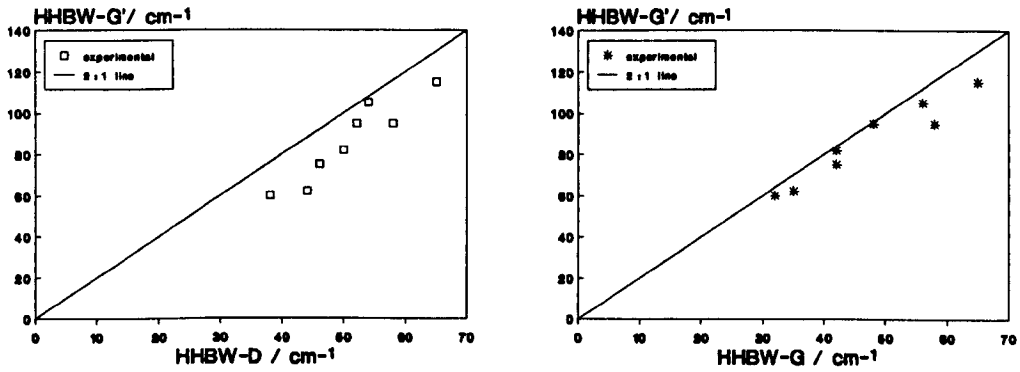

Fig.2.26 The half-height-bandwidth (HHBW) of the G'-line as a function of **(a)** the HHBW of the D-line and **(b)** the HHBW of the G-line, of the carbon fibre Raman spectrum.

CHAPTER 3

STRAIN DEPENDENCE OF THE RAMAN SPECTRUM OF CARBON FIBRES UNDER TENSION

3.1. Literature review.

The influence of stress or strain on the carbon fibre Raman spectrum has rarely been considered in the literature to date. In fact, the references on the stress or strain dependence of the Raman spectrum of carbon fibres are limited in a small number of publications **[Robinson 1987, Galiotis 1988a, Sakata 1987]**. On the other hand, the strain-induced shifts of the Raman or Infra-Red spectrum of polymers such as polyethylene or polypropylene, **[Bretzlaff 1983, Wool 1986]**, polymeric fibres such as Kevlar or polydiacetylene **[Galiotis 1985, Robinson 1986]** and diamond type crystals **[Anastassakis 1970, Cerdeira 1972]** have been reported and theoretical treatments of these effects have been proposed **[Ganesan 1970, Tashiro 1990]**.

In general, the Raman (or Infra-Red) frequencies of a crystalline material are related to a distinct vibrational mode of the scattering (or absorbing) species and to combinations and overtones of these vibrational modes **[Woodward 1972, Turrell 1972]**. Therefore, any change in the parameters that affect the vibrational mode will alter the vibrational (Raman or Infra-Red) spectrum of the material. In Chapter 1 it was shown how the classical mechanical approach of the molecular vibration problem can yield the unique frequency values (eigenvalues) of each vibrational mode, through the Wilson GF method and the secular equation of motion (eq. 1.10). In that equation the $\mathbf{G}$ matrix represented the kinetic energy of the molecular cell, and the $\mathbf{F}$ matrix expressed the potential energy of the system **[Woodward 1972]**. The fundamental assumption in the mechanical treatment of the molecular vibrations is that all vibrational motions are harmonic, i.e. the force constants of the vibrating molecules or atoms are properties of the system, independent of the temporary displacements.

However, experimental observations of vibrational frequency shifts of polymers **[Bretzlaff 1983, Wool 1986]** and carbon fibres **[Robinson 1986, Galiotis 1988a, Sakata 1987]** under mechanical deformations, have strongly questioned the validity of the harmonic treatment of the molecular vibration problem.

3.1.1. *Experimental evidence of the strain sensitivity of the vibrational spectrum.*

The application of compressive uniaxial stress on the Raman spectrum of silicon crystals, along two crystallographic axes of the material, was found to introduce positive shifts (frequency increase) of the Raman line, located at about 523 cm^{-1} **[Anastassakis 1970]**. From the observed splittings of the Raman peak (different rates of shifting) along the two crystallographic axes, experimental values for the "phenomenological coefficients" were derived. These coefficients describe the changes in the force ("spring") constants of the scattering species with applied strain. Similar effects were observed on the first order Raman spectrum of other diamond-type materials **[Cerdeira 1972]**.

The study of the Infra-Red spectrum of stressed polyethylene and polypropylene **[Bretzlaff 1983]** yielded the following macroscopic expression relating the frequency change to the applied stress:

$$\Delta\nu(\sigma) = \nu(\sigma) - \nu(0) = \alpha_{\sigma}\cdot\sigma \qquad (3.1)$$

where $\Delta\nu(\sigma)$ is the mechanically induced frequency shift, α_{σ} is the mechanically induced frequency shifting coefficient, at constant temperature, and σ is the applied uniaxial stress. The coefficient α_{σ} was found to be a function of temperature, morphology, thermal history and stress history **[Wool 1986]**. An important observation that temperature can also alter the vibrational spectrum of polymers **[Bretzlaff 1983]** is summarised in the following relationship :

$$\Delta\nu = \alpha_{c}\cdot\Delta f_{c} + b_{c}\cdot\Delta T \qquad (3.2)$$

where $\Delta\nu$ is the frequency shift, f_{c} is the force on a single chain, T is the temperature and α_{c} and b_{c} are the single chain stress and temperature coefficients of frequency shifting, respectively. The above expressions (equations 3.1, 3.2) have been also verified for the Raman spectrum of stressed polyethylene **[Wool 1986]**.

The effect of axial load on the Raman spectrum of PAN based, pitch based and rayon based carbon fibres was examined using Laser Raman Spectroscopy **[Robinson 1987]**. The strain dependence of the G line was

obtained for a loading direction parallel to the polarisation of the incident light. This strain dependence was found to be linear up to fibre fracture. The strain dependence of other spectral lines (D and G') of a high modulus carbon fibre under tension has also been reported in literature **[Galiotis 1988a]**.

Splittings and shifts of the G-line of highly oriented graphite fibres were found to be polarisation dependent **[Sakata 1987]**. The results were also used to obtain the phenomenological coefficients of the graphite cell. It should be noted here that the strain dependence of the Raman line for a 490 GPa graphite fibre was found to be about -28 cm^{-1}/ % of applied strain, when the stress vector was parallel to the light polarisation and only -8 cm^{-1}/ % , when perpendicular. However, these values were calculated for maximum stresses equivalent to only 0.15 % of applied tensile strain. In addition the experimental scatter as revealed in this work, was quite large, reaching in some cases 2 cm^{-1}.

3.1.2. *Theoretical considerations of the vibrational frequency strain dependence.*

When an external load is applied to a polymer chain, molecular deformation occurs through changes in the internal coordinates such as the bond length and the bond angles **[Bretzlaff 1983, Tashiro 1990]**. Should the force constants, that simulate the bond's reaction to externally induced deformation, remain unaffected, there would be no change in any of the matrices of the secular equation of motion (eq.1.10), and in turn, there would be no change in the vibrational frequencies of the material, as they are calculated by the determinant of that equation. Therefore, in an attempt to account for the stress and strain dependence of the Raman frequencies of crystalline polymers as well as, carbon fibres, the carbon-carbon potential energy function has been assumed to be strongly anharmonic **[Bretzlaff 1983]**. In other words, the material force constants are not literally constants but are considered to depend upon the interatomic deformations. For a simple diatomic molecule, such a situation is better simulated by an anharmonic potential function, of the kind proposed by Morse **[Morse 1929]**:

$$U(\Delta r) = D\cdot\left(1 - \exp(-a\cdot\Delta r) \right)^2 \qquad (3.3)$$

where Δr is the displacement (r_0-r) of the interatomic distance, and D and a are constants. The second derivative of equation 3.3, with respect to the displacement Δr, gives the force constant F for the bond stretching between the two atoms **[Ganesan 1970, Tashiro 1990]**:

$$F = 2\cdot a^2\cdot D\cdot\left(2\cdot\exp(-2\cdot a\cdot\Delta r) - \exp(-a\cdot\Delta r) \right) \qquad (3.4)$$

The dependence of the force constant F upon the molecular deformation Δr indicates that an increase in the bond distance by Δr due to extensional forces, will slightly reduce the value of the force constant F. Since the vibrational frequency ν is proportional to $\sqrt{F}$ **[Fitzer 1988d, Tashiro 1990]** this will result in a decrease of the frequency value for that vibrational mode. A schematic representation of the anharmonic Morse potential U (equation 3.3) and the resulting displacement-dependent force constant F (equation 3.4) are shown in figure 3.1a and b.

For complex lattice configurations such as diamond **[Ganesan 1970]** and graphite **[Sakata 1987]**, but also for single polymer chains, such as polyethylene **[Bretzlaff 1983]** and polyoxymethylene **[Tashiro 1990]**, the molecular vibrations can be modelled satisfactorily by the "quasi-harmonic" approximation. This treatment assumes very small changes in the internal coordinates R of the system (bond length, bond angles) and, hence, allows the interpretation of an anharmonic system as being harmonic but with a variable (stress and temperature dependent) force or "spring" constant **[Bretzlaff 1983]**. To recapitulate:

(1) The application of stress or strain to a crystalline material introduces frequency shifts to the vibrational (Raman and Infra-Red) spectrum of these materials.

(2) These frequency shifts can be explained in terms of changes in the Hamiltonian of the system (kinetic plus potential energy).

(3) Alterations can occur only in the potential energy term since there is no mass change with the application of external load.

(4) These changes are theoretically verified, by assuming anharmonic type of potential energy, or in other words, strain dependent type of material force "constants".

3.2. Experimental.

Axial tensile load can be applied to single carbon fibres by means of a microextensometer, as shown schematically in figure 3.2. Single fibres are mounted on the jaws of this device by gluing the fibre-ends between the metallic surface of the jaw and aluminum foil tabs. Special attention is given, so that the glue, prior to solidification, does not run along the free-standing length of the fibre, over the experimental gauge length. The latter is measured by a micrometer positioned on the drive that controls the slide of the microextensometer jaws. Subsequently, the microextensometer is positioned on the experimental stage of the Raman setup (fig.2.3). The induced strain can be calculated from the fibre elongation over the initial gauge length.

The Raman spectrum of a carbon fibre can then be obtained from various points along the fibre gauge length, and at various levels of applied strain. The whole procedure of the Raman spectrum derivation and analysis has been described in details in the previous chapter (§ 2.2). The high resolution mode of the spectrometer is exclusively employed in this part of the project, since accurate measurements of the relative displacements of the Raman lines with applied strain are required. The spectral resolution of this mode, for the 514.5 nm excitation wavelength, is 0.68 cm^{-1} for the D-line (at 1355 cm^{-1}), 0.66 cm^{-1} for the G-line (at 1580 cm^{-1}) and 0.58 cm^{-1} for the G′-line (at 2700 cm^{-1}).

For each type of fibre, the Raman spectrum was obtained at increments of applied strain (of 0.1%). At least 4 filaments per fibre type have been strained up to failure. The calculated frequency values for the Raman band under observation are subsequently plotted as a function of applied strain. At first approximation, a linear least-squares fit is applied to the frequency - strain data. The standard error of the slope, as well as, the standard error of the intercept can be calculated.

3.3. Results.

The sensitivity of the Raman spectrum of carbon fibres upon an externally applied strain has been investigated in this chapter. All prominent frequency lines of the carbon fibre Raman spectrum have been monitored at discrete levels of strain up to fibre failure. The G-line of the carbon fibre spectrum has attracted particular attention. Alongside the study of the G-line, the strain sensitivity of the disorder induced D-line, as well as, the strain sensitivity of the second-order G'-line, have also been examined.

3.3.1. *The strain dependence of the G-line of carbon fibres in tension.*

The effect of applied tensile strain on the G-line of the HMS (7 μm) fibre Raman spectrum is clearly demonstrated in the high resolution spectra of figure 3.3. The position of the G-line at 1.0% of applied strain, just before fibre fracture, has shifted from the ~1580 cm^{-1} value of the unstrained fibre to a lower frequency. Additionally, a small increase in the line bandwidth can be observed. The frequency shift of the G-line of the HMS fibre as a function of the tensile applied strain is presented in figure 3.4a. The frequency shift from the 1580 cm^{-1} value of the unstrained fibre is plotted on the y-axis, while the applied strain, calculated from the elongation of the initial fibre gauge length is plotted on the x-axis. The estimated error in the x-axis is ±0.01% strain for a 10 mm gauge length, since the micrometer precision is of the order of ±1 μm.

The frequency of the G-line of the HMS fibre appears to shift linearly with tensile strain (fig.3.4a). The least-squares-fitted line to the experimental data exhibits a slope of -11.4 cm^{-1}/% of applied strain. The standard error of the slope is calculated to be ±0.3 cm^{-1}/%. The slope of this line is defined as the Raman Frequency Gauge Factor (RFGF) in tension, for the G-line of the HMS fibre. This term will be consistently used to express the strain dependence of the carbon fibre Raman frequencies, throughout this thesis.

The half-height-bandwidth (HHBW) of the G-line for the HMS fibre is also affected by the tensile strain (fig.3.4b). Its strain dependence appears to be non-linear, particularly over 0.5% of applied strain. Just

before the fibre fracture the HHBW has increased by ~6 cm^{-1} from the initial value of 30 cm^{-1} for the free of strain fibre.

The strain dependence of the G-line, has been derived for all ten carbon fibres of Table 2.1. The corresponding RFGFs have been calculated assuming a linear relationship between Raman frequency and tensile strain. The results of this analysis are presented in Table 3.1. The type of carbon fibre, its modulus and the ratio I_D/I_G are also displayed in this Table. The strain sensitivity of the G-line is shown figures 3.5, 3.6 and 3.7, for each fibre series, i.e. the 7 μm series, the 5 μm series and the "morphology" series, respectively. In theses three graphs, the Raman frequency shift, plotted on the y-axis, is calculated from the actual frequency value $\nu(\varepsilon)$ of the G-line at applied strain ε, offset by the frequency value $\nu(0)$ of the same Raman band in the unstrained fibre. The most important observations that can be made are listed below:

(a) The RFGF is proportional to the fibre modulus for fibres which have been produced under the same manufacturing route. The higher the fibre modulus, the greater the calculated absolute value of the RFGF (fig.3.5 - 7 μm series and fig.3.6 - 5 μm series).

(b) The strain dependence of the G-line of carbon fibres exhibiting similar tensile moduli but different surface morphology is broadly proportional to the "amount of crystallinity" of the fibre surface, as this is described by the "disorder" ratio I_D/I_G. The higher the surface crystallinity (and the lower the intensity ratio), the greater the (absolute) RFGF value. (fig.3.7 - "morphology" series).

(c) The RFGF value is related to the characteristic intensity or "disorder" ratio I_D/I_G , regardless the fibre modulus or the fibre manufacturing route. This is demonstrated in figure 3.8, where the RFGF for the G-line of carbon fibres is plotted as a function of this ratio. The values for both the RFGF and the ratio I_D/I_G for the IM43 and the XA fibres have been obtained by treating the merged G-D′ lines as one band, since discrimination of these two two lines cannot be achieved (Chapter 2, §§ 2.3, 2.4).

The effect of fibre surface treatment on the RFGF of the G-line.

The effect of fibre surface treatment on the strain dependence of the Raman spectrum has also been examined. With respect to the high modulus 7 μm fibre, the measured RFGF values for the treated (HMS) and the untreated form (HMU) were obtained for the well distinguished G-line (Chapter 2) and are reported in Table 3.1.

As mentioned previously (§ 2.3) the surface treatment of the intermediate modulus 5 μm IM43 fibre did not introduce any change to the strain sensitivity of the merged G-D′ line of the Raman spectrum of this fibre. The measured RFGF values for the untreated form of the IM43, the IMA, the standard treated version IMD, and the heavily surface treated type IMF, are displayed also in Table 3.1.

The small variations in the values of the RFGF with fibre surface treatment, for both types of fibres reported above, are within the standard error of the slope of the linear fit, and therefore, can be considered as insignificant.

The effect of laser power on the RFGF of the G-line.

The laser power effects on the position of the Raman frequencies of carbon fibres have been reported in Chapter 2. The results have shown that the Raman frequency is sensitive to laser power, when the strain is (constant) zero and also that the Raman frequency is sensitive to strain, when the laser power is constant. What has not yet been considered is the overlapping effect of the varying laser power and, therefore, the fibre temperature in the locality of the focal spot and the externally induced strain on the fibre. Thus, the strain dependence of the G-line for the HMS fibre was examined at various levels of laser power: 0.5 mW, 1 mW, 2 mW, 3 mW and 4 mW on the sample. The results of this experiment are shown in figure 3.9. The parallel lines that describe the strain dependence of the G-line indicate that the RFGF is independent of the probing laser power. Furthermore, the HHBW of this line was not affected by the laser power. The RFGF of the merged G-D′ line of the IM43 fibre was also found to be independent of the laser power.

3.3.2. *The tensile strain dependence of other Raman lines of carbon fibres.*

It is not only the frequency of the graphitic G-line of the carbon fibre Raman spectrum which is strain sensitive. All prominent Raman frequency bands of the HMS fibre exhibit a significant strain dependence. The results are summarised in Table 3.2.

Similarly to the graphitic G-line, the D-line of the HMS fibre also shifts to lower values in the Raman spectrum with applied strain, at a rate of -10.1±0.4 $cm^{-1}/\%$, comparable to that of the G-line of the HMS fibre.

On the other hand, the other "disorder" induced feature, the D'-line (appearing as the "shoulder" of the main graphitic peak) exhibits a strain dependence of -5.4±0.8 $cm^{-1}/\%$. With regard to the half-height-bandwidth of each line, the D-line follows the pattern of the graphitic G-line by broadening over 0.5% applied strain, whereas the D'-line appears to retain its initial bandwidth. However, as the G-line masks partially the D' "shoulder" line (Chapter 2, fig.2.11), the accuracy of this measurement is questionable. Since none of these two lines has been independently characterised in this study, (the D'-line is present in all fibre spectra of Chapter 2), the fitting parameters of the weaker feature are only approximately estimated.

The highest strain sensitivity exhibited by a Raman line in the HMS Raman spectrum, is the one of the second-order G'-line, located at about 2700 cm^{-1}. The strain dependence of this line for the HMS fibre is calculated as 25.3±0.4 $cm^{-1}/\%$ of tensile strain. The strain broadening of the HHBW of this band is also particularly pronounced over ~0.5% of tensile strain. The impressively high frequency shift with applied strain exhibited by this line reconfirms its assignment as a second-order feature.

3.4. The strain dependence of the Raman spectrum and the structure of carbon fibres.

While the vibrational frequency shift with applied strain has been theoretically explained in terms of anharmonicity of the material force constants **[Bretzlaff 1983, Tashiro 1990]**, the rate of the strain dependence as well as, the strain-broadening of the individual Raman bands of carbon fibres, can provide substantial information, with respect to the structure of this material.

In materials with crystallites exhibiting a distribution of angle orientation to the principle axis, such as carbon fibres, a uniaxially applied load is expected to introduce a distribution of stresses upon the individual crystallites. The vibrational frequencies of overstressed and understressed crystallites appear at slightly lower or higher values than those of the crystallites subjected to the average stress. In contrast to the reported asymmetric broadening of the Raman bands in stressed polymers **[Bretzlaff 1983, Wool 1986]**, the observed broadening of the carbon fibre Raman lines was rather symmetric for all pronounced bands of the spectrum. The vast difference, in terms of crystallinity, between the phases that comprise the polymeric fibres, may account for this different spectroscopic (and mechanical) behaviour.

The Raman frequency of every single line in the Raman spectrum was found to be - at a first approximation - linearly dependent upon applied strain :

$$\nu(\varepsilon) = \nu(0) + \alpha_{\varepsilon} \cdot \varepsilon \qquad \Leftrightarrow \qquad (3.5a)$$

$$\Delta\nu(\varepsilon) = \nu(\varepsilon)-\nu(0) = \alpha_{\varepsilon} \cdot \varepsilon \qquad (3.5b)$$

where $\nu(\varepsilon)$ is the value of the Raman frequency at applied strain ε, $\nu(0)$ is the value of the Raman frequency of the unstrained fibre, $\Delta\nu(\varepsilon)$ is the Raman frequency shift induced by the applied strain ε at constant temperature and α_{ε} is the Raman Frequency Gauge Factor (RFGF), which expresses the rate at which the carbon fibre Raman frequencies change with

the externally applied strain. The above equation is equivalent to the empirical expression of equation 3.1, that related the stress induced frequency shift $\Delta\nu(\sigma)$ in the Infra-Red spectrum of polymeric chains to the applied stress σ:

$$\Delta\nu(\sigma) = \alpha_{\sigma} \cdot \sigma \qquad (3.1)$$

where α_{σ} was the mechanically induced frequency shifting coefficient **[Bretzlaff 1983]**. A comparison of these two equations 3.5 and 3.1, shows that for the same amount of frequency shift $\Delta\nu$, the α_{ε} factor (RFGF) of our study is actually equivalent to the coefficient α_{σ} multiplied by the tangential (at 0.0% strain) fibre modulus (assuming that the off-axis stresses are negligible compared with the axial stress σ):

$$\alpha_{\varepsilon} = \alpha_{\sigma} E_f \qquad (3.6)$$

The above expression allows the representation of the Raman frequency shift as a function of the applied stress, by simply dividing the calculated RFGF value by the fibre quoted tensile modulus E_f. However, the application of this equation should be carried out with caution, as the average fibre modulus is not always equal to the modulus in the fibre surface, where the Raman data are obtained from.

3.4.1. *The strain dependence of the carbon fibre Raman spectrum and the carbon fibre modulus.*

The strain dependence of the carbon fibre Raman frequencies and particularly of the G-line, assigned to the E_{2g} vibrational mode of graphite, was found to follow an approximately linear relationship with the intensity or "disorder" ratio I_D/I_G (fig.3.8). With respect to the fibre modulus, the strain sensitivity of the Raman frequencies follows the same linear relationship only for fibres produced by the same technology. A graphical representation of the findings of Table 3.1, shows that the modulus - RFGF linear relationship is valid only for the fibres of the same series (fig.3.10). This experimental relationship can be expressed in

mathematical terms:

$$\alpha_{\varepsilon} = k \cdot E_f \qquad (3.7)$$

where α_{ε} is the RFGF for the G-line in tension, E_f is the axial (average) fibre modulus and k is a constant related to the fibre structure and the specific fibre series.

A physical interpretation of the above equation implies that the Raman Frequency Gauge Factor α_{ε} is should be zero either when the modulus tends to zero, or, when the fibre is subjected to a load that does not have a component along the a-axis of the graphite crystallites (fig.1.1). Since the E_{2g} vibrational mode in the graphite lattice is related to in-plane (a-plane) motions, the RFGF of the corresponding G-line on the Raman spectrum should be strongly dependent upon alterations of the C_{11} elastic constant of graphite (§ 1.1.2). This elastic constant is the main contributor to the axial fibre modulus **[Dresselhaus 1988]**.

It should be noted, here, that although the RFGF vs modulus line was not forced to go through the zero point (fig.3.10), it intercepts the RFGF axis very close to that value, confirming the validity of the above analysis. The small offset may be due to the influence of the RFGF values of fibres such as the XAS and IM43, where the strain dependence of the G-line can not be individually measured, as it is merged with the D′-line (§§ 2.3 & 2.4).

It is known that higher modulus products can be derived from the same precursor, primarily by increasing the graphitisation temperature **[Dresselhaus 1988]**. The change of the fibre crystallinity is, therefore, related to the graphitisation temperature and finally to the fibre modulus. A simple model of the carbon fibre structure, shown in figure 3.11, was employed to verify the relation of the Raman strain dependence with the fibre crystallinity and its modulus. According to this model, the carbon fibre consists of two distinct regions: a well crystalline phase A (which contains the Raman scattering cells) and a non-crystalline (disordered) phase B. An analytical explanation of the RFGF-fibre modulus relationship has been attempted in Appendix A1. The fundamental precondition of this model and its analysis is an equal stress situation prevalent between the two fibre phases. This modelling explains, in a simplified manner, the larger frequency shifts with applied strain in high modulus fibres (Appendix A1).

A careful observation of equations 3.6 and 3.7 can reveal that the constant k, which expresses the slope of the RFGF versus fibre modulus relationship, for fibres produced under the same manufacturing route, is identical to the stress dependence, or, stress induced frequency shifting coefficient α_σ :

$$\alpha_\sigma = k \qquad (3.8)$$

Equations 3.6 (or 3.7) can be employed to derive the apparent stress dependence coefficient α_σ from the experimentally measured strain dependence coefficient α_ε and the (average) fibre modulus:

$$\alpha_\sigma = \frac{\alpha_\varepsilon}{E_f} \qquad (3.6a)$$

where α_σ is the "apparent" stress dependence coefficient. The term "apparent" is used to distinguish it from the directly experimentally measured stress dependence coefficient.

3.4.2. *The stress sensitivity of the carbon fibre Raman spectrum and the carbon fibre structure.*

Applying the above analysis to the results of Table 3.1, the apparent stress dependence of the G-line for all carbon fibres tested can be derived. The outcome of this conversion is shown in Table 3.3. The apparent stress dependence coefficient (and the constant k) for the 7 μm fibre series is about -2.9 cm^{-1}/GPa, whereas for the 5 μm fibre series it has a value of about -2.25 cm^{-1}/GPa. It can be seen that, for the "morphology" fibre series, the α_σ coefficient (i) approaches the 7 μm series value for the LF-neg, (ii) it is identical to the 5 μm series value for the LF-neut fibre and (iii) it deviates away from either of these values for the LF-pos fibre. A graphical representation of these findings is shown in figure 3.12.

The two major points that need to be addressed are : (a) why all fibres produced by the same technique, regardless of the final graphitisation temperature and modulus, possess vibrational frequencies

equally sensitive to tensile stress and (b) how the changes in the fibre structure and morphology imposed by an alternative manufacturing process could alter the apparent stress sensitivity.

The finding that the Raman frequency stress sensitivity, for both a high and a low modulus fibre, is the same, implies that under the same externally applied stress the crystallite units within these fibres "feel" the same amount of stress along their a-axis. The latter argument is in full agreement to the equal stress model, introduced in the previous section (§ 3.4.1), applied for the fibre structure simulation of figure 3.11 and analysed in Appendix A1.

Despite the fact that the crystallites have a distribution of angular orientation about the fibre axis, a majority of them are well aligned to the fibre axis, as the peak of the distribution at zero degrees indicates (fig.3.13). Therefore, it can be stated that the majority of these units are subjected to the same stress as the average value. The equal stress model has been extensively used in literature to study the response of the microstructure to external deformations **[Ruland 1967, Allen 1988,1989]**. Shearing mechanisms in misorientated crystallites simply result in higher macroscopic strains required, in order to apply a certain amount of axial stress.

An additional problem arises with the observation that a change in the manufacturing route can reduce or increase the apparent stress sensitivity of the G-line (Table 3.3). One of the serious obstacles in our attempt to understand this phenomenon is the lack of information regarding the fibre manufacturing technology and the main differences between different production routes. Nevertheless, the experimental findings may, on their own, provide a clue for the effect of the microstructure upon the carbon fibre properties. The value of the stress dependence parameter α_σ for the 5 μm diameter technology fibres is found to be ~-2.25 cm^{-1}/GPa. As a result of the morphological control during the production of the 5 μm fibre series, the value of the apparent stress dependence α_σ rises (in absolute value) to ~-2.6 cm^{-1}/GPa for the LF-negative fibre, which resembles the surface morphology of the HMS 7 μm fibre and drops (in absolute value) to ~-2.1 cm^{-1}/GPa for the LF-positive fibre.

The proposed explanation is based on the well publicised skin-core effect in carbon fibres and is described by a model for the three "morphology" fibres, schematically illustrated in figure 3.13. It is

believed that the morphological control used during carbon fibre production reduces the radial anisotropy of the carbon fibre structure. The LF-negative fibre exhibits the most crystalline surface of all three "morphology" fibres, as verified by the Laser Raman characterisation (Chapter 2). It should also present the most pronounced skin-core discrepancies (and therefore, radial modulus distribution **[Chen 1983]**) since all three fibres are engineered in such a way, so that their average Young's modulus is similar. On the other hand, the LF-positive fibre is thought to exhibit the least pronounced skin-core effect and therefore the most uniform radial modulus distribution of all three "morphology" fibres. As shown in figure 3.13, the most crystalline region of each fibre is its surface. The surface Young's modulus is, therefore, higher than the average Young's modulus. Bearing in mind that the strain dependence of the Raman frequency (RFGF) is measured very close to the fibre surface, the conversion of the strain dependence to stress dependence by dividing the RFGF value with the average fibre modulus may lead to erroneous results. The stress dependence of the G Raman frequency should be the same for all carbon fibres, as explained a few paragraphs above. Any variation of the apparent stress dependence α_σ coefficient for fibres with similar average moduli is simply due to the difference between their surface moduli. Since the stress dependence of the Raman frequencies should be a constant parameter for all carbon fibres, equation 3.6 can be employed in the derivation of the real surface modulus of a carbon fibre:

$$E_f(\text{surface}) = \frac{\alpha_\varepsilon}{\alpha_\sigma^*} \qquad (3.6b)$$

where the α_ε is the experimentally measured strain dependence (RFGF) of the Raman frequencies (from the surface) of the carbon fibre and α_σ^* is the constant stress dependence of the Raman frequencies calculated, via equation 3.6a for a carbon fibre with a uniform radial distribution of modulus.

If the LF-positive fibre, which exhibits the least pronounced skin-core effect of all the examined fibres, is considered as satisfying the requirement of a uniform radial modulus distribution, then the value $-2.1\ cm^{-1}/GPa$ calculated as the stress dependence of the Raman frequencies for that fibre, is a realistic approximation for the α_σ^* value.

A preliminary study of the application of equation 3.6b on the RFGF results accumulated up to now was carried out. The estimated surface Young's modulus for the LF-neg fibre (average modulus 378 GPa) was found to be ~475 GPa. The surface modulus for the LF-neut fibre (average modulus 378 GPa) was estimated as ~410 GPa, while for the LF-pos fibre the surface and average modulus coincide, as this fibre has been assumed to exhibit a radially homogeneous structure and provided the α_{σ}^{*} value.

The use of equation 3.6b for estimating the surface modulus of carbon fibres, should be restricted only for fibres that exhibit a distinct Raman G-line, since only this band is related with the in-plane vibrational mode in the graphite cell (the E_{2g} vibrational mode, fig.1.14) and, consequently, with the modulus along the a-plane (C_{11}=1060 GPa, Chapter 1). Therefore, the application of this equation would not give reliable results for the IM43 and the XAS fibres for which the RFGF has been derived for the merged G-D′ band. ▮

Table 3.1. The tensile Raman Frequency Gauge Factor (RFGF) of the G-line (E_{2g} vibrational mode) of carbon fibres.

Fibre	Diameter (μm)	Modulus (GPa)	Tens.strain to failure (%)	I_D/I_G	RFGF ($cm^{-1}/\%$)
HMS	7	390	1.0	0.36	-11.4 ±0.4
IMS	7	305	1.5	0.85	- 8.9 ±0.4
XAS(*)	7	230	1.5	0.80	- 7.0 ±0.6
LF58	5	405	1.1	0.60	- 9.0 ±0.4
LF53	5	370	1.3	0.85	- 8.5 ±0.4
LF48	5	335	1.5	0.90	- 7.5 ±0.5
IM43(*)	5	305	1.8	0.80	- 6.9 ±0.6
LF-neg	5	378	1.0	0.50	-10.0 ±0.4
LF-neut	5	378	1.1	0.70	- 8.6 ±0.5
LF-pos	5	364	1.1	0.95	- 7.7 ±0.6
HMU	7	390	1.0	0.28	-11.4 ±0.3
IMA(*)	5	305	1.8	0.80	- 7.2 ±0.5
IMF(*)	5	305	1.8	0.80	- 7.0 ±0.5

(*) For the IM43 and the XAS fibres, both the intensity ratio and the RFGF value are with respect to the merged G-D' band.

Table 3.2. The tensile Raman Frequency Gauge Factor (RFGF) and the half height bandwidth (HHBW) for all lines of the HMS carbon fibre.

Raman line	Frequency (cm^{-1})	RFGF ($cm^{-1}/\%$)	HHBW (cm^{-1}) at ε= 0%,	0.5%,	1.0%
G-line	~1580	-11.4	30	32	36
D-line	~1355	-10.1	38	40	45
D'-line	~1620	~-5.4	~30	~30	~30
G'-line	~2700	-25.3	60	63	68

Table 3.3. The apparent tensile stress dependence of the G-line of carbon fibres.

Fibre	RFGF (cm^{-1}/%)	Modulus (GPa)	Stress dependence cm^{-1}/GPa
HMS	-11.4 ±0.4	390	-2.92 ± 0.15
IMS	- 8.9 ±0.4	305	-2.91 ± 0.17
XAS(*)	- 7.0 ±0.6	230	-3.04 ± 0.30
LF58	- 9.0 ±0.4	405	-2.22 ± 0.12
LF53	- 8.5 ±0.4	370	-2.29 ± 0.15
LF48	- 7.5 ±0.5	335	-2.24 ± 0.18
IM43(*)	- 6.9 ±0.6	305	-2.26 ± 0.25
LF-neg	-10.0 ±0.4	378	-2.64 ± 0.14
LF-neut	- 8.6 ±0.5	378	-2.27 ± 0.16
LF-pos	- 7.7 ±0.6	364	-2.11 ± 0.20

The apparent stress dependence of the G-line of the carbon fibre Raman spectrum is calculated by dividing the RFGF (strain dependence) - Table 3.1, column 2- by the average tensile modulus E_f of the fibre - Table 3.1, column 4. For the stress dependence error estimate, both the standard error on the RFGF value and a fixed error of ±5 GPa for the modulus value, have been taken into account. In the case of the star (*) marked fibres XAS and IM43, it should be reminded that the reported values for the RFGF are with respect to the merged G-D′ line (Chapter 2) and not to the G-line on its own.

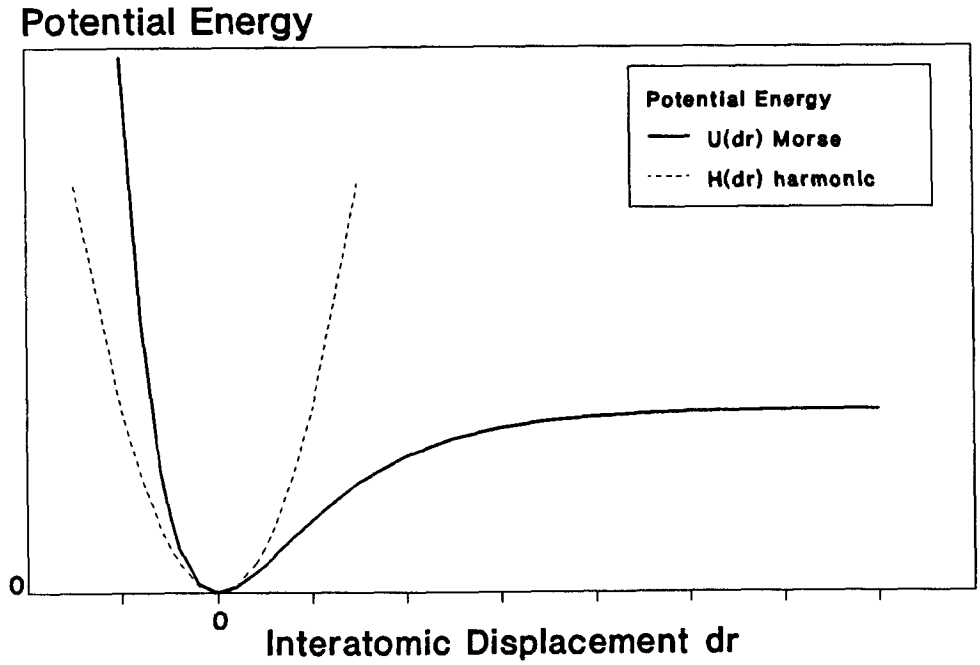

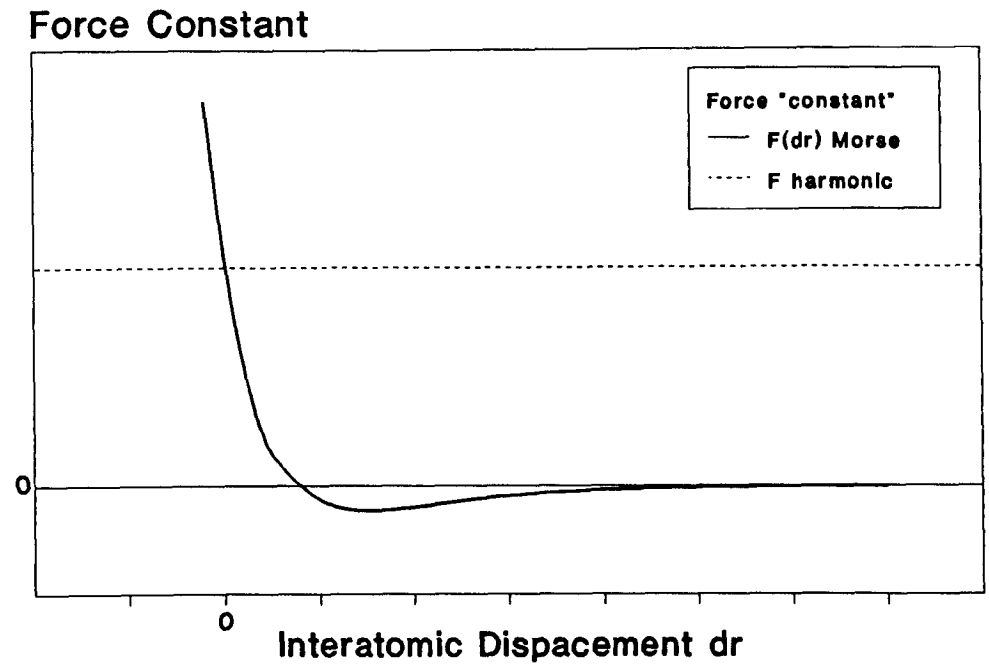

Fig. 3.1 **(a)** The Morse potential function and **(b)** the corresponding force "constant" for a diatomic molecule. The dotted lines in (a) and (b) represent the harmonic potential and the harmonic force constant, respectively.

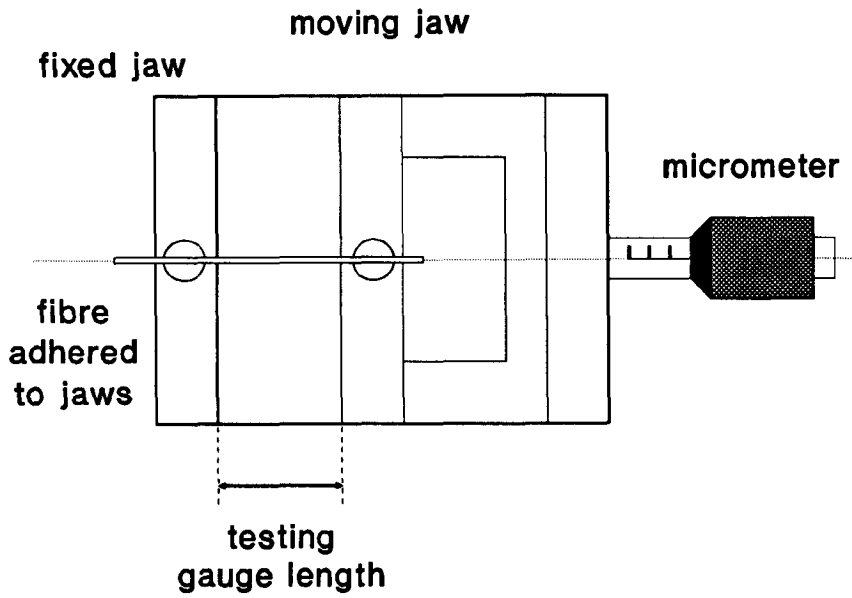

Fig.3.2 Sketch of the microextensometer used for tensile testing of single filaments.

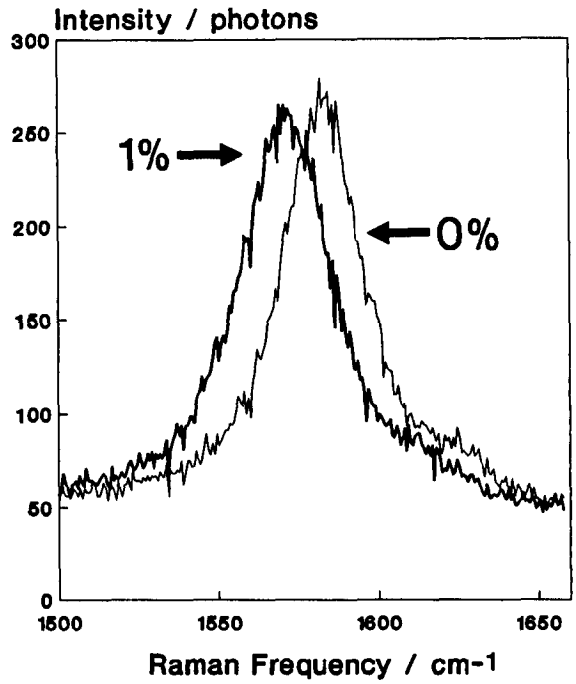

Fig. 3.3 The high resolution Raman spectrum of the HMS fibre G-line at 0.0% and 1.0% applied tensile strain.

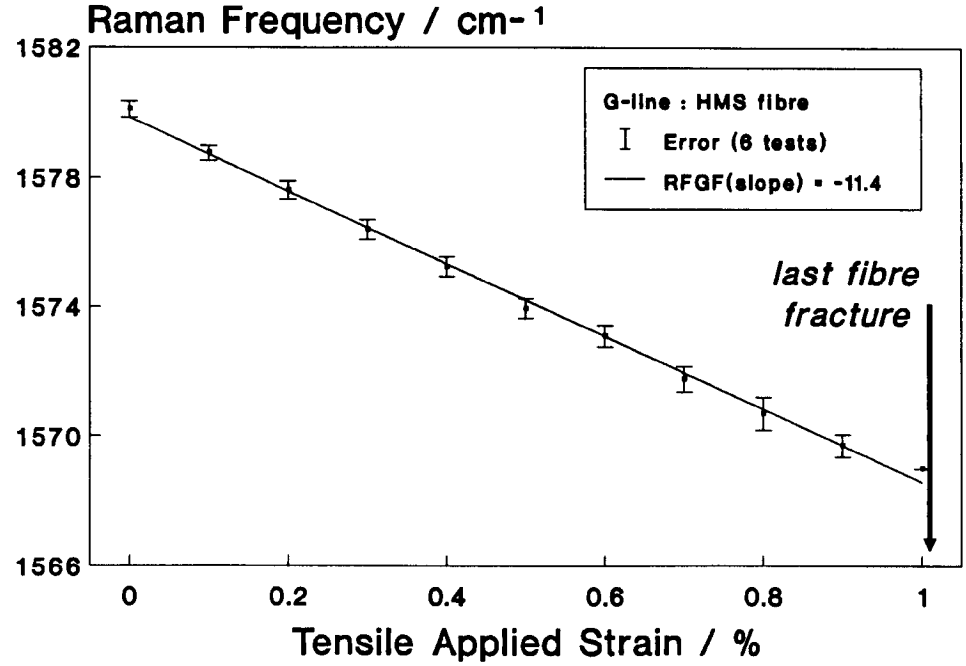

Fig. 3.4 **(a)** The strain dependence of the G-line of the HMS fibre. The Raman Frequency Gauge Factor (RFGF) expresses the slope of the least-squares fitted line to the experimental data.

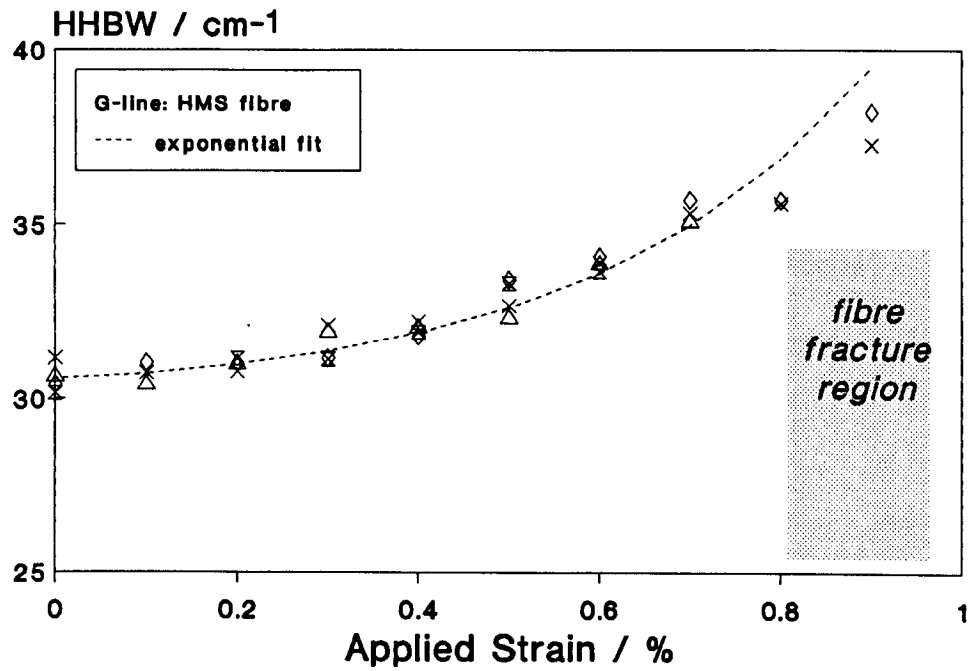

Fig.3.4 **(b)** The effect of tensile strain on the half-height-bandwidth (HHBW) of the G-line of the HMS fibre.

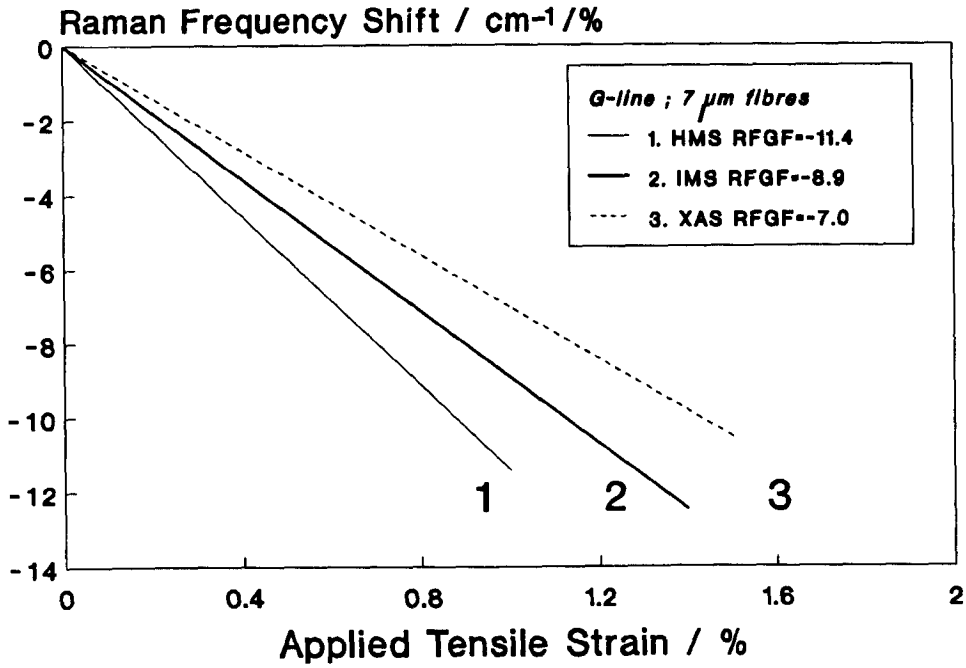

Fig. 3.5 The strain dependence of the G-line for the 7 μm fibre series.

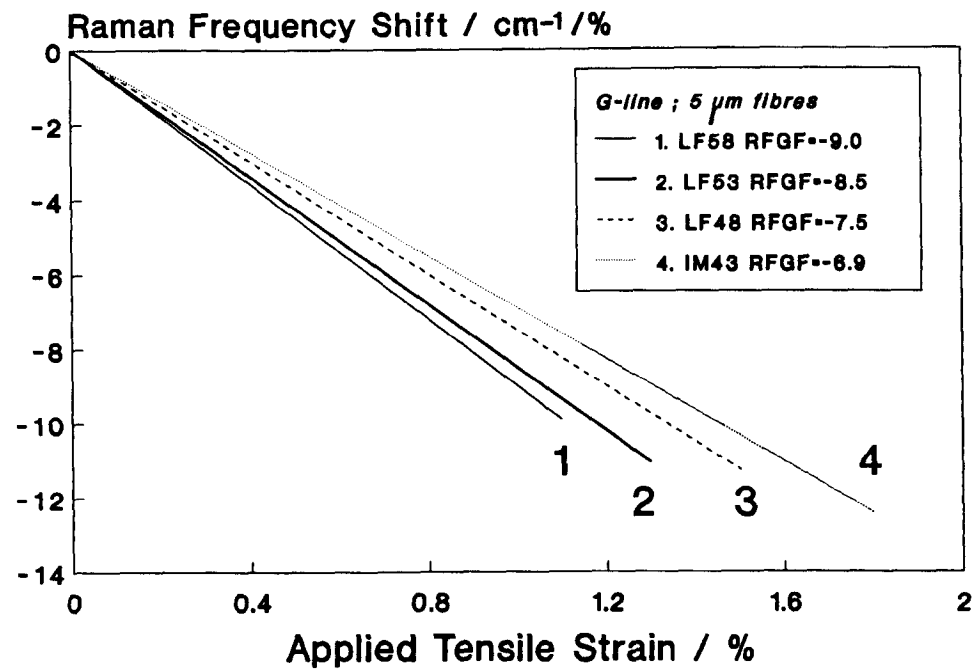

Fig. 3.6 The strain dependence of the G-line for the 5 μm fibre series.

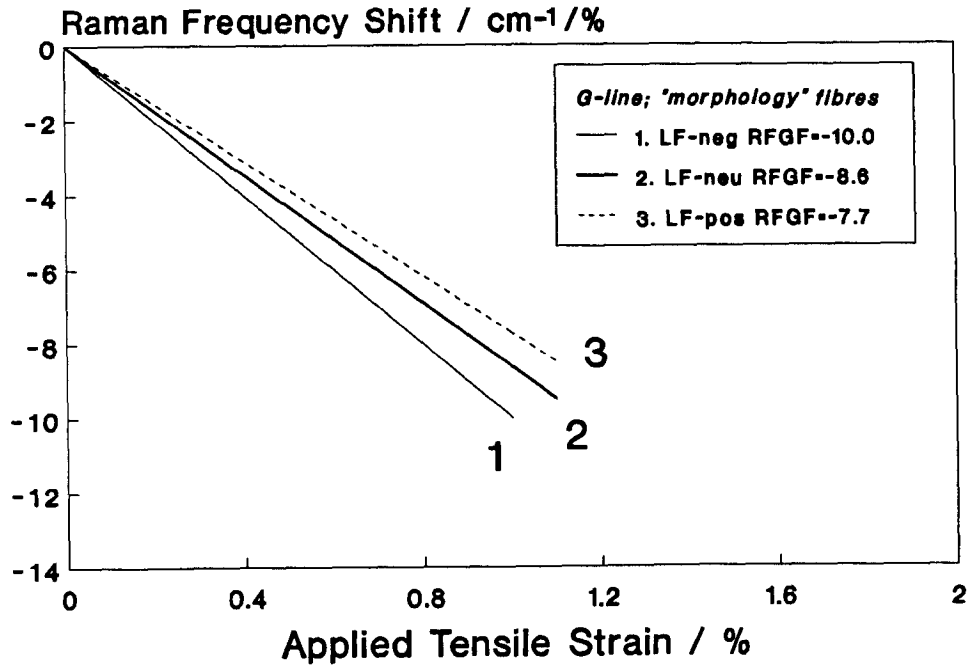

Fig. 3.7 The strain dependence of the G-line for the "morphology" fibre series.

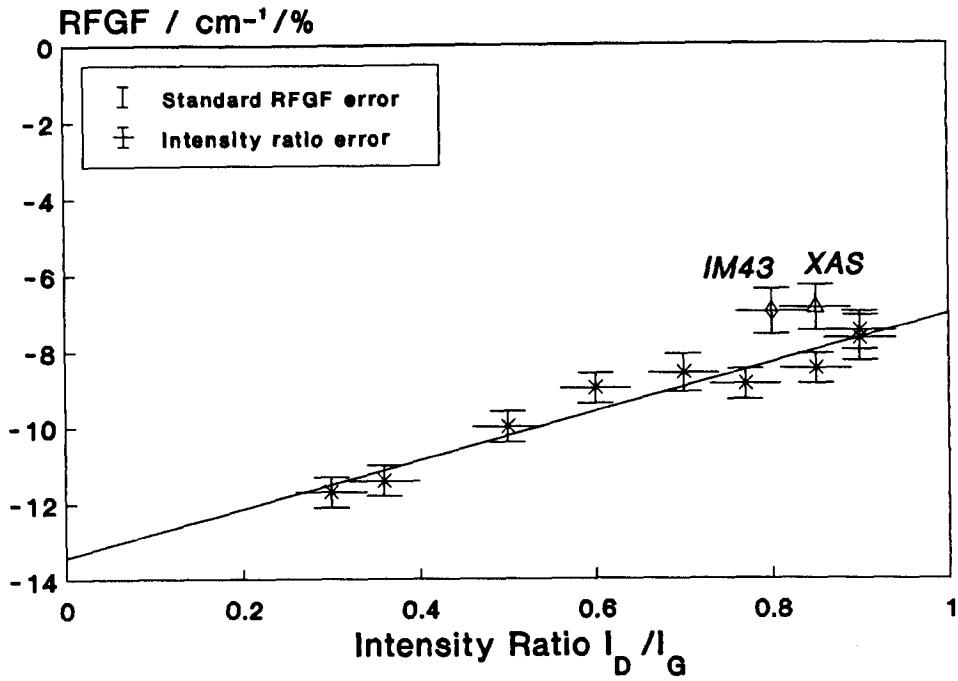

Fig. 3.8 The Raman frequency strain dependence (RFGF), as a function of the intensity ratio I_D/I_G (or $I_D/I_{(G-D')}$ for the IM43 and the XAS fibres, where the two features have merged).

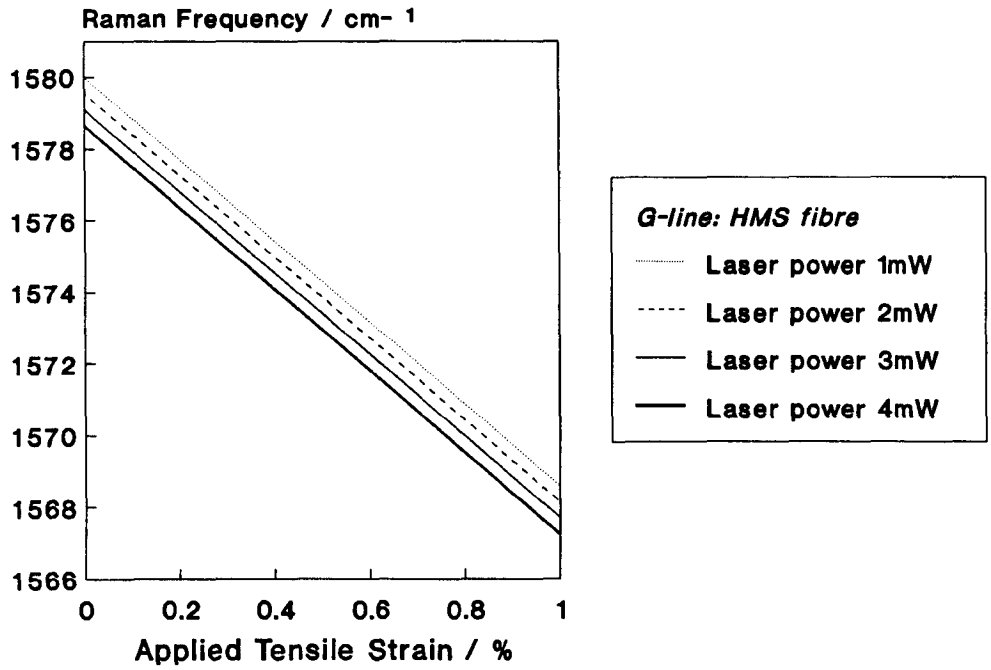

Fig. 3.9 The strain dependence of the G-line for the HMS fibre at various levels of power of the laser incident beam.

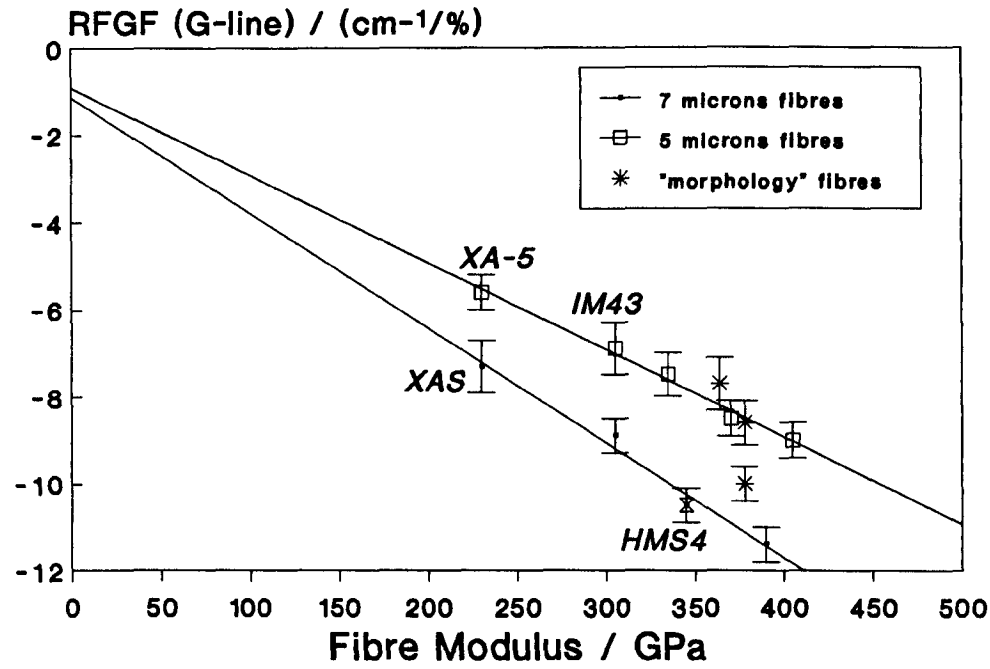

Fig.3.10 The strain sensitivity (RFGF) of the G-line (G-D′ band for the IM43 and XAS), as a function of the fibre tensile modulus.

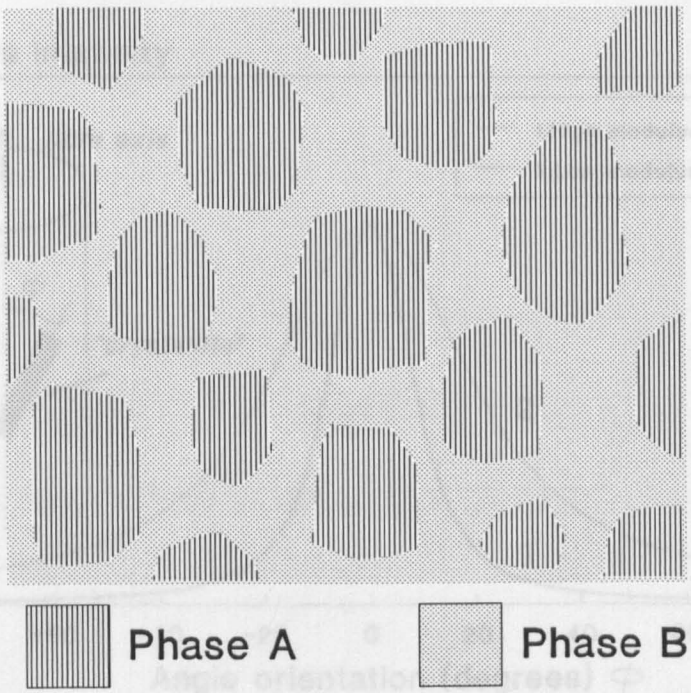

Fig.3.11 A model of the carbon fibre structure, comprising two distinct phases: the crystalline phase (A) and the disordered phase (B).

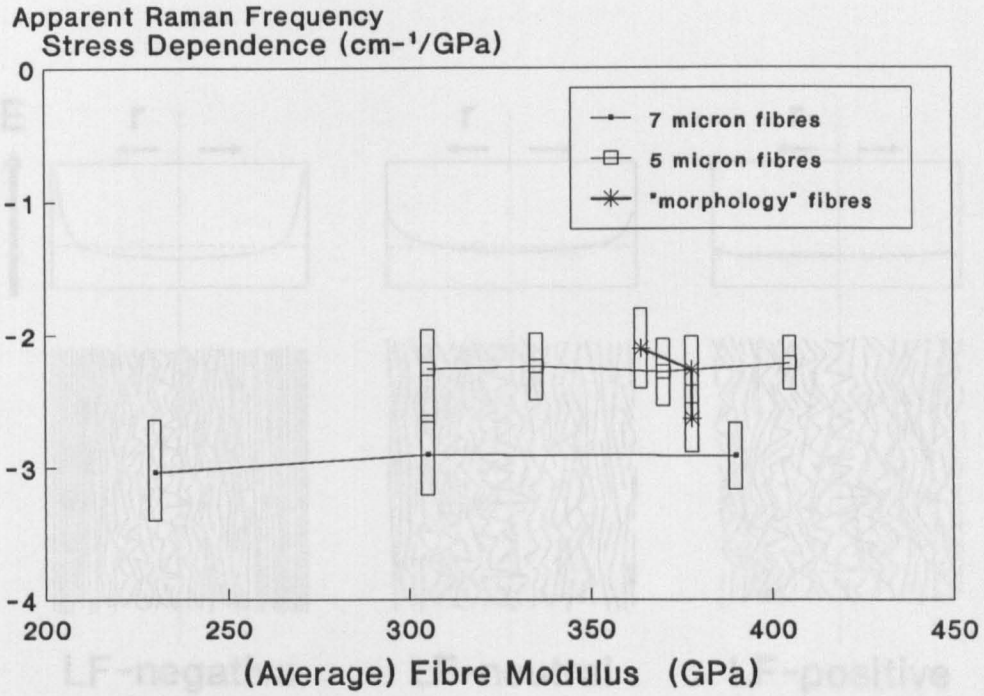

Fig.3.12 The apparent stress dependence coefficient, α_σ=RFGF/E_f, for the G-line of carbon fibres, as a function of the fibre tensile modulus.

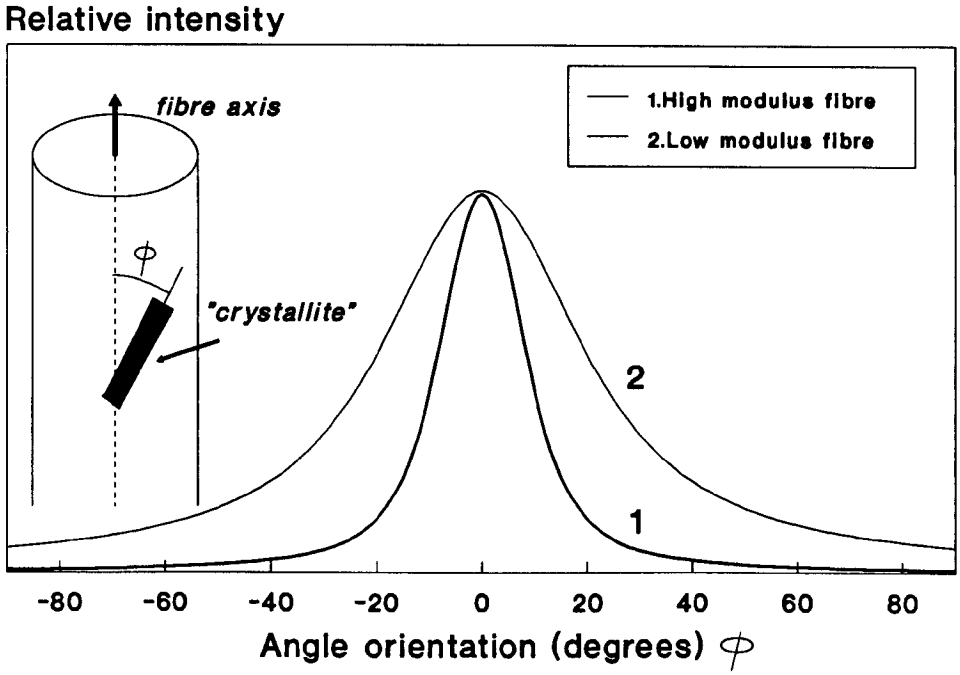

Fig.3.13 Typical angle orientation distribution for carbon fibres of varying crystallite perfection, and therefore, modulus **[Dresselhaus 1988]**.

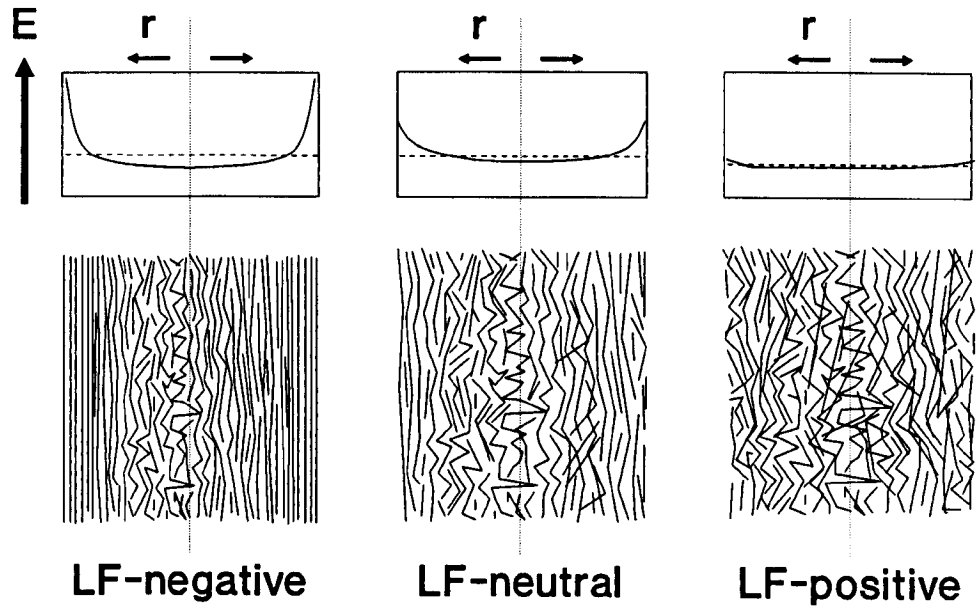

Fig.3.14 Structural model of the "morphology" fibres, that relates the skin-core effect to the modulus distribution along the fibre diameter.

CHAPTER 4

COMPRESSIONAL BEHAVIOUR OF CARBON FIBRES

4.1. Literature review.

The compressional behaviour of carbon fibres can also be monitored using Laser Raman Spectroscopy. The objective of the current investigation is to find a way to derive the carbon fibre Raman frequency strain dependence in compression, and, in sequence, to use this information in order to study the compressive properties of single carbon fibres. A series of compressive studies on unidirectional composites have indicated that composite compressive properties such as, strength, modulus, failure mode and post failure characteristics, are highly dependent on the intrinsic compressive properties of the fibres themselves **[Hancox 1975, Piggott 1981]**. As the compressional behaviour of fibrous composites is one of the most important parameters in the design of high performance materials **[Greszczuk 1981]**, it is necessary to support the design process with well characterised constituent materials.

A variety of tests and techniques have been employed to date, for the study of the compressional behaviour of single fibres. One of the most common single fibre tests is the "elastica loop" test, which in its initial version, was used to measure the tensile strength and modulus of single glass filaments **[Sinclair 1950]**. As the looped fibre is restricted between two microscope slides, by pulling the two fibre ends, the loop is gradually reduced in size. In theory, the ratio of the major axis to the minor axis of the loop should remain constant and equal to a value of 1.34, as long as the fibre behaves elastically **[Jones 1971]**. The strain at any point along the fibre loop can be calculated simply as $\varepsilon = r/R$, where r is the fibre radius and R is the curvature radius at that point. The maximum strain is developed at the head-loop point, and therefore, this is the area where the first failure is bound to occur. The outer surface of the looped fibre is under tension and the inner under compression. The onset of inelastic or non-hookean behaviour can be detected by the rapid increase in the loop axis ratio.

The elastica loop test has been used to study the failure mode on single aramid **[Greenwood 1974, Zwaag 1988a]** and other polymeric fibres **[Zwaag 1988b]**. The kink-band formation of the compressive side of these fibres has been attributed to a plastic deformation process which is activated before any elastic instabilities develop. The same technique has

been applied on Kevlar fibres. The plastic nature of the deformations at very low compressive strains has been attributed to the separation of the microfibrils that compose the Kevlar fibre **[Greenwood 1974]**. The molecular structure of Kevlar fibres has been identified to be the key factor for the poor compressional behaviour of these fibres **[Dobb 1981]** and their composites **[Greenwood 1974]**.

The elastica loop test has also been applied on carbon fibres **[Jones 1971]**. The initial intention of the aforementioned investigation was the study of the tensile strength of polyacrylonitrile-(PAN)-based and cellulose-based carbon fibres of various heat treatments. However, the initiation of failure at the compressive side of the looped fibre, in highly graphitised fibres, indicated that a buckling instability mechanism is activated during the compression of highly anisotropic fibres, as carbon fibres.

The dual nature of the load, i.e. tensile and compressive, on the same fibre cross-section during the elastica loop test, introduces additional difficulties in the attempt to distinguish the failure mechanisms in compression of carbon fibres. Therefore, axial compression tests on single fibre model composites were considered to provide a more appropriate loading configuration, of purely compressive nature, along the fibre axis. Thus, single pitch based carbon fibres were embedded in epoxy resin and the specimens were compressed in the fibre axis direction **[Hawthorne 1975]**. Fine compression induced cracks were directly observed to occur in all but the lowest modulus fibres, where usually only one failure was apparent. Similar observations were reported in the case of axial compression tests of specimens with a bundle of fibres embedded in the resin block **[Hahn 1986]**. The compressive strength was then calculated by assuming that the fibre Young's modulus is the same in tension and compression. The findings that axial compression fracture first initiates at the outer fibre surface **[Hawthorne 1975]** is in accordance with the view that some carbon fibres exhibit a more axially aligned texture and a more graphitic outer surface compared with the fibre core (Chapters 2 and 3). This skin-core effect is of significant importance as far as the compressional behaviour of carbon fibres is concerned, since the existence of a radial anisotropy induces a non-homogeneous distribution of the Young's modulus throughout the cross-section of the fibre (Chapter 3).

With respect to the compressive mode of failure of carbon fibres, there is an uncertainty, or at least lack of clarity in most of the reported investigations. The fine compressive induced cracks, observed on single fibres embedded in a block of resin **[Hawthorne 1975]**, have been attributed to a shear mode of deformation for glassy carbon fibres, which progressively changes to microbuckling as the fibre anisotropy (and modulus) increases. Paradoxically, in the same investigation, the mechanism of buckling deformation of the well-oriented and less constrained crystallites of the highly anisotropic carbon fibres was thought to involve primarily "crystallite regions weak in shear". This explanation is in contradiction with the initial statement, assigning the microbuckling mode of compressive failure to the highly crystalline and anisotropic fibres **[Hawthorne 1975]**.

In a recent investigation **[Dobb 1990]**, fibre recoil tests were conducted on PAN-based and pitch-based carbon fibres and the fracture surfaces were examined under the Scanning Electron Microscope. The main conclusion of this study was that all carbon fibres fail in compression by kink-band formation. However, the morphology of this kink-band differs with the fibre origin. PAN-based carbon fibres kink by microbuckling, while pitch-based fibres kink by shear **[Dobb 1990]**. In another investigation, the compressional behaviour of pitch-based carbon fibres, was linked to structural features such as the crystallite dimensions and orientation **[Crasto 1990]**. Therein, it was noted that high modulus PAN-based fibres are expected to exhibit similar compressional behaviour to the pitch-based ones, as the 3-dimensional crystallinity developed in these fibres at the last stages of graphitisation, starts resembling the sheet-like graphite structure of the pitch-based filaments.

The argument as regards the nature of the compressive failure of carbon fibres seems to be endless: Compressive tests on single PAN-based carbon fibre composites **[Boll 1990]**, supported by SEM micrographs from the fractured surface of intermediate and low modulus carbon fibres, gave no evidence of fibre microbuckling at all. On the contrary, the most common mode was initial failure by shear, which could develop to crashing damage, shear sliding or longitudinal stepped splitting.

A classical elastic instability analysis has recently been employed to study the microbuckling of polymer fibres, by modelling the fibre as a composite structure on its own and the idealised polymer chain as the

structural unit [DeTeresa 1985]. This analysis is equivalent to a model developed to study the "shear" mode of failure of unidirectional composites [Rosen 1965] and not surprisingly, predicts similar results. The interaction of neigbouring chains was also incorporated, by extending the model to include a bundle of chains instead of one. Finally, the buckling stress was predicted to be equal to the shear modulus of the fibres and yielded the limiting value for the compressive strength.

To verify the validity of the above model a new method was developed for applying well defined and uniform compressive strain to single filaments [DeTeresa 1988]. Single fibres were bonded to the compressible side of a rectangular transparent polymer beam, by means of a thin clear acrylic spray. The beam was subsequently loaded either in 3-point bending, 4-point bending or cantilever beam configurations [DeTeresa 1982, 1984, 1988]. The load was transmitted to the fibre through the acrylic film, which at the same moment could support the fibre against global (Euler) instabilities. The strain on the compressive surface and hence on the fibre, could be accurately determined as a function of the position along the beam, from the elastic beam theory equations, according to the loading configuration. The critical compressive strain to failure was then calculated as soon as the first fibre failure, in a form of kink-band, microbuckling, or fibre fracture, was observed by optical microscopy. The compressive strength was subsequently calculated from the strain data, assuming that the fibre Young's modulus in tension and compression is the same. A wide range of fibres, such as polymeric and carbon, were examined under this technique. The compressive strengths calculated were about one third of the theoretically predicted ones [DeTeresa 1985, 1988]. This discrepancy was attributed to internal residual fibre stresses developed during fibre manufacturing (which may cause premature nucleation of kink-bands on the polymeric fibres) and to missalignment of the fibre polymeric chains.

Unfortunately, the technique has not been successful in assessing the compressive failure in carbon fibres. That was due to the fact that it is not optically possible to trace any kink-band on opaque and black fibres, such as carbon fibres. However, the method described above, seems to provide an excellent tool for applying well defined compressive loads to single filaments and with a suitable modification to the monitoring facilities, it can solve the problem of the optical inaccessibility, as will be demonstrated in the following section.

4.2. The Cantilever Beam (CB) technique combined with LRS.

In the previous chapter (Chapter 3) the fibre tensile deformation at molecular level was monitored using Laser Raman Spectroscopy (LRS). As demonstrated there, the strain dependence of the Raman frequencies of carbon fibres and particularly the dependence of the graphite vibrational mode E_{2g}, gave a measure of the carbon atom bonds sensitivity to an external load applied to the fibre. To monitor the Raman frequencies of carbon fibres under compression, a suitable loading configuration should be designed, in order to apply well defined compressive loads on single filaments.

However, to compress a single fibre in air is not an easy task to perform, as Eulerian instabilities will develop at very low applied loads. Therefore, a modified version of the Cantilever Beam (CB) technique **[DeTeresa 1988]** was employed for subjecting compressive loads to single filaments, having the following advantages, over other compressive techniques: (a) a uniform load is applied to the fibre cross-section, in contrast to the elastica loop test **[Sinclair 1950, Jones 1971]** and (b) a reduction to the "effective gauge length", since a gradient of strain is applied along the fibre length.

The main modification to the initial Cantilever Beam test **[DeTeresa 1988]** is the use of LRS to detect the integrity of the fibre, instead of optical microscopy.

4.2.1. *The mechanics of the cantilever beam (CB).*

The design of the Cantilever Beam rig is shown in figure 4.1. The beam can be flexed up or down, by means of an adjustable screw, the deflector, subjecting the fibre - which is bonded to the top surface - to compressive or tensile loads, respectively. The maximum deflection of the neutral axis of the beam, at the point of application of the load, is given by **[Timoshenko 1961]** :

$$\delta_{max} = \frac{P \cdot L^3}{3 \cdot E \cdot I} \qquad (4.1)$$

where P is the applied bending force by the deflector to the free end of the beam, L is the free length of the beam (fig.4.1a), E is the Young's modulus of the beam material and I is the moment of inertia of the beam cross-section. The deflection δ_{max} can measured by a dial gauge micrometer attached to the top surface. The bending moment M developed along the cantilever beam, at distance x from the fixed end of the CB is given as a function of the applied force and the free beam length, by :

$$M(x) = P \cdot L \cdot (1 - x/L) \qquad (4.2)$$

The strain ε, then, at any position x along the beam and y away from the neutral axis (fig. 4.1b), is calculated by:

$$\varepsilon(x,y) = \frac{M \cdot y}{E \cdot I} \qquad (4.3)$$

Once the fibre is well-bonded to the beam, the compressive strain at the top surface of the beam can be transmitted to the fibre; therefore, the compressive strain in the fibre, at any distance x from the fixed end of the CB, can be derived by substituting equation 4.2 to equation 4.3 :

$$\varepsilon(x,\frac{t}{2}) = \frac{P \cdot L \cdot (1 - x/L) \cdot t}{2 \cdot E \cdot I} \qquad (4.4)$$

where t is the thickness of the beam. The undetermined parameter in the above equation, P/EI, can be substituted after rearranging equation 4.1 as follows:

$$\frac{P}{E \cdot I} = \frac{3 \cdot \delta_{max}}{L^3} \qquad (4.1a)$$

Finally, the compressive strain distribution $\varepsilon(x)$ along the fibre on the beam can be calculated as a function of the geometry of the beam, the distance x from the fixed end, and the introduced deflection δ_{max} at the free end of the beam :

$$\varepsilon(x) = \frac{3 \cdot t \cdot \delta_{max}}{2 \cdot L^2} \cdot \left(1 - \frac{x}{L} \right) \qquad (4.5)$$

The above equation is valid only under the following conditions: (1) if $L/\delta_{max}>10$, to satisfy the elasticity calculations, (2) if the beam material exhibits identical compressive and tensile modulus and (3) if the beam material does not relax within the range of applied loads and the time required for the completion of the experiment.

4.2.2. *Materials and sample preparation.*

The beams employed in our CB experiments were made out of PMMA. Extended mechanical testing on this material **[Tetlow 1990]** has shown that it satisfies the conditions set above, up to a maximum strain of 1.5%. The PMMA grade selected (ICI's Perspex™) is a water-clear transparent material. The selection of the beam material was based on the requirement that it should not be Raman active in the region of the spectrum where the monitoring frequencies of the carbon fibres appear. In fact, due to its acrylic nature, the PMMA Raman bands lie at about 1450 cm^{-1} and 1770 cm^{-1} and, therefore, do not interact with either the graphite G (1580 cm^{-1}) and the "disorder" D (1355 cm^{-1}) lines of the carbon fibre spectrum (fig. 4.2). PMMA sheets were cut into rectangular bars of thickness 5.5 mm ± 0.1 mm and width 10 mm ± 0.1 mm. The length of each bar was sufficiently longer than the free length of the CB rig (50 mm) to allow for beam clamping (fig. 4.1).

The test specimens were prepared by aligning single carbon filaments on the top surface of the beam parallel to its long axis and approximately to the center of its width. The fibre ends were glued to the beam. In turn, the beam was positioned under the Raman microscope to check whether any initial load has been introduced to the fibre due to handling. To verify that, the frequency of the obtained spectra was referred to the strain-frequency calibration curve for that specific type of fibre (Chapter 3). All specimens found to be pre-stressed were discarded. Subsequently, the fibre was bonded on the beam by spraying it with a layer of optically transparent acrylic adhesive (Krylon™). The thickness of the film was carefully kept in the order of magnitude of the fibre diameter to eliminate its effect on the elastic calculations of the cantilever beam. Finally, the film was dried for several hours at room temperatures in a vacuum oven, to degas any solvent agents trapped in the film.

The carbon fibres tested in this part of the project are the three

7 μm fibres (HMS, IMS, and XAS), the four 5 μm fibre (LF58, LF53, LF48 and IM43-750 - or IM43) and finally the three "morphology" lab fibres (LF-positive, LF-neutral and LF-negative). Their mechanical and Raman spectroscopic properties at equilibrium and in tension have been presented in the relevant paragraphs of chapters 2 and 3 (Tables 2.1, 2.2 and 3.1).

4.2.3. *Tracking along the fibre with the LRS probe.*

The last step before laser Raman scanning along the bonded fibre, is to mount the prepared specimen on the cantilever rig. Then, the free end of the beam is sufficiently deflected to yield the required compressive strain distribution on the fibre. The maximum compressive strain is developed at the fixed end of the cantilever beam and according to equation 4.5, for x=0:

$$\varepsilon_{max} = \frac{3 \cdot \delta_{max} \cdot t}{2 \cdot L^2} \qquad (4.5a)$$

The fibre compressive strain at the free end of the beam is zero, as is clearly indicated by equation 4.5, for x=L. It is noteworthy that such a testing configuration reduces the effective fibre gauge length, as the fibre is submitted to a gradient of strain. As mentioned earlier, the fibre can be subjected to a gradient of tensile as well as compressive strain, by simply reversing the deflection direction of the cantilever beam. The top surface is then under tensile load, as a result of the change in the sign of the bending moment. Finally the whole cantilever rig can be positioned on the experimental stage (fig.2.3) and translated along the Raman microscope, enabling the acquisition of the Raman spectrum of carbon fibres as a function of the distance x from the fixed end of the CB and, hence, as a function of compressive applied strain in the fibre.

In addition, a reflection optical microscope was also included in the experimental configuration. The Raman spectrum acquisition and analysis is hereafter identical to the procedure described in Chapter 2. The laser power on the specimen was always kept below 1 mW, since during preliminary testing, problems due to the heating up of the adhesive were constantly observed. Thus, the resulting melting of the film could eliminate its supporting role and, therefore, have an adverse effect upon the experiment.

4.3. Results.

The carbon fibre frequency employed in this experiment as the Raman "probe" is the G-line appearing at about 1580 cm^{-1} of the Raman spectrum (Chapters 2 and 3). The lack of any report in literature with reference to the effects of applied compressive strain on the Raman frequencies of carbon fibres marks out the necessity of such an experiment, for the completion of the Raman characterisation of carbon fibres, commenced in Chapter 2.

4.3.1. *Verification of the applicability of the CB/Raman technique.*

To ascertain the applicability of the CB for loading fibres, an attempt was made to compare the strain dependence of the carbon fibre Raman frequencies using the CB, with that obtained by means of a microextensometer. The beam was deflected downwards, so that the top surface, where the fibre was bonded, was subjected to a tensile load as defined by the equations 4.1 to 4.5. The monitoring Raman frequency (G-line) was then obtained as a function of distance x from the fixed end of the cantilever beam, and subsequently of tensile strain, through the equation 4.5. Figure 4.3a shows the frequency shift of the G-line, for an HMS fibre as a function of the tensile strain applied with the cantilever beam configuration. The "frequency shift" represents the difference in the value of the Raman frequency of the strained fibre and the value of the strain-free fibre in air. In figure 4.3b, the frequency shift of the G-line for the same type of fibre, is plotted as a function of the tensile strain, which in this case, was applied on the fibre in air, by means of a microextensometer (ME) (Chapter 3). The almost identical slope of the least-square fitted line in the two graphs (figs 4.3 a&b) is a proof of the efficiency by which the acrylic film transfers the applied load from the surface of the solid beam to the bonded fibre and a verification of the accuracy of the beam equations for the current geometry.

It is interesting to note that, in figure 4.3a, the fracture of the fibre is indicated by the drop of the Raman frequency to the value of the stress-free fibre. This occurs because the broken fibre is "frozen" into position under the acrylic film, and therefore, the load transfer mechanism

is activated in the vicinity of discontinuity (studied in detail in Chapter 5), in contrast with the test in air (ME test), where the fibre floats in the space, free of stresses, after fracture. The Raman Frequency Gauge Factor (RFGF - § 3.3.1), calculated from testing the fibre in air and on the CB, is displayed in Table 4.1, for 4 representative carbon fibres. It can be seen, that within the experimental error, both tests yielded similar values. Hence, the validity of the CB/Raman technique is independently verified.

4.3.2. *Compressional behaviour of carbon fibres using LRS.*

The application of the CB/Raman technique is demonstrated in detail for two representative carbon fibres; the HMS (7 μm) and the IM43-750 (5 μm). The Raman frequency shift of the G-line of the HMS high modulus fibre as a function of the compressive applied strain is shown in figure 4.4. The Raman frequency shift is positive with compressive applied strain, or, in other words, the Raman frequency corresponding to the G-line, increases from the strain-free value of 1580 cm^{-1}, as the compressive strain increases, following a nearly linear trend, up to the first compressive failure. The latter appears at ~0.55% of applied strain as is indicated by a sudden drop of the Raman frequency, initiated at ~0.45% of applied compressive strain. Microscopic examination revealed that this frequency drop corresponded to the presence of a well defined "shear-like" fracture of the fibre, as shown in the photograph of figure 4.5. Not surprisingly, since the fibre is still encapsulated under the acrylic film, beyond that first fibre fracture, the frequency picks up again until a second frequency drop occurs corresponding to a second fibre break. This pattern of behaviour is repeated to higher applied compressive strains (fig.4.4), as the occurrence of the fibre breaks increases, in an expected manner, since the fibre reaches faster its critical compressive strength.

The slope of the frequency shift with applied compressive strain describes the strain dependence in compression for this type of fibre and for this specific vibrational mode. The slope of this least-squares fitted line (fig.4.4) gives the compressional Raman Frequency Gauge Factor (RFGF), having a similar definition to the RFGF in tension. The compressional RFGF for this case, was calculated to be 10.5 ± 0.6 $cm^{-1}/\%$ of compressive strain, slightly less (in absolute terms) than the corresponding value in

tension (-11.7 cm^{-1}/ %).

A different behaviour is exhibited by the intermediate modulus IM43-750 fibre, as shown in figure 4.6 for three different fibres. The Raman frequency shift (of the G-D′ band in this case) still increases linearly with the applied compressive strain, exhibiting a higher experimental scatter, up to a value of compressive strain, beyond which the frequency fluctuates about a plateau value. The plateau initiation strain ranges between 0.75% and 0.85% of compressive strain. The formation of the plateau and the considerable increase in experimental scatter beyond that level of strain indicate a form of compressional "failure". Indeed, careful microscopic observations at the plateau onset region, revealed the presence of a bulge, as shown in figure 4.7, equivalent to local yielding of the material. However, no cohesive failure or splitting of the fibre was observed, as in the case of the HMS fibre (fig.4.5). At higher applied strains subsequent bulges were also observed.

The compressional studies were also undertaken for ten types of fibres listed in Table 2.1. A number of parameters need to be noted, defined and clarified before summarising the results for all fibres:

(a) The mode of compressive failure.

Only two types of fibre (the HMS and the LF-neg) exhibit a clear catastrophic failure mode, the "shear-like" fibre fracture, shown in figure 4.5, for the HMS fibre. In all the remaining fibres, fibre defects seem to be the reason for local bulging formations (fig.4.7), which, however, do not affect the fibre loading capability in compression. On the contrary, a gradual reduction in the strain sensitivity of the Raman frequency and the subsequent frequency plateau formation appears to lead to a yielding form of fibre compressive failure.

(b) The critical compressive strain to failure.

The definition of the critical strain to failure in compression is not as easy as it would be if the mode of compressive failure was common in all carbon fibres. While failure by fracture provides a distinct value of strain to account for the failure strain, the bulging formation does not cause total collapse of the fibre structure and the frequency plateau is not, always, clearly initiated just after the first bulge. Therefore, the critical compressive strain to failure is defined as follows; for the fibres exhibiting failure by fracture, the failure strain is calculated as

the average value of compressive strain of the first failure, out of all fibres of that type tested; for the fibres exhibiting compressive bulges and gradual yielding, two values should be mentioned. The first is the average value of strain, out of all fibres of each type tested, at which the first bulge was observed on the fibre. The second corresponds to the onset of a permanent frequency plateau. While the first bulge formation strain is characteristic for individual fibres, the onset of the frequency plateau becomes clearer as the number of tested samples rises. Therefore, the latter gives a more macroscopic view of the compressional behaviour of the fibre. To overcome the difficulty in the definition of the compressive failure by bulging/yielding, the term "bulge initiation" is selected to describe the strain at which the first bulging appears on the fibre, while the term "fibre yielding" is used to note the frequency plateau formation and the reduction of the fibre Raman strain sensitivity to additional applied strain. In most of the fibres that exhibit bulging/yielding in compression, the Raman frequency plateau has not fully developed within the range of applied strain allowed by the elastic limitations of the cantilever beam material (e.g. XAS fibre, fig.4.8c). Therefore, in these cases, only a lower limit for the yield point can be defined.

(c) The RFGF in compression.

The strain dependence of the Raman frequencies in tension is defined as the slope of the linear region prior to the first (catastrophic or local) failure indication. Therefore, the RFGF in compression is defined in a similar manner (figs.4.4, 4.6). As with the tensile results, the RFGF in compression is greater, the higher the nominal tensile modulus of the fibres, provided that they have been produced using the same manufacturing route. Also, the RFGF in compression is greater, the lower the "disorder" ratio I_D/I_G. However, all RFGF values in compression are consistently lower than the corresponding values in tension.

The results of the CB/Raman compressional studies of all carbon fibres of this investigation are displayed in Table 4.2. This Table includes the nominal (average) fibre modulus, as quoted by the manufacturer, the Raman intensity ratio I_D/I_G , as measured in Chapter 2, the tensile and compressive RFGF, as calculated in this Chapter, the observed mode of compressive failure and finally the critical compressive strains, as defined in the preceding paragraphs.

4.3.3. *Raman frequency vs compressive and tensile strain.*

A universal view of the carbon fibre Raman frequency sensitivity upon an externally applied load is presented by merging the tensile and compressive data. This treatment has been applied to the results for the HMS fibre (by merging the data of figures 4.3a and 4.4). In the resulting graph (fig.4.8a), the Raman frequency shift is plotted against the applied strain; positive values indicate the tensile strain and negative values the compressive strain. The produced characterisation curve (fig.4.8a) reveals some interesting aspects of the mechanical behaviour of the fibre. Both the tensile strain to failure and the critical compressive strain to failure can be directly detected by the decay of the Raman frequency shift at ~1.0% (tensile) and at -0.55% (compressive) applied strain (fig 4.8a). Indirectly, the change in the material stiffness is indicated by the change in the slope of the Raman frequency shift with strain (RFGF).

The Raman frequency shift of the G line of the IMS fibre as a function of the applied (tensile and compressive) strain is shown in figure 4.8b and the Raman frequency shift of the merged G-D′ band of an XAS carbon fibre is presented in figure 4.8c.

The Raman frequency vs applied strain curves for the 5 μm series of fibres are shown in figures 4.9a to d.

Similar characterisation curves for the three "morphology" fibres are produced in figures 4.10a to c, corresponding to the LF-pos, LF-neut and LF-neg fibres, respectively. The most significant observation is that the mode of failure changes. While the LF-positive and LF-neutral fibres exhibit bulging/yielding in compression, the LF-negative fails in compression by fracture. Thus, this particular type of fibre, the LF-negative, seems to show the transition point for the compressive mode of failure.

4.4. Discussion.

4.4.1. *Critical compressive strain to failure.*

Previous studies on axial compression of single carbon fibres embedded in a block of resin **[Hawthorne 1975]**, have reported that, PAN-based 345 GPa modulus fibres exhibited compressive strain to failure of 0.45%, (while an amount of 0.15% of initial thermal residual compressive strain was estimated). Pitch based carbon fibres exhibited compressive strain to failure inversely proportional to their Young's tensile modulus, ranging from 0.14% for high modulus fibres to 1.5% for low modulus ones. In another investigation, where the fibre recoil test was employed to study the compressional behaviour of carbon fibres **[Dobb 1990]**, the intermediate modulus fibre failed in compression at 0.3% of strain and the low modulus fibre at 0.7% of strain.

In the present study, while the fibres that failed by fracture (HMS, LF-neg) provided a distinct value for the critical compressive strain to failure, the detection of the "yield" point for the rest of the fibres (Table 2.1), possessed some degree of uncertainty. It can be stated that these fibres perform quite well in compression, withstanding compressive strains comparable in magnitude, with those in tension. In some cases, the "yield" point cannot be detected below the value of 1.6% compressive strain (XAS fibre, fig.4.8c), which is the limit for the elastic behaviour of the cantilever beam material. In this case, only a lower limit for the compressive strain to failure can be estimated.

An additional difficulty in the detection of the "yield" point of the IM43 (5 μm) and XAS (7 μm) fibres is the fact that the monitoring frequency band for these fibres, is not the "graphitic" G-line, but the merged feature of the G and D′ lines, which even in tension exhibit a different rate of shifting with strain (Table 3.2). If the disorder D′-line is really dominant in this merged feature, then is expected to slow down significantly the rate of frequency shifting in compression.

A direct conversion of the strain data to strength values, could lead to erroneous estimates if the compressive modulus of carbon fibres is considered equal to the tensile modulus. The difficulty to assess the compressive modulus of carbon fibres has led to estimations for the compressive strength, where the compressive modulus factor was totally

ignored **[Dobb 1990]**, or disregarded, due to lack of experimental evidence **[Hawthorne 1975, Ohsawa 1990]**. Indeed, strain hardening effects during tensile loading of carbon fibres have been earlier observed **[Curtis 1968]**, while more recently, strain softening phenomena during compressive loading of carbon fibres have been detected **[Henrat 1987]**. A careful investigation of the material stiffness in compression is a prerequisite before any conversion of compressive strain into stress is attempted.

4.4.2. *Modes of compressive failure.*

The literature reports regarding the mode of failure of carbon fibres are rather vague and sometimes contradictory (§ 4.1.1). The inconsistent use of terms such as failure by shear, microbuckling or kink-band, unfortunately, does not offer a solid background, which can accommodate the observations of the current investigation. Therefore, the attempted discussion will be primarily based on (a) the optical observations via the low resolution reflection microscopy, (b) the strain data obtained by the Raman probe and finally (c) the model for the carbon fibre structure, an account of which can be found in Chapter 3 (fig.3.14).

Only one distinct mode of compressive failure was detected in the series of PAN based carbon fibres, examined in this project. This is demonstrated by the "shear-like" fracture of the HMS fibre, shown in the micrograph of figure 4.5. The morphology of the first and the subsequent fibre breaks is of a "shear" nature, propagating at an angle of about 45° with respect to the fibre axis. This mode of failure is synonymous with low compressive strains to failure and is associated with the intrinsic sheet-like or ribbon-like structure of these fibres **[Crasto 1990]**. The low amount of disordered carbonaceous material within the highly oriented surface crystallites of the pitch and high modulus PAN fibres, induces shear failure between the basal planes of the highly oriented graphite structure **[Dobb 1990]**. Nevertheless, other investigators advocate the view that the highly oriented layers of graphite are vulnerable to Eulerial microbuckling instabilities, in accordance to the chain or crystal microbuckling theories **[DeTeresa 1985,1988]**. This type of fibre failure was observed only on fibres with low "disorder" (intensity) ratio ($I_D/I_G \leq 0.50$).

It should be pointed out, that the mode of failure is not directly

related to the fibre modulus. The 390 GPa HMS fibre exhibited a "shear-like" failure, while the higher modulus (and smaller diameter) 405 GPa LF58 fibre exhibited only local bulgings and gradual yielding. This implies that by controlling the morphology of the carbon fibre surface, catastrophic failures can be prevented. In addition, higher compressive strains to failure can be achieved.

The type of local compressive failure, shown in figure 4.7 for an IM43-750 fibre, consists of a formation of a bulge and can be attributed to a fibre defect. It is very localised and it does not affect the load carrying capability of the fibre. In fact, the fibre can sustain a significant amount of compressive strain even after subsequent bulges have been formed.

The "morphology" 5 μm diameter fibres LF-neutral and LF-negative should provide a hint as to what the structural requirements are, that make the one of the two modes of failure more preferable than the other. Both fibres have a manufacturer's quoted Young's modulus of 378 GPa and tensile strength of about 4.1 GPa. However, the first exhibits local compressive failures by bulging and subsequent "yielding" at higher strains, while the second fails by a "shear-like" fracture. The substantial structural difference that is responsible for the improvement in the compressional behaviour is revealed in the Raman spectra of the two fibres (fig.2.10, 2.13). The main differences in terms of Raman response from the surface of these fibres are detected in the broadness of the Raman bands and value of the "disorder" ratio I_D/I_G . A more careful look to their "real intensity" Raman spectra reveals that is not only the rise of the disorder features (D-line and graphitic shoulder) that has occurred, but also the drop of the graphitic G-line (fig.2.13) that has attributed to the increase of the "disorder" ratio. The above observation is in good agreement with the two-phase model for the structure of high strength PAN based carbon fibres **[Johnson 1988]**. According to this model one phase is the classic layer graphite plane structure, while the second is the "disordered" structure. An optimum proportion of the "disordered" phase within the graphite layers, may well account for higher strains to compressive failure, by simply permitting localised deformations **[Dobb 1990]**.

The "shear-like" mode of failure (fig.4.5) is most probably due to the skin-core effect of the carbon fibre structure, as detected in Chapter 3. The highly crystalline fibre surface consists of large crystallites highly oriented to the fibre axis. Such a fibre surface displays a Raman spectrum

with a low "disorder" ratio. In addition, fibres with a highly crystalline surface present a more pronounced skin-core effect (Chapter 3). This skin-core effect results in a modulus gradient, with the surface material having a higher Young's modulus than the core **[Chen 1983]**. Therefore, for a given compressive strain, the surface layers will bear a greater proportion of compressive stress than the core and so early failure is expected to initiate in the outer surface **[Hawthorne 1975]**. This is either due to shear between the graphite planes **[Dobb 1990]** or to Eulerian instabilities and microbuckling of the crystallites themselves **[Crasto 1990, DeTeresa 1988]**.

The results of surface characterisation Raman studies over a wide range of carbon fibres (Chapter 2), combined with the compressive studies on carbon fibres presented in this chapter, can offer a prediction regarding the compressive mode of failure without having to refer to the fibre modulus, the fibre diameter or the fibre production route. The "disorder" ratio I_D/I_G has a critical value of 0.50 (fig. 4.11). Fibres with an I_D/I_G ratio less than that, fail in compression by fracture, while those with ratio over 0.50, exhibit the characteristic bulge formation and a gradual yielding type of "failure".

The two types of fibre failure can be assigned to the models of fibre structure, displayed in the sketch of figure 3.14. The first (fibre fracture) corresponds to a highly surface crystalline fibre, with well oriented graphite planes around the peripheral layers and strong radial anisotropy, while the second (fibre "yielding") corresponds to a more homogenised surface-core structure.

4.4.3. *Compressive modulus of carbon fibres.*

The non-linear elasticity of carbon fibres has been recognised in literature and both hardening effects during tensile loading **[Curtis 1968]**, as well as softening phenomena during compressive loading of carbon fibres **[Henrat 1987]** have been experimentally ascertained.

The non-linear elasticity of carbon fibres can be detected in the Raman frequency - strain curves of paragraph § 4.3.3. It is obvious that the unified tensile and compressive strain versus Raman frequency curves (figs. 4.8 to 4.10) exhibit a pronounced non-linearity. The linear treatment of the Raman frequency - strain data in tension and compression was only a first approximation of the response of the material structure

and, therefore, its Raman spectrum, to the externally applied strain. In our quest to derive the compressive modulus of carbon fibres, both approaches will be employed. At a first approximation, the linear treatment can arrive at a quick estimate of the compressive modulus, based in already processed data.

(a) Linear treatment of the Raman data.

The strain sensitivity of the Raman spectrum of carbon fibres suggests that a correlation between the Raman Frequency Gauge Factor (RFGF) and the modulus of the fibre exists. The relation between the RFGF and the fibre surface crystallinity, as this is expressed by the ratio I_D/I_G , has been demonstrated in figure 3.8. However, the surface crystallinity of the fibre can be altered and still yield a fibre with the same (average) modulus, by tailoring the fibre morphology during manufacture. Therefore, a correlation of the RFGF of the fibre with its modulus should be carefully defined only for fibres that have been produced following the same manufacturing route, as explained in Chapter 3. The significance of this observation has been demonstrated in figure 3.10, where the tensile RFGF is linearly dependent upon the fibre tensile modulus, for fibres of the same series. A change in diameter, with all the morphological alterations that this implies, moves the RFGF values to a different level. Hence, the following empirical relationship has already been derived, per fibre series:

$$\alpha_\varepsilon = k \cdot E_f \qquad (3.7)$$

where α_ε describes the linear tensile strain dependence of the carbon fibre Raman frequency (G-line), E_f is the tensile modulus value as this is quoted by the manufacturer and the parameter k is the apparent stress dependence coefficient for the particular series of fibres, as defined in Chapter 3.

The physical interpretation of the equation 3.7 is that in high modulus, highly crystalline fibres, most of the applied strain to the fibre goes directly into stretching the atomic bonds in the graphite crystal and, consequently, into changing the bond length, which affects the Raman frequency. On the other hand, in lower modulus fibres, with highly misoriented crystallites, only a part of the applied strain acts

effectively on the atomic bonds of the graphite crystal, while another fraction of this load is expected to induce crystallite realignments, rotations, shear deformations etc, which are not related to the monitoring vibrational frequency. Therefore, for the same amount of externally induced strain, the frequency change observed in lower modulus fibres will be smaller compared to the high modulus case, resulting in a lower RFGF (absolute) value. Based on the above analysis, an equivalent relationship to the one of equation 3.7 can be derived, concerning, this time, the compressional RFGF and the compressive modulus of carbon fibres:

$$\alpha_{\varepsilon}^{c} = k \cdot E_{f}^{c} \qquad (4.6)$$

where α_{ε}^{c} is the compressional strain dependence of the carbon fibre Raman frequency, E_{f}^{c} is the compressive modulus of the carbon fibre (unknown), and k is the same parameter as in equation 3.7.

The difference in the measured RFGF values in tension and compression (Table 4.2) may be due to crystallite rotations, entanglements, and shear deformations, which can develop easier in the fibre under compression than in the fibre under tension, as the fibre structure flaws and defects can allow local collapse of the crystallites without fracture. Therefore, the actual contraction of the bonds in the crystallites, during compressive loading, is lower than the extension of the same bonds, for an applied strain of the same magnitude.

The compressive modulus of the carbon fibre can then be calculated by dividing the two equations, 3.7 and 4.6, by parts:

$$E_{f}^{c} = \frac{\alpha_{\varepsilon}^{c}}{\alpha_{\varepsilon}^{t}} \cdot E_{f}^{t} \qquad (4.7)$$

Equation 4.7 denotes that the ratio of the RFGFs in compression to tension is equivalent to the ratio of the moduli, respectively. This ratio is displayed also in Table 4.3 for all fibres tested. The estimated compressive fibre modulus (Table 4.3), can now be used to calculate the compressive strength of the tested carbon fibres. The frequency plateau formation strain (yield strain) is related to the fibre compressive strength, since the fibre beyond this strain can hardly take up any further

load. As mentioned earlier, when this plateau formation has not fully develop within the examined strain range, only a lower limit for the yield strain can be estimated.

It is worth mentioning that improvement of the fibre compressive strength can be achieved by preventing compressive failure by "shear" fracture (Table 4.3). In addition, most of the fibres with good post-compressive failure behaviour appear to exhibit more-or-less similar (lower limit of) compressive strength values (Table 4.3).

With respect to the estimated values of compressive strength, displayed in Table 4.3, two points should be borne in mind. Firstly, these values carry with them the uncertainty in the definition of the yield strain, pointed out earlier. Secondly, the reference tensile modulus value employed in equation 4.7 is the average fibre modulus, as quoted by the manufacture. In view of the findings of Chapter 3, the two fibres that fail in compression by fracture, have a much higher surface modulus, since they exhibit a pronounced skin-core effect. A source of error may be then included in the calculation of the compressive modulus for these fibres, as the Raman results are obtained from the fibre surface.

The analysis of the compressional behaviour of carbon fibres in this paragraph, has been based on the assumption that there is a linear drop of the carbon fibre Raman frequencies in tension and a linear rise in compression. However, in some cases, the linear approximation of the Raman frequency strain dependence, might lead to erroneous results as it does not take into account non-linear effects in the deformation of carbon fibres. Although a different value for the compressive modulus has been derived, the strain dependence of the Young's modulus advocated in literature **[Hughes 1986, Arsenovic 1988]** has not been yet properly addressed. A non realistic outcome of this analysis is the observation of the sudden change of the fibre modulus at the 0% strain point (see Raman frequency vs strain curves - figs. 4.8 to 4.10). There is no physical interpretation that can accommodate such an abrupt transition. On the other hand, the frequency plateau at high compressive strains is formed rather in a gradual, than in a sudden and abrupt manner. Furthermore, a non-linear treatment of the Raman data may allow a reasonable estimation of an upper limit of the fibre compressive strength, by extrapolating the modelling of the experimental data to higher compressive strains.

(b) Non-linear treatment of the spectroscopic data.

A more cautious study of the relationship between the Raman frequency shift and applied strain (figs.4.8 to 4.10) employs a higher degree polynomial to approximate the Raman frequency data. A second degree polynomial fitted to the frequency data over the whole range of applied strain gives a very good correlation coefficient (Table 4.4) and satisfies the physical requirement that the frequency change through the 0% strain point follows a smooth transition described by a contiguous function. The polynomial equation expressing the Raman frequency shift strain dependence $f(\varepsilon)$ can be expressed in mathematical terms:

$$f(\varepsilon) = a_0 + a_1 \cdot \varepsilon + a_2 \cdot \varepsilon^2 \ (+ \ldots) \qquad (4.8)$$

where ε is the applied strain, and a_0, a_1 and a_2 are the polynomial coefficients. They are listed along with the correlation coefficient of each polynomial regression, in Table 4.4. The first derivative of equation 4.8, describes the slope of the Raman frequency shift with strain, i.e. the Raman Frequency Gauge Factor (RFGF). Evidently, the RFGF is not any more a constant number, but a strain dependent quantity defined as:

$$\alpha_\varepsilon(\varepsilon) = \frac{d\, f(\varepsilon)}{d\varepsilon} = a_1 + 2 \cdot a_2 \cdot \varepsilon \ (+ \ldots) \qquad (4.9)$$

where $f(\varepsilon)$ is the Raman frequency shift regression function, ε is the applied strain and a_1,a_2 are the polynomial coefficients of equation 4.8. In fact, the coefficient a_1 expresses the RFGF at zero applied strain, while the coefficient a_2 describes the rate of change of the RFGF with strain.

Since the relationships developed in equations 3.7 and 4.6 should be valid at every level of strain, the linear strain dependence of the RFGF, as this was derived in equation 4.9, should be accommodated by a corresponding strain dependence of the fibre modulus E_f or/and the parameter k (equations 3.7 and 4.6). However, the parameter k is constant, at least for the same fibre (Chapter 3). Furthermore, recent experimental studies **[Hughes 1986]** on the non-linear elastic behaviour of carbon fibres have suggested that the tensile stiffness of carbon fibres should not only be expressed in terms of the average Young's modulus, but in the form:

$$E_f(\varepsilon) = E_f(0)\cdot\left(1 + b\cdot\varepsilon\right) + \ldots , \qquad (4.10)$$

where $E_f(\varepsilon)$ is the strain dependant fibre Young's modulus, $E_f(0)$ is the modulus of the strain free fibre, ε is the applied strain and b is a constant. The experimental data for the variation of the fibre elastic modulus with strain for PAN-based fibres **[Dresselhaus 1988, Hughes 1986]** are shown in figure 4.12. Therefore, the RFGF - fibre Young's modulus relationship for the strain dependent RFGF should be:

$$\alpha_\varepsilon(\varepsilon) = k \cdot E_f(\varepsilon) \qquad (4.11)$$

where $\alpha_\varepsilon(\varepsilon)$ is the strain dependent Raman Frequency Gauge Factor, $E_f(\varepsilon)$ is the strain dependent fibre Young's modulus and k is the apparent stress dependence of the specific fibre series. The physical interpretation employed to explain the RFGF - Young's modulus relationship in the linear treatment of the spectroscopic data (§ 4.4.3a) can also justify the scaling of the strain dependent RFGF to the strain dependent modulus. As an additional amount of axial strain tends to realign the fibre crystallites in the loading direction, their misorientation against the fibre axis is reduced. Improved alignment of the graphitic crystallites in the loading direction results in increased fibre stiffness, in accordance with well established principles of the structure of carbon fibres **[Ruland 1967, Fourdeux 1973]**. Additionally, improved alignment of the fibre crystallites is equivalent, by definition, to enhanced fibre crystallinity. The equal stress model, discussed in Chapter 3 (fig.3.11 and Appendix A1), has already demonstrated how the improvement in the fibre crystallinity results in the increase of the strain sensitivity of the Raman spectrum, and, therefore, the RFGF of the fibre.

Since the Raman frequency shift function $f(\varepsilon)$ is fully defined for all the fibres of this project (Table 4.4), so is the $\alpha_\varepsilon(\varepsilon)$, through equation 4.9. Therefore, a measurement of the fibre Young's modulus at a distinct level of strain ε_0 is enough to make the $E_f(\varepsilon)$ function definable for the whole range of strain, (in which $\alpha_\varepsilon(\varepsilon)$ is defined):

$$E_f(\varepsilon) = \frac{\alpha_\varepsilon(\varepsilon)}{\alpha_\varepsilon(\varepsilon_0)} \cdot E_f(\varepsilon_0) \qquad (4.12)$$

The manufacturer's quoted value for the fibre Young's modulus corresponds to measurements up to 0.4% applied strain. For the purposes of the current analysis, this value has been considered as the tangential modulus at 0.0% strain.

The application of the model described by the equation 4.12 is illustrated in figure 4.13, where a second degree polynomial $f(\varepsilon)$ is fitted on the Raman frequency shift - applied strain curve for the LF58 fibre.

A noteworthy observation is that, for each fibre series, the Raman frequency versus applied strain curve simply pivots about the zero strain-zero shift (0,0) point, as the nominal (average) fibre modulus changes. This is demonstrated by the 5 μm series fibres in figure 4.14. Such an observation corresponds to the finding that the only parameter that changes substantially with the fibre modulus is the coefficient a_1 of the regression polynomial to the frequency-strain curves, i.e. the RFGF value at 0% applied strain (Table 4.4). On the contrary, the rate of change of the RFGF, expressed by coefficient a_2, changes only marginally, with the initial tangential fibre modulus.

The fibre modulus as a function of the applied strain is eventually evaluated by applying the equations 4.8 and 4.12 to the Raman frequency shift - strain curves. Figures 4.15 to 4.17 display the modulus strain dependence of the 7 μm, the 5 μm and the "morphology" fibres, respectively. The rate of modulus change with applied strain $\left(dE_f(\varepsilon)/d\varepsilon \right)$ is directly related to the coefficient a_2 (Table 4.4) of the regression polynomial, through equation 4.12. As a consequence, the strain dependence of the fibre modulus appears to be independent of the initial (0%) tangential value. This implies that the modulus softening (and/or hardening) with strain is the same in the skin and the core of a fibre with a pronounced radial anisotropy.

The derivation of an estimate for the compressive strength of carbon fibres can now be attempted. Since the fibre modulus is not a constant number, but a strain dependent quantity, the fibre stress, $\sigma_f(\varepsilon)$, at any level of strain, ε, can be calculated through the equation:

$$\sigma_f(\varepsilon) = \int_0^{\varepsilon} E_f(\varepsilon) \cdot d\varepsilon \qquad (4.13)$$

where $E_f(\varepsilon)$ is the strain dependent fibre modulus, defined in equation

4.12. In fact, equation 4.13 can produce the stress - strain curve for the specific fibre. If $\varepsilon=\varepsilon^{*}$, where ε^{*} is the yield strain of the fibre in compression, then the defined integral of equation 4.13 produces a value for the compressive strength of the carbon fibre. The application of equation 4.13, to derive the stress - strain curve from the estimated fibre modulus and, eventually, from the Raman frequency - strain data, is demonstrated for the LF58 fibre in figure 4.18.

The results of the non-linear treatment of the Raman frequency-strain data are displayed in Table 4.5. As noted earlier, only the fibres that fail in compression by fracture (HMS and LF-neg) can provide a distinct value for the critical compressive strain to failure. The experimental data for the rest of the examined fibres have provided only the lower limit of the yield strain in compression. Nevertheless, the polynomial treatment of the experimental data has facilitated the estimation of an upper limit for the yield point in compression, which corresponds to the compressive strain at which the fibre modulus becomes zero. This value can be obtained from equation 4.12, or, from the extrapolation of the modulus-strain curves of figures 4.15 to 4.17, to zero modulus values. The whole procedure is demonstrated for the LF58 fibre in figure 4.18. The zero modulus point (fig.4.18b) corresponds to the predicted Raman frequency plateau formation in the Raman frequency versus applied strain curve (fig.4.18a) and to the maximisation of the compressive stress in the constructed stress - strain curve (fig.4.18c).

The findings of Table 4.5 reconfirm that the change in the mode of failure results in a genuine improvement in the fibre compressive strength, while the initial fibre modulus does not seem to affect the yield strength of the fibre in compression, but only marginally (fig.4.19). The uncertainty in the estimated value of the compressive strength is quite large, but this is mainly due to the uncertainty in the detection of the yield point in compression. This weakness can be dealt with in future work by selecting another cantilever beam material, that will allow the continuation of the experiment to higher compressive strains. The estimation of the compressive strength is much more accurate for the fibres that fail in compression by fracture, which provide a distinct critical compressive strain value. In two out of the ten tested fibres, the XAS and the IM43, an additional source of error may lie in their own Raman spectrum and its strain dependence, since the monitoring frequency is not the pure G-band (Chapters 2 and 3).

The validity of our predictions is verified by experimental findings from compression testing on unidirectional XAS carbon fibre/epoxy resin composites **[Haeberle 1990]**. In that investigation the tangential longitudinal compressive modulus of the composite material was reported to decrease from about 130 GPa in the stress free composite to about 55 GPa at about 2.0% compressive strain (fig.4.20). Even at this level of applied strain no apparent failure of the fibres could be observed. However, specimen failure initiation even at this level of applied strain, was detected at the region of the specimen grips, implying that the loading configuration might still be responsible for the compressional behaviour of the compo site, rather than the intrinsic properties of the fibres themselves. This in good agreement with our findings that, particularly the XAS fibre is still capable of carrying a significant amount of compressive load over 1.6% of applied compressive strain.

A conversion of the reported composite compressive modulus values into fibre compressive modulus was undertaken using the law of mixtures and a fibre volume fraction of 60%. The estimated fibre compressive modulus at 2.0% of compressive strain was then found to be about 90 GPa, which compares favourably with a value of 85 GPa obtained by the analysis of this chapter (fig.4.15). The application of the law of mixtures to deduce the fibre strength at 2.0% of composite strain, resulted in a value of about 3.2 GPa. Applying equation 4.13 on the XAS fibre data, the estimated fibre stress at 2.0% compressive strain was calculated about 3.1 GPa, exceptionally close to the composite derived value. ▮

Table 4.1. Comparison of the microextensometer and the Cantilever Beam results for the Raman Frequency Gauge Factor.

Fibre	RFGF tension microextensometer (ME) ($cm^{-1}/\%$)	RFGF tension Cantilever Beam (CB) ($cm^{-1}/\%$)
HMS	-11.4	-11.7
IMS	- 8.9	- 9.0
XAS(*)	- 7.0	- 7.3
IM43(*)	- 6.9	- 7.2

(*) indicates that the G and D′ bands are merged.

Table 4.2. Results of the compressional CB/Raman studies on carbon fibres.

Fibre	Tensile modulus GPa	Intensity ratio I_D/I_G	RFGF(Tens) $cm^{-1}/\%$	RFGF(Comp) $cm^{-1}/\%$	bulge initiation strain/%	Compressive fibre yield strain/ % -freq plateau	Mode of compressive failure
HMS	390	0.35	-11.7	10.5	-	**0.55**	**fracture**
IMS	305	0.85	-8.9	6.8	0.80	>1.2	yielding
XAS	230	0.80	-7.3	5.1	0.90	>1.6	yielding
LF58	405	0.60	-9.0	6.8	0.55	>1.1	yielding
LF53	370	0.85	-8.5	6.3	0.65	>1.2	yielding
LF48	335	0.95	-7.5	4.9	0.70	>1.0	yielding
IM43	305	0.80	-7.0	4.7	0.75	>0.9	yielding
LF-neg	378	0.50	-10.0	7.0	-	**0.55**	**fracture**
LF-neut	378	0.70	-8.6	6.3	0.60	>0.9	yielding
LF-pos	364	0.95	-7.7	5.5	0.65	>1.0	yielding

Table 4.3. Estimated compressive modulus and strength of carbon fibres (linear treatment of the Raman frequency - applied strain data).

Fibre	Tensile modulus GPa	RFGF(C) RFGF(T)	Estimated compressive modulus/GPa	Compressive fibre yield strain/% -freq plateau	Compressive yield strength GPa
HMS	390	0.90	350	**0.55**	**1.9**
IMS	305	0.77	235	>1.2	>2.8
XAS	230	0.70	160	>1.6	>2.6
LF58	405	0.76	310	>1.1	>3.4
LF53	370	0.73	270	>1.2	>3.2
LF48	335	0.65	220	>1.0	>2.2
IM43	305	0.67	205	>0.9	>1.9
LF-neg	378	0.70	265	**0.55**	**1.5**
LF-neut	378	0.73	275	>0.9	>2.5
LF-pos	364	0.71	260	>1.0	>2.6

Table 4.4. Quadratic regression of the Raman frequency - applied strain data.

Quadratic coefficients	figure of reference	a_0 cm^{-1}	a_1 $cm^{-1}/(\%)$	a_2 $cm^{-1}/(\%)^2$	correlation coefficient r^2
Fibre					
HMS	4.8a	0.05	-10.61	-1.42	0.9985
IMS	4.8b	-0.40	-7.74	-1.36	0.9955
XAS	4.8c	-0.18	-6.72	-1.08	0.9987
LF58	4.9a	-0.07	-7.98	-1.67	0.9991
LF53	4.9b	-0.08	-7.41	-1.74	0.9994
LF48	4.9c	-0.11	-5.97	-1.72	0.9974
IM43	4.9d	-0.13	-6.13	-1.83	0.9940
LF-neg	4.10a	-0.40	-8.73	-2.07	0.9987
LF-neut	4.10b	-0.01	-7.35	-1.98	0.9976
LF-pos	4.10c	-0.17	-6.15	-1.56	0.9981

Table 4.5. Estimated compressive modulus (at yield point) and strength of carbon fibres (non linear treatment of the Raman frequency - applied strain data).

Fibre	Compressive fibre yield strain/% (lower limit)	Compressive fibre yield strain/% upper limit (extrapolated value)	Estimated compressive strength lower limit/(GPa)	Estimated compressive strength upper limit/(GPa)
HMS	**0.55**	-	1.8	2.0
IMS	>1.2	2.8	2.8	4.3
XAS	>1.6	3.0	2.7	3.5
LF58	>1.1	2.4	3.4	4.7
LF53	>1.2	2.1	3.1	3.9
LF48	>1.0	1.8	2.4	2.9
IM43	>0.9	1.7	2.0	2.5
LF-neg	**0.55**	-	1.7	1.9
LF-neut	>0.9	1.9	2.6	3.5
LF-pos	>1.0	1.8	2.7	3.5

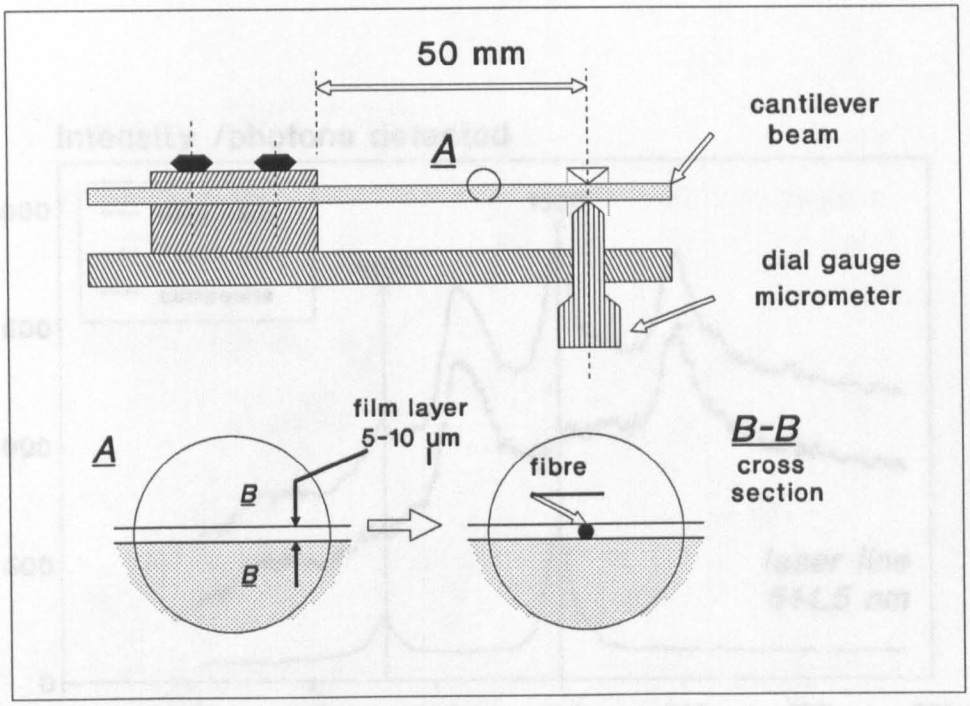

Fig.4.1a Schematic illustration of the Cantilever Beam (CB) assembly.

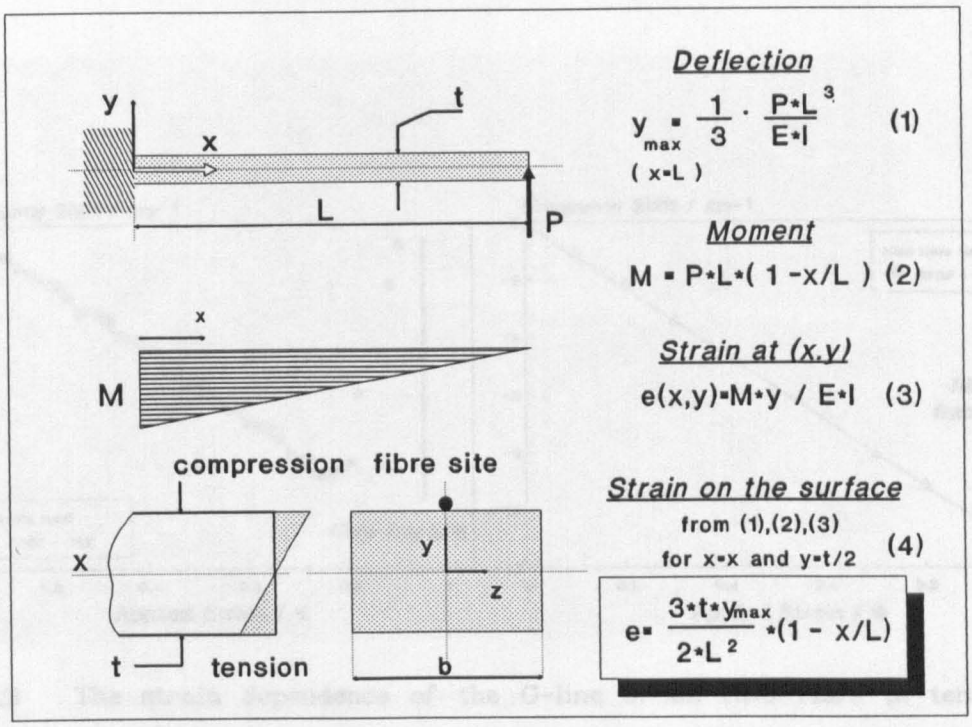

Fig.4.1b Elastic calculations along and across the Cantilever Beam.

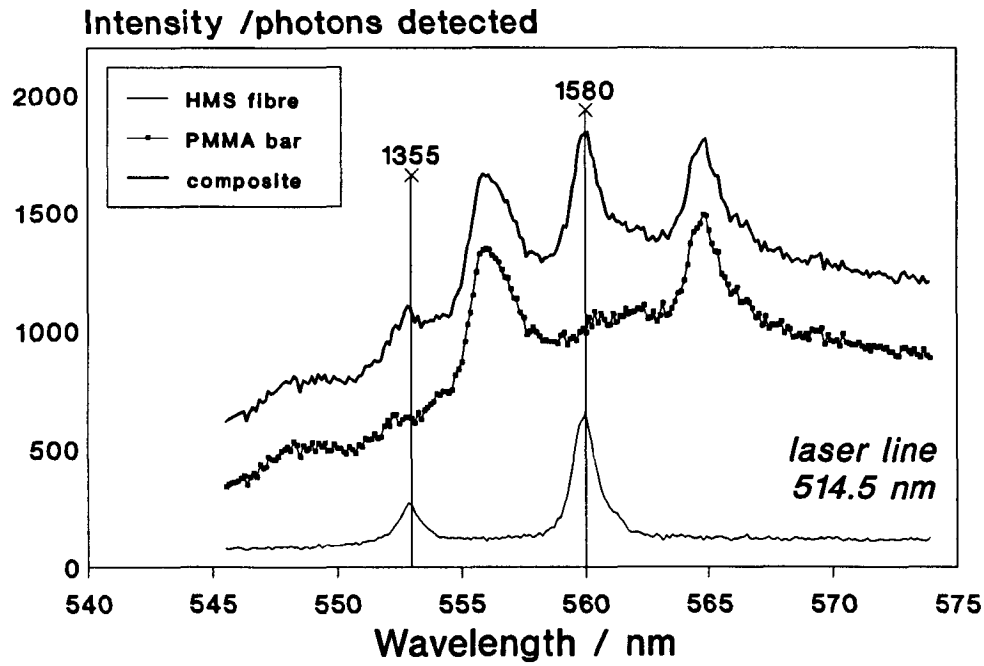

Fig.4.2 The Raman spectrum (first order region) from a HMS carbon fibre, the PMMA bar surface and the HMS carbon fibre bonded to the bar.

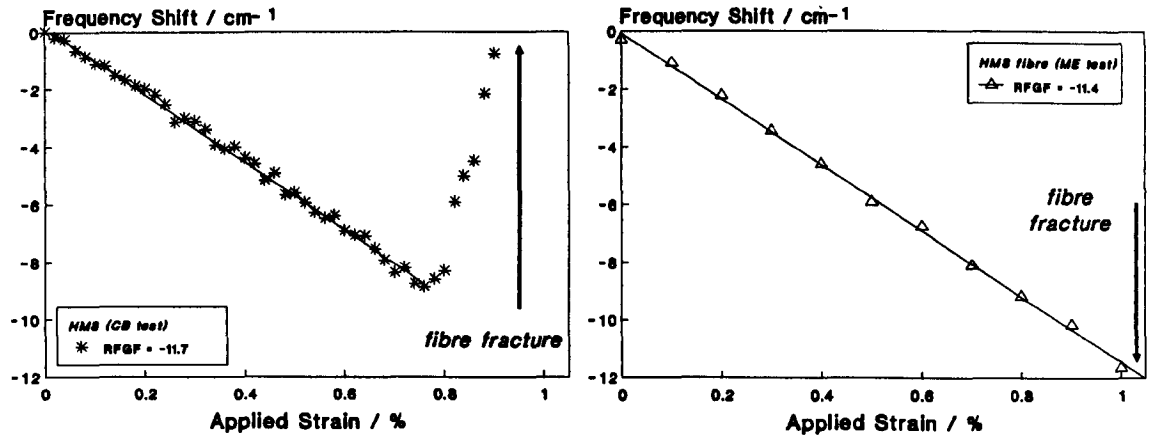

Fig.4.3 The strain dependence of the G-line of an HMS fibre in tension, derived by using the Cantilever Beam (CB) technique and the microextensometer (ME) method (Chapter 3).

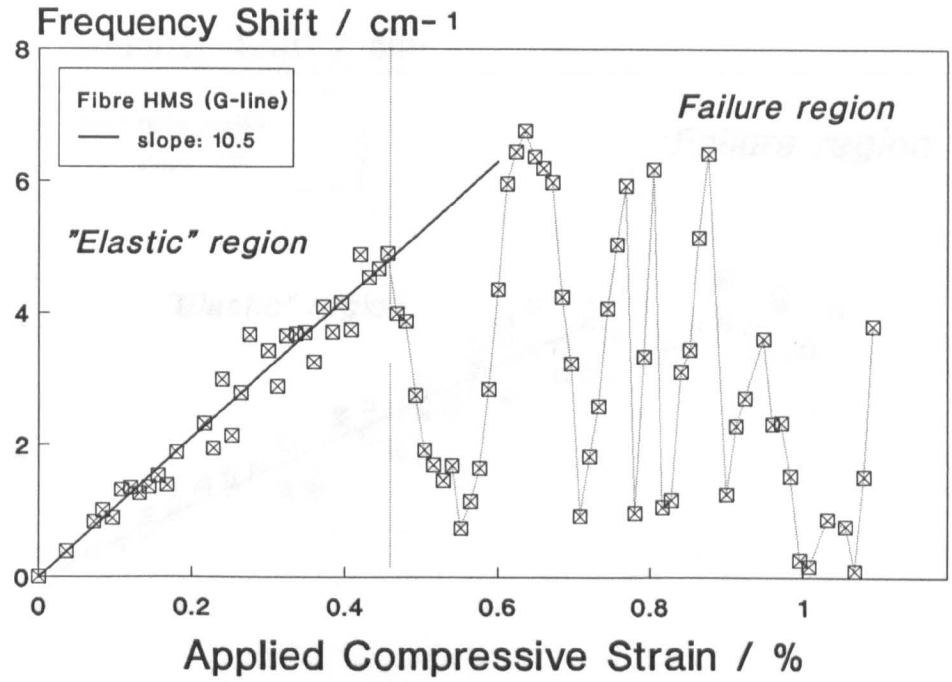

Fig.4.4 The Raman frequency shift of the G-line for the HMS carbon fibre, as a function of compressive applied strain.

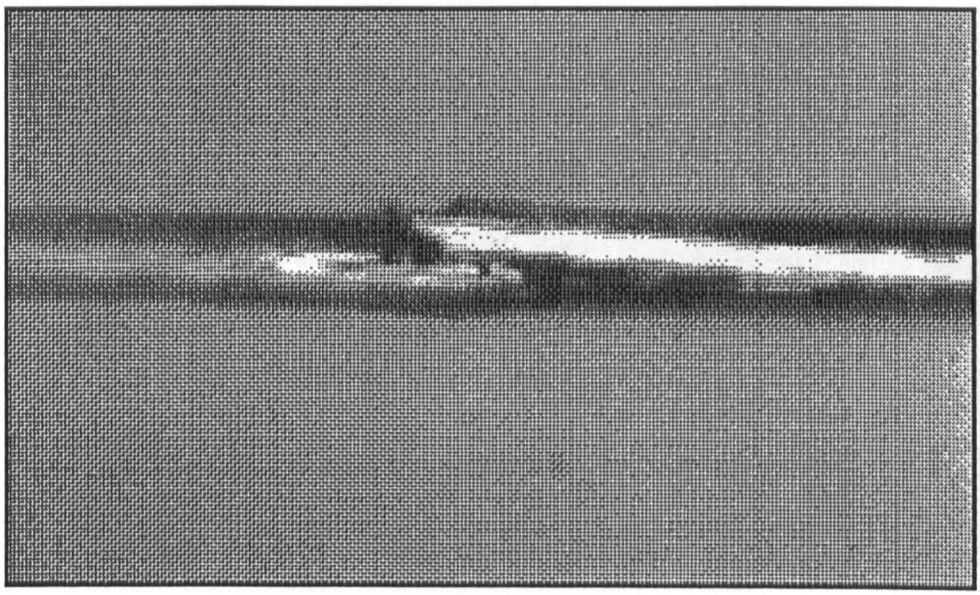

Fig.4.5 Micrograph of a fibre compressive fracture on an HMS fibre. The scale is indicated by the fibre diameter, which is 7 μm.

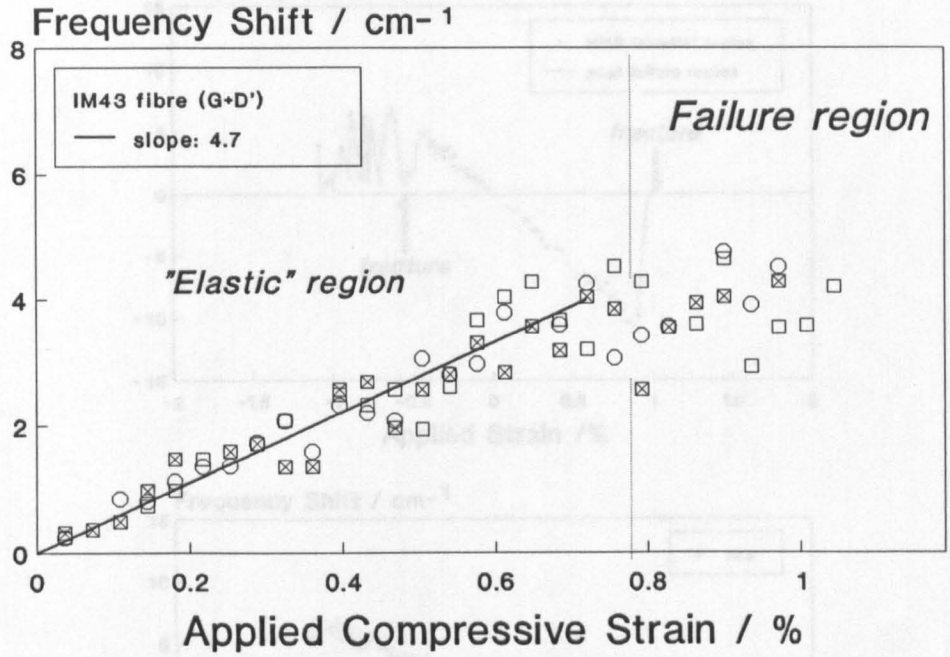

Fig.4.6 The Raman frequency shift of the G-D′ band for the IM43 fibre, as a function of compressive applied strain.

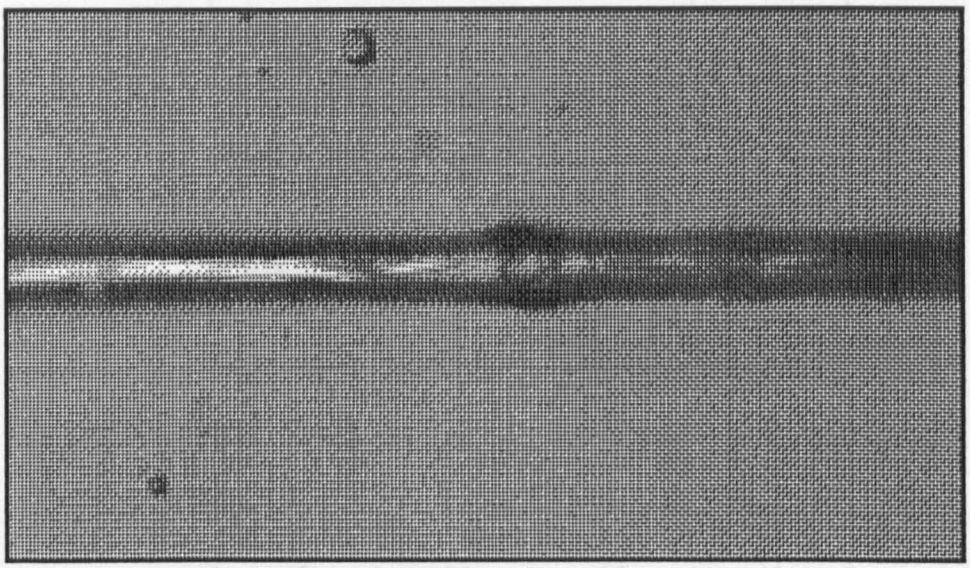

Fig.4.7 Micrograph of a "bulging" formation on the IM43 fibre in compression. The scale is indicated by the fibre diameter, which is 5 μm.

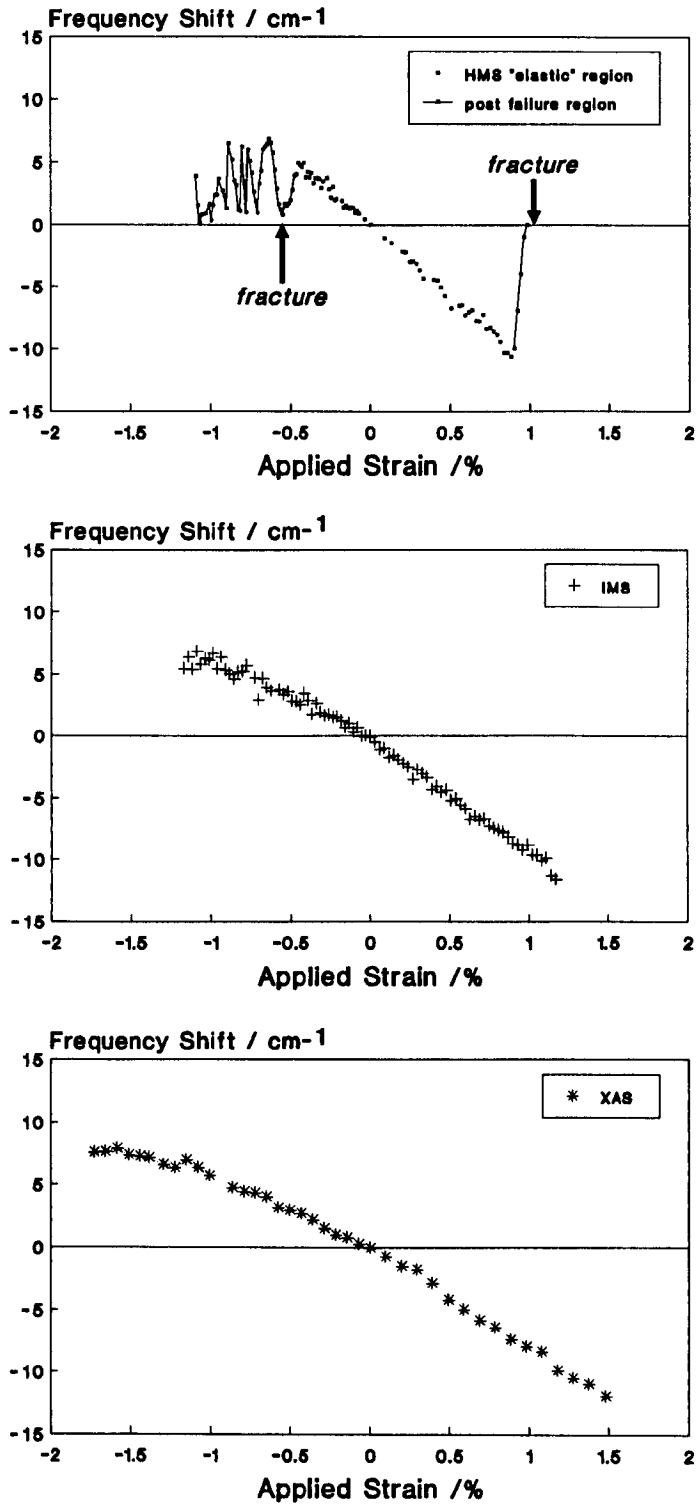

Fig.4.8 The Raman frequency shift as a function of applied strain (compressive and tensile) for **(a)** the HMS, **(b)** the IMS and **(c)** the XAS fibres (the 7 μm diameter series).

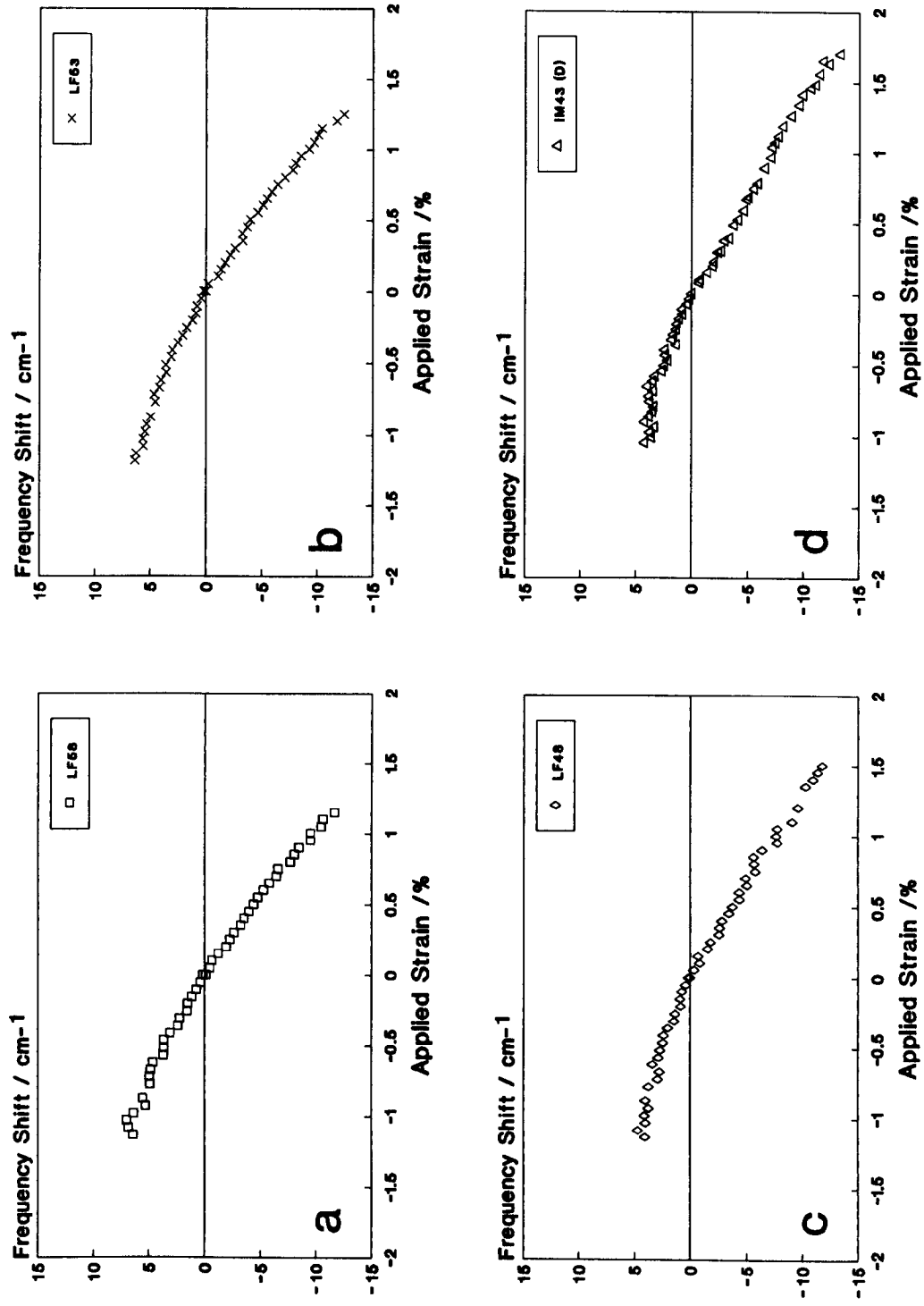

Fig.4.9 The Raman frequency shift as a function of applied strain (compressive and tensile) for **(a)** the LF58, **(b)** the LF53 and **(c)** the LF48 and **(d)** the IM43 fibres (the 5 μm diameter series).

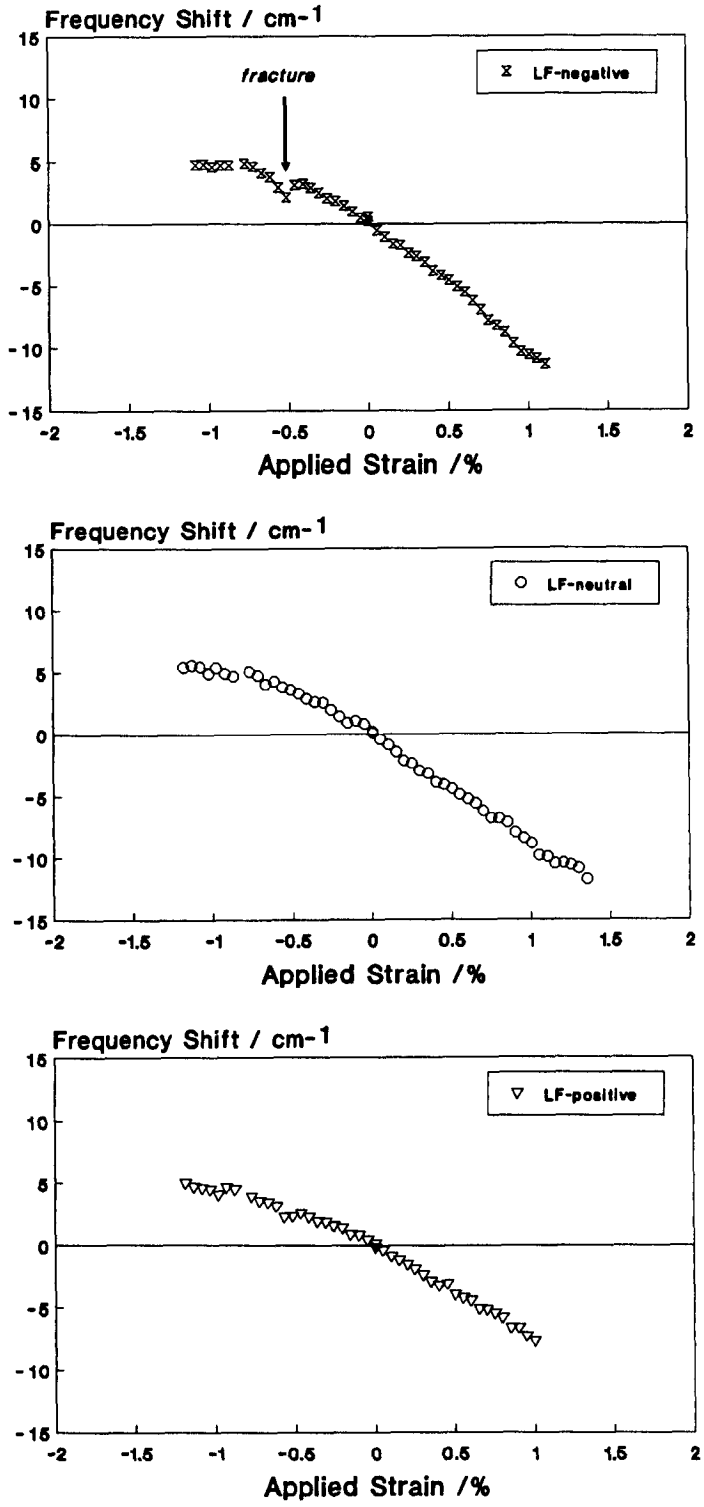

Fig.4.10 The Raman frequency shift as a function of applied strain (compressive and tensile) for the **(a)** LF-negative, **(b)** LF-neutral and **(c)** LF-positive fibres (the "morphology" series).

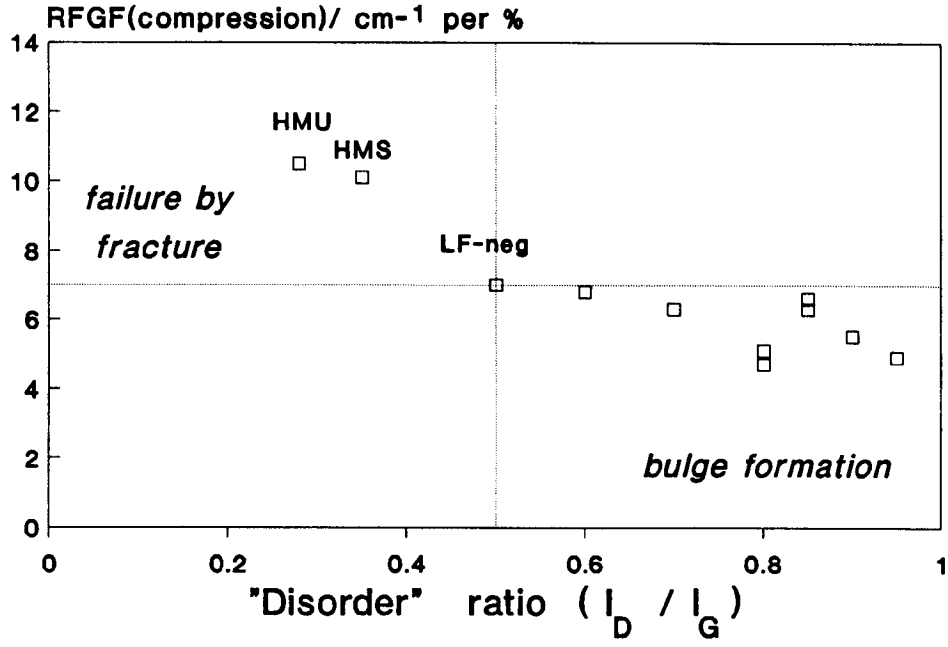

Fig.4.11 The mode of failure in compression as a function of the fibre Raman intensity ratio I_D/I_G and the compressional Raman Frequency Gauge Factor.

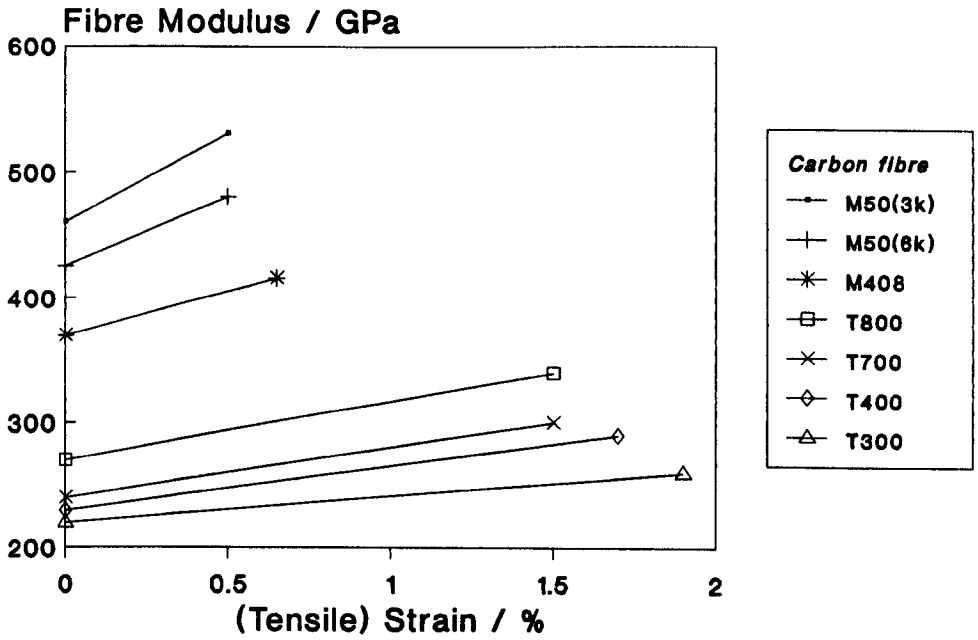

Fig.4.12 Tensile strain dependence of the Young's modulus of various carbon fibres, according to Hughes [Hughes 1986].

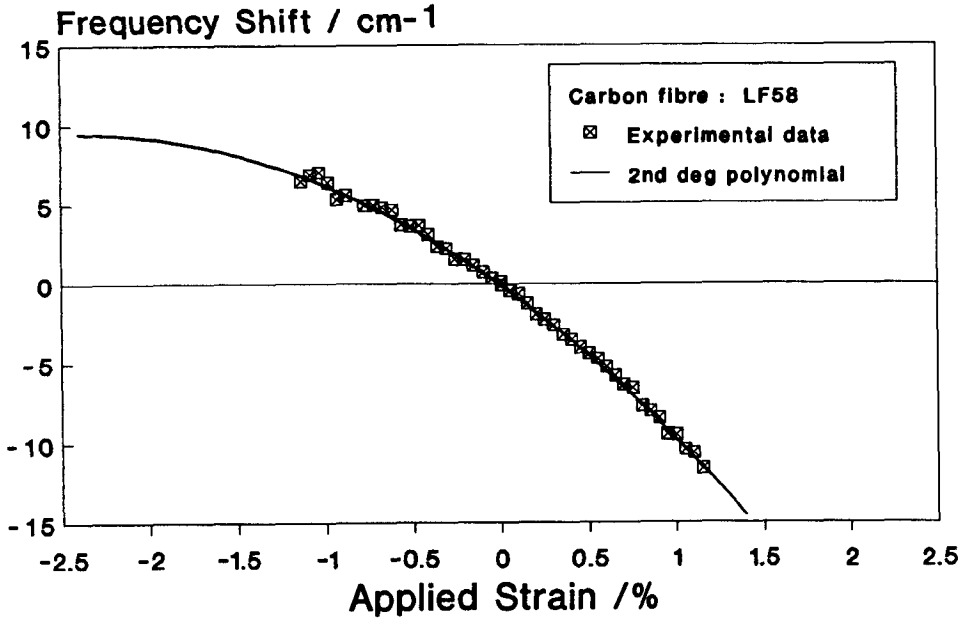

Fig.4.13 Second degree polynomial regression applied to the Raman frequency shift vs applied strain data of the LF58 fibre.

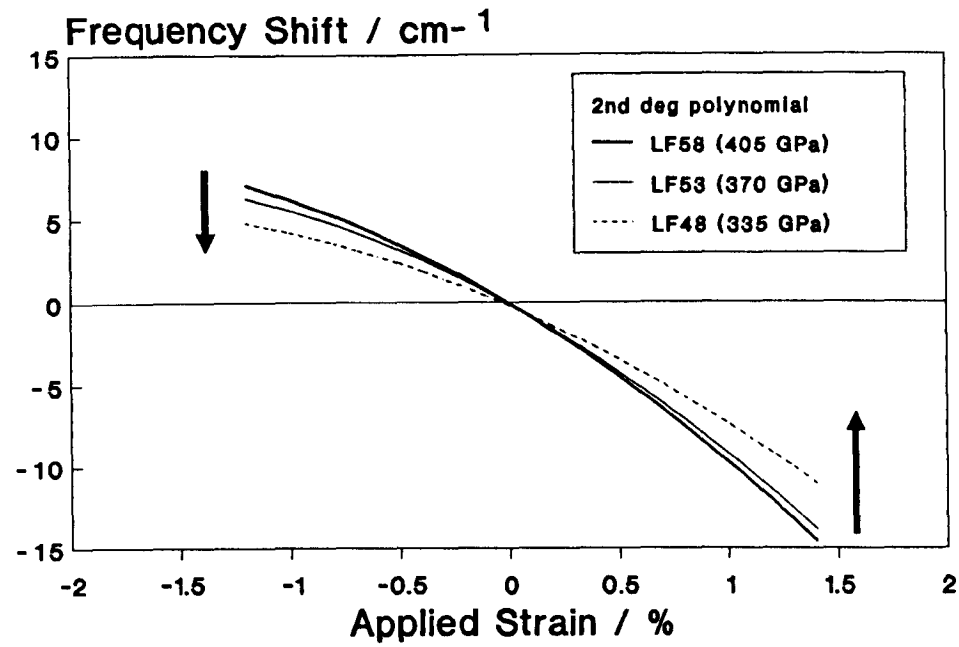

Fig.4.14 Second degree polynomial regression curves for three laboratory 5 μm fibres.

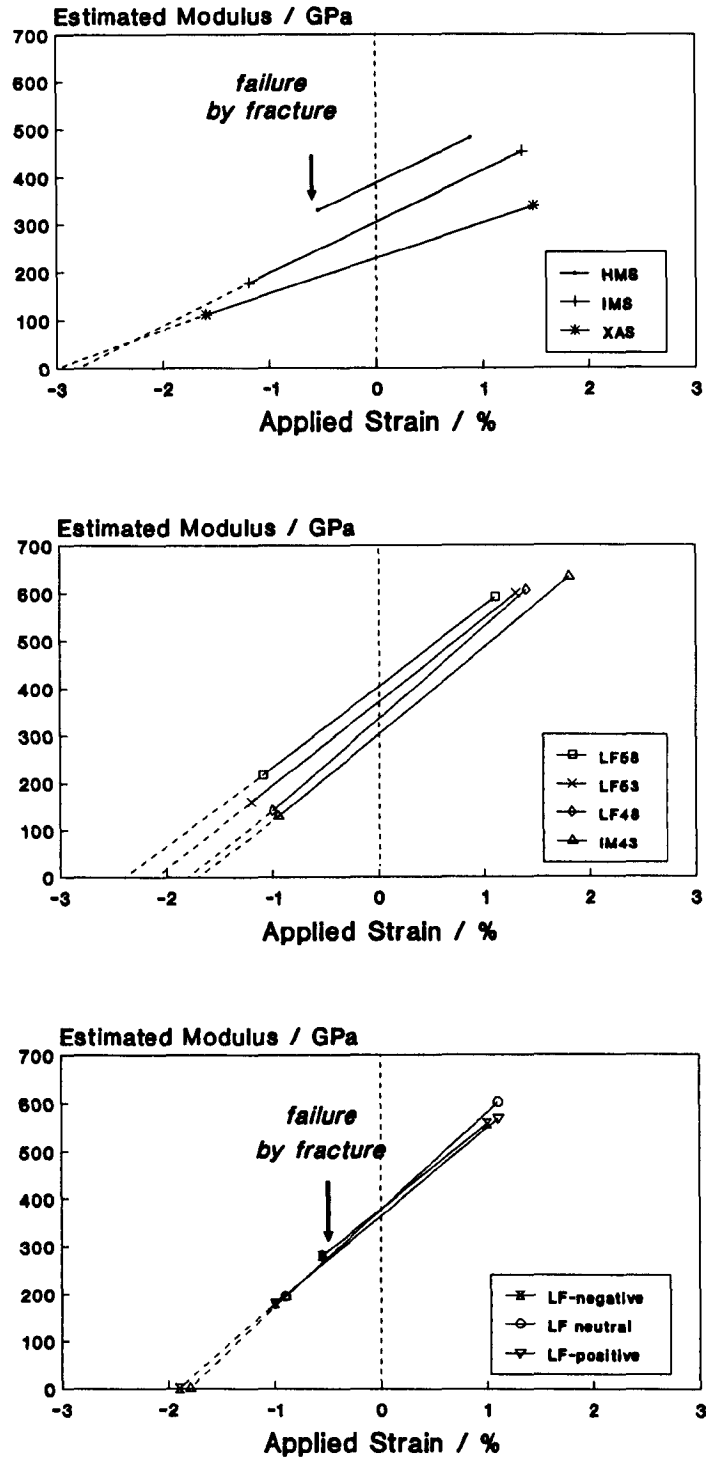

Fig.4.15 (top), 16 (middle), 17 (bottom). The strain dependence of the fibre modulus, as calculated through equation 4.12, for the 7 μm series, the 5 μm series and the "morphology" fibre series, respectively.

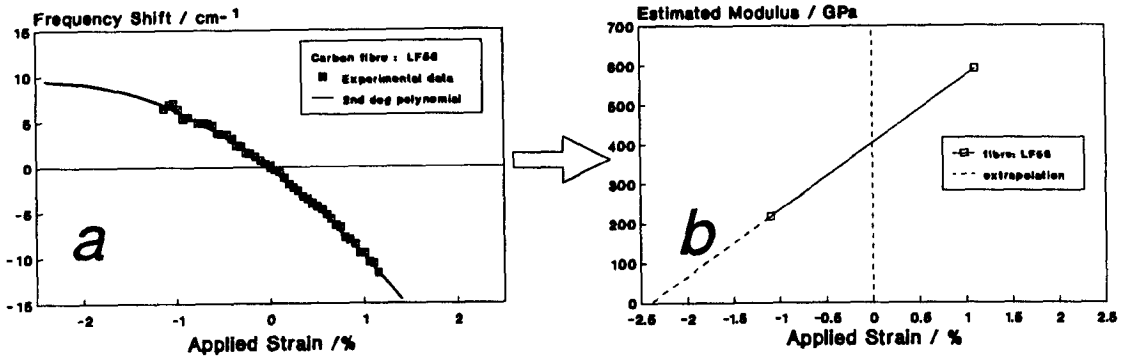

a. Raman frequency - strain curve

b. Equation 4.12 : modulus - strain curve

c. Equation 4.13 : Stress - strain curve

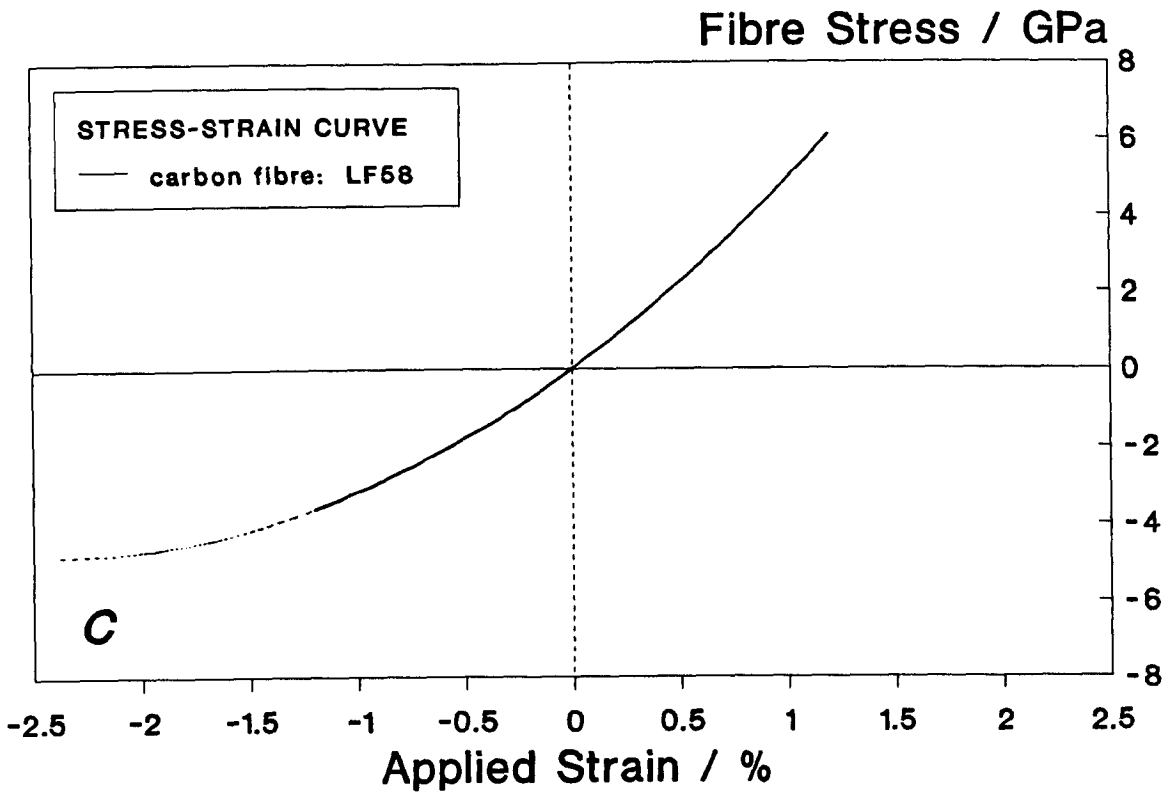

Fig.4.18 Sequential derivation of the fibre modulus strain dependence and the fibre stress - strain curve, from the Raman frequency vs strain curve of the LF58 carbon fibre.

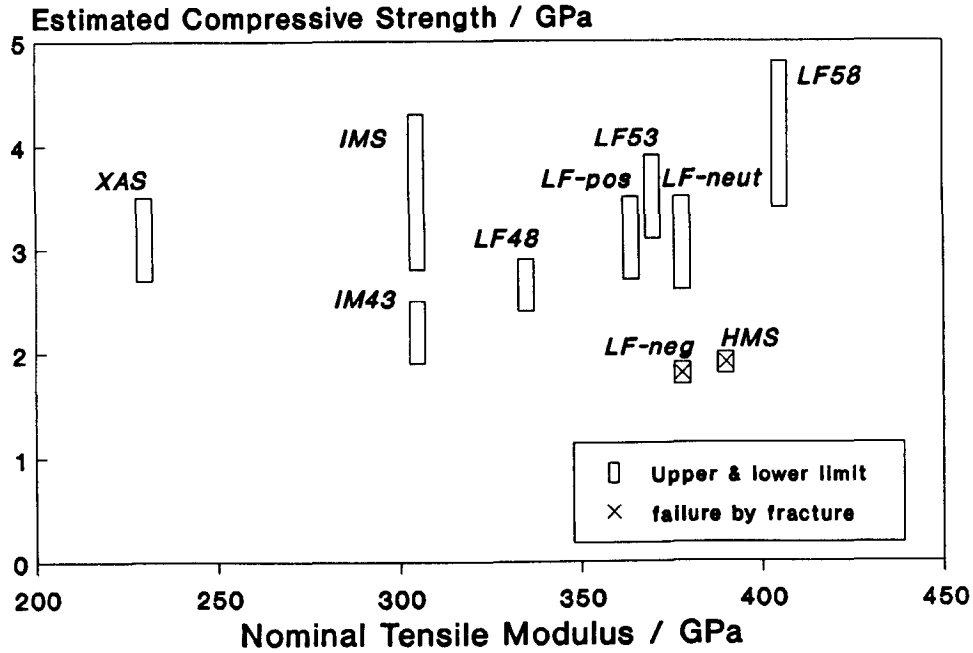

Fig.4.19 The estimated compressive strength of carbon fibres, as a function of the nominal tensile fibre modulus.

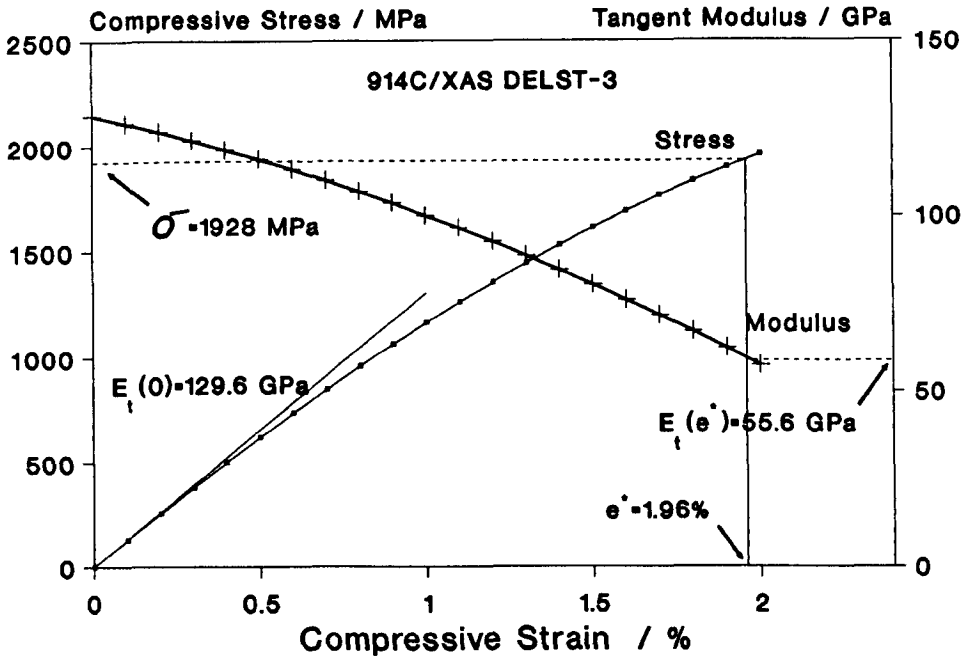

Fig.4.20 The compressive stress - strain curve and the tangent modulus with compressive strain, for a 60% fibre volume fraction XAS carbon fibre/ epoxy resin unidirectional composite [Haeberle 1990].

CHAPTER 5

INTERFACIAL STUDIES ON CARBON FIBRE/EPOXY RESIN SYSTEMS

5.1. Literature review on reinforcement mechanisms.

Carbon fibre composites satisfy a number of the most important requirements for an ideal engineering material, such as high strength, high toughness and low weight. With respect to the filament component, carbon fibres can be produced with high specific strength and high specific stiffness. In addition, carbon fibres exhibit high creep resistance, good thermophysical properties and excellent damping characteristics **[Donnet 1984]**. In order to get the most of these properties, the fibres must be accommodated into a low modulus and density matrix (binding) material, which should carry out the following functions **[Kelly 1966, Dresselhaus 1988]** :

(i) protect the fibre surface, so that surface abrasion is avoided,

(ii) join the numerous filaments together, but at the same time, prevent a brittle crack to run across the composite,

(iii) allow the economic processing of the fibre composite material into useful geometrical configurations, and,

(iv) above all, provide a means by which the load is transferred successfully to the reinforcing phase: the fibres.

The load applied to the soft, binding component has to be transmitted to the strong filament through their boundary region, the interface **[Hull 1981]**. Without a mechanism of load transfer, there would be no reinforcement and the composite properties would be those of the matrix material, diminished by the pores. The role of the interface in the composite structural integrity is better appreciated when it is realised that 1 in^3 of a 50% fibre composite with a fibre diameter of 7.5 μm, contains approximately 6500 in^2 interface area **[Chamis 1974]**.

5.1.1. *Nature and role of the interface/interphase.*

The interface between fibre and matrix has been defined as the common surface to both constituents and the immediate region around it. It has mechanical and physical properties that differ from those of the fibre and the matrix. For analysis purposes only it is considered to be of zero thickness **[Chamis 1974]**. However, in real terms, some additional features

have to be taken into consideration; during the fabrication of a composite a huge amount of free fibre surface has to be converted to a well-bonded, force-transmitting interface. In the manufacturing process, various factors participate in altering, locally, the properties of both surfaces, because of absorption, chemical reactions and differential thermal effects. These activities may extend from a few nanometers to a few hundred nanometers depth **[Megerdigian 1987]**, making it more meaningful to talk about the *interphase* between the constituents, than about their interface **[DiBenedetto 1978]**. The complexity of the interphase is illustrated by the schematic model of figure 5.1. The model takes into account morphological differences of the fibre surface compared to its inner structure **[Jones 1971, Guigon 1984]**, absorption of chemical species during manufacturing and possible altering of the polymer structure in the region of the interaction **[Drzal 1983 a&b]**.

Various models have been developed to simulate the nature of the interaction (or bonding) between fibre and matrix. The types of bonds existing at the interphase are described by current adhesion theories **[DiBenedetto 1978, Hull 1981]** and can be classified into at least three categories: mechanical, physical, and electrochemical.

The mechanical bond can arise through interlocking of the one component into the other (fig.5.2a). The liquid phase can run into cracks and pores of the coarse solid phase. The effectiveness of this bond can be enhanced by the surface roughness. Additionally, the mechanical bond may arise through frictional resistance to the sliding of the one surface over the other (fig.5.2b). This frictional type of bond can be promoted by the existence of high stresses acting normal to the contact surface, such as thermal residual stresses **[Broutman 1970, DiBenedetto 1978]**.

The physical bond depends on the fibre/matrix compatibility. The thermodynamic wetting of a solid surface by an electrically neutral liquid phase, can be measured through the determination of the contact angle between the fibre and the matrix (fig.5.3). Good thermodynamic wetting is characterised by small contact angle, while poor wetting by wide angle **[DiBenedetto 1978, Hull 1981]**.

Chemical bonding can be either due to electrostatic attraction between two oppositely charged atoms (ionic bond), or to covalent interaction, where the electronic orbits are shared between interacting atoms. Secondary bonding can arise from Van der Waals forces acting between the molecules **[Hull 1981]**.

Finally, "autohesion" bonding characterises the phenomenon, where polymer molecules may diffuse in the molecular network of the other phase. This phenomenon may be promoted by the presence of solvents and plasticity agents **[Hull 1981]**.

Once the adhesion between the two constituents has been achieved, through the aforementioned interactions at atomic and molecular level, then the load transfer mechanism can be considered as a primarily mechanical process **[Chamis 1974]**.

When a fibrous composite is loaded in the direction of the aligned fibres, a macroscopically uniform stress field acts at the cross-section normal to the loading direction. Since the two constituents have entirely different elastic properties, the integrity of the composite depends on the ability of the fibre/matrix interface to accommodate the displacements developing at that region, i.e., the uniform stress state is perturbed by the transfer of load to the fibres through the interface. If the fibre stiffness is much higher than the matrix stiffness ($E_f >> E_m$), the assumption that the fibres carry almost all the axial load and the matrix is subjected almost exclusively to shear, is the basis of the "shear-lag" analysis **[Cox 1952, Dow 1963]**. The "shear-lag" theory is the result of the first attempt to describe the complex interactions between fibre and matrix, using elastic concepts.

5.1.2. *Models of load transfer.*

The load transfer mechanism in a fibre/matrix system is activated in the vicinity of a discontinuity. Such discontinuities are the fibre ends and the fibre breaks. Fibre breaks can occur either during the manufacturing process or during loading, even while the whole composite is still intact. Therefore, the study of the stress field at the fibre/matrix interphase and, particularly, the study of the distribution of the shear stress along the interface of the fibre/matrix system, is a necessary requirement before any evaluation of the interfacial strength is attempted. The stress field at the interface comprises a combination of thermal residual stresses, curing shrinkage stresses, and stresses induced by external loading **[Broutman 1970]**. It is also dependent upon the fibre arrangement, the fibre and matrix elastic properties, the resin curing

temperatures, the differential expansion coefficients of the two constituents, as well as the geometry and the locus of the discontinuities **[Chamis 1974, Carrara 1968]**. A review of the stress transfer theories is presented in the following paragraphs.

(a) Analytical treatments.

For a better understanding of the force field at the interphase of a fibre/matrix system, the illustration of figure 5.4 presents the stresses acting on a material element **[Chamis 1974]**. Axial (σ_x), radial (σ_r) and tangential stresses (σ_ϑ), as well as, shear stresses (σ_{rx} or τ_{rx}), compose a very complicated force field, which has to be simplified, in order to obtain an analytical solution.

The basic assumptions of the "shear-lag" analysis **[Cox 1952]** require that in a short fibre embedded in a block of resin (i) both constituent materials behave elastically, (ii) their interface is infinitely thin and (iii) there is perfect adhesion between fibre and matrix **[Hull 1981]**. In addition to these, it is assumed that the lateral stiffness of the fibre is equal to that of the matrix. According to this analysis the rate of transfer of load from the matrix to the fibre is proportional to the relative interfacial displacement u (at a certain distance x from the fibre end) when the fibre is present and the displacement v (at the same position) when the fibre is absent, following the formula:

$$\frac{dP_f}{dx} = H\cdot(u-v) \qquad (5.1a)$$

Since the force on the fibre is given by $P_f=E_f\cdot A_f\cdot(du/dx)$, (where E_f is the fibre Young's modulus and A_f is its cross-section) and the strain in the matrix is given by $\varepsilon=dv/dx$, the differential equation that describes the system is :

$$\frac{dP_f^2}{dx^2} = H\cdot\left(\frac{P_f}{E_f\cdot A_f} - \varepsilon\right) \qquad (5.1b)$$

The boundary conditions for this problem are described by the requirement

that the fibre ends are free of axial forces. The complete solution of the above equation yields the fibre axial stress distribution $\sigma_f(x)$ and the interfacial shear stress (ISS) distribution $\tau(x)$:

$$\sigma_f(x) = E_f \cdot \varepsilon \cdot \left\{ 1 - \frac{\cosh\,[\beta \cdot (L/2-x)]}{\cosh\,[\beta \cdot L/2]} \right\} \qquad (5.1c)$$

$$\tau(x) = E_f \cdot \varepsilon \cdot \left\{ \frac{G_m}{2 \cdot E_f \cdot \ln(R/r)} \right\}^{1/2} \cdot \left\{ \frac{\sinh\,[\beta \cdot (L/2-x)]}{\cosh\,[\beta \cdot L/2]} \right\} \qquad (5.1d)$$

$$\text{where} \quad \beta = \left\{ \frac{2 \cdot G_m}{E_f \cdot r^2 \cdot \ln(R/r)} \right\}^{1/2}, \qquad (5.1e)$$

$\sigma_f(x)$ is the axial fibre stress at a distance x from the fibre end, $\tau(x)$ is the interfacial shear stress (ISS) at a distance x from the fibre end, E_f is the fibre Young's modulus along its X-axis, L is the fibre length, ε is the macroscopically applied strain, G_m is the matrix shear modulus and R/r is the ratio of radii of the binder with respect to the fibre. The ratio R/r expresses the influence of the constituent volume fraction on the fibre and interfacial stresses.

According to this model, the smaller the R/r ratio the higher the maximum ISS (appearing at the fibre end) and the faster the decay of this ISS value as the distance from the fibre end increases. However, a great deal of criticism has been voiced over the validity of the assumptions of the above model with respect to (a) the elastic behaviour of the constituents **[Dow 1963]**, (b) the perfect bonding **[Piggott 1980, 1987]** and (c) the regular arrangement of the fibres in real composites **[Broutman 1970]**. The lack of consideration of lateral force field **[McCartney 1988]** as well as the failure to take into account stress concentrations effects at the fibre ends **[Broutman 1974, Carrara 1968]** have also been noted. Nevertheless, the fundamentals of the shear-lag analysis have never been seriously argued. On the contrary, they have been employed, under more cautiously selected preconditions, by other researchers who incorporated in their study the effects of plasticity **[Dow 1963]**, frictional forces **[Piggott 1980, Outwater 1956]** and three dimensional (3D) elasticity **[McCartney 1988]**, to derive more elaborate analytical expressions.

Plasticity effects due to matrix yielding were taken into account in the model of Dow **[Dow 1963]**, in which the stresses in the vicinity of a discontinuity were calculated by assigning gradually diminishing values of matrix modulus, corresponding to the degree of yielding. The physical model employed in that analysis consisted of a single fibre embedded in the matrix material, with the force being applied either on the fibre, or on the binder (matrix). The latter simulates more successfully the situation encountered in a single fibre model composite, particularly, during the fragmentation procedure. The (elastic) interfacial shear stress distribution $\tau(x)$ is given by the formula **[Dow 1963]**:

$$\tau(x)= \frac{\lambda}{4} \cdot \left\{ \frac{P_m}{A_m \cdot (E_m/E_f) + A_f} \right\} \cdot \left\{ \frac{\sinh \{\lambda \cdot (L-x)/d_f\}}{\cosh \{\lambda \cdot L/d_f\}} \right\} \qquad (5.2a)$$

$$\text{where } \lambda= 2 \cdot \sqrt{\left\{ \frac{2 \cdot \sqrt{2} \cdot (G_f/E_f) \cdot \left(1 + (A_f/A_m) \cdot (E_f/E_m)\right)}{(\sqrt{2} - 1) + (G_f/G_m) \cdot \left(\sqrt{(A_m/A_f)+2} - \sqrt{2}\right)} \right\}}, \qquad (5.2b)$$

P_m is the force applied to the binder, E is the Young's modulus, G is the shear modulus, L is the length of the embedded fibre, A is the cross sectional area, d is the diameter, while the subscripts "f" and "m" stand for fibre and matrix, respectively. According to this analysis, the maximum ISS appears always at the fibre end. The application of this model on an aluminum oxide/aluminum system **[Dow 1963]** resulted in extremely high shear stresses and the matrix was expected to yield first **[Dow 1963]**.

An investigation of the shear stress distribution along fibre fragments in composites, taking into account stresses arising from thermal coefficient mismatch **[Chamis 1974]**, yielded the following expression for the ISS :

$$\tau(x) = \tfrac{1}{4} \cdot \lambda \cdot E_f \cdot \left(\varepsilon_c + \Delta T \cdot (a_c - a_f)\right) \exp(-\lambda \cdot x/d_f) \qquad (5.3a)$$

$$\text{where } \lambda = \frac{2 \cdot (G_m/E_f)^{1/2}}{(p - 1)^{1/2}}, \qquad (5.3b)$$

p is the fibre packing coefficient, for either hexagonal or square array, ε_c is the composite strain, a_c is the composite thermal expansion coefficient, a_f is the fibre thermal expansion coefficient, ΔT is the temperature difference between manufacturing and working temperatures, and G_m, E_f, d_f are as described in previous models. All the quantities included in the calculations refer to the value of the property in the direction of the fibre alignment, ignoring effects in the lateral direction.

In the Cox **[Cox 1952]** and Dow **[Dow 1963]** treatments the fibre volume fraction was incorporated in the ratio R/r. Chamis's **[Chamis 1974]** analysis attempted a different approach. By introducing a full composite model, the influence of the neighbouring fibres to the force field around the fibre end is acknowledged. However, the matrix layer of thickness δ, surrounding the fibres, influences only the matrix and interface displacement calculations **[Chamis 1974]** and not the final interfacial shear stress expression (equation 5.3a).

Another elastic transfer model has been derived **[Piggott 1980]**, assuming (a) perfect fibre/matrix bonding, (b) no yielding or slip at the interface (c) orderly arrangement of fibres and (d) constant matrix strain at the ring of nearest neighbours of the fibre under examination. The final expression for the ISS is given by:

$$\tau(x) = \frac{1}{2}\cdot n\cdot E_f\cdot \varepsilon\cdot \frac{\sinh\{n\cdot(L-x)/r\}}{\cosh\{n\cdot L/r\}} \qquad (5.4a)$$

$$\text{where} \quad n = \left\{ \frac{2\cdot E_m}{E_f\cdot(1+\nu_m)\cdot \ln(p/V_f)} \right\}^{1/2}, \qquad (5.4b)$$

E_f is the fibre Young's modulus, E_m is the matrix Young's modulus, ε is the matrix applied strain, L is the fibre length, r is the fibre diameter, ν_m is the matrix Poisson ratio, p is the fibre packing coefficient, V_f is the fibre volume fraction, x is the distance from the fibre end. A schematic and qualitative description of the interfacial shear stress distribution along a fibre fragment, based on the elastic transfer models presented up to now **[Cox 1952, Dow 1963, Chamis 1974, Piggott 1980]**, is given in figure 5.5.

The effect of poor adhesion was incorporated in a modified version of the last model **[Piggott 1980]** to describe the shear stress profile in fibre

reinforced polymers, where frictional slip is assumed as a common mechanism of stress transfer between polymer matrix and fibres. In this case, the adhesion is taken into account with the introduction of a parameter *a*, ranging from 0 to 1, to describe the state of adhesion from none to perfect, respectively. While in a portion of the fibre length mL (m<1) only frictional constant shear stresses occur, the ISS distribution for the rest of the fibre is limited by the matrix yielding shear strength. A schematic description of the interfacial shear stress distribution in this case, shown in figure 5.6, indicates that the maximum value of the ISS does not necessarily occur at the fibre end. According to the frictional slip model, the ISS near the fibre end appears to be constant and lower than the maximum, and its value is controlled by the normal compressive stresses acting on the fibre/matrix interface **[Piggott 1980]**.

The theoretical models discussed so far, have set no conditions or restrictions concerning the shear stress field at the fibre end. However, as stated in a three dimensional study of the fibre/matrix interface **[Smith 1970]**, the shear stress at the interface must be zero at the location of the broken fibre. This situation arises from the symmetry of the stress tensor and from the fact that, at the fracture surface of the fibre, the shear stresses should be zero **[McCartney 1988]**.

In an axisymmertic stress distribution model recently proposed **[Whitney 1987]**, the fibre is considered as an orthrotropic material. The developing stresses are represented by a decaying exponential function multiplied by a polynomial. The final expression for the fibre axial stress and the interfacial shear stress are **[Whitney 1987]** :

$$\sigma(x) = \left(1 - \left(4.75 \cdot \frac{x}{L_c} + 1\right) \exp\left(-4.75 \cdot \frac{x}{L_c}\right)\right) \cdot A_1 \cdot \varepsilon_0 \qquad (5.5a)$$

$$\tau(x) = -4.75 \cdot \mu \cdot A_1 \cdot \varepsilon_0 \cdot \left(\frac{x}{L_c}\right) \exp\left(-4.75 \cdot \frac{x}{L_c}\right) \qquad (5.5b)$$

$$\text{where} \quad \mu = \left\{ \frac{G_m}{E_{1f} - 4 \cdot \nu_{12f} \cdot G_m} \right\}^{1/2}, \qquad (5.5c)$$

x is the distance from the fibre end, L_c is the critical transfer length, A_1 is a function of fibre and matrix properties and volume fraction, ε_0 is

the applied strain, G_m is the matrix shear modulus, E_{1f} is the fibre Young's modulus along its axis, ν_{12f} is the fibre Poisson ratio.

A correction was attempted in the above expressions **[Netravali 1989a]** to deal with misprints that eliminated thermal stresses in the original analysis **[Whitney 1987]**. In fact, the final corrected form yields no change to the resulting ISS distribution. The advantage of the modified formula, however, is that it expresses the ISS as a function of the fibre diameter, rather than the critical transfer length, which facilitates the comparison with other models. The modified expression for the interfacial shear stress is given by:

$$\tau(x) = 4\cdot\mu^2\cdot A_1\cdot\varepsilon_0\cdot(x/d)\ \exp(-4\cdot\mu\cdot x/d) \qquad (5.6)$$

The most recent 3-dimensional analysis to our knowledge **[McCartney 1988]** provides a model for which three problems can be studied by altering the boundary conditions: (1) a matrix crack in a perfectly fibre/matrix bonded system, (2) a matrix crack in a system where frictional bonding precedes perfect bonding, and, (3) a broken fibre in a perfectly bonded fibre/matrix system. The basic assumptions of this analysis are: (i) the fibres have a precise cylindrical shape so that surface roughness effects do not arise, (ii) the two constituents behave elastically, and (iii) the shear stresses are zero at the tip of the broken fibre, for reasons explained previously. In addition, Poisson ratio mismatches are taken into account, whereas for the broken fibre case, residual thermal stresses seem to have been ignored, since no thermal terms were entailed in this particular set of calculations. The analysis takes into account the fibre volume fraction V_f, which is considered proportional to the ratio r^2/R^2, where r is the fibre radius and R is the radius of the matrix cylinder surrounding the filament. The interfacial shear stress is described by :

$$\tau(x) = \frac{r\cdot\sigma_f^{\infty}}{4\cdot q}\cdot f(x) \qquad (5.7a)$$

$$f(x) = \frac{p^2-q^2}{r}\exp\left\{\frac{-(p-q)x}{r}\right\} + \frac{p^2-q^2}{r}\exp\left\{\frac{-(p+q)x}{r}\right\} \qquad (5.7b)$$

where σ_f^{∞} is the fibre stress far from the discontinuity, and p and q are

functions of the fibre and matrix modulus, the Poisson ratios, the volume fractions and the applied strain.

A very useful observation can be made from the study of the matrix crack where the fibre is partially frictionally constrained **[McCartney 1988]**. For this case the maximum ISS occurs even further away from the fibre end, compared with the broken fibre model, at a distance equal to the length of the frictional region. Thus, it is expected, that also for the broken fibre case, similar behaviour may develop, should a partial bond or debonding extend from the broken fibre tip. Such a claim, however, requires further theoretical support.

The elimination of the shear stresses at the fibre end is schematically illustrated in figure 5.7. This figure shows the substantial difference in the shape of the ISS distribution along a fibre fragment, as proposed by the last two models, compared with the classical shear-lag elastic models (fig.5.5) and the frictional slip model (fig.5.6), discussed previously. All the above analytical models (with the exception the last **[McCartney 1988]**) have been particularly criticised for their failure to evaluate the magnitude of the stress concentration at the location of the discontinuity. These stress concentration effects have been observed in all photoelastic studies.

(b) Photoelastic observations and numerical treatments.

Undeformed epoxy resin is optically isotropic. However, when reinforced with fibres, resin adjacent to the fibres becomes optically anisotropic due to elastic stresses arising from (i) resin shrinkage during cooling from the curing temperatures and (ii) external loading of the whole system. If the resin is sufficiently transparent the stress birefringence can be studied under polarised light **[Ashbee 1988]**. By employing two-dimensional photoelastic analysis methods the stress field around the fibre can be studied, using stress optic laws to evaluate birefringent patterns.

Schuster [1964], using a 50 μm diameter fibre concluded that (a) the stress build up was completed within 5 fibre diameters from the fibre end (b) the maximum value of the ISS appeared at about 1/2 fibre diameter from the fibre tip and (c) the magnitude of the maximum ISS was calculated to be 2.5 times the composite stress, giving an estimated stress concentration

factor of 2.5.

Comparable results concerning the stress concentration factor were reported in a photoelastic investigation of a Dural bar/ Araldite system [**Tyson 1965**]. An important point in this investigation was the observation that the maximum shear stress appeared at an angle of 45° to the fibre direction, which implies that the interfacial shear stress is the projection of this maximum stress to the axis of the fibre alignment.

Fibre end geometry effects have been examined in detail in another photoelastic investigation [**McLaughlin 1966**]. Two-dimensional models were designed, employing steel rods as filaments. Tapered and square-ended (end face unbonded) fibres, exhibited a concentration factor of 5, followed by squared-end bonded fibres (factor 4). The lowest concentration factor was exhibited by the round-ended fibre.

A 3-dimensional elastic analysis, employing finite elements [**Carrara 1968**], was carried out to study the interfacial shear stress for different fibre-end geometries: ellipsoidal, blunt (squared) and tapered ends (fig.5.8). The results for broken-end (face) bond and intact bond agree with those of the photoelastic studies mentioned previously [**McLaughlin 1966**]. The stress concentration factor, here, is defined as the ratio of the calculated shear stress to the uniform tensile stress σ_a applied on the model. The tapered-ends case exhibits the lowest stress concentration factor of all [**Carrara 1968**].

In another FE approach, which employed a 3-phase elastic analysis [**Broutman 1974**], an interfacial layer was introduced around the fibre, with a different Young's modulus than either the fibre or the matrix alike. The higher the interfacial modulus E_i the stronger the shear stress concentrations (normalised over the composite stress) at the tip of the fibre and the faster the decay of the shear stress as it diminishes in less than 2 fibre diameters from the fibre end.

More recent studies have employed the method of finite differences to assess the interfacial stress field [**Zang 1983**]. However, such a method can be used only for plane-ended fibre models. According to the latter approach, the shear stress concentration factor at the fibre end is equal to the maximum value the shear stress reaches, divided by the average shear stress. The application of that model on a boron fibre/epoxy system resulted a value for this factor of 2.2 [**Zang 1983**] .

In another finite difference analysis **[Termonia 1987]** the relation between the ISS, the critical fibre length L_c and the moduli ratio E_f/E_m was studied for a short fibre model composite. By relating the adhesion efficiency to the interphase thickness, it was concluded that any decrease in the interphase thickness would result in a dramatic increase of the fibre critical length. A reduction in the matrix diameter surrounding the fibre in the Termonia model led to an extremely slow build up of strain and poor efficiency in the load transfer between fibre and matrix. This result is in total disagreement with most of the theoretical analyses, where a reduction in the ratio R/r causes a dramatic rise of the maximum ISS values. For a system with $E_f/E_m=20$, the stress concentration factor was found to approach the value of 1.5.

In most of the aforementioned analytical and numerical studies the term "R/r" was extensively used to denote the volume fraction of the system under investigation. Furthermore, this ratio expresses the field of influence of the interphasial stresses upon the interface. A study of the fracture mechanics of composite materials **[Cherepanov 1979]** has shown that the interphase extends about 5 fibre radii around the embedded filament. Beyond that boundary its contribution to the interfacial stress field near the broken or short fibre is negligible.

A detailed review of the various approaches aiming to predict the interfacial shear stress distribution along short fibres or fibre breaks has been presented so far. These treatments have employed analytical, numerical and photoelastic techniques to assess the stress field around a filament embedded in a matrix. The maximum interfacial shear stress (ISS) the interface can carry may be limited by the matrix properties or by the intrinsic properties of the interface itself. This maximum ISS value corresponds to the interfacial strength of the system, or, the strength of the interfacial bond. Direct measurements of the interfacial strength can be performed by employing a number of experimental configurations, as presented in the following section.

5.1.3. *Experimental methods to assess the interfacial strength.*

Interfacial shear strength (IFSS) measurements can be conducted either indirectly, employing full composite tests, or directly, using single fibre model composites.

Tests classified in the first category involve standard short beam specimens subjected to shear, beam specimens subjected to four-point bending, or transverse loading **[Chamis 1974]**. The interfacial shear strength (IFSS) in all theses cases is evaluated only qualitatively, through the measurement of other quantities, such as interlaminar shear strength, transverse strength, or, flexural strength of the composite **[Chamis 1974]**. As no direct analytical expression/model exists to relate the aforementioned quantities with the interfacial shear strength, the derivation of realistic values of the IFSS depends on the correct interpretation of the measured quantity in each case. Any erroneous assumption concerning the stress field in a full composite can produce misleading conclusions.

Tests classified in the second category are described as "direct" as they can yield nominal values of "interfacial shear strength". Although it has been argued that single fibre tests are not true and realistic composite tests, still they are gaining in popularity, because they can be easily performed, specimen preparation can be easily controlled and the costs involved are low.

Well established tests in this category are the pull-out test (or button test) **[Broutman 1970, Chamis 1974]**, a variation of which is the microbond or droplet test **[Miller 1987]**, the microindentation test **[Mandell 1980, 1986, Tse 1985]**, the shear debond and the transverse tensile debond tests **[Broutman 1974, Hawthorne 1974]** and finally, one of the most popular in its category, the fragmentation test (FT) **[Kelly 1966, Fraser 1975]**.

A brief review of the experimental techniques for the assessment of the fibre/matrix interfacial shear strength will follow, with extended reference to the FT since a modified version of it has also been employed in this programme of work.

(a) Interfacial shear strength (IFSS) measurements.

A common and easily performable test for measuring the interfacial shear strength of the fibre/matrix interface is the "pull-out" test **[Chamis 1974, Broutman 1970]**. A fibre of a certain length L is embedded in a matrix button (fig.5.9a) and the force P required to detach the fibre from the resin is recorded. The interfacial bond strength can be subsequently derived by employing the fibre properties and geometry, the matrix properties and the pull out force as the only known parameters **[Grey 1984, Pitkethly 1989]**.

A shear-lag type of analysis **[Greszczuk 1969]** yielded an expression for the maximum interfacial shear stress at the interface as a function of the average shear stress ($\tau_{av} = P/2\pi rl$), the interface modulus G_l, the interface thickness b_l, and the fibre modulus E_f. The interfacial shear strength (IFSS) was then calculated using the above analysis and the value of force P when pull-out occurred. However, this analysis being purely elastic, ignored frictional forces contributing to the interfacial shear strength **[Grey 1984]**, acting not only after debonding occurs but even prior to that. Another difficulty arising from the shear-lag analysis is that parameters such as shear modulus and thickness of the interphase are unknown **[Pitkethly 1989]**. To overcome this problem an arithmetic method has been developed, so that parameters like the aforementioned, are eliminated from the calculational process **[Pitkethly 1989]**. The applicability of the pull-out technique to thin fibres, less than 10 μm diameter, can be problematic, as extremely small embedded lengths are required. Another version of the pull-out technique is the "microbond" or "droplet" test **[Miller 1987]**. According to this modification, the fibre is pulled out of a resin droplet instead of a block, which has been deposited on the surface of the fibre (fig.5.9b).

One of the most expensive tests developed to measure, in situ, the interfacial bond strength is the "microdebonding" or "microindentation" test **[Mandell 1980, 1986, Tse 1985, Cadwell 1989]**, which on one hand the advantage of being one of the few tests conductible on real composites, but on the other hand has the disadvantage of requiring complicated instrumentation. It is worth adding here that although it is performed on full composites, it is still considered a single fibre test by virtue of its loading conditions **[Galiotis 1991]**. The compressive load is applied,

selectively, to individual fibres, oriented normal to a polished surface, by means of a microindentator (fig.5.9c); the interface is observed microscopically between loading steps until debonding occurs, which is defined as the detachment of the fibre from the surrounding matrix material. The data are then deduced to values of "interfacial shear strength" through a finite element (FE) programme, which employs a simplified model of a fibre surrounded by matrix with uniform properties beyond the interface **[Mandell 1986]**. Fully automated versions of this test have also been developed, to facilitate data accumulation **[Tse 1985, Cadwell 1989]**. However, the precision of the estimated strength values depends on the validity of the assumptions of the FE model.

Direct shear and tensile strength values for the interface have been estimated by the "shear debond" and the "tensile debond" tests, respectively **[Broutman 1970, Hawthorne 1974]**. With regard to the shear debond test, a short fibre is embedded into a rectangular column of resin. The specimen is axially compressed (fig.5.9d) and the stress is transferred to the embedded fibre by interfacial shear stresses at the fibre ends. The load is increased until interfacial failure (debonding) is detected in the form of interfacial brightening near the fibre ends. The shear strength τ^* is then calculated by the empirically derived relationship:

$$\tau^* = 2.5 \cdot \sigma_{av} \qquad (5.8)$$

where σ_{av} is the average stress on the specimen, the moment that interfacial failure occurs. The factor "2.5" expresses the shear stress concentration factor at the ends of a short fibre and has been derived as the average concentration factor calculated by various analytical models **[Broutman 1970]**. This test is not applicable to high modulus graphite fibres, or any fibre of low compressive strain to failure, because these fibres fail in compression before the initiation of interfacial shear failure **[Hawthorne 1974]**.

The tensile debond test is designed to measure the interfacial tensile strength (transverse to the fibre direction) of a fibre/resin system. A curved-neck resin specimen containing an aligned fibre is compressed along the fibre direction (fig.5.9e). When interfacial tensile debonding occurs,

at the curved-neck area, the debond stress S, for elastic deformations, is given by **[Broutman 1970]**:

$$S = \frac{\sigma_m \cdot (\nu_m - \nu_f) \cdot E_f}{(1+\nu_m) \cdot E_f + (1-\nu_f - \nu_f^2) \cdot E_m} \qquad (5.9)$$

where σ_m is the axial stress in the minimum cross section, ν is the Poisson ratio, E is the Young's modulus, and the subscripts "f", and "m" denote fibre and matrix respectively.

This type of test is not applicable to carbon fibres or any other fibres of low strain to failure **[Hawthorne 1974]**; for these fibres, only lower limits for the interfacial tensile (debond) strength can be estimated, since fibre failure normally precedes interfacial debonding.

(b) The fragmentation test.

The fragmentation test (FT), or, the single filament critical length method, was originally based on the observation of the multiple fibre fracturing phenomenon in a system consisting of brittle tungsten fibres embedded in copper matrix **[Kelly 1966]**. In its classical form, the FT is conducted on a brittle fibre embedded in a dogbone shaped block of matrix material, with high strain to failure. The specimen is subjected to axial tensile load in the fibre direction. Before any fracture occurs, both fibre and matrix are deformed equally. When the fibre strain attains a critical value, the fibre breaks. The point where the first fibre failure occurs corresponds to the weakest part of the fibre due to the presence of flaws and imperfections. This treatment is in accordance with the widely accepted view that the fibre strength is a property dependent upon the statistical distribution of flaws and imperfections along the fibre length **[Rosen 1964]**. After the first break, the load on the fibre fragments is transmitted from the matrix to the fibre by shear through the fibre/matrix interface, in the vicinity of the fibre breaks **[Cox 1952, Dow 1963]**. As the applied tensile load increases new fibre breaks develop. Beyond a certain level of strain no further fibre breaks occur, as the developing stresses cannot attain high enough magnitude to cause additional fibre fractures. The fragmentation test (FT) **[Kelly 1966, Fraser 1975]** has recently become

one of the most popular single fibre tests for assessing the fibre/matrix interfacial bond **[Drzal 1983 a&b, Bascom 1986, Jacques 1987, Favre 1990]**.

Initially, the FT was employed to study the interface of metallic matrix systems that can undergo plastic flow **[Kelly 1966]**. As the applied load increases, the interfacial shear stresses rise dramatically near the fibre ends, as predicted by all theoretical models. As soon as these stresses reach the shear yield strength τ_m of the matrix, plastic flow develops. Subsequently, the matrix yielding propagates along the remaining fragment length and introduces a constant shear stress field along it. If that fragment length is less than a critical value, the axial stress in the fibre cannot reach the fibre strength levels and, therefore, the fragmentation process is terminated. That critical length L_c is defined by a simple balance of forces, assuming constant shear force:

$$L_c = \frac{d_f}{2} \cdot \frac{\sigma_f(L_c)}{\tau_m} \qquad (5.10a)$$

where d_f is the fibre diameter, τ_m is the matrix shear yield strength, $\sigma_f(L_c)$ is the fibre tensile strength at gauge length equal to the critical length L_c. Rearranging the Kelly's equation, the critical length can be normalised over the fibre diameter, to define the critical aspect ratio:

$$\frac{L_c}{d_f} = \frac{\sigma_f(L_c)}{2 \cdot \tau_m} \qquad (5.10b)$$

Since the first confirmation of the above model for metal matrix systems **[Kelly 1966]** many attempts have been made to extend the applicability of the matrix yielding modelling to polymer matrix composites. The current trend is to calculate the quantity denoted as τ_m from experimentally measured L_c values. This quantity is no longer considered a matrix property **[Narkis 1988]**, but an interfacial property of the fibre/matrix system, which has been defined as interfacial shear strength **[Drzal 1983a]**, shear adhesion strength **[Drzal 1983b]**, yield stress of the matrix or the interphase **[Netravali 1989 a&b]**, stress transfer coefficient **[Fraser 1975]**, or interfacial stress transfer parameter **[Favre 1990]**. The calculation of this parameter still requires a constant shear stress distribution across the interface and can be derived by rearranging equation 5.10a:

$$\tau = d_f \cdot \frac{\sigma_f(L_c)}{2 \cdot L_c} \qquad (5.10c)$$

The constant shear stress requirement is satisfied either when there is matrix yielding as in metal matrices **[Kelly 1966]** or when frictional reinforcement is the main mechanism of load transfer **[Piggott 1980]**.

The derivation of the interfacial shear strength using equation 5.10c has two major drawbacks. The first is related to the fact, that by the end of the fragmentation process a broad distribution of fragment lengths ranging from $L_c/2$ to L_c is obtained **[Narkis 1988]**.

The second drawback is due to the statistical distribution of the fibre strength and its dependence on the fragment length, as well as on the handling of the fibres and the fabrication of the model composite **[Narkis 1988]**. It has also been argued that the use of the fibre strength for the estimation of the interfacial strength of the fibre/resin system, through equation 5.10c, overestimates the value for the parameter τ, as the peak stress in the middle of the fragments is always less that the fragment strength **[Netravali 1989a]**. However, the measurement of this peak stress in the middle of each fragment is not possible, using conventional data acquisition systems.

The critical length data collection can be carried out either by laborious optical observations, by computerised optical data acquisition **[Waterbury 1990]**, or by acoustic emission techniques **[Narisawa 1985, Netravali 1989b]**. In sequence, the critical length input to equation 5.10c is estimated from the average fragment length multiplied by 4/3 **[Oshawa 1978, Jacques 1987]**, or employing Weibull statistics **[Drzal 1983a, Bascom 1986]**. The fibre strength at the level of the critical length is obtained by conducting tensile tests at different gauge lengths and then extrapolating to the value of L_c, either linearly **[Favre 1990]**, or employing Weibull statistics **[Netravali 1989a]**. The use of Weibull statistics can lead to erroneous results **[Favre 1990]**, as a two parameter Weibull distribution fit typically yields variance values of ±50% **[Narkis 1988]**. Even more complicated computations have been attempted for a more accurate derivation of the Weibull parameters, by using Monte-Carlo simulation techniques **[Netravali 1989b]**.

While the quest to estimate a value of "τ" (eq.5.10c) has led to complicated, and expensive data acquisition and data processing techniques,

the validity of the fundamental equation itself (eq.5.10c) has always been in doubt; in fact, the whole interpretation of the fragmentation test results can be erroneous, if the basic assumption under which the equation 5.10c was derived, is not satisfied. This assumption requires constant shear stress at the fibre/matrix interface, which may be true for metal matrix composites, but not necessarily true for polymer matrix composites **[Narkis 1988, Galiotis 1991]**. The argument that at high strains the interface yields in shear and, therefore, constant shear stress prevails along this region **[Jacques 1987]**, is not supported by the experiment as the fragmentation process is completed at deformations much below the matrix critical yielding strain **[Galiotis 1991]**.

5.2. Experimental.

Fragmentation tests have been conducted on single carbon fibre/epoxy model composites. During the fragmentation test, the Raman spectrum of the embedded fibre has been derived as a function of position along the specimen and as a function of composite applied strain.

5.2.1. *Materials.*

The effect of fibre surface treatment, as well as, fibre modulus upon the carbon fibre/epoxy interfacial properties have been investigated in the following systems:

S1. HMU / MY-750, untreated high modulus carbon fibre in MY-750 epoxy resin (post-cured).

S2. HMS / MY-750, surface treated high modulus carbon fibre in MY-750 epoxy resin (post-cured), and

S3. IMD / MY-750, surface treated intermediate carbon fibre in MY-750 epoxy resin (post-cured).

The surface treatment of the carbon fibres has been carried out by the manufacturer (Courtaulds Grafil plc). No details of this procedure have been revealed. The manufacturer's quoted values for the mechanical properties of the fibres and the resin are shown in Table 5.1.

5.2.2. *Specimen preparation.*

Some model composites were provided by Courtaulds Grafil plc while others were prepared at QMW following the same procedure, as described in details below. Single carbon fibres were aligned in rubber dogbone shaped moulds, using glue tabs at both ends. Care was taken to avoid fibre prestretching or slacking in the mould. The MY-750 epoxy resin was first heated up in an oven at 40°C for 30 minutes and was then mixed with HY-951 hardener at a ratio 4 : 1 by weight. The mixture was stirred well and returned into the oven at 40°C under full vacuum for 8 minutes. The mixture was subsequently poured into the rubber moulds and repositioned into the oven at 60°C for 2 hours. As the specimens were set, they were removed from

the moulds and kept at room temperature for a day. The post-curing process required heating the specimens to 120°C at a rate of 0.25°C per minute in a temperature rate controlled oven. They were kept at this temperature for 1 $^{1}/_{2}$ hours and then were allowed to cool normally. The post-cured samples were ground to bring the embedded fibre at about 100 μm from the resin surface and were subsequently polished to enhance the optical transparency of the matrix. The final geometry of the specimen prior to testing is shown in figure 5.10.

A typical stress-strain curve for the post cured epoxy MY-750/HY-951 is shown in figure 5.11. The curve was derived after testing an epoxy specimen on an Instron mechanical tester, at a strain rate of 0.19 min^{-1}. The calculated values of the initial epoxy modulus up to 0.5% strain was found to be 2.6 GPa, while the ultimate tensile strength of the material σ_{m}^{*} was found to be ~65 MPa. The shear yield stress or the shear strength τ_{m}^{*} of the epoxy can be determined from the above tensile strength value using one of the failure criteria **[Kinloch 1983]**. The von Mises criterion ($\tau_{m}^{*} = \sigma_{m}^{*} / \sqrt{3}$) yields a value of about 38 MPa for the shear strength, while the Tresca criterion ($\tau_{m}^{*} = \sigma_{m}^{*} / 2$), gives a value of about 32 MPa for the epoxy shear strength. However, these values, may underestimate the true τ_{m}^{*} at the fibre resin interface, since the shear strength of thin polymer layers (such as the *interphase*) is pressure dependent **[Briscoe 1978, Kinloch 1983]**.

5.2.3. *Tensile testing of model composites.*

The dogbone specimen is mounted on the tensile jig, by clamping both its ends between metal grips. The tensometer grips can be pulled apart by a screw-thread mechanism which induces extensional deformations to the specimen. Two strain gauges (gauge resistance 350 ± 1.0 and gauge factor 2.09) are attached to the top and the bottom surface of the dogbone specimens and the specimen strain is derived from the resistance measurements using a Digital Multimeter. The use of one strain gauge at each surface is necessary to assess any unwanted bending stresses due to uneven grip tightening. The strain gauge performance exhibits reduced accuracy over 3.0% of applied strain, according to the manufacturer's specifications.

The tensometer is secured on the experimental stage (fig.2.3), which

in turn, can be translated along the microscope objective lens. Therefore, the whole specimen can be scanned by the Laser Raman probe, and in parallel, it can be studied optically through the specially modified Raman microscope.

5.2.4. *Raman spectroscopy on model composites - Spatial filtering.*

A serious technical obstacle may arise in the attempt to obtain the Raman spectrum of embedded in resin carbon fibre, due to the presence of strong resin Raman activity in the spectral region, where the fibre monitoring Raman frequencies are located. For example, in the case of a carbon fibre/epoxy resin system, the graphite peak appears at about 1580 cm^{-1} whereas the resin signal is located at about 1605 cm^{-1}. Spatial filtering techniques have then to be employed, to reduce the resin Raman interference in the overall spectrum.

The spatial filtering is applied to the backscattered light, which carries the frequency information, just before it enters the spectrometer. The aim of this technique is to reject, as much as possible, that portion of the light beam which is "rich" in resin frequencies. Schematically, the spatial filtering procedure is shown in figure 5.12. The smaller the pinhole diameter of the spatial filter (fig.5.12), the higher the proportion of the actual carbon signal in the backscattered beam that enters the spectrometer. However, although the focal spot on the fibre is 2 μm, it is extremely difficult to insert a pinhole of the same order of magnitude, as considerable light aligning problems will arise. In reality, there is always a portion of "wanted" frequencies that is filtered out which, in turn, results in longer exposure times for the acquisition of spectrum of reasonable quality. The impressive efficiency of spatial filtering is shown in figure 5.13 for three different pinhole diameters employed in the collection of Raman signal from a HMS carbon fibre/MY-750 epoxy resin model system.

5.3. Strain mapping on model composites using LRS.

As extensively described in the previous chapters, Laser Raman Spectroscopy (LRS) has been successfully employed to measure deformations in single fibres, at microscopic level (Chapters 3 and 4). The property that can be directly measured is the Raman frequency of the material. Thus, the experimentally derived frequency-strain relation can be used as the calibration curve for deriving the strain in the fibre. Using this technique, single fibres embedded into a resin matrix can be employed not only as a reinforcement constituent but in tandem, as an "internal strain gauge". Consequently, (a) the efficiency of the load transfer mechanism in continuous fibre composites can be assessed, (b) the strain transfer profiles can be derived for short fibres, or for fragmented long filaments, (c) the fibre transfer length can be measured at any level of strain and finally (d) the fragmentation process can be precisely monitored.

In general, a number of requirements have to be satisfied in order to achieve a precise and reliable mapping of the strain along embedded filaments. With respect to the fibre, it has to be a Raman active material, i.e., to possess a distinguishable Raman frequency. This Raman frequency has to be strain dependent, which usually is the case for crystalline materials, such as carbon fibres. Furthermore, the fibre should be able to withstand exposure to laser light without being damaged. This condition is fully satisfied for carbon fibres, as the heat treatment temperatures during manufacture, reach much higher levels than those developing in the fibre as a result of local laser heating. With respect to the resin, it has to be reasonably transparent to allow the light penetration and it should not fluoresce at the excitation wavelength. Finally, the matrix material should not exhibit Raman activity over the fibre frequency region. In the event of such Raman frequency overlap, special spectroscopic techniques, such as spatial filtering (see § 5.2.4), have to be employed in an attempt to minimise the matrix Raman signal.

While the applied strain on the dogbone specimen is measured by strain gauges, the strain transferred in the fibre through the resin, is calculated by monitoring the Raman vibrational frequencies of the fibre. The monitoring Raman frequency for all tests in this chapter was the Raman G-line or the G-D′ band, when the two features are merged (Chapter 2). The

frequency, at a first approximation, has been assumed to relate linearly to strain, and hence, the Raman Frequency Gauge Factor (Chapter 3) is a constant number for each fibre. Consequently, the Raman frequency ν_i obtained at any point i along the fibre, could be converted to fibre strain by the following equation:

$$\varepsilon_i = \frac{\nu_i - \nu_0}{\alpha_\varepsilon} \qquad (5.11)$$

where ε_i is the fibre strain at the point i, α_ε is the Raman Frequency Gauge Factor (RFGF) for the fibre under investigation, ν_i is the value of the Raman frequency at point i along the fibre and ν_0 is the value of the Raman frequency of the stress free carbon fibre, obtained from spectra of the fibre in air.

5.4. Interfacial Shear Stress evaluation.

The main concern at this stage is to find a simple and valid expression that relates the fibre strain (derived through measurement of the fibre Raman frequencies) to the interfacial shear stress. This will allow the evaluation of the shear forces that act at the locus of the fibre/matrix interface.

5.4.1. *The balance of forces model.*

In the shear-lag theory the matrix is assumed to carry only shear stresses and the fibres only tensile stresses **[Hull 1981]**, as long as the fibre is much stiffer than the matrix component. In a volume element of a composite, the stresses around a fibre element are shown in figure 5.14. Assuming that the shear stress acts circumferencially on the fibre/matrix interface, the force equilibrium along the x-axis requires : $\sum F_x = 0 \Rightarrow$

$$\left(\sigma(x) + \frac{d\sigma(x)}{dx}\,dx\right)\cdot\pi r^2 - \sigma(x)\cdot\pi\cdot r^2 - 2\cdot\pi\cdot r\cdot\tau(x)\cdot dx = 0 \qquad (5.12)$$

Solving that equation for $\tau(x)$, the interfacial shear stress can then be expressed as **[Greszczuk 1969, Piggott 1980, Agarwal 1980]** :

$$\tau(x) = \frac{r}{2}\cdot\frac{d\,\sigma(x)}{dx} \qquad (5.13)$$

where $\sigma(x)$ is the axial stress acting on the fibre cross section and in the direction of the fibre alignment and r is the fibre diameter. Photoelastic observations have shown that the interfacial shear stress also varies with the radial distance from the fibre/matrix surface. It possesses its maximum value on the contact boundary and falls off quadratically along the radial coordinate **[Carrara 1968, Tyson 1965]**. Therefore, for the derivation of equation 5.12, describing the balance of forces around the fibre element, the calculation of the interfacial shear force is based on the approximation that this force acts on the fibre matrix boundary and not

beyond it. The next step of this procedure involves the implementation of the fibre strain ε_f in equation 5.13. Considering the fibre and the matrix as linear thermoelastic solids, the stress-strain-temperature relation in the fibre direction is given **[Sokolnikoff 1956]**:

$$E_f \cdot \varepsilon_f = \sigma_f - \nu \cdot (\sigma_r + \sigma_\vartheta) + E_f \cdot \alpha_f \cdot \Delta T \qquad (5.14a)$$

where σ, ε, T correspond to stress, strain and temperature respectively, E is the Young's modulus α is the linear thermal expansion coefficient and ν is the Poisson ratio (radial strain over axial strain); the subscripts f,r,ϑ indicate the axial (fibre direction), the radial and the tangential coordinates, respectively. Differentiating equation 5.14a, over the variable x, i.e. the distance coordinate along the fibre direction we obtain:

$$E_f \cdot \frac{d\varepsilon_f}{dx} = \frac{d\sigma_f}{dx} - \nu \cdot \left(\frac{d\sigma_r}{dx} + \frac{d\sigma_\vartheta}{dx} \right) + \frac{d}{dx}\left(E_f \cdot \alpha_f \cdot \Delta T \right) \qquad (5.14b)$$

For single fibre composites, the transverse stresses are generally constant along the fibre length as finite element treatments and analytical models have shown **[Carrara 1968, McCartney 1988]**; therefore the transverse stresses term in equation 5.14b is eliminated. The above deduction is not valid for the region very close to the fibre end (less than 2 fibre diameters) as such discontinuities introduce significant (off axis) stress concentrations **[Carrara 1968]**. The thermal stresses induced during manufacturing, as expressed by the thermal term in equation 5.14b, do not vary along the fibre length. Hence, these two simplifications, allow the rewriting of equation 5.14b in the form:

$$\frac{d\sigma_f}{dx} = E_f \cdot \frac{d\varepsilon_f}{dx} \qquad (5.14c)$$

Substituting equation 5.14c to equation 5.13, the expression relating the axial fibre strain (measurable by the Raman probe) and the interfacial shear stress, is finally derived:

$$\tau(x) = E_f \cdot \frac{d_f}{4} \cdot \left(\frac{d\varepsilon_f}{dx} \right) \qquad (5.15)$$

The outcome of this analysis, equation 5.15, enables the interrelationship of the interfacial shear stress $\tau(x)$ with the fibre strain distribution $\varepsilon_f(x)$. The latter can be measured using the Laser Raman "probe".

5.4.2. *Modelling of the fibre strain data.*

A functional representation of these strain data with respect to the distance from the fibre end, is necessary, if equation 5.15 is to be applied. The data modelling involves a curve fitting to the set of pairs (x, $\varepsilon_f(x)$), where x is the position of the laser Raman probe along the fibre and $\varepsilon_f(x)$ is the fibre strain measurement at that specific position. The resulting continuous function $\varepsilon_f(x)$ is uniquely defined along the fibre transfer length and the goodness of the fit is dependent on the data scatter, but also on the selection of the interpolation function. The interpolation function has to be flexible enough to interpret the strain tendency along the whole range of definition, as well as, sensitive enough to assess quickly any strain alterations. Fifth degree polynomial and spline interpolations have been found to satisfy the aforementioned requirements. The polynomial regression was found to give a fast and quite accurate solution, by using commercially available software, while the more realistic interpolation of the cubic spline routines required tedious manual input of numerous data to main frame computer. However, the final outcome, the calculated interfacial shear stress distribution ISS(x), did not differ substantially, as was confirmed by comparative analysis of the same set of data (Appendix A2). Thus, all fibre strain distributions to be presented in the following paragraphs have been interpolated using a 5th degree polynomial function.

5.5. Results.

To study the interfacial properties of carbon fibre/ resin systems, the fragmentation process of the embedded fibre under tensile strain has been carefully monitored and the strain distribution along the fibre has been accurately obtained using the laser Raman probe, as described in previous paragraphs.

The major steps in the experimental procedure for the derivation of the fibre strain distribution, during the carbon fibre/epoxy fragmentation tests, are described below:

(1) the Raman spectrum of the fibre is optimised by spatial filtering of the backscattered light, so that is clearly resolved from the resin signal and is obtainable in a reasonable exposure time (preferably below 1 minute);
(2) prior to the Raman frequency mapping, at every level of applied strain, the whole Fragmentation Gauge Length (FGL) is optically scanned, to detect and identify any fibre fracture;
(3) prior to the first fibre fracture, the Raman frequency mapping is carried out at large steps (normally 1 mm in length), within the FGL, to sample the average fibre strain at various levels of applied strain;
(4) when the first fibre fracture occurs, the Raman frequency mapping is restricted to a selected region within the FGL, the Raman Gauge Length (RGL) and is carried out in a much smaller step (normally of 10, or 20 μm).

At the saturation of the fibre fracture process, the following two, primary, results are accumulated: the Raman frequency of the embedded fibre as a function of position along the selected Raman Gauge Length (RGL), at various levels of applied strain, and a map of the fibre fracture as it develops along the selected Fragmentation Gauge Length (FGL). The first yields the point-to-point strain distribution along the fibre, through equation 5.11, while the second provides the data for a conventional fragmentation test analysis on the fibre/resin system under investigation.

5.5.1. *System 1 : HMU / MY-750.*

The Raman spectrum of an HMU fibre embedded in MY-750 resin at 0.0% of applied strain is shown in figure 5.15. The G-line of the carbon fibre 1580 cm^{-1} and the epoxy resin band at 1605 cm^{-1} can be clearly seen. The Raman spectral details for both constituent materials are also displayed in Table 5.2.

The strain dependence of the HMU carbon fibre has been investigated in Chapter 2. Throughout the fragmentation test, the resin frequency peak remained fixed in position at about 1605 cm^{-1}. This is expected for amorphous materials, as the externally applied strain does not contribute to molecular bond extensions at the atomic level.

(a) Strain mapping in system 1 (HMU/MY-750).

The Fragmentation Gauge Length (FGL) for this experiment was 30 mm, i.e. the fibre fracture process was monitored along a distance of 30 mm. The Raman Gauge Length (RGL) is a region of about 10 mm within the FGL, scanned point-to-point by the laser Raman probe. For the HMU/MY-750 test the FGL began at a micrometer reading of 10.00 mm while the RGL started at a micrometer reading of 20.00 mm. Therefore, this notation is assigned to the x-axis of the relevant figures (figs. 5.16, 5.17). The FGL was scanned at a step of 1 mm at 0.0%, 0.3% and 0.6% applied strain. The calculated fibre strain distribution, at these three levels of applied strain, is shown in figure 5.16. While at 0.0% and 0.3% applied strain there was no fibre fracture detected and the fibre carried a quite uniform load, at 0.6% applied strain two fibre failures were observed. The dramatic fibre Raman frequency change observed in the failure regions revealed the existence of the two fibre breaks (fig.5.16). From the next level of applied strain, and onwards, the RGL was scanned at every 20 μm.

Additional fibre fractures occurred in the RGL at 1.0% applied strain. The strain distribution along the created fibre fragments is shown in figure 5.17a. In all five fragments (F1, F2, ... F5, fig.5.17a), the strain builds up linearly with distance from the fragment end, in a fashion that is in agreement with most theories of frictional reinforcement **[Piggott 1980, Outwater 1956]** and the fundamental concepts of the classical

fragmentation test **[Kelly 1966, Drzal 1983a]**. The gap between the fragments, at this level of applied strain (1.0%) ranged between 20 to 40 μm.

At an applied strain of 2.0% no more fibre breaks developed within the RGL, although outside the RGL a few more fibre failures were generated. The strain distribution along the RGL is shown in figure 5.17b. Obviously, no dramatic change in the strain profiles has occurred, apart from further stretching of a few fragments to reach higher strains at the middle of their length. However, the gap between the fragments has increased to about 60 μm in average, indicating that the fibre fragments are sliding apart from each other. There were no more fibre breaks formed beyond 2.0% applied strain over the whole FGL. The fragmentation process had at this stage reached the saturation level, for the whole specimen.

To study the load transfer capability of the system at high applied strains, the specimen was taken to 3.0% applied strain and two of the fragments in the RGL (fragments F3 and F4) were scanned with the laser Raman probe. The calculated strain distribution is displayed in figure 5.17c. Although the shape of the strain profiles has not been significantly altered, the maximum fibre strain has dropped. The gap between the fragments, at this level of strain had increased to about 90 μm.

(b) Conventional fragmentation studies on system 1.

The principle on which the fragmentation test is based, as described in § 5.1.3, requires constant shear stress on the interface **[Kelly 1966, Fraser 1975]**. If this condition is satisfied then the fragment critical length L_c, the fibre diameter d and the fragment strength at gauge length equal to the critical length $\sigma_f(L_c)$ are required to calculate τ_m, (equation 5.10c). As mentioned earlier, the ambiguity in the above analysis is primarily due to the complicated statistical treatments required to obtain a value for the critical length L_c and the fibre strength at very small gauge lengths. The treatment of the fragmentation test data, presented below, is based on two assumptions. With respect to the critical fragment length L_c the widely used convention $L_c=(4/3)l_{av}$ **[Ohsawa 1978]**, as well as the straightforward equation $L_c=l_{av}$, (where l_{av} is the arithmetic average of all fragment lengths in the FGL) **[Bascom 1986, Favre 1990]**, which yields 30% higher values, were employed. With respect to the fibre strength

values, it was assumed that the *maximum* fibre stress, achieved just before the last fibre fracture, would give a reasonable estimate of the fibre strength at lengths very close to the critical length. On the other hand, the *average maximum* fibre stress developed on the fibre or fibre fragments, can be calculated from the maximum fibre strain developed in the fibre fragments during the test. This value corresponds to the peak stress on the fragment **[Netravali 1989a]** and it has been considered to give a more reliable input for equation 5.10c, than the statistically derived value for the fibre strength.

The number of fibre fracture occurrences as a function of the matrix applied strain ε_m is plotted in figure 5.18, for the system 1 (HMU/MY-750). The average fragment length l_{av} was calculated as 2050 μm or 2.05 mm, for the HMU/MY-750 fibre/resin system. The application of the classical fragmentation analysis and the equation 5.10c to the HMU/MY-750 system data, gives the critical fragment length and the interfacial shear strength τ, - if we accept that designation for the τ parameter. The minimum and the maximum estimate of the interfacial shear strength for this system, are calculated to be 4 GPa and 6 GPa, respectively (Table 5.3).

(c) Interfacial shear stress (ISS) distribution in system 1 (HMU/MY-750).

In the case of the untreated fibre HMU/epoxy resin system, the fundamental assumption of the classical fragmentation analysis, that the load is transferred to the fibre by constant shear stress at the interface, is not that far from reality. The strain distribution profiles of figures 5.17a to 5.17c, have shown that frictional in nature forces acting on the fibre/resin interface, consist the main reinforcement mechanism for this type of system. However, a more accurate and point to point derivation of the shear stresses at the interface can be achieved via the analysis presented in § 5.4, which obeys strictly the "shear-lag" principles, without making any *a priori* assumption about the shear stress variability. The evaluation of the interfacial shear stress (ISS) along the fibre fragments, formed during the fragmentation process, can be conducted through equation 5.15 :

$$\tau(x) = E_f \cdot \frac{d_f}{4} \cdot \frac{d\left(\varepsilon_f(x)\right)}{dx} \qquad (5.15)$$

where, to recall, $\tau(x)$ is the ISS distribution along the fragment length, E_f is the fibre modulus, d_f is the fibre diameter and $\varepsilon_f(x)$ is the fibre strain distribution along the fibre fragment. As discussed and explained in § 5.4, the interpolation function chosen to describe the strain data along the fragment transfer length, was a 5th degree polynomial. This type of interpolation was employed even in cases of nearly linear strain profiles, to guarantee an overall consistent treatment of all experimental data. The correlation coefficient for all regressions was over 0.98.

Once the ε_f function has been defined for every fragment strain profile, it can be input to equation 5.15 to yield the interfacial shear stress (ISS) distribution $\tau(x)$ along the whole fragment length. Figure 5.19 demonstrates the ISS distribution on a fibre fragment at (a) 1.0%, (b) 2.0% and (c) 3.0% applied strain. The ISS varies between 4.0 and 7.0 MPa, while it exhibits a maximum, in all profiles, at about 800 μm from the fragment end. This analysis has been carried out for all fragments that have been displayed in the figures 5.17a to 5.17c. The results for all the profiles are presented in Table 5.4.

A graphical representation of the maximum ISS data as a function of the matrix applied strain is given in figure 5.20. The term "maximum ISS" denotes the maximum in the value of the interfacial shear stress developed on each fragment transfer length (two per fragment). The maxima from all fragments are averaged at each level of applied strain to produce the average (mean) maximum ISS at this level of strain. The experimental scatter in the average maximum ISS is indicated by the standard deviations (+/−) of the mean.

The average maximum ISS over all the analysed profiles was calculated to be about 4.3 MPa at 1.0% applied strain and reached the value of 5.6 MPa ± 1.6 MPa at 2.0% applied strain. At higher applied strains, the reduction in the load transfer capability of the system, as this is indicated by the drop in the maximum fragment strain and the increased data scatter of figure 5.19c, is reflected by the significant decrease of the average maximum ISS to just below 4.0 MPa. The maximum ISS value that an individual profile ever achieved was 9.6 MPa.

The interfacial shear strength (IFSS) of the fibre/resin system can be approximated by the peak value the average maximum ISS ever attained throughout the experiment. In the case of the HMU/MY-750 system it was found to be 5.6 ± 1.6 MPa.

5.5.2. *System 2 : HMS / MY-750.*

The Raman spectrum for the surface treated carbon fibre HMS/MY-750 system, in the region of interest, is hardly different from that of system 1 (fig.5.15). As expected, the HMS carbon fibre Raman peak shifts to lower frequencies with applied strain, at a rate of -11.4 ± 0.4 cm^{-1} per % applied strain, while the epoxy band remains stationary, as explained previously.

(a) Strain mapping in system 2 (HMS/MY-750).

Interfacial Raman studies were conducted on two specimens of system 2, to check the consistency and the repeatability of the collected data. Recognising the significance of the strain rate and the possible effect different loading rates can have upon the interfacial properties of the fibre/resin system, one test was carried out at a strain increment of 0.2% up to 2.0% and step of 1.0% beyond that level, while the second test was incremented at every 1.0% applied strain all the way through the end of the experiment. The total fragmentation gauge length FGL was in both tests 30 mm.

Strain mapping prior to fibre fracture.

In order to ensure that the embedded fibre was not subjected to residual thermal strains due to the specimen preparation and the resin curing process, the strain along the whole FGL was monitored by the laser Raman probe, prior to the tensile testing of the specimen. Residual tensile strains of about 0.15% and 0.05% were measured in the fibre of the first and the second specimen, respectively, despite the fact that the axial residual stresses in post-cured specimens are supposed to be compressive **[Chamis 1974, Nairn 1985]**. Hence, the initial offset tensile strain in the fibre should be in effect even higher than 0.15%, if compressive thermal strains were taken into account. This tensile offset fibre strain seems to be a permanent feature of all specimens tested for the current investigation and is apparently due to the handling of the single fibre

during the specimen preparation. In the attempt to align the fibre along the dogbone specimen axis, small extensional load of that order can easily be imposed.

In both specimens, the fibre strain was monitored at discrete matrix applied strain intervals until the first fracture occurred at an applied strain of 0.8%. For example, during the testing of the second specimen, the fibre strain was found to increase linearly with applied strain, preserving the 0.05% initial strain as offset to the nominal external applied strain. The strain distribution along the fibre FGL up to 0.8% applied strain is presented as a function of the position along the FGL, in figure 5.21a and as a function of the applied strain, in figure 5.21b. The linear increase of fibre strain with the matrix applied strain (fig. 5.21b), parallel to the expected 1:1 ratio shows the efficiency of the matrix-to-fibre load transfer mechanism, prior to the first fibre fracture.

Strain mapping after first fibre fracture.

The development of the fibre fragmentation process in the first specimen is described below. At applied strain of ε_m=0.8% the first fibre fracture occurred at about 16.7 mm along the FGL (fig.5.22a). The fibre break is clearly indicated by the dramatic drop of the fibre strain to zero values at the locus of fracture. The maximum fibre strain is about 0.95% strain, preserving consistently the initial offset of 0.15% (first specimen).

At the next level of applied strain, ε_m=0.9%, the fibre fragmentation process has started to accelerate. Three more fibre fractures have developed within the RGL, which is lying between 12.00 mm and 19.00 mm of the FGL scale (fig.5.22b). Already, the middle fragment is shorter than twice the critical transfer length L_t, which is the required fragment length to allow full development of load, in the current system. The longer fragments on either sides of the middle fragment are susceptible to further increase of strain.

In fact, at the next level of applied strain, ε_m=1.0%, they have broken into 3 smaller fragments (fig.5.22c). It is interesting to observe at this point, that the "newly" formed fibre breaks, are accompanied by extended areas of "strain-free" regions, on both sides of the fracture, possibly associated with debonding.

The strain distribution along the fibre fragments of the RGL at applied strain of ε_m=1.2% is shown in figure 5.22d. Further fractures have occurred on the two long fragments of the previous strain level. It is interesting to note here, that the fracture of the fragment lying between 12.7 mm and 14.8 mm (fig.5.22d) was capture while scanning this length with the laser Raman probe. The moment of fracture the fragment had attained a strain of 1.4%. This fibre strain corresponds to a fracture stress of about 5.5 GPa, which gives a very good estimate of the fibre strength at the critical fragment length L_c level. From this point onwards up to the end of the test the maximum fibre strain did never exceed the value of 1.25% (5.22e to 5.22g).

In figure 5.22e the fibre strain distribution is presented for the whole RGL, at applied strain of ε_m=1.4%. It seems that the fragmentation process has been completed, as none of the fragments could reach to strains higher than 1.25%. of applied strain. As mentioned earlier, the ten fibre fragments in the RGL have been given code names (F1, F2, ... , F10) for quick reference. As soon as no more fibre fractures occurred in the RGL the maximum fibre strain in all ten fragments peaked up again. This is demonstrated in figure 5.22f, where the applied strain has stepped up to 1.6%. By scanning the whole FGL with the optical microscope, it was found that no more fibre breaks had occurred (fig.5.23) and, therefore, the fragmentation procedure had reached saturation over the whole specimen gauge length FGL. A schematic representation of the fibre fracture propagation up to 1.6% applied strain is displayed in figure 5.24.

As the applied strain was increased to 1.8% (fig.5.22g), a new, distinct and impressive type of failure was unfolded as is clearly seen in fragments F6 and F10 of the RGL. This interfacial type of failure is revealed by the drop of the maximum fibre strain combined with the appearance of asymmetric "shouldering" in the strain profile of those two fragments (F6, F10). This effect is not detectable by the optical microscope.

Further increase of load beyond 1.8% applied strain has caused only relaxation of the maximum fragment strains, as demonstrated in figures 5.22h and i, for 4%, and 5% applied strain, respectively. At this level, the Raman mapping of the RGL has been restricted to only three representative fragments F1, F2 and F8. They have been selected because they correspond to the longest (F2=0.98 mm), the shortest (F8=0.47 mm) and the closest to the average fragment length (F1=0.65 mm), fragments of the

RGL. It should be, finally, noted, that the average gap between the fragments in the RGL for the HMS/MY-750 system, started at about 10-20 μm at low applied strains and never exceeded 40 μm at high applied strains, exhibiting a distinctly slower propagation rate compared with the untreated fibre system.

One last observation concerning the optical patterns evident along the fibre fragments, should be pointed out; alternating bright and dark "patches" along the fragments were observed with the reflection microscope, at all levels of strain. However, they were present, only along the transfer length L_t of the fibre fragments, i.e. along the strain take-up regions of the fragment length. A schematic presentation of the above observation is shown in figure 5.25.

(b) Conventional fragmentation studies on system 2.

The number of fibre breaks as a function of applied strain for the low strain rate test (first specimen) described above, was found to compare very well with the high strain rate test (second specimen), as shown in figure 5.23. Therefore, as far as the classical fragmentation studies are concerned, there is no apparent effect to the fibre fracture process, whether a fragmentation test is completed within one or four days (required for a detailed Raman mapping). The histogram of figure 5.26 shows the distribution of fragment lengths for the HMS/MY-750 system, for an FGL of 30 mm. The results from both tests are presented in individual and cumulative manner. The average fragment length, l_{av}, was found to be 640 μm. Therefore, the interfacial shear strength (IFSS) values obtained by employing the classical FT analysis (eq.5.10c) on the HMS/MY-750 system are 18.5 MPa and 21 MPa for the minimum and the maximum estimate, respectively (Table 5.5).

(c) Interfacial shear stress (ISS) distribution in system 2 (HMS/MY-750).

The fibre strain profiles of figures 5.22a to 5.22i have been converted to ISS distributions following the balance of forces model (§ 5.3). A fifth degree polynomial, $\varepsilon_f(x)$, has been fitted to the strain data obtained from the fibre break up to the maximum fibre strain. The

derivative of the fibre strain along the fragment length, d $[\varepsilon_f(x)]$ /dx, was then definable and the interfacial shear stress $\tau(x)$ was derived by employing equation 5.15. To demonstrate this procedure, the regression polynomial $\varepsilon_f(x)$ and the ISS distribution $\tau(x)$ for the representative fragment F1 are plotted on the same graph (fig.5.27).

The experimental fibre strain build up from the left-hand side of fragment F1 at 0.9% applied strain, the fitted 5th degree interpolation to the data points and the derived ISS distribution along the fragment, are clearly shown in figure 5.27a. The fibre strain is plotted against the left y-axis (units: %) and the interfacial shear stress is plotted against the right y-axis (units: MPa), while the x-axis indicates the distance from the left-hand side fragment end (units: mm). With respect to the fibre strain, it is obvious that even in early, "low" strain fractures, there is some debonding present in a region of about 20 μm length from the fibre end. The sequential nearly zero strain values at a distance of 20 μm from the tip of the break, yield zero fibre strain gradient, dε/dx, which in turn, produces a zero shear stress at the fibre end. Beyond this region, the following strain take up is accompanied by a fast increase of the ISS, which reaches to a maximum of ~32 MPa at 120 μm away from the fibre tip. As the fibre strain approaches its maximum value for this level of applied strain, the ISS decays smoothly from the maximum of 32 MPa, to zero values at the middle of the fragment.

At ε_m=1.0% (fig.5.27b), the overall profile remains unchanged and so does the ISS distribution; however the maximum ISS increases now to 36 MPa. This indicates that the fibre/resin interface can accommodate even higher shear stresses and the initial debonding at the fibre end did not undermine the load transfer capability of the well-bonded fragment length.

At ε_m=1.2%, where the long fragment broke during scanning, the strain distribution and the ISS distribution of the same profile are shown in figure 5.27c. It seems that the debonding at the fibre tip has started to propagate along the fragment length, without, however, withholding the maximum ISS from a further rise to 41 MPa. The increase of the debonded region has also shifted the position of the maximum ISS about 20 μm further into the middle of the fragment. The "new" fibre fracture occurred at a distance of about 650 μm from the initial break, forming the final length of fragment F1.

At ε_m=1.4%, the fibre strain profiles and the ISS distribution of the

entire fragment F1, are shown in figure 5.27d. The "new" fibre fracture seems to have affected the maximum ISS value at the side of the "old" fibre fracture, which slightly dropped from 41 MPa to ~38 MPa. The maximum interfacial shear stress in the neighbourhood of the new break is considerably lower (31 MPa). The negative sign for the ISS on the right hand side of fragment F1 (fig.5.27d), is simply a result of the negative gradient of the fragment strain, as it drops from the maximum value in the middle of the fragment to zero values at the right-hand side fragment end. The three distinct regions denoted by the letters A, B and C correspond to the debonded, the ISS take-up and the well-bonded sections of the fragment length. The subscripts L and R simply refer to the left and right-hand side of the fragment, close to the "old" and the "new" break, respectively. Two observations can be made at this stage; (a) the debonded length (A_R) initiated from the "new", high applied strain (1.2%) break is much longer than the debonded length (A_L) observed at the side of the "old", low applied strain (0.9%) break; (b) the maximum ISS on the newly formed profile (right-hand side) is 7 MPa lower than the maximum value on the old (left-hand side) profile.

As the applied strain increases to 1.6% (fig.5.27e) and to 1.8% (fig.5.27f), it brings about only marginal increase in the maximum ISS. Its value on the left-hand side profile rises back to 41 MPa at 1.6% applied strain and to 42 MPa at 1.8% applied strain. On the other hand, the more recently formed profile, exhibits maximum ISS values of 33 MPa and 34 MPa at 1.6% and 1.8% applied strain, respectively, and always lags behind the left-hand side values.

The profiles of fragment F1 at 4.0% and 5.0% applied strain are, finally, shown in figures 5.27g and 5.27h, respectively. The maximum ISS on both sides and at both strain levels, has dropped dramatically to ~20 MPa and seems to be unaffected by any further applied strain increase beyond that level. The debonded length on the left side, A_L, has increased over 100 μm and has caught up with debonded length on the right-hand side, A_R. The interfacial shear stress in the region of the debonded length is fluctuating between 0 and 8 MPa and could easily be represented by a constant value of about 5 MPa. In the meanwhile, the ISS take up-region is still prominent, although it cannot drive the ISS to values significantly higher than 20 MPa.

The maximum ISS on both profiles of fragment F1 (fig.5.27a to h) is plotted as a function of applied strain, in figure 5.28. It can be seen

that the maximum ISS on the left-hand side profile (neigbouring to the "old", i.e. low strain fibre break) increases until the high strain fibre fracture affects the whole region. Soon after the new fibre break, both maxima of the ISS, on the left and the right-hand side of fragment F1, possess lower values than the one just before the new fracture. As no further fracture occurs in the region, the maximum ISS on both sides recovers successfully, but only temporarily. At higher applied strains (a) the interfacial degradation and debonding next to the fibre breaks propagates further and (b) the fibre strain in the middle of the fibre fragment relaxes, both resulting in a reduction of the ISS values.

The arithmetic values for the maximum ISS for fragment F1, as well as, for all fragments in the RGL, at all levels of strain, are displayed in Table 5.6. The average value of the maximum ISS over all fragments in the RGL is plotted as a function of the applied strain ε_m, in figure 5.29. The average maximum ISS in the HMS/MY-750 system just after the first fibre fracture in the model composite, is found to be about 32 MPa.

The average maximum ISS increases with applied strain and reaches an upper limit of 36 ± 7 MPa at about 1.6% applied strain. This value provides a good estimate of the interfacial shear strength (IFSS) of the HMS/MY-750 system. The large error bars at each level of applied strain are not only due to calculational errors (incorporated in strain reading errors, goodness of fit of the 5th degree polynomial, modulus and diameter measurements errors) but are also due to the sudden drop of the maximum ISS values in the vicinity of high strain energy fibre breaks. The above statement is strongly supported by the example of the maximum ISS as a function of applied strain for the F1 fragment, clearly demonstrated in figure 5.28. It is, therefore, appropriate to call the "error" bars of figure 5.29, real experimental scatter, instead. Beyond 1.8% applied strain the maximum ISS shows a significant reduction and forms a plateau at about 20 MPa.

5.5.3. *System 3 : IMD / MY-750.*

The study of the intermediate modulus fibre/resin interface using the Laser Raman technique had been the most difficult of all three systems, as the Raman spectrum of this fibre, and, in particular, the monitoring G-D' frequency band, is 3 times weaker in intensity and 3 times broader in bandwidth than the G-line of the HMS fibre (Chapter 2). In addition, this frequency band (G-D') is shifted about 15 cm^{-1} closer to the resin band at 1605 cm^{-1} and is less strain sensitive, with a RFGF of only -7.0 $cm^{-1}/\%$. Therefore, successful monitoring of this band requires efficient spatial filtering which, in turn, results in much longer data acquisition time. The spectrum of an IMD fibre embedded in MY-750 epoxy resin is shown in figure 5.30. Although the carbon fibre Raman signal is hardly distinguishable, it was still possible to resolve it, since the resin frequency band is well characterised, in terms of its position and bandwidth and shows no strain dependence. The quantified details of the Raman spectrum for the IMD/MY-750 system are summarised in Table 5.7.

(a) Strain mapping in system 3 (IMD/MY-750).

As a consequence of the weak carbon fibre signal in the Raman spectrum of system 3 and the spatial filtering required to reduce the resin contribution, the exposure time for a reasonable spectrum was at least 90 seconds. As a result, the scanning of a large RGL, at a small strain increment, for a wide range of strains from 0% to 4.0% , could take considerable time to complete and relaxation parameters would, therefore, have to be considered. To avoid this additional complication three individual experiments on three different samples of this system were performed. Experiment 1 covered an RGL of 2 mm from the first fibre fracture at 1.2% applied strain and then at 1.3%, 1.5%, 1.6% and 1.8% applied strain. Experiment 2 covered an RGL of 2 mm from the first fibre failure at 1.0% and then at a step of 0.5% up to 4.0% applied strain. Finally, experiment 3 covered an RGL of 1 mm from 1.2%, when the first fibre fracture was observed and then in steps of 0.2% until 2.5% applied strain.

Strain mapping prior to fibre fracture.

In all 3 experiments, Raman spectra were obtained from 20 different points along the 20 mm FGL, to assess the efficiency of load transfer, prior to first fibre fracture. As in the study of system 2, an initial preloading of the single filament in the order of 0.1% fibre strain was observed, due to the fibre handling during the sample preparation. Taking into account this value of prestretching as a strain offset, the fibre followed the matrix applied strain in a one to one ratio all the way up to the first filament break, in a similar fashion to that of system 2, as presented earlier in figures 5.21a,b.

Strain mapping after first fibre fracture.

To avoid repetition the strain distribution along the fibre fragments of the RGL is demonstrated for only three levels of applied strain (1%, 2% and 3%), for the experiment 2, in figures 5.31a to c. The scale in the x-axis denotes the micrometer reading along the FGL, while the y-axis shows the calculated fibre strain.

The only fragment present at 1.0% exhibits very sharp strain take up profiles on both sides, as shown in figure 5.31a. The transfer length required, i.e. the length from the end of the fragment in which the fibre strain reaches its maximum, was measured to be less than 200 μm. At 2.0% applied strain the initial fragment has fractured into 5 smaller fragments, as can be seen in figure 5.31b. At this level of applied strain, the fragmentation has reached the saturation level within both the RGL and the FGL. Beyond 2.0% applied strain, failure along the well-bonded region of the fibre started to initiate (fig.5.31c) with parallel increase of the debonded length next to the fibre tips. Further increase of the applied strain resulted in relaxation of the fibre strains The gap between the fragments throughout the experiment did not exceed 20 μm.

Similar optical patterns to those obtained by the reflection microscope from the HMS fragments, were also present in the IMD/MY-750 system. Alternating bright and faint regions were spread along the transfer length of all fragments. A uniform "darker" field covered the whole middle part of all fragments longer than two transfer lengths ($2L_t$). The schematic representation of figure 5.25, modelling the illumination patterns of the HMS fragments, is also valid in the case of the IMD fibre.

(b) Conventional fragmentation studies on system 3.

The accumulation of data from three complete fragmentation tests on this system, has produced a large number of fibre fragments. To check the repeatability of the results in each of the experiments carried out, figure 5.32 shows the number of fibre breaks present in the FGL (20 mm for each specimen) as a function of applied strain for each one of the three experiments. The average fragment length l_{av} was calculated to be about 370 μm. In the histogram of figure 5.33, produced from all three experiments on the IMD/MY-750 system, the mode of the fragment length distribution at the end of the fragmentation process, is very close to the arithmetic average calculated, proving that this distribution can be considered as "normal" when a sufficient number of fragments are accumulated.

The interfacial shear strength of the system, can be then calculated according to the classical fragmentation analysis through equation 5.10c. A minimum and a maximum estimate for the interfacial shear strength of system 3 (28 MPa and 44 MPa, respectively) have been calculated according to established methodologies **[Netravali 1989b, Favre 1990]** (Table 5.8).

(c) Interfacial shear stress (ISS) distribution in system 3 (IMD/MY-750).

The development of a fragment profile, representative of experiment 3 (system 3), was chosen to demonstrate the application of the balance of forces model for the derivation of the ISS (§ 5.4) at three levels of applied strain. The increased data scatter in all the strain profiles (fig.5.34a to c), compared with the similar profiles for the HMS/MY-750 system in figures 5.27a to h, is due to the following two reasons:

(a) the reduced accuracy in the Raman frequency reading obtained from the IMD/MY-750 system. This has its origin at both the high standard error in the RFGF value of the fibre (RFGF=-7 ± 0.6 $cm^{-1}/\%$, Chapter 3) and the errors involved in the discrimination of the carbon fibre from the strong resin signal (fig.5.30);

(b) the fact that the transfer length L_t for the specific system is less than 200 μm, whereas for the HMS/MY-750 was well over 300 μm (fig.5.27). Therefore, as the translation step is fixed to 10 μm (dictated

by the precision of the translation micrometer), the resolution of the L_t mapping was 1.5 times lower than that of the HMS system.

At applied strain ε_m of 1.4%, the strain and interfacial shear stress (ISS) distributions along the transfer length of the selected profile are plotted against the distance from fibre fracture (fig.5.34a). The ISS reaches a maximum at about 50 μm from the fibre break and decays to zero towards the middle of the fragment.

At 1.8% applied strain (fig.5.34b), the maximum ISS peaks at 66 MPa, while the debonded region next to the fibre tip is now more pronounced. From that point onwards the interfacial shear stresses start to relax.

The dramatic change of the fibre strain profile at 2.2% applied strain (fig.5.34c) is accompanied by: (a) an impressive expansion of the debonded region A adjacent to the fibre tip, (b) a replacement of the elastic stress transfer by an almost frictional mechanism of reinforcement at this region, (c) a shift of the ISS take-up region B towards the middle of the fragment and (d) a dramatic reduction of the maximum ISS down to 35 MPa. It is worth mentioned here, that the length of the selected fragment is about 600 μm (only half is shown in figures 5.34a to c), which is longer than the average fragment length for this system. The whole pattern of behaviour, is a remainder of the degradation of the strain profiles F6 and F10 of the HMS/MY-750 system at 1.8% applied strain, presented in figure 5.22g.

In figure 5.35 the maximum ISS values for the selected IMD/MY-750 profile are plotted as a function of the applied strain. As can be seen, the maximum ISS reaches approximately 65 MPa at 1.8% applied strain (see also fig.5.34b) and then decreases to 30 MPa at ε_m=2.5% applied strain. On the same figure, the distance D from the fibre tip, at which the maximum ISS appears, is also plotted on the right-hand y-axis as a function of the applied strain.

As with the system 2, the calculated maximum ISS values for all fragments of all 3 tests for the IMD/MY-750 system and at all levels of applied strain, are displayed in Table 5.9. From these data, a universal plot of the average maximum ISS versus applied strain can be compiled (fig.5.36). At each level of applied strain the maximum ISS data from individual profiles have been averaged, while the standard deviation of all available values gives an indication of the experimental scatter. As mentioned earlier, this experimental scatter is not only due to

uncertainties of the strain measurement, but also to real variations in the strength of the fibre/resin system, indicated by the strain history of each fibre fragment (i.e. at what level of applied strain it was formed and how close to other preexisting failures it occurred).

The upper limit of the average maximum ISS for the IMD/MY-750 system, as calculated over 10 fragment profiles and 3 different experiments, is 66 MPa ±15 MPa. This value is considered as a good approximation of the interfacial shear strength (IFSS) of the IMD/MY-750 system.

5.6. The fibre fracture characteristics in model composites.

In the preceding paragraphs, the fragmentation process of a single carbon fibre embedded in a resin matrix was thoroughly investigated, for three selected carbon fibre systems. Both the strain distribution along the fibre fragments and the interfacial shear stress (ISS) distribution constitute the basis for an "interfacial fracture mechanics" type of analysis. As introduced in § 5.5.2, (fig.5.27d) three distinct regions can be observed on every fibre fragment.

The region adjacent to the fibre break, denoted as "debonded length" A, is defined as the region of the fibre along which either the fibre strain, $\varepsilon_f(x)$, is zero, or, the derivative of fibre strain with distance, $d\varepsilon_f(x)/dx$, is almost constant. These two conditions imply that, either there is a detachment of the fibre from the resin binder, due to interfacial crack propagation, or, the mechanism of reinforcement is exclusively frictional. In both cases, the elastic stress transfer, as defined by all theoretical models (§ 5.1.2), has been interrupted.

The region designated as "ISS take-up length" B, (fig.5.27d), is located along the fragment length, from the end of the debonded length A to the point where the ISS reaches a maximum. In mathematical terms, throughout region B, the absolute value of the second derivative of the fibre strain with distance, $d^2\varepsilon_f(x)/dx^2$, or, the absolute value of the first derivative of the ISS, $d\tau(x)/dx$, is positive. The physical interpretation of the latter is that, in region B, the ISS should be constantly rising to reach its maximum value. Areas where the ISS rises temporarily to reach local maxima and drops again are excluded (fig.5.27d). The merging of regions A and B constitutes the well defined length D, which is the distance from the fibre end to the point where the maximum ISS develops (D=A+B).

Finally, the well-bonded length C (fig.5.27d), corresponds to the section of the fragment where the ISS decays from its maximum to a zero value in the middle of the fragment. It should be clarified, at this point, that since the fibre length, on which equation 5.15 is applied to derive the ISS distribution, is the transfer length L_t, on each side of the fragment, the total debonded length A is the sum of the debonded length A_L on the left-hand side of the fragment and the debonded length A_R on the right-hand side of the fragment ($A=A_L+A_R$). Similarly, $B=B_L+B_R$ and $C=C_L+C_R$.

The development of these three characteristic lengths A,B and C throughout the whole fragmentation test has been dealt with for all three systems of our investigation.

5.6.1. *The characteristic lengths A,B and C on system 1.*

For the HMU/MY-750 system (figs. 5.17a to c and 5.19a to c) the almost linear increase of strain along the fibre fragment requires a constant shear forces field. It is not, therefore, a coincidence that both the classical fragmentation test analysis and the model of § 5.4, yield almost identical estimates for the Interfacial Shear Strength (IFSS), which is literally constant at about 6.0 MPa along the fragment. The characteristic lengths A, B and C for this system can be defined only by taking the analysis of § 5.6 to the limits of its applicability. Since on system 1 the fibre appears to be poorly bonded to the matrix, the strain energy release during fibre fracture is dissipated by the compliant interface. Therefore, the resulting frictional load transfer requires that the whole fragment length should be considered as virtually "debonded length" A, while the ISS take-up length B and the well-bonded length C are eliminated.

5.6.2. *The characteristic lengths A,B and C on system 2.*

During the demonstrative study of the ISS distribution on fragment F1 (figs 5.27a to h) of the HMS/MY-750 system (§ 5.5.2c), the characteristic lengths A, B and C were first introduced, in parallel to the evaluation of the ISS profiles at various levels of applied strain. The debonded length A_L (adjacent to the left-hand side fibre break), initiated by the fibre fracture at low applied strain (ε_m=0.9%), propagates only by 20 μm at this level of strain (fig. 5.37a); it subsequently elongates to ~70 μm at 1.8% applied strain, when the maximum ISS reaches its upper limit for this specific profile (fig.5.28). Beyond that level of strain it exhibits an upwards trend, attaining 150 μm at the end of the experiment. On the other hand, the debonded length A_R, initiated by a high applied strain fibre fracture (ε_m=1.4%), is much longer (150 μm, fig.5.37a), close to its plateau value. The total debonded length $A=A_L+A_R$ along fragment F1 reached 300 μm at the end of the test.

The ISS take-up length B_L and B_R for either sides of fragment F1 ranges between 100 μm and 150 μm throughout the whole test (fig.5.37b). The ISS take-up length B_L, corresponding to the low strain fibre failure on the left, starts at about 110 μm at 1.0% applied strain and seems to increase gradually to about 140 μm at 2.0% applied strain. It is noticeable that the ISS take-up length B_R, affiliated to the high strain fibre failure, is slightly but consistently higher than the corresponding B_L length, at the side of the low strain fibre fracture (fig.5.37b).

Finally, the well-bonded length C for fragment F1 decays in an exponential fashion, from 220 μm at ε_m=1.4%, just after the fragment is formed, to about 100 μm at the end of the experiment (fig.5.37c).

The average total characteristic lengths A, B and C have been derived over all the fibre strain profiles of system 2. The average total debonded length A_{av}, calculated over all the fragments scanned by the Laser Raman probe, is plotted as a function of applied strain in figure 5.38. It can be seen that the debonded length increases rapidly, as long as the fragmentation process continues. The increase of the debonded length is due as much to the debonding propagation in the already existing fibre strain profiles, as it is due to the significantly higher values of the "newly" formed regions A, propagating next to high strain fibre breaks.

On the contrary, the total ISS take-up length B_{av}, averaged over all tested profiles, increases slightly from about 220 μm at the start of the fragmentation to just below 300 μm, at the point of saturation of the fragmentation process (fig.5.39). There is no further rise beyond that applied strain. The reasonable assumption that the ISS take-up length is equally distributed on both sides of each fragment (fig.5.37b), leads to the conclusion that even when there is no debonding near the fibre end (A=0), the maximum ISS on the fibre profile next to the fibre break, will appear at a distance of $B_{av}/2$ =110 μm from the fibre tip, or, in other words, at 16 fibre diameters, at 1.0% applied strain. The maximum value this length ($B_{av}/2$) has reached is ~140 μm, or ~20 fibre diameters, at 1.6% applied strain and beyond.

The region which is dramatically affected during the fragmentation process is the total well-bonded length C_{av} (fig.5.40). Before the first fracture the well-bonded length can be assumed to cover the whole observation gauge length. It is drastically reduced to about 200 μm at the point of saturation and, beyond that level, it gradually drops to 100 μm in

a complementary fashion to the increase of the debonded length A_{av} (fig.5.38). It can be, therefore, stated that the debonded length A propagates at the expense of the well-bonded length C, leaving unaffected the transitional region between them, which has been denoted as the ISS take-up length B.

When fibre fracture occurs, a significant amount of the fibre strain energy is released due to elastic fibre recoiling, schematically shown in figure 5.41. The recoiling forces that develop introduce shear forces at the fibre/resin interface. In the case of a compliant and poorly bonded system, the rapid strain energy release is dissipated along the whole fragment length, breaking the weak fibre/resin bonds. On the completion of the recoiling movements there are still contact regions between fibre and resin. Thus, frictional forces can be activated at the interface, provided that normal stresses are present in the region. Normal stresses at the fibre/resin interface have been calculated in various theoretical **[McCartney 1988, Piggott 1978]** and FE models **[Carrara 1968]** and are attributed to Poisson contraction effects and thermal coefficient mismatches.

In well-bonded fibre/resin systems, the abrupt recoiling movement of the two fibre ends on each side of the fibre break leads to debonding at the locality of the fibre tips. The higher the fracture strain, the longer the debonded length along the fragment (fig.5.37a). However, as the interfacial strength IFSS of system 2 is much higher than the IFSS of System 1, as the developed maximum ISS values indicate (figs 5.20 and 5.29), the debonding is sustained within a portion of the whole fragment length. It is quite possible that the fierce recoiling forces are not fully withheld by the catastrophic debonding at the fibre tip, but they can still reach well bonded regions of the interface. If they exceed the local strength at the interface of these well bonded regions, they can eventually cause local yielding. Hence, these recoiling forces are considered as the origin of the shape of the ISS distribution on the fragment after the fibre fracture (and the development of the region B). On the other hand, the magnitude of the maximum ISS calculated from the fibre strain distribution lags behind the interfacial strength of the system due to the stress relaxation on the fibre fragment after fracture.

5.6.3. *The characteristic lengths A,B and C on system 3.*

The characteristic lengths A,B and C have also been calculated for the IMD/MY-750 system. The average value has been produced at each level of applied strain over the total number of profiles present in the RGL. All 3 tests on this system have been fully considered.

The total debonded length A_{av} for system 3 is plotted as a function of applied strain in figure 5.42. This characteristic length (A_R+A_L) is impressively constant, below 40 μm, up to the completion of the fragmentation process for the IMD/MY-750 system (fig.5.32). This behaviour is in contrast to the debonding propagation in system 2 (fig.5.38). Presumably, the higher strain fibre fractures cannot produce recoiling forces capable to tear the fibre/resin interface for one or more of the following reasons: (a) the strain energy release at the fibre fracture occurring at a certain level of applied strain, is lower for lower modulus fibres, since the strain energy stored in a fibre is proportional to the fibre Young's modulus and, therefore, the recoiling forces are considerably weaker; (b) the fibre/resin interface is tougher, i.e. the higher interfacial shear strength of this system restricts the debonding propagation at very low levels.

The onset of dramatic debonding propagation after 2.0% applied strain (saturation point for the fragmentation of system 3), shown in figure 5.42, coincides with the diminishing of the maximum ISS, shown in figure 5.36. Therefore, a distinct mode of interfacial failure is observed at this point. It is activated just after the maximum ISS has attained its upper limit and very close to the distance from the fibre end where this maximum ISS has been achieved; experimental evidence of such a behaviour is given by the fibre strain profile of figures 5.34b and c, where the collapse of the load transfer capability occurs just as the maximum ISS reaches 65 MPa. This type of failure has also been observed on the HMS/MY-750 system; fragments F6 and F10 of system 2, shown in figures 5.22f and g, exhibit identical behaviour to the one demonstrated in figures 5.34b and c, for the system 3. The high interfacial shear stresses calculated for system 3 (66 ± 15 MPa), signify that the interfacial type of failure they initiate has not its locus on the resin, which should have yielded at shear stresses of about 38 MPa (Von Mises estimate of the MY-750/ HY-951 resin/hardener system yield stress, § 5.2.2), but at the interphase, the properties of which are strongly dependent on both constituents (fibre and resin).

Attempts to model the fibre resin interphase as third phase layer between the fibre and the matrix **[Agarwal 1979, Broutman 1974]**, led to the conclusion that interphase with higher modulus than the matrix strengthen the fibre/resin adhesion, allowing higher interfacial stresses to develop and eventually higher composite strength to be achieved.

The average total ISS take-up length B_{av} does not seem to be significantly affected by the applied strain (fig.5.43). Nevertheless, within the region from 1.0% to 2.0%, it shows a tendency to rise from about 80 μm to 120 μm. Assuming that this length is fairly equally distributed on both sides of the fibre fragments, it extends over $B_{av}/2$ = 50 μm (10 IMD fibre diameters) along the half fragment length at 1.0% applied strain, and stabilises at about 60 μm (12 IMD fibre diameters) over 2.0% applied strain.

The study of the characteristic lengths of system 3 is completed with the total well-bonded length C_{av}, which decays in a similar fashion as in system 2, but stabilises at a higher level of about 130 μm (fig.5.44). It is again interesting to note that the debonded length and the well-bonded length exhibit a behaviour that complement each other, as a careful inspection of figures 5.42 and 5.44 can reveal.

The identification of the failure mechanisms at the fibre/matrix interface requires a comprehensive explanation of the initiation, the nature and the evolution of the characteristic lengths described in this section. While the debonded length A_{av} and the well-bonded length C_{av} have been more or less treated in accordance to the above requirements, the region B_{av} denoted as ISS take-up length, is not as yet fully understood.

5.7. The interfacial shear stresses and the strength of well bonded carbon fibre/epoxy resin systems.

The analytical models of load transfer (§ 5.1.2) predict the maximisation of the interfacial shear stress at the tip of the fibre end, according to the classical shear-lag approach **[Cox 1952, Dow 1963, etc]**, or very close to the fibre end, according to more recent approaches that required a stress-free fibre end surface **[Whitney 1987, McCartney 1988]**. The application of these models to the two surface treated carbon fibre/epoxy resin systems of our investigation, e.g. the HMS/MY-750 and the IMD/MY-750, results in to maximum theoretical ISS estimates, summarised in Table 5.10, for 1.0% applied strain.

The experimentally obtained maximum ISS at 1.0% applied strain (§ 5.5) for both HMS/MY-750 and IMD/MY-750 systems, as well as the distance from the fibre end over which this value was achieved, are summarised in Table 5.11. The distance from the fibre break the maximum ISS develops consists of the characteristic lengths A and B, on the one side of the fibre strain profile (half of the averaged values A_{av} and B_{av} which refer to the whole fragment length, - see figure 5.27d). Since all theoretical models assume good bonding throughout the fibre/matrix interface, the debonded length A can be disregarded from the experimental findings, to make comparison with theory easier. Therefore, the theoretically predicted ISS at distance B from the fibre end can be calculated (Table 5.12).

Comparing the maximum ISS data predicted by the analytical models to those experimentally derived, two pronounced discrepancies can be immediately detected. The first concerns the distance from the fibre end at which the ISS reaches its maximum value, on every single fragment profile. This distance is associated with the characteristic length B and coincides with that when the debonded length tends to zero. As mentioned before, this distance increases slightly with applied strain, from about 16 fibre diameters (at first fibre fracture) to about 20 fibre diameters (at the end of the fragmentation process) for the HMS/MY-750 system and from about 10 fibre diameters to 12 fibre diameters for the IMD/MY-750 system (§§ 5.6.2 and 5.6.3). The second discrepancy concerns the relative maximum ISS between the two fibre systems themselves. While all analytical models predict higher ISS values for the higher modulus fibre system, at the same applied strain (τ is directly proportional to the fibre modulus E_f, or at

least to the $\sqrt{E_f}$), the inverse relationship has been found experimentally (Table 5.11).

5.7.1. *The effects of interfacial yielding to the ISS.*

To explain these discrepancies we should consider the effects of extremely high shear stresses which according to all theoretical models (Table 5.10) develop in the vicinity of the fibre end. Let $\tau(x)$ to be the function that describes the theoretical ISS distribution on a given fibre profile (fig.5.45) and let IFSS to be the interfacial shear strength of that fibre/resin system, constant at any point along the fibre.

At low applied strain ε_1 the IFSS line does not intersect the $\tau_1(x)$ function and, therefore, the maximum ISS on the fragment develops at (or very close to) the fibre tip and is evaluated by the function τ_1 (fig.5.45). This has been experimentally proven by Raman interfacial studies of short Kevlar fibres embedded in epoxy resin **[Jahankhani 1991 a&b]**.

The problem becomes more complicated when the applied strain ε_2 introduces an ISS distribution $\tau_2(x)$ that intersects with the IFSS of the system (fig.5.45). This region of the fibre interface, between the fibre tip x=0 and the intersection point x=b, is subjected to extremely high shear stresses, that exceed the interfacial strength IFSS of the system. This is the region where yielding of the interfacial material is expected to occur.

It is widely accepted that the fibre/resin interphase/interface is a very difficult region to characterise (§ 5.1.1). Its mechanical properties have been assumed to be strongly influenced from both the fibre and the matrix. Since the yielding process in polymers is not manifested by a sharp transition from the elastic to plastic behaviour (see stress-strain curve for the MY-750 resin, in figure 5.11), but by a gradual "softening" of the material, the yielding process at the interphase can be also considered as such.

Following this perspective, the region between the fibre tip x=0 and the intersection point x=b, is a region of gradually softened interface and the degree of modulus softening is proportional to difference of the shear stresses and the IFSS of the system ($\tau_2(x)$-IFSS). At the fibre tip, where this difference is maximised, the load transfer capability of the interface

has been mostly degraded. The load transfer efficiency has been recovered at x=b (fig.5.45). However, in the case where the fibre end has been formed as a result of fibre fracture, the strain energy release accompanying this fracture, can cause a temporary and recoverable stress relaxation on the remaining fragments.

This "gradual interfacial yielding" approach can be identified in the behaviour of the characteristic length B, the ISS take-up length. The fact that it exists even at 1.0% of applied strain, in both systems 2 and 3, indicates that, this region of gradual yielding should have been formed the moment the fibre fractures, through the fibre recoiling forces (§ 5.6). This interpretation explains why the ISS take-up length B is the least affected by the increase in the applied strain, for all three characteristic lengths (figs. 4.38 to 4.40, for the HMS/MY-750 system and figs. 4.42 to 4.44 for the IMD/MY-750 system).

Beyond the applied strain level at which the maximum ISS attained it upper limit, the length B remains unaffected (figs 5.39 for the HMS/MY-750 system and 5.43 for the IMD/MY-750 system). However, the fast propagation of the debonded length A "forces" the ISS take-up length B to shift towards the fragment center, at the expense of the well-bonded length C. The reduction of the maximum ISS values, after they had reached the IFSS limit of both systems 2 and 3 (figs. 5.29 and 5.36), is most probably due to plastic yielding of the whole matrix material (and not only at the interface), since over 2.5% applied strain the modulus of the bulk resin is significantly reduced (stress-strain curve for MY-750, fig.5.11).

Having identified the characteristic length B (the ISS take-up length) as the region where extremely high shear stresses have induced local gradual yielding of the interface, it can be, eventually, understood why the measured maximum ISS for the high modulus fibre (system 2) lags behind the maximum ISS for the lower modulus fibre (system 3). The numerical examples displayed in Table 5.12 show the theoretically predicted ISS value that develops at distance B from the fibre tip, on both systems, 2 and 3. The calculations have assumed applied strain ε_m=1.0%, and ratio R/r=5. The required values for the mechanical properties of the systems 2 and 3 have been obtained from Table 5.1 and the values for the characteristic length B, at 1.0% applied strain, of each system are the experimentally derived ones. A schematic description of the finding of Table 5.12 is given in figure 5.46. While the maximum ISS for the HMS/MY-750 system is always higher than the one for the IMD/MY-750 for the same value of x, this

reverses, when the ISS is measured at different distances B for each system.

The experimentally calculated maximum ISS at 1.0% applied strain (Table 5.11) is in an excellent agreement with two theoretical models, developed by Chamis **[Chamis 1974]** and by Whitney **[Whitney 1987]**. The analytical formula employed for the second, was the modified Netravali **[Netravali 1989a]** equation (eq.5.6), which has the advantage to give the distance from the fibre end normalised over the fibre diameter **[Netravali 1989a]** and not over the unknown transfer length **[Whitney 1987]**. Two of the models predict max ISS values lower by a factor of 1.5, compared to the experimental results **[Cox 1952, Piggott 1977]** and finally, two more analyses yield ISS values far too low, but for different reasons; Dow's model **[Dow 1963]** predicts very low stresses at the fibre end, while McCartney's model **[McCartney 1988]** predicts extremely high shear stresses at the fibre tip (see Table 5.10), resulting in abrupt increase of the ISS within a few fibre diameters from the fibre end.

5.7.2. *The interfacial shear strength IFSS.*

The interfacial shear strength (IFSS) of the carbon fibre/epoxy system was defined as the peak value attained by the average maximum ISS. The experimental scatter in the individual maxima indicates that there is a distribution of IFSS for a given system, similar to the distribution in the tensile strength of individual fibres. The IFSS for each one of the three systems studied in our investigation can be traced from the plot of the maximum ISS as a function of applied strain. These plots have already been produced in figures 5.20, 5.29 and 5.36 for the systems S1, S2 and S3 respectively. The interfacial strength results are summarised in Table 5.13.

The IFSS of untreated fibre system, HMU/MY-750 is comparable with the conventional fragmentation test result (fig.5.47). The almost frictional type of load transfer in this system, shown in the strain mapping of the Raman gauge length (figs 5.17a to c), is in accordance with the assumption of the classical fragmentation test, that constant shear forces act at the interface **[Kelly 1966]**.

The surface treated fibre systems (S2,S3) exhibit a different behaviour. The shear stresses are not constant at the interface, even at applied strain much higher than the saturation level of the fragmentation process. There are still well bonded regions on a fibre fragment, as well as totally debonded sections and areas where a gradual yielding model of behaviour can apply. The underestimation of the IFSS of strong interface systems by the conventional fragmentation analysis (fig.5.47) is virtually due to the lack of information of the stress field around the fibre and the local failures the fracture process has initiated (§ 5.6).

Figure 5.48 shows how the maximum ISS attainable on a fragment, can be miscalculated by ignoring the stress field variation on the fibre and, therefore, the interface. The classical fragmentation test (FT) analysis takes into consideration the average fragment length and the fibre strength at gauge length equal to the fragment length. As the FT analysis is also been based on a balance of forces model to derive the shear stress at the interface (§ 5.1.3b, eq.5.10a), the derivative of the assumed fibre strain distribution, i.e. the slope along the strain profile (fig.5.48), reveals the source of the miscalculation of the maximum ISS on the fibre fragment.

In both systems 2 and 3, the fibres had been subjected to the same surface Standard treatment, as it has been quoted by the manufacturer (Courtaulds Grafil plc). In addition, since the same resin has been employed as the matrix material, it can be expected that the IFSS values of these systems are strongly dependent upon the carbon fibre surface structure **[Tuinstra 1970]**. The trend that lower modulus fibres exhibit better adhesion to resin has been experimentally verified in various FT studies **[Drzal 1883 a&b, Favre 1990]**. It is, therefore, absolutely necessary to understand the relation between the IFSS of a system and the fibre surface structure.

5.7.3. *The interfacial failure mechanisms.*

The strength of adhesive joints is determined by the mechanical properties of the materials making up the joint and by the local stresses in the joint **[Bikerman 1968]**. According to the weak boundary layers concept **[Sharpe 1972]**, "clean failure" in adhesion is highly uncommon. The failure is essentially always cohesive, in the adhesive or adherents or both.

Following this principle it has been concluded from photoelastic

measurements **[Bascom 1986]** that shear yielding of the matrix is the most possible reason for stress transfer limitations and not the fibre/resin interfacial strength. However, there were some reservations upon the universal validity of the above statement, since experimental evidence had shown that for high modulus, surface treated and untreated, carbon fibres (HM Hercules) and untreated low modulus fibres (AU Hercules) the locus of failure during the fragmentation test was within the highly graphitic layers of the skin of the carbon fibre **[Drzal 1983 a&b]**. The locus of failure was detected from fibre segments attached on the resin path, or the resin side of the debonded interface, after microtoming the tested specimens. In the case of surface treated low modulus fibre/resin systems, the locus of failure was assumed to be out of the fibre, since no trace of carbonaceous material could be found on the resin path of microtomed specimens. Critics of the last finding argued that in sectioning through a region in which the resin has been plastically deformed, it is at least possible that in the microtoming operation interfacial separation occurred due to relaxation of the highly stressed resin **[Bascom 1986]**.

As it has been extensively reported (§ 5.1), the fibre/resin interface binding the fibre, just next to the fibre end, is subjected to the most complex and fierce stress field than any other region along the fibre fragment. However, when this fibre end has been formed as a result of a fibre fracture, the extremely high recoiling forces that develop (§ 5.6, fig. 5.41) play an important role in debonding initiation rather than the load transfer mechanism. The only means through which these recoiling forces are transmitted from the fibre to the resin is again the interface or interphase. The locus of the debonding failure, either within the fibre boundary layers or within the matrix boundary layers, is the most susceptible region of the interface.

It was, therefore, attempted to explore the interfacial region next to the fibre fracture without destroying or sectioning the specimen, by utilising the Laser Raman probe. The gap between the two fragments after the fibre fracture occurs, as reported in paragraph 5.5, increases rapidly with applied strain for system 1, reaching 90 μm at 3.0% of applied strain, and moderately for system 2, attaining 40 μm at 3.0% applied strain. The diameter of the laser focal spot is only 2 μm, assuring that many spectra could be obtained from the gap region with out interaction of the neighbouring fragments. The path of this quick experiment on the HMS/MY-750 system is shown in the sketch of figure 5.49. The spectrum from position

(1), taken from the fibre within 10 μm from the fracture face, is a typical fibre/resin spectrum like that of figure 5.15. The spectrum from position (2), taken in the middle of the gap, exhibits an impressive graphitic G-line, although there was no fibre in view. This is a strong proof of existence of graphitic segments that can be found along the fracture path, in the HMS/MY-750 system. Confirmation of the above observation can be provided from the spectrum in position (3), taken out of the fibre fracture path within 10 μm in the resin. This is a pure resin spectrum, identical to the one corresponding to the resin material in figure 5.15. This effect indicates that the weakest region in the fibre/matrix interface is located within the boundary layers of the fibre surface.

With respect to the Raman spectrum of the gap in the IMD/MY-750 system, the results were not as revealing as with the high modulus fibre. The Raman spectrum from inside the gap looked very much alike to the resin spectrum out of the fracture path. It was therefore, assumed that no significant amount of fibre segments were removed from the fibre surface after the fibre fracture. In turn, the interfacial type of failure observed on this system, should have its locus on the resin side of the interface. However, since the Raman spectrum of the IMD carbon fibre is so weak in intensity, compared to the HMS fibre and the resin spectrum itself, a very small amount of scattering species probably still adhered on the resin fracture path in the gap, would give such a low intensity contribution, that would be overshadowed by the secondary Raman feature of the resin at ~1578 cm^{-1} (figs.5.15, 5.30).

Nevertheless, the surface morphology of the intermediate modulus carbon fibres, is the structural parameter that makes the fibre/resin interface tougher and less susceptible to shear. Even untreated IM fibre/resin systems exhibit much stronger interfacial behaviour than the equivalent untreated high modulus fibre system (system 1). Complementary conventional fragmentation tests on a IMA/MY-750 system (untreated carbon fibre of intermediate modulus), have yielded an average fragment length l_{av}=740 μm, which in turn, corresponds to a τ (IFSS) maximum estimate of ~18 MPa, according to the classical FT analysis. Radial anisotropy in these intermediate modulus fibres is hardly detected, as the Raman studies (Chapter 2) and other investigations have proven **[Chen 1983, Donnet 1984]**; in addition, surface treatment does not affect the spectral features of the IM fibres, in sharp contrast to the high modulus fibres (Chapter 2). It is, therefore, concluded in IM fibre/epoxy resin systems, the removal of fibre

surface layers is not the primary mechanism through which the surface treatment enhances the interfacial strength of the composite system. Oxidative surface treatment is thought to allow the deposition of chemical groups on the fibre surface, which interact with the polar epoxy matrix contributing to a higher fibre/matrix interfacial shear strength **[Drzal 1983 a&b].** ▮

Table 5.1. Material properties (Interfacial studies).

Property	HMU	HMS	IMD	MY-750
Young's Modulus [tensile; GPa]	390	390	305	2.6
Strain to failure [tensile; %]	0.9	0.9	1.8	~6.0
Tensile Strength [MPa]	3200	3200	5500	65
Thermal expansion coeff. [x10^{-6}/K]				60
longitudinal	(-1.4 to -0.5)		(-.5 to 1.0)	-
transverse	(5 to 12)		(5 to 12)	-
Diameter [μm]	~6.9	~6.9	~5.0	-

The mechanical properties and diameter of the fibres are quoted by the manufacturer (Courtaulds Grafil plc). The modulus is measured on a tow up to 0.4% applied strain. The thermal expansion coefficients have been obtained from literature sources **[Donnet 1984, Dresselhaus 1988, Hull 1981]**. The resin properties are quoted by the manufacturer.

Table 5.2. The Raman spectrum of the HMU/MY-750 system.

Material	Peak	Raman Frequency (cm^{-1})	HHBW (cm^{-1})	RFGF (cm^{-1}/%)
HMU fibre	E_{2g}(G)	1580	30	-11.7
	D'-line	1623	30	~-5.4
MY-750 epoxy	Main peak	1605	20	0
	leading edge	1578	≈6	0

HHBW : half-height-bandwidth;

RFGF : Raman Frequency Gauge Factor (Chapter 3).

Table 5.3. Classical Fragmentation test results for the HMU/MY-750 system.

IFSS (τ) estimate equation 5.19c	L_c /μm	L_c/d	τ/MPa
minimum estimate *	2730	~390	4.1
maximum estimate **	2050	~295	6.0

* for $L_c = (4/3)\, l_{av}$ $\sigma_f = (\sigma_f^{peak}) = 3.2$ GPa

** for $L_c = l_{av}$ $\sigma_f = \sigma_f^{max} = (\varepsilon_f^{max} E_f) = 3.5$ GPa

L_c is the critical fragment length,

l_{av} is the average experimental fragment length (end of the FT),

σ_f^{peak} is average maximum fibre strain over all fragments.

d is the fibre diameter, 7 μm for the HMU fibre,

σ_f^{max} is the maximum fibre stress during the experiment, calculated from the fibre modulus E_f=390 GPa and the the maximum fibre strain ε_f^{max} observed with the Raman probe during the Raman mapping of the RGL.

Table 5.4. The maximum ISS and the distance D it appears from the fibre end for the HMU/MY-750 system.

Fragment Profile		ε_m=1.0%		ε_m=2.0%		ε_m=3.0%	
		max ISS	D	max ISS	D	max ISS	D
F1	left	4.8	150	9.6	750	-	
	right	3.7	350	4.5	550		
F2	left	3.9	400	4.3	550	3.5	600
	right	3.5	400	4.2	500	3.3	600
F3	left	4.9	900	6.5	900	4.4	900
	right	4.9	700	5.3	950	4.3	950
F4	left	4.2	750	6.0	800	-	
	right	4.3	750	5.3	850		
F5	left	4.6	450	6.2	800	-	
	right	4.0	550	4.6	750		

F1, F2, ... ,F5, fragment code name, as in figure 5.17,

left, right refers to the relevant profile of each fragment,

max ISS, denotes the maximum ISS value in MPa,

D, denotes the distance from the fibre end that the max ISS appears, in mm, and, finally,

The measurement error is in the order of 4%. An additional 5% error may be due to diameter and fibre modulus variations influencing the result of equation 5.15.

Table 5.5. Classical Fragmentation test results for the HMS/MY-750 system.

IFSS (τ) estimate equation 5.19c	L_c /μm	L_c/d	τ/MPa
minimum estimate *	853	~122	18.5
maximum estimate **	640	~ 90	20.9

* for $L_c = (4/3)\, l_{av}$ $\quad \sigma_f = (\sigma_f^{peak}) = 3.7$ GPa

** for $L_c = l_{av}$ $\quad \sigma_f = \sigma_f^{max} = (\varepsilon_f^{max} E_f) = 5.5$ GPa

L_c is the critical fragment length at the end of test,

l_{av} is the average fragment length at the end of the FT,

σ_f^{peak} is the arithmetic average maximum axial stress over all fragments within the RGL, which has been used in past fragmentation studies to approximate the fibre strength **[Netravali 1989 b]**, and, finally,

σ_f^{max} is the maximum fibre stress ever attained at the moment of fibre fracture (F1 at ε_m=1.2%). This gives an excellent approximation of the fibre strength at the critical length level. The fibre modulus is E_f=390 GPa and the fibre diameter is d=7 μm.

Table 5.6. The maximum ISS results for the HMS/MY-750 system.

Fragment Profile		Matrix Applied Strain e_m (%)									
		0.8	0.9	1.0	1.2	1.4	1.6	1.8	3.0	4.0	5.0
F1	L		32	36	40	38	41	44	-	18	21
	R				-	32	33	35	-	17	18
F2	L				25	34	38	34	21	25	19
	R				24	32	39	35	28	27	19
F3	L				23	23	24	35	-	-	-
	R			37	21	24	32	33	-	-	-
F4	L			26	30	38	36	43	-	-	-
	R			36	35	36	44	48	-	-	-
F5	L			30	30	34	31	38	-	-	-
	R		33	33	39	44	43	46	-	-	-
F6	L		28	34	37	42	33	19	-	-	-
	R	33	31	36	44	47	48	32	-	-	-
F7	L	31	32	33	34	34	36	39	-	-	-
	R			39	35	40	34	46	-	-	-
F8	L			33	24	26	29	38	19	16	19
	R				31	26	34	33	29	22	18
F9	L				42	31	32	42	-	-	-
	R			32	25	31	31	36	-	-	-
F10	L			24	34	36	46	27	-	-	-
	R		31	30	40	43	44	21	-	-	-

F1, F2, ... , F10, are the fragment codes as defined in fig.5.22e. L,R indicate the left and the right side of the fragment. The calculated values for the max ISS are in MPa. The dash (-) implies that the fragment has not been scanned by the Raman probe and the unfilled space imply that the fragment had not yet been formed. The measurement error in the reported values is in the order of 4%. An additional 5% error is due to diameter and fibre modulus variations.

Table 5.7. The Raman spectrum of the IMD/MY-750 system.

Material	Peak	Raman Frequency (cm^{-1})	HHBW (cm^{-1})	RFGF ($cm^{-1}/\%$)
IMD fibre	(G+D') line	1595	90	~-7.0
MY-750 epoxy	Main peak	1605	20	0
	Leading edge	1578	≈6	0

HHBW : half-height-bandwidth;

RFGF : Raman Frequency Gauge Factor (Chapter 2).

Table 5.8. Classical Fragmentation test results for the IMD/MY-750 system.

IFSS (τ) estimate equation 5.19c	L_c /μm	L_c/d	τ/MPa
minimum estimate *	490	~98	28.0
maximum estimate **	370	~74	44.0

* for $L_c = (4/3)\, l_{av}$ $\quad \sigma_f = (\sigma_f^{peak}) = 5.5$ GPa

** for $L_c = l_{av}$ $\quad \sigma_f = \sigma_f^{max} = (\varepsilon_f^{max} E_f) = 6.5$ GPa

L_c is the critical fragment length at the end of test,

l_{av} is the average fragment length at the end of the FT,

σ_f^{peak} is the arithmetic average maximum axial stress over all fragments within the RGL, which has been used in past fragmentation studies to approximate the fibre strength **[Netravali 1989b]** and, finally,

σ_f^{max} is the maximum fibre stress ever ever achieved. It is, thus, considered as an excellent approximation of the fibre strength at the level of critical length. The fibre diameter d=5 μm and the fibre modulus E_f=305 GPa complete the key notation of the above table.

Table 5.9. The maximum ISS results from 3 tests for the IMD/MY-750 system.

Test No 1. Profile	Matrix Applied Strain ε_m (%)				
	1.2	1.3	1.5	1.6	1.8
A1	42	65	60	85	80
A2	36	46	46	43	67
A3		50	66	57	54
A4		67	56	64	58
A5			80	61	77
A6			47	70	48

Test No 2. Profile	Matrix Applied Strain ε_m (%)					
	1.0	1.5	2.0	2.5	3.0	4.0
B1		30	45	36	34	26
B2		32	52	48	45	35
B3	41	35	59	36	39	26
B4	40	48	58	42	43	41

Test No 3. Profile	Matrix Applied Strain ε_m (%)						
	1.2	1.4	1.6	1.8	2.0	2.2	2.5
C1	50	51	64	65	55	35	28
C2	56	60	77	57	58	76	60
C3			58	56	82	28	29
C4				49	56	63	70

The maximum ISS value for each fibre profile of all tests is given in MPa. The measurement error for each value is in the order of 8%. An additional 5% error is due to the diameter and fibre modulus variations.

Table 5.10. The theoretical maximum ISS for systems 2 and 3 at ε_m=1.0%.

Model	System	R/r=5	R/r=15	R/r=100
Cox-1952 eq. 5.1	HMS/MY-750	110	85	65
	IMD/MY-750	97	75	57
Dow-1960 eq. 5.2	HMS/MY-750	32	35	16
	IMD/MY-750	31	32	14
Chamis-1970 eq. 5.3	HMS/MY-750	88	49	18
	IMD/MY-750	78	43	15
Piggott-1977 eq. 5.4	HMS/MY-750	91	75	60
	IMD/MY-750	81	67	53
Netravali-1989 eq. 5.6	HMS/MY-750	72 /at 10r from fibre end		
	IMD/MY-750	64 /at 12r from fibre end		
McCartney-1988 eq. 5.7	HMS/MY-750	238 /1.3r	102 /3r	46 /12r
	IMD/MY-750	225 /1.3r	85 /3r	39 /12r

Ratio R/r=5 has been calculated to approximate well the cylinder of influence around the fibre resin interface **[Cherepanov 1979]**; the same value has been found to yield matching theoretical estimates to experimentally derived fibre strain profiles, in short Kevlar fibres **[Jahankhani 1989]**. On the other hand, the ratio R/r=15 has been selected to simulate the resin cylinder defined by the depth of the fibre position under the resin surface, during our experiments. Finally, the ratio R/r=100 was considered as a fairly reasonable representation of the fibre volume fraction in a single carbon fibre composite.

Table 5.11. The experimental maximum ISS for systems 2 and 3 at ε_m=1.0%.

Experiment (§ 5.5)	Max ISS (MPa) at e_m = 1.0%	Distance from the fibre end it appears (incl.debondind D=A+B, and excluding debonding D=B)	
		A+B	B
HMS/MY-750	32	150μm ≈ 42r	110μm ≈ 32r
IMD/MY-750	40	60μm ≈ 24r	50μm ≈ 20r

Table 5.12. The theoretical ISS at distance "B" from the fibre end.

Theoretical Model; R/r=5 ε_m = 1.0%	HMS; ε_m=1.0%		IMD; ε_m=1.0%	
	ISS at x=0	ISS at x=B=32r	ISS at x=0	ISS at x=B=20r
Cox; eq.5.1	110	18	97	27
Dow; eq.5.2	32	1	31	3
Chamis; eq.5.3	88	36	78	42
Piggott; eq.5.4	91	20	81	28
Netravali; eq.5.6	0*	25	0*	40
McCartney; eq.5.7	0*	1	0*	7

* according to these models the maximum ISS does not appear at the fibre tip, but a few diameters inside the fibre profile. The corresponding value and distance for the systems 2 and 3 are given in Table 5.10. The values for the characteristic length B, at 1.0% applied strain, for each system, are the experimentally derived ones.

Table 5.13. Interfacial shear strength of carbon fibre/epoxy resin systems

Fibre/resin System	IFSS /MPa	Applied Strain /% at which the IFSS was calculated
S1. HMU/MY-750	5.6 ± 1.6	~ 2.0%
S2. HMS/MY-750	36.0 ± 6.0	~ 1.6%
S3. IMD/MY-750	66.5 ± 15.0	~ 1.6%

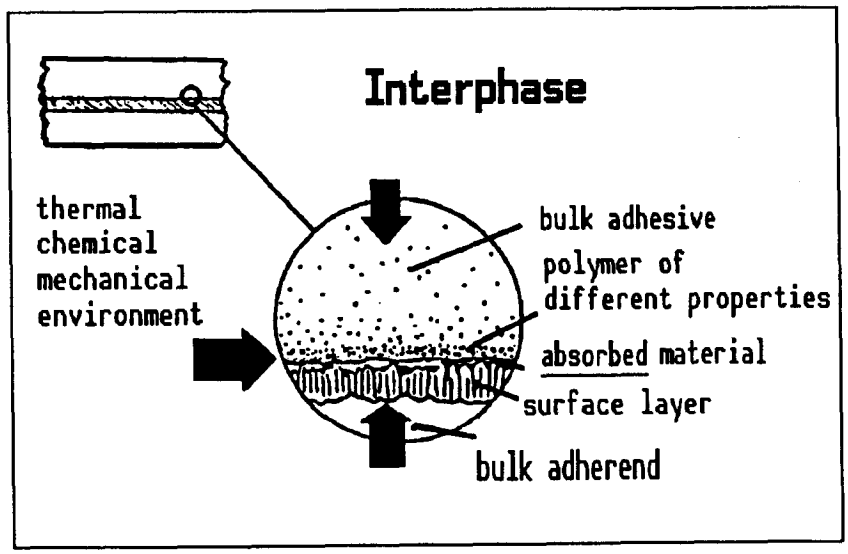

Fig.5.1 A schematic model of the fibre/matrix interface, proposed by Drzal **[Drzal 1983a]**.

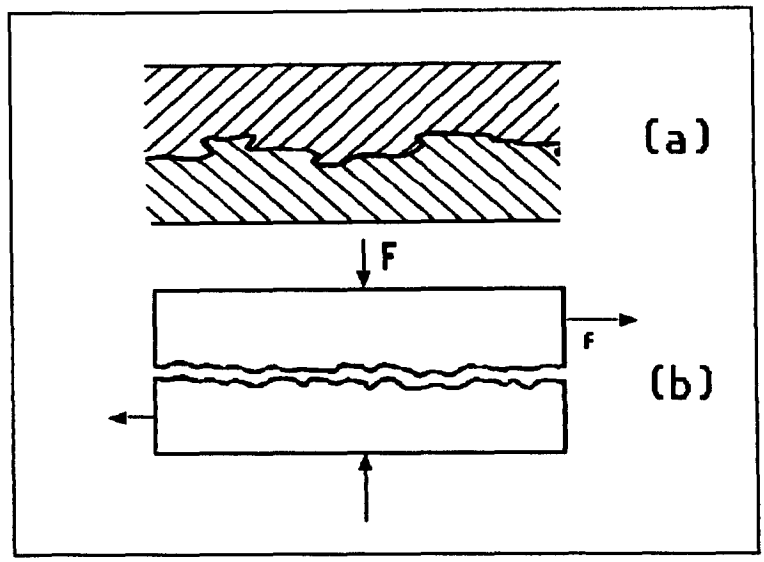

Fig.5.2 (a) Mechanical bond through interlocking of one component into the other **[Hull 1981]**, and

(b) through frictional resistance to the sliding of one surface over another **[DiBenedetto 1978]**.

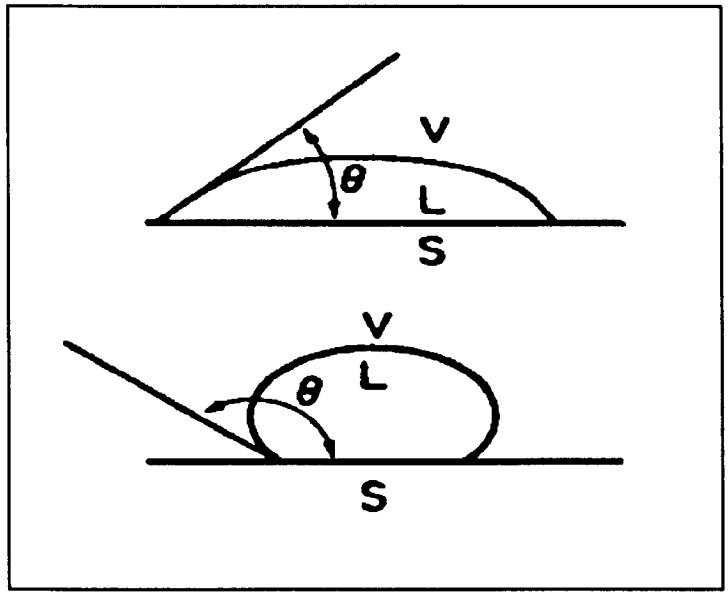

Fig.5.3 The thermodynamic wettability of a solid surface by a liquid phase can be evaluated by the contact angle θ. Small contact angle characterises good wetting **[DiBenedetto 1978]**.

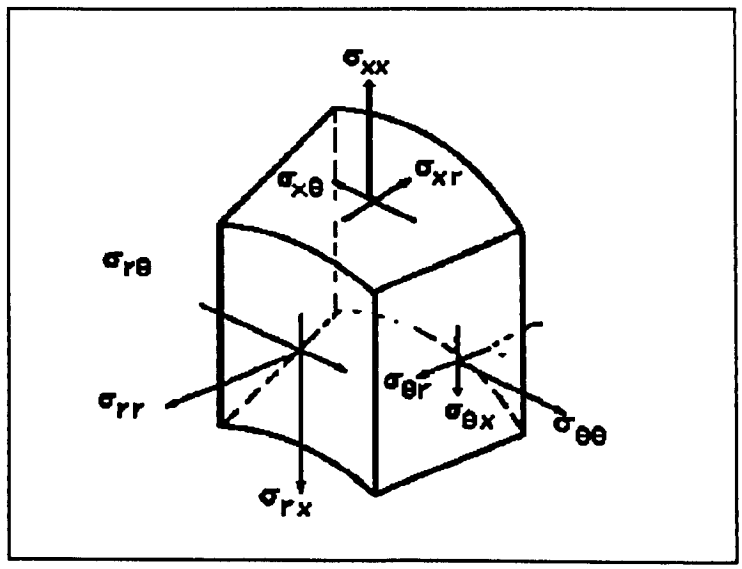

Fig.5.4 The stresses acting on an infinitesimally small element in a cylindrical coordinates system **[Chamis 1974]**.

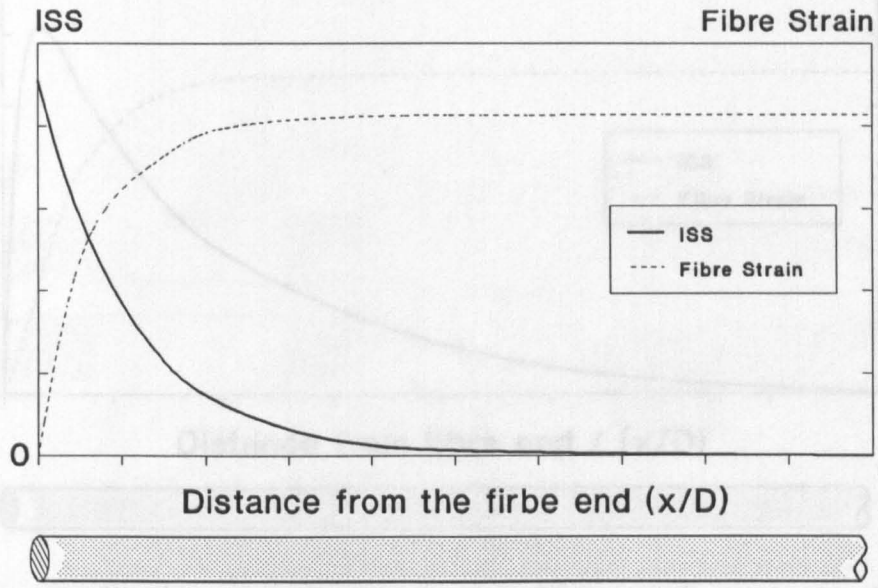

Fig.5.5 Qualitative presentation of the fibre strain and the interfacial shear stress (ISS) distributions on a fibre fragment, according to the elastic load transfer models **[Cox 1952, Dow 1963, etc]**.

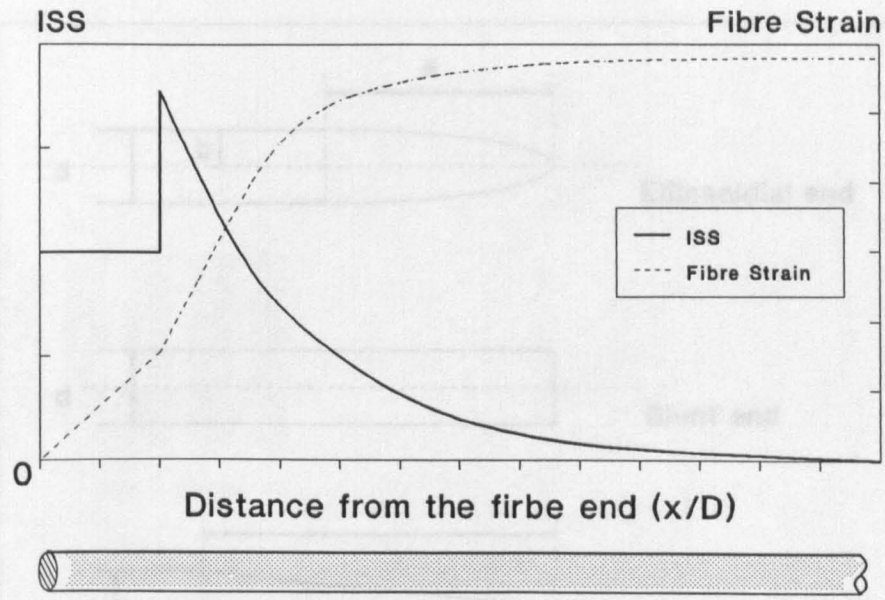

Fig.5.6 Qualitative presentation of the fibre strain and the interfacial shear stress (ISS) distributions on a fibre fragment, according to the frictional slip load transfer model **[Piggott 1980]**.

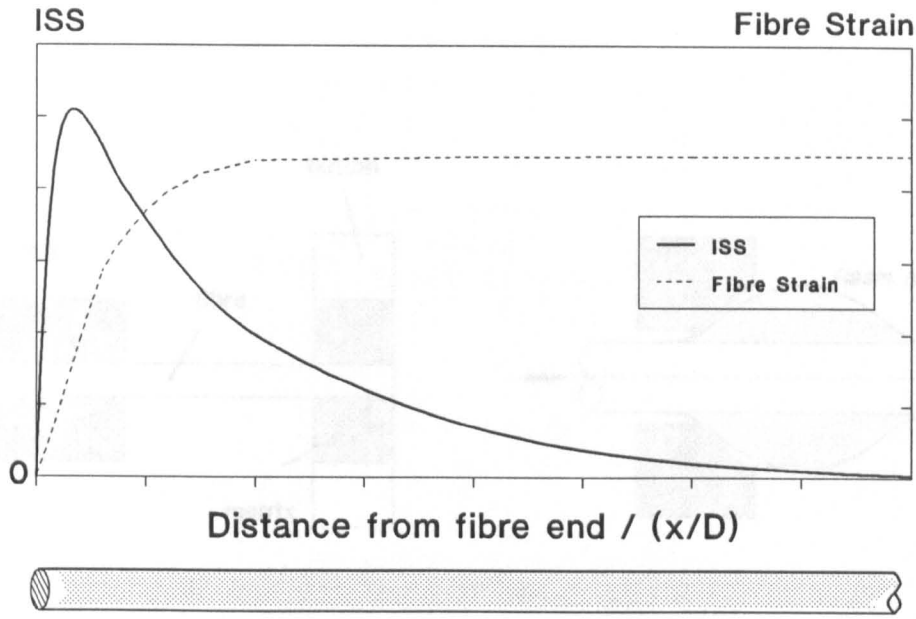

Fig.5.7 Qualitative presentation of the fibre strain and the interfacial shear stress (ISS) distributions on a fibre fragment, according to the elastic transfer models, requiring zero shear stresses at the fibre ends **[Whitney 1987, McCartney 1988, Netravali 1989a].**

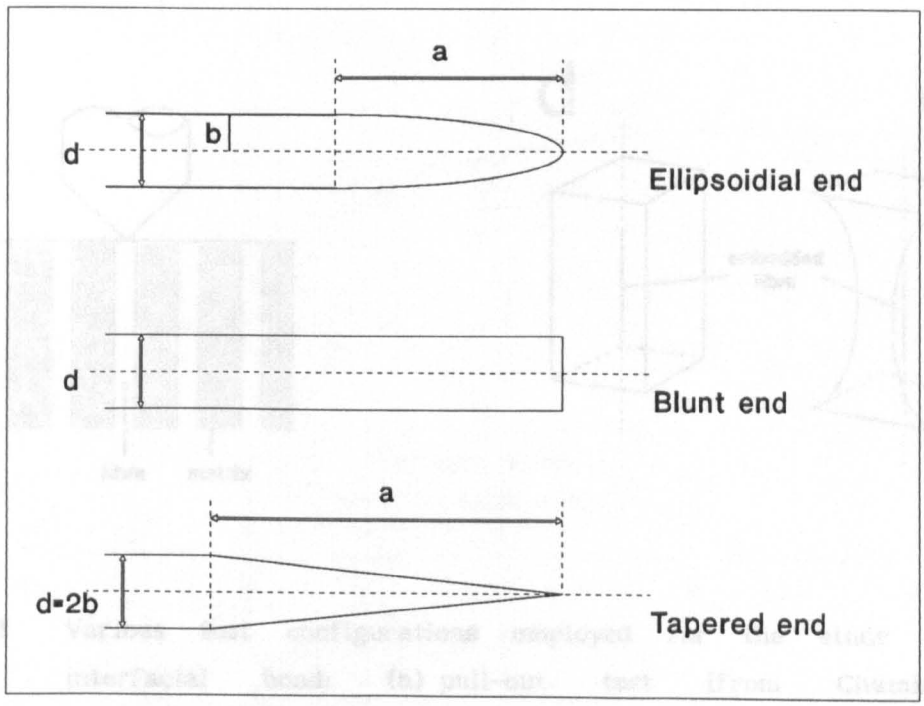

Fig.5.8 Fibre end geometries, employed in the Finite Element study of the interfacial shear stresses around a short fibre, by Carrara **[Carrara 1968].**

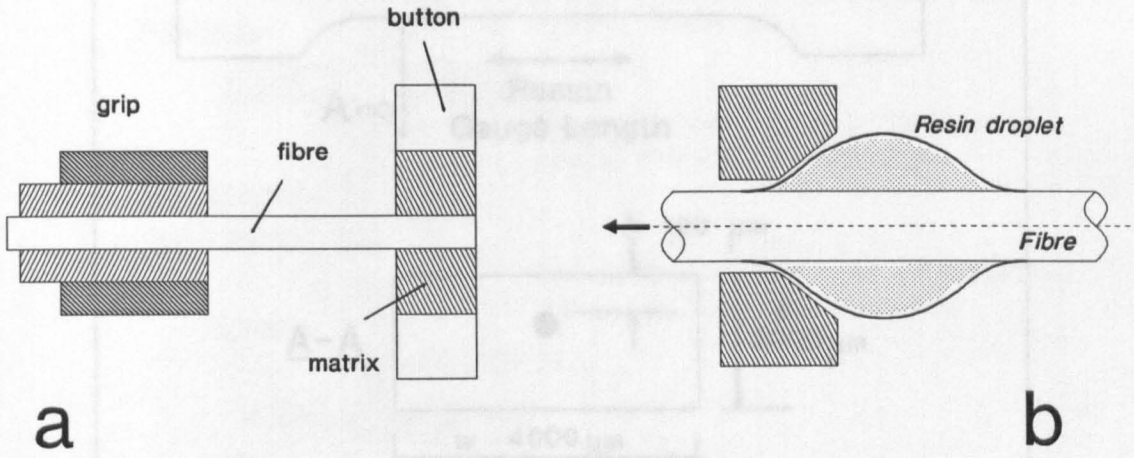

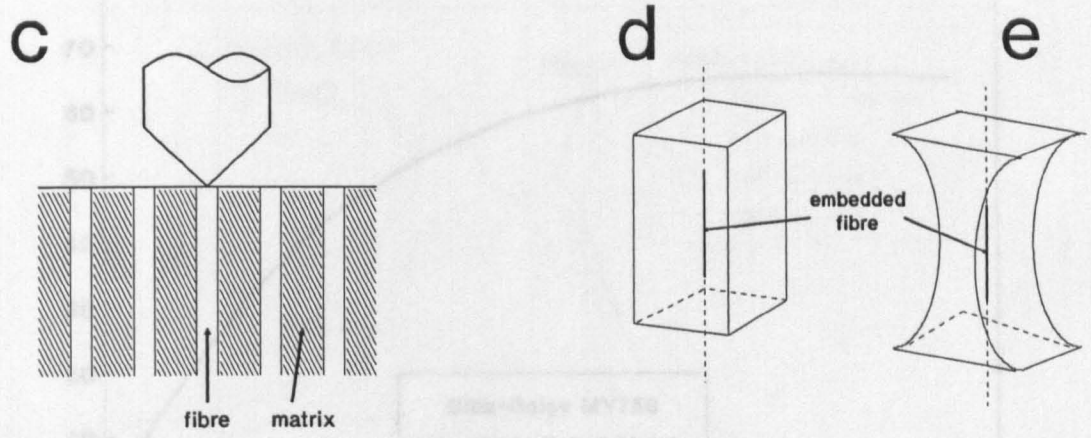

Fig.5.9 Various test configurations employed for the study of the interfacial bond: **(a)** pull-out test **[from Chamis 1974]**, **(b)** droplet test **[Miller 1987]**, **(c)** microindentation test **[Tse 1985]**, **(d)** shear debond test and **(e)** tensile debond test **[Broutman 1970]**.

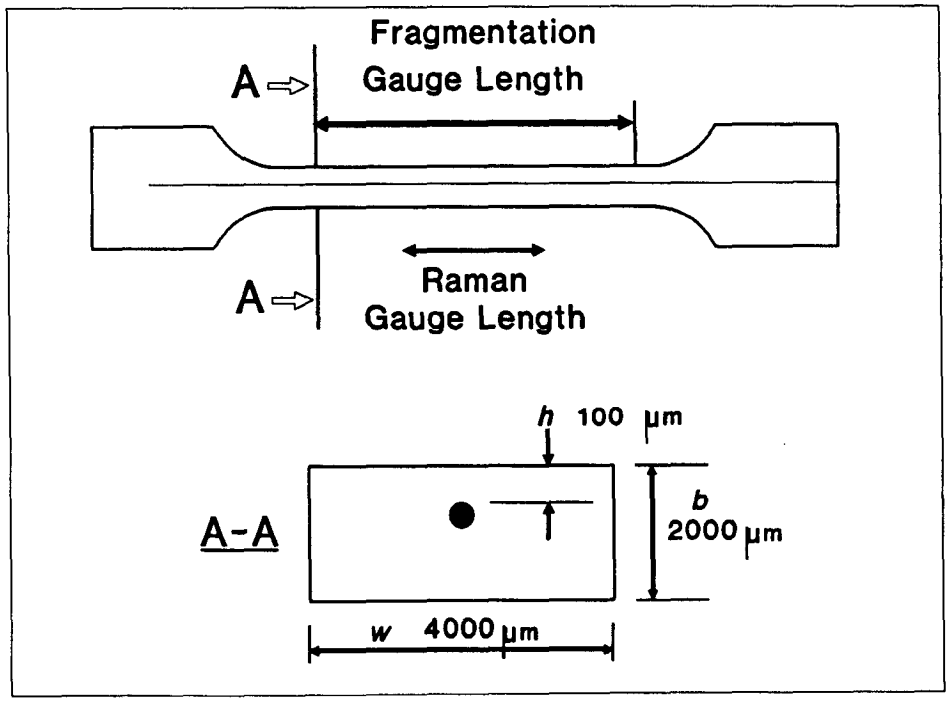

Fig.5.10 The "fragmentation test" specimen geometry.

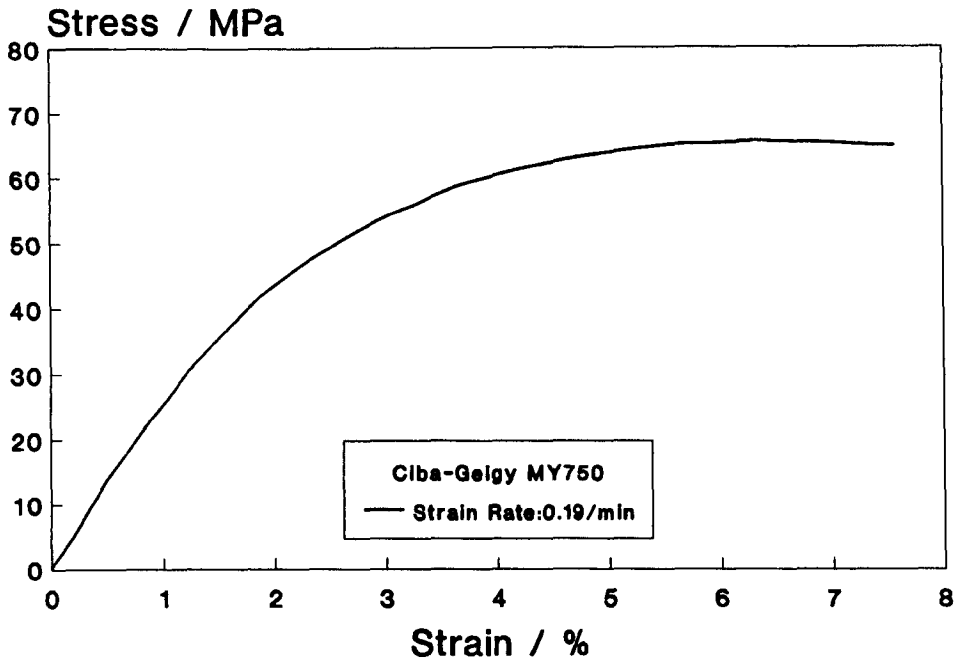

Fig.5.11 Stress-strain curve for the MY-750 epoxy resin.

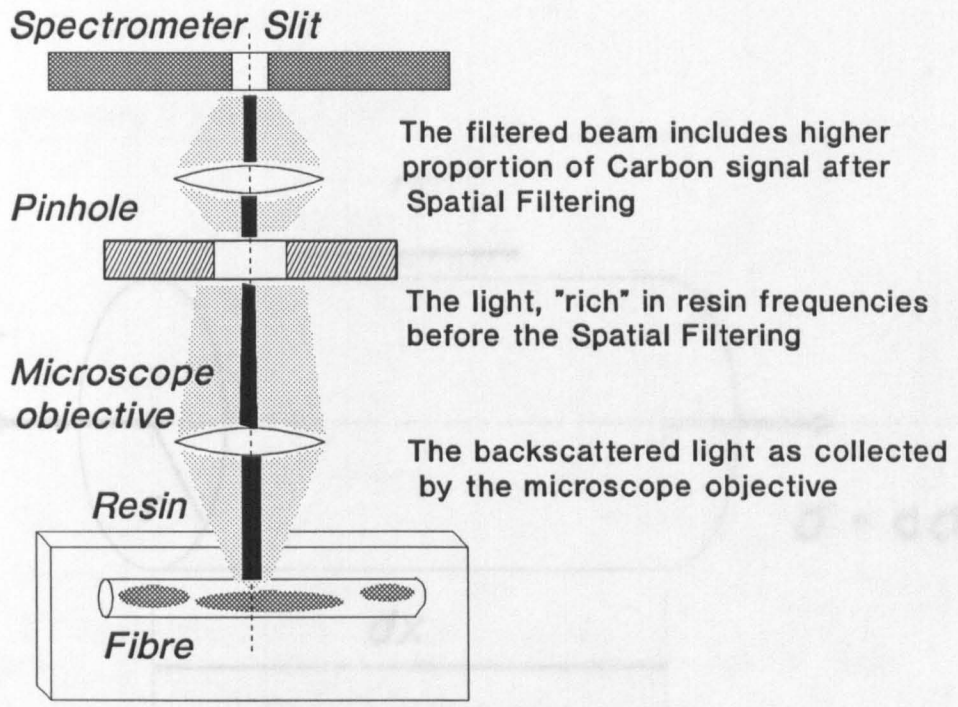

Fig.5.12 Schematic illustration of the "spatial filtering" process of the backscattered laser light.

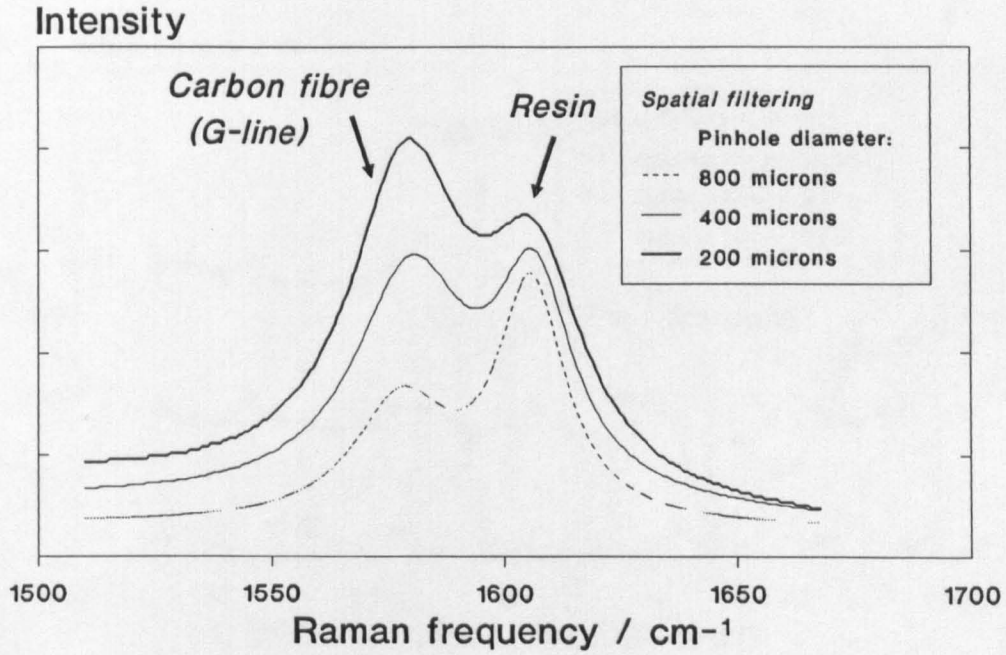

Fig.5.13 The effect of "spatial filtering" on the Raman signal of an HMS carbon fibre embedded in MY-750 epoxy resin.

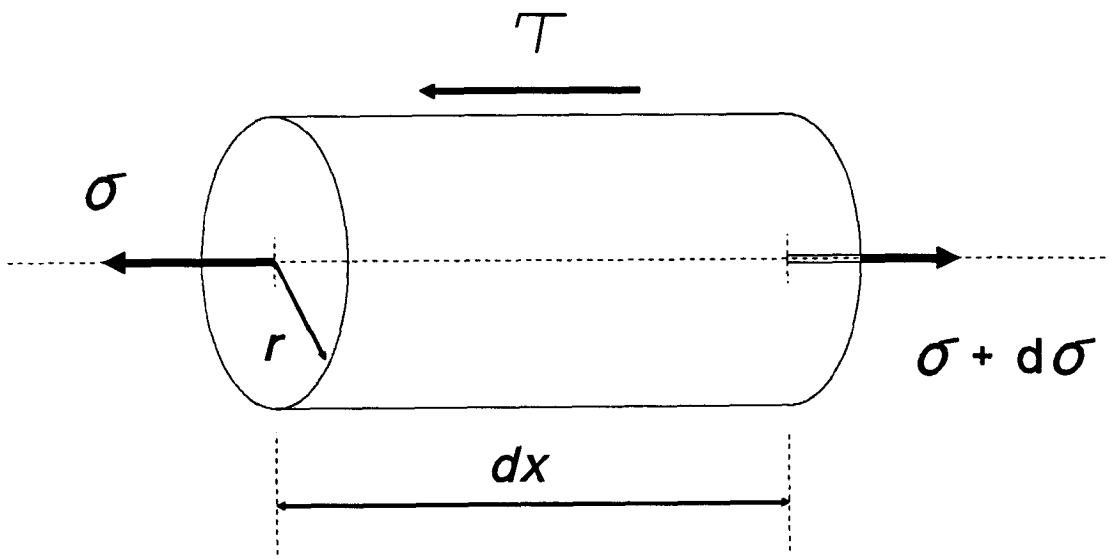

Fig.5.14 Simplified stress field on an infinitesimally small fibre element embedded in a matrix (balance of forces model).

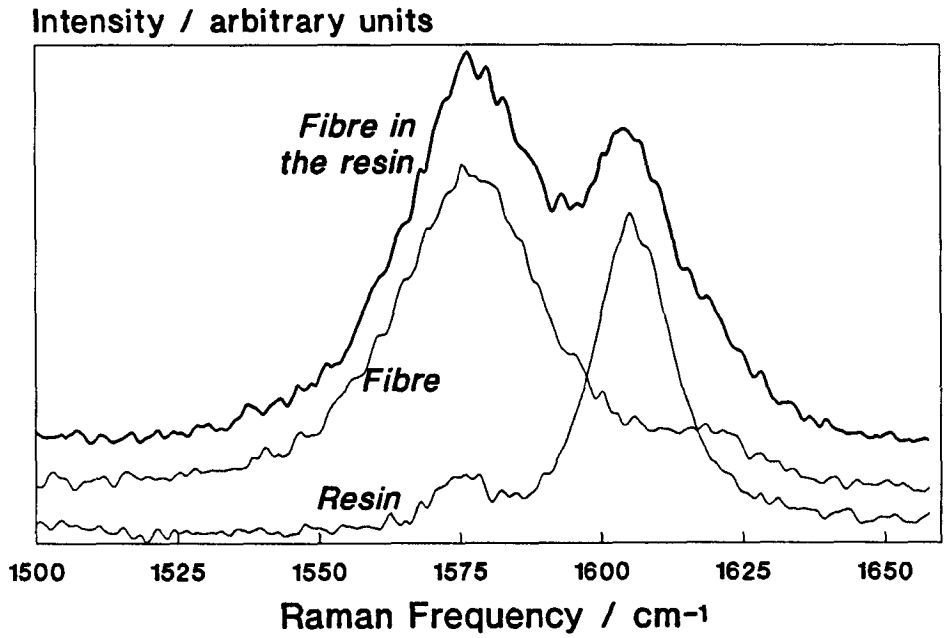

Fig.5.15 The Raman spectrum of the HMU fibre in MY-750 resin.

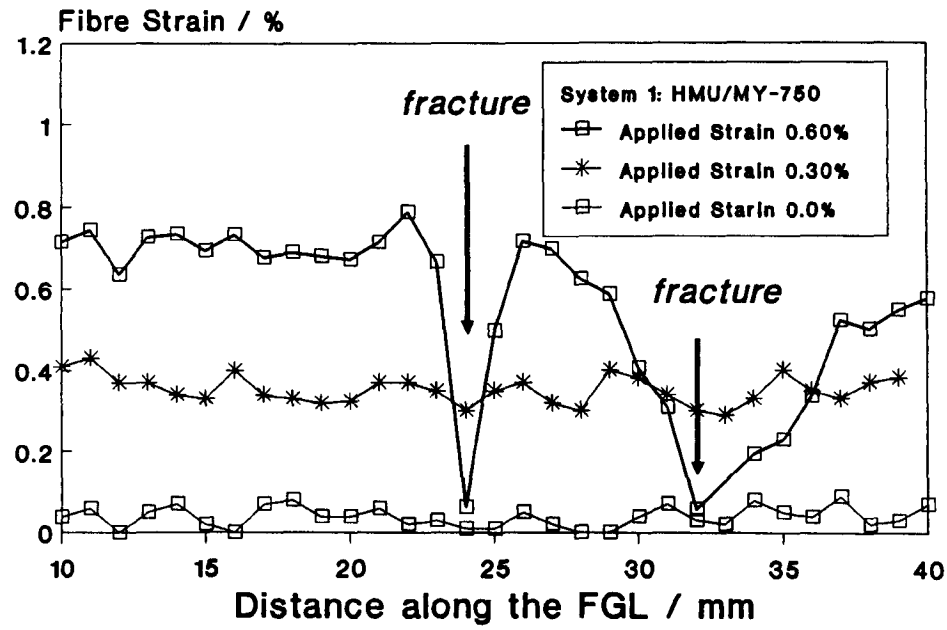

Fig.5.16 Fibre strain distribution in the HMU/MY-750 system at 0.0%, 0.3% and 0.6% applied strain.

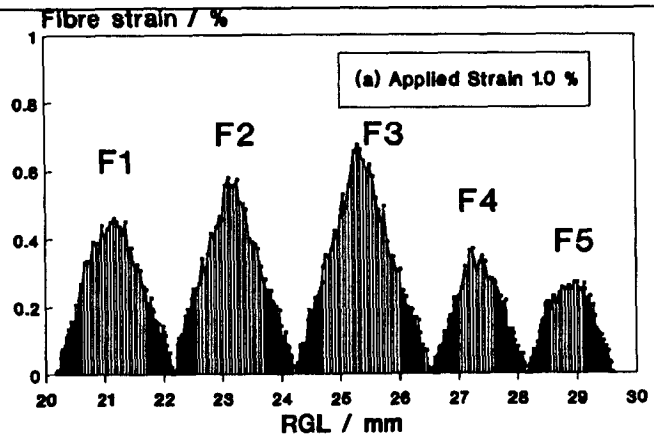

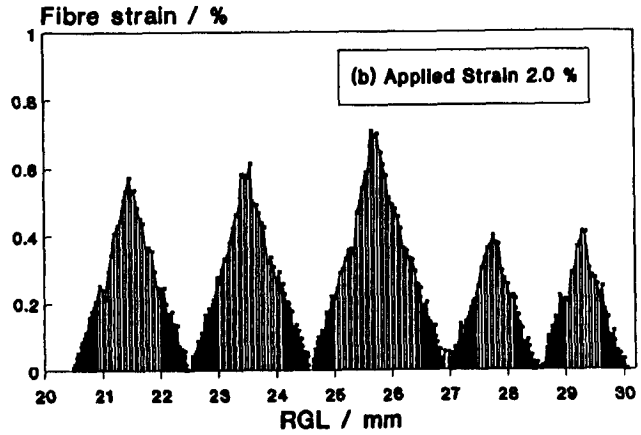

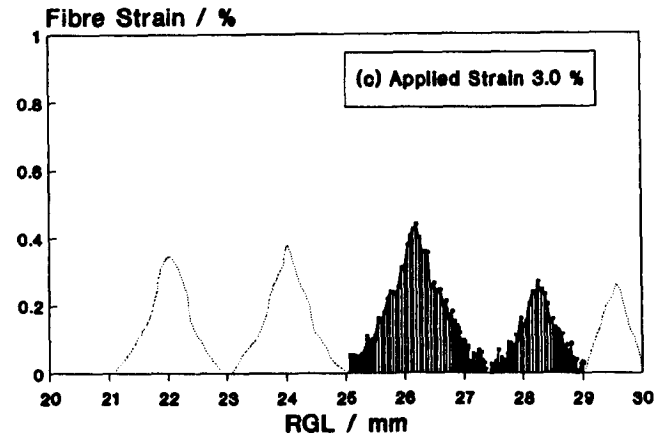

Fig.5.17 Fibre strain along the RGL of the HMU/MY-750 system at applied strain of **(a)** 1.0%, **(b)** 2.0% and **(c)** 3.0%.

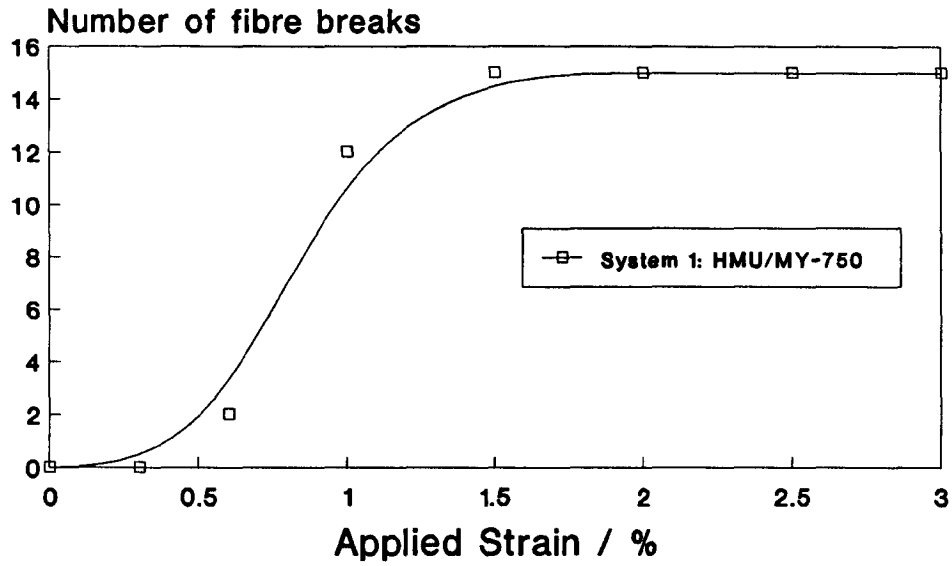

Fig.5.18 Number of fibre breaks as a function of applied strain, within a Fragmentation Gauge Length (FGL) of 30 mm, for the HMU/MY-750 system.

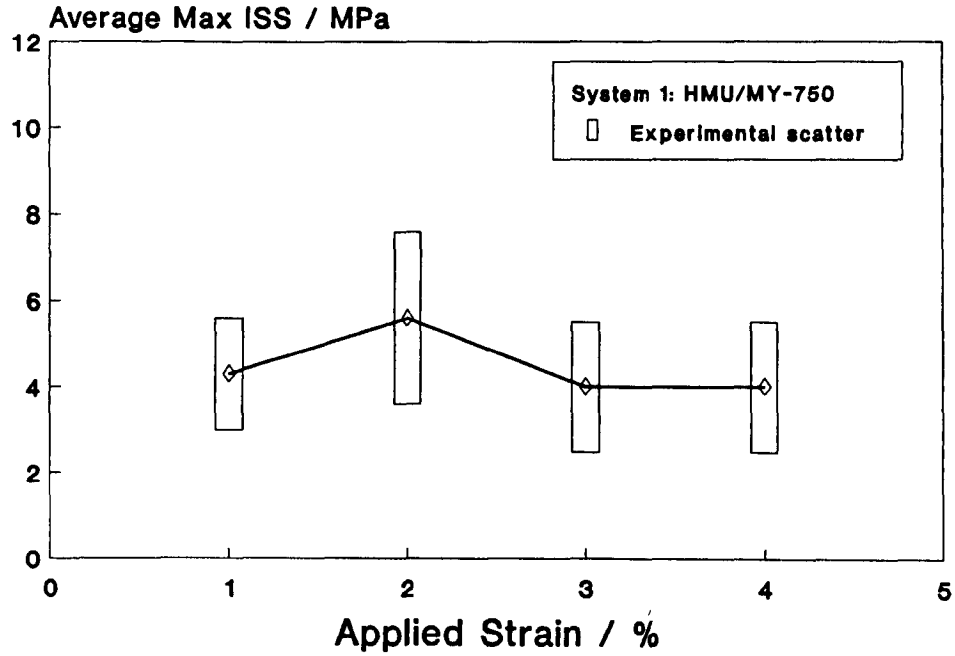

Fig.5.20 The average maximum ISS (over all fragments tested) as a function of applied strain for the HMU/MY-750 system.

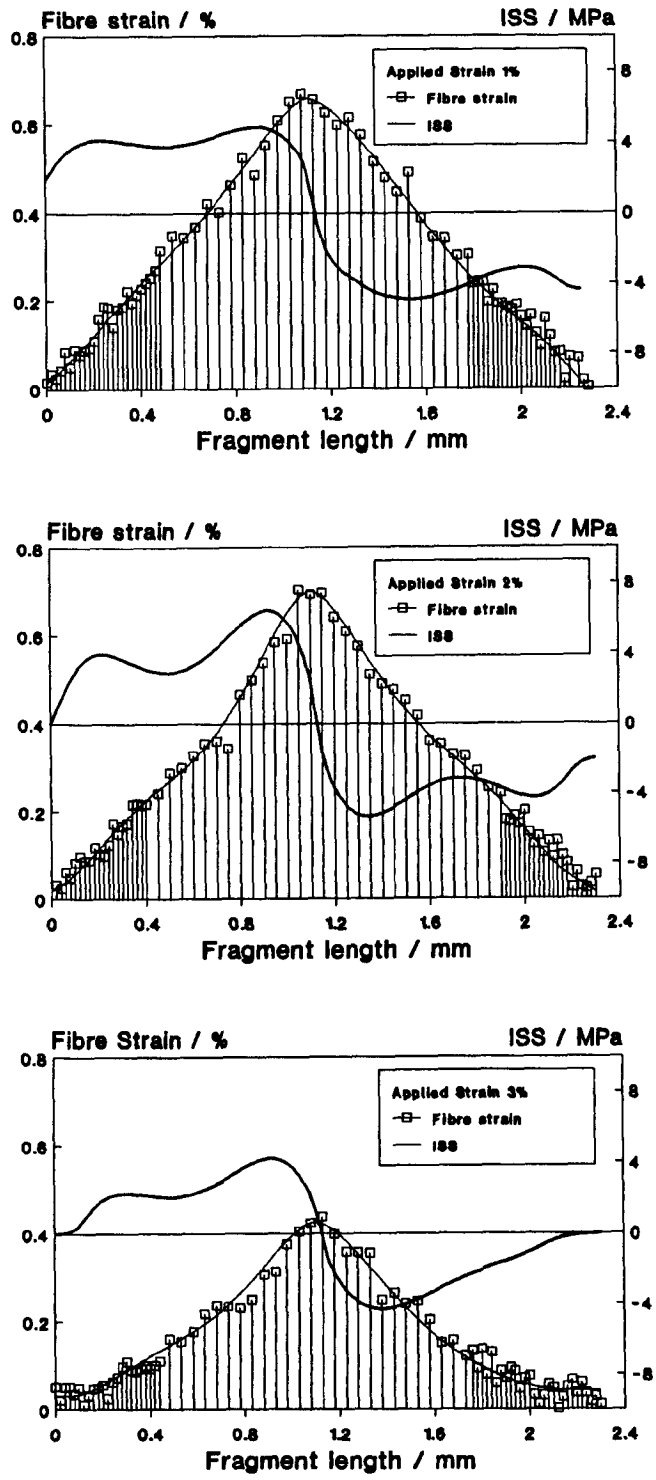

Fig.5.19 The fibre strain and the interfacial shear stress (ISS) distributions along a typical fragment of the HMU/MY-750 system at applied strain of **(a)** 1.0%, **(b)** 2.0% and **(c)** 3.0% .

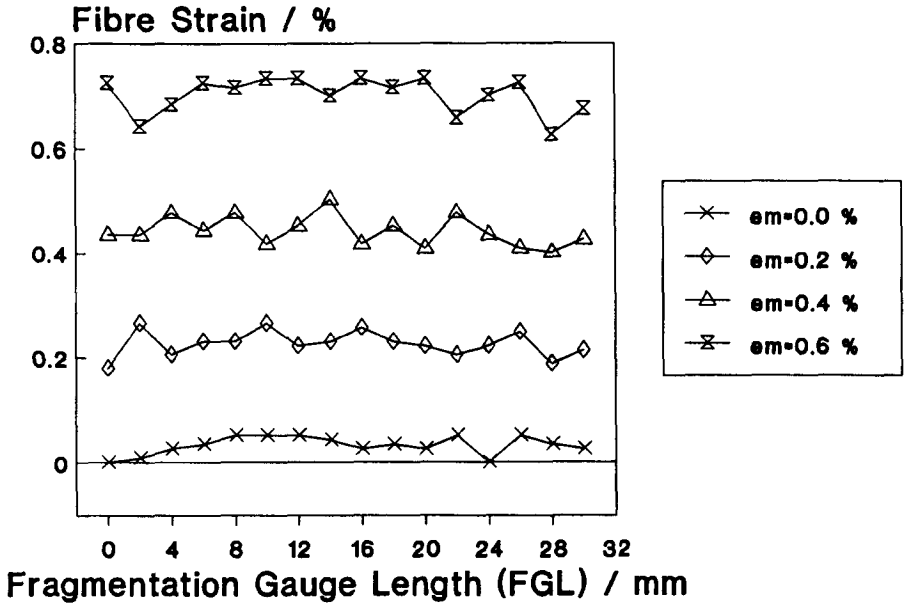

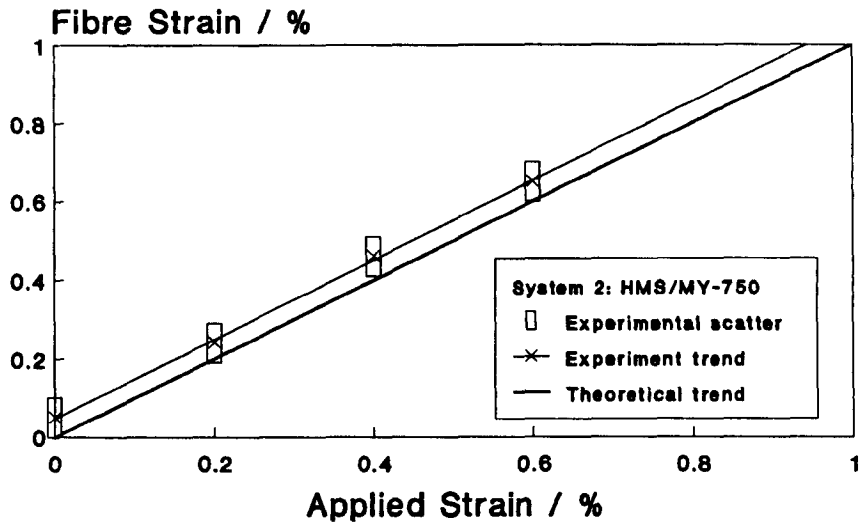

Fig.5.21 Typical fibre strain distribution along the FGL for the HMS/MY-750 system, prior to first fibre fracture, plotted :
(a) as a function of position along the FGL, and
(b) as a function of applied strain.

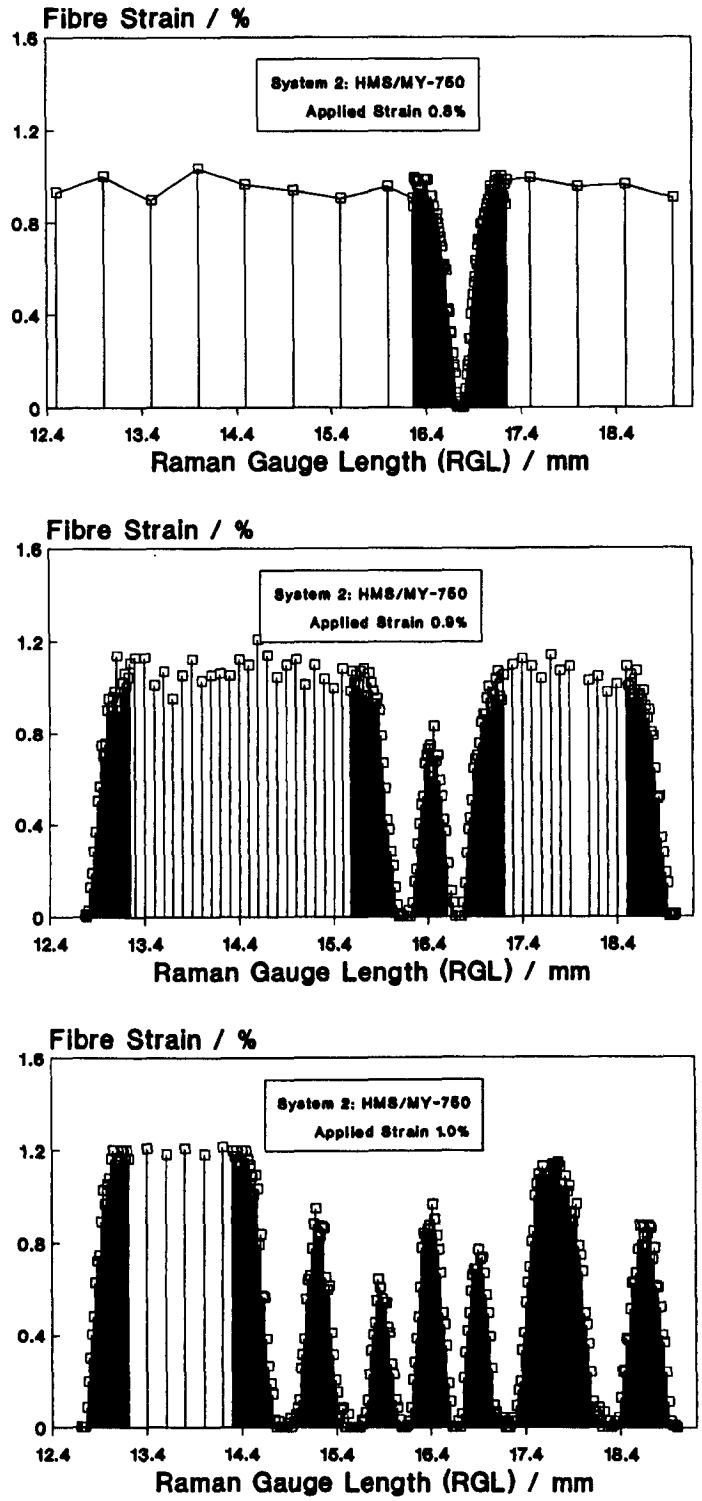

Fig.5.22 Fibre strain distribution along the RGL of the HMU/MY-750 system at applied strain of **(a)** 0.8%, **(b)** 0.9%, **(c)** 1.0% .

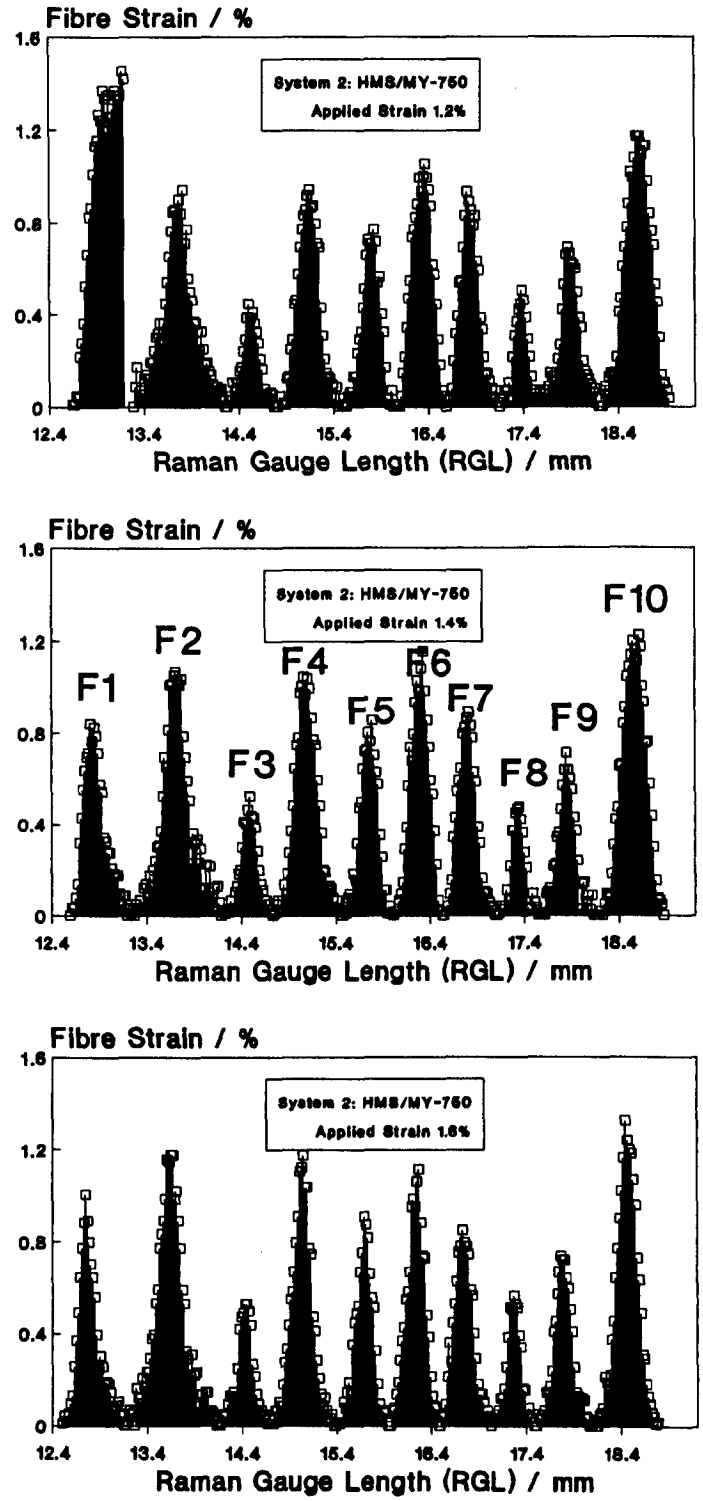

Fig.5.22 Fibre strain distribution along the RGL of the HMU/MY-750 system at applied strain of **(d)** 1.2%, **(e)** 1.4%, **(f)** 1.6% .

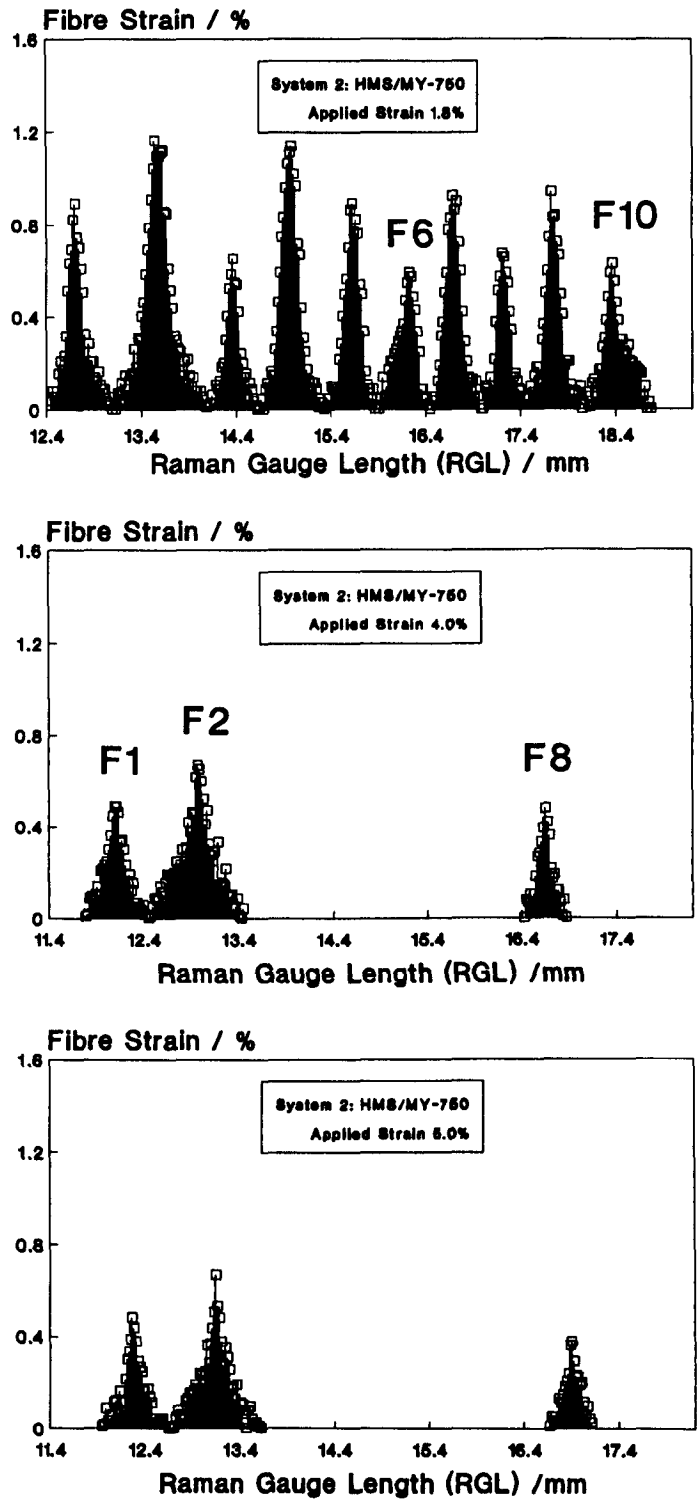

Fig.5.22 Fibre strain distribution along the RGL of the HMU/MY-750 system at applied strain of (g) 1.8%, (h) 4.0% and (i) 5.0% .

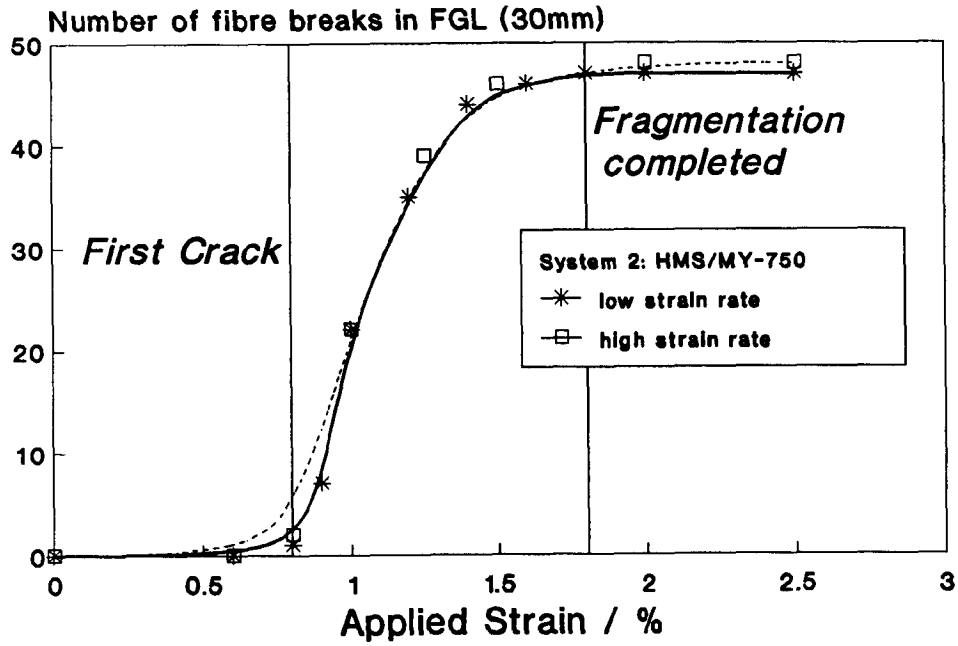

Fig.5.23 Number of fibre breaks as a function of applied strain, within a Fragmentation Gauge Length (FGL) of 30 mm for the HMS/MY-750 system.

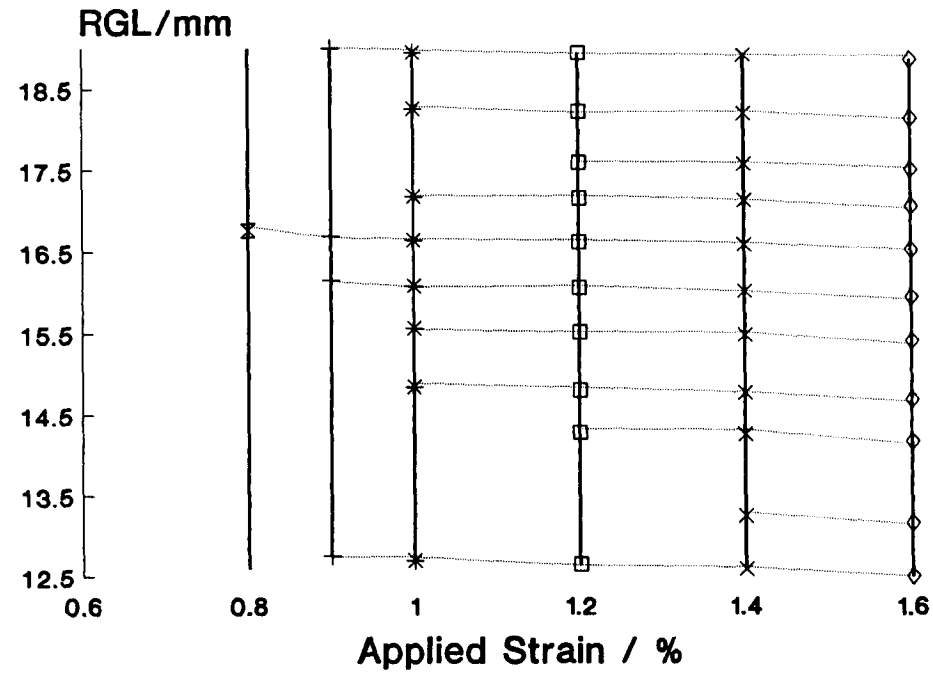

Fig.5.24 Sketch of the fibre fracture propagation within the RGL, for the HMS/MY-750 system.

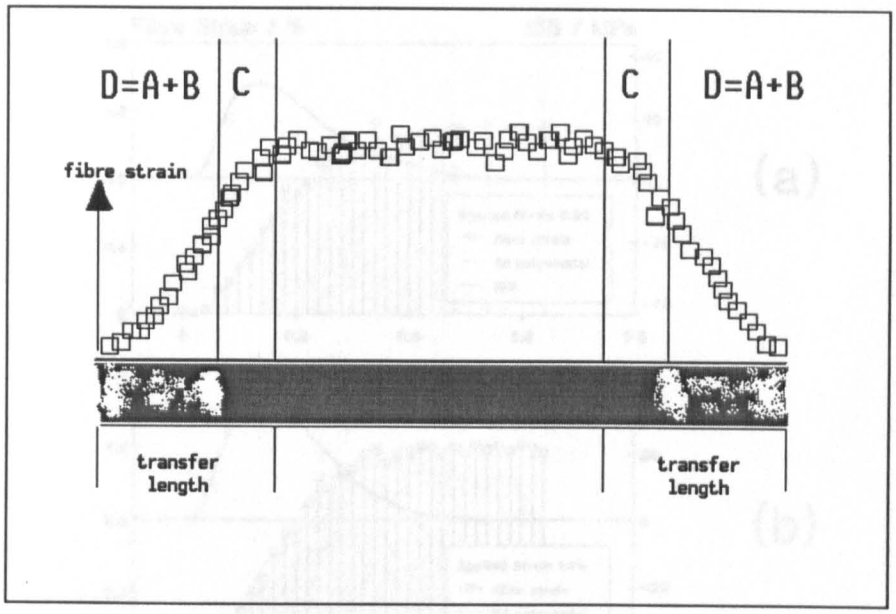

Fig.5.25 Schematic illustration of the alternating bright and dark patches observed by the reflection microscope on a portion of the transfer length of the fibre fragment. The distance D coincides with the distance from the fibre end the maximum ISS appears.

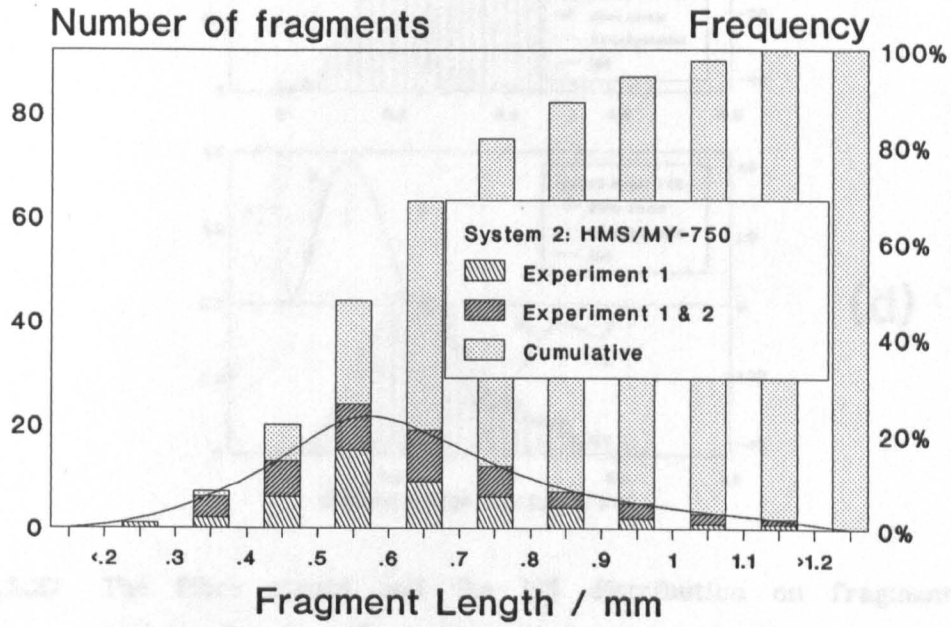

Fig.5.26 Histogram of the fragment length distribution at the end of the fragmentation process for the HMS/MY-750 system.

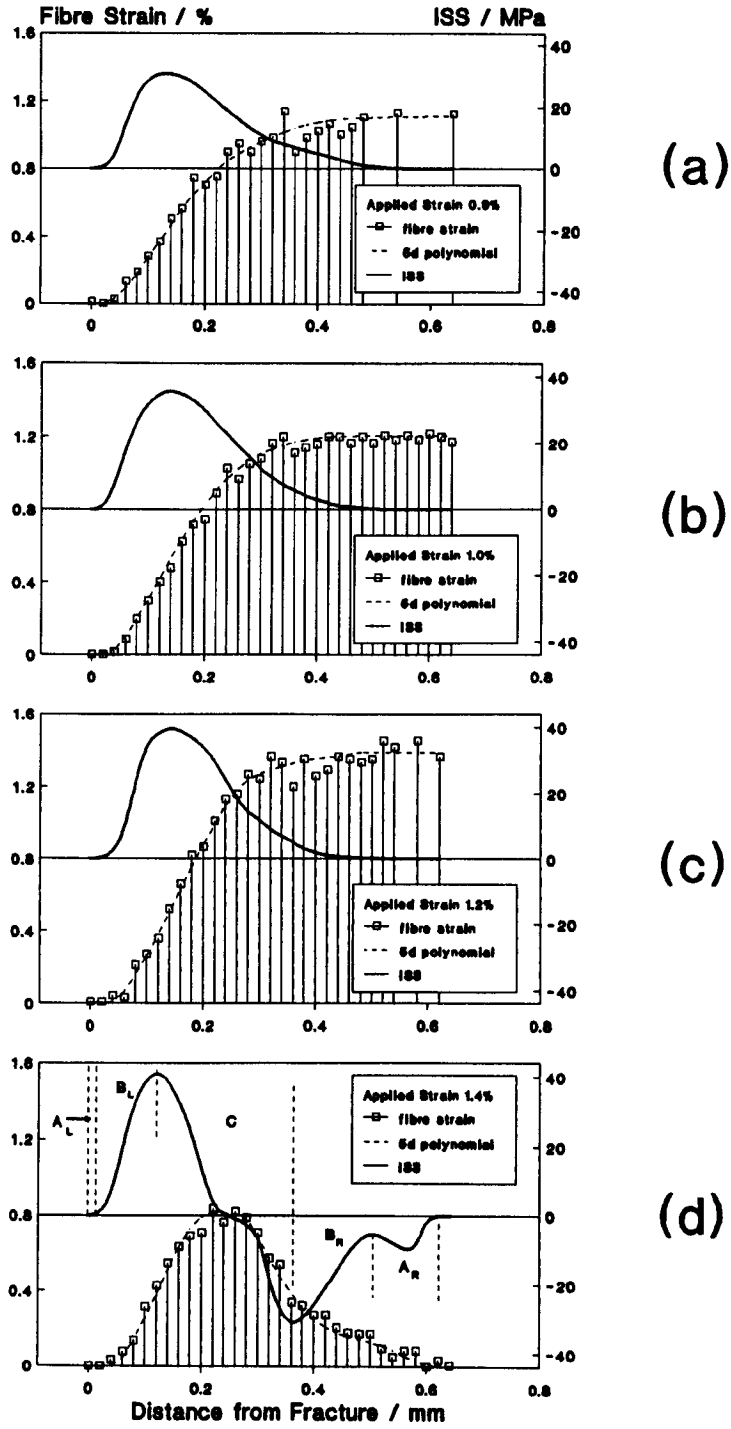

Fig.5.27 The fibre strain and the ISS distribution on fragment F1 of system 2, at subsequent levels of applied strain : (a) 0.9%, (b) 1.0%, (c) 1.2%, (d) 1.4%.

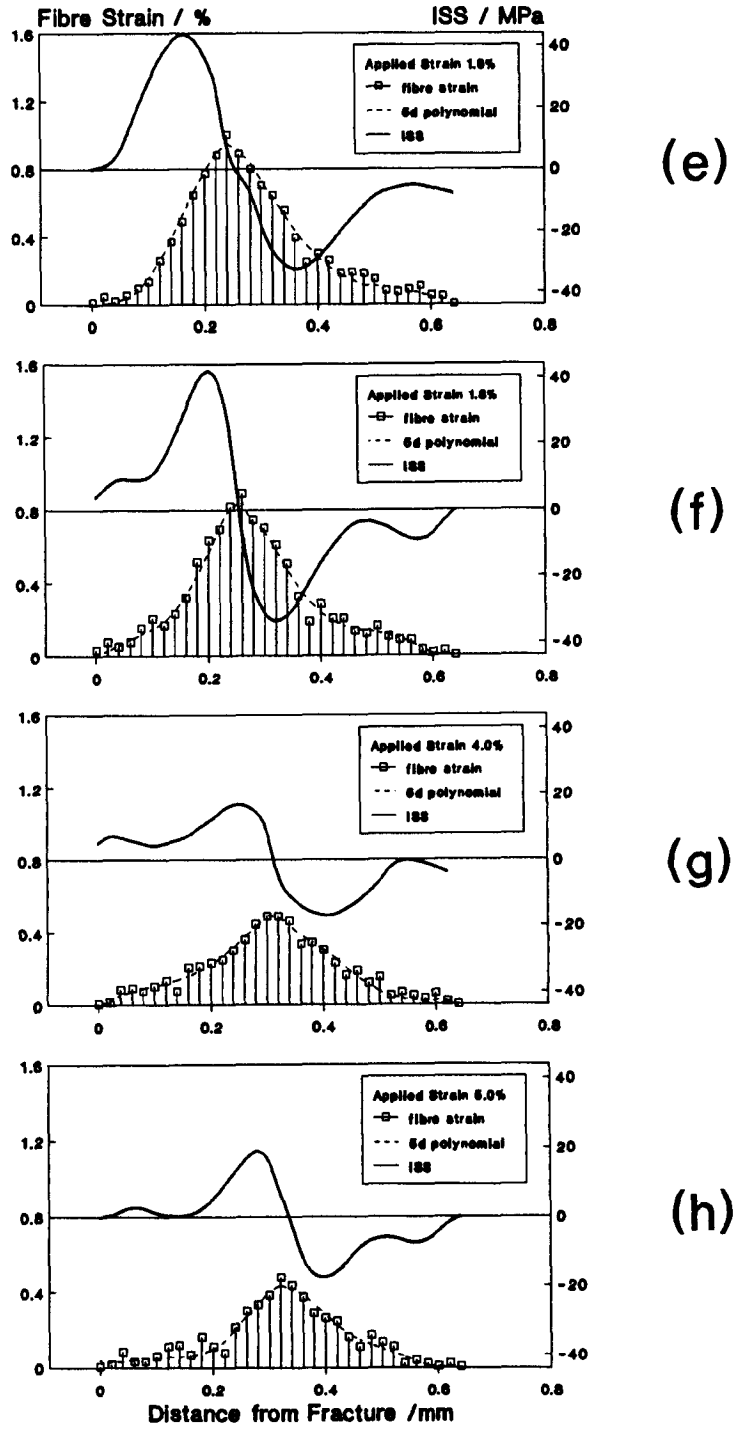

Fig.5.27 The fibre strain and the ISS distribution on fragment F1 of system 2, at subsequent levels of applied strain : (e) 1.6%, (f) 1.8%, (g) 4.0%, (h) 5.0%.

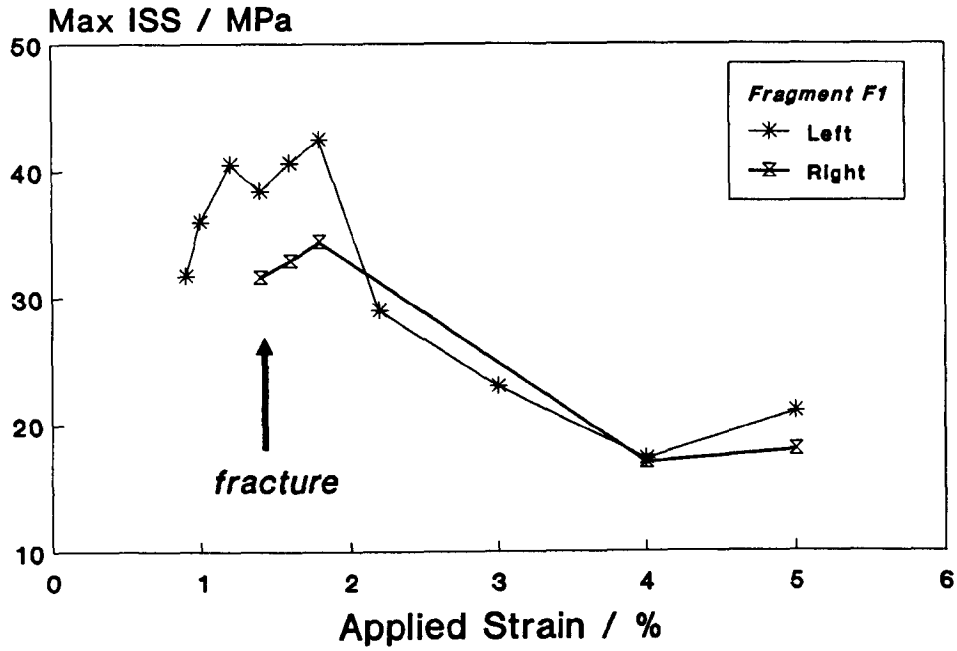

Fig.5.28 The maximum ISS on both profiles of fragment F1, as a function of applied strain.

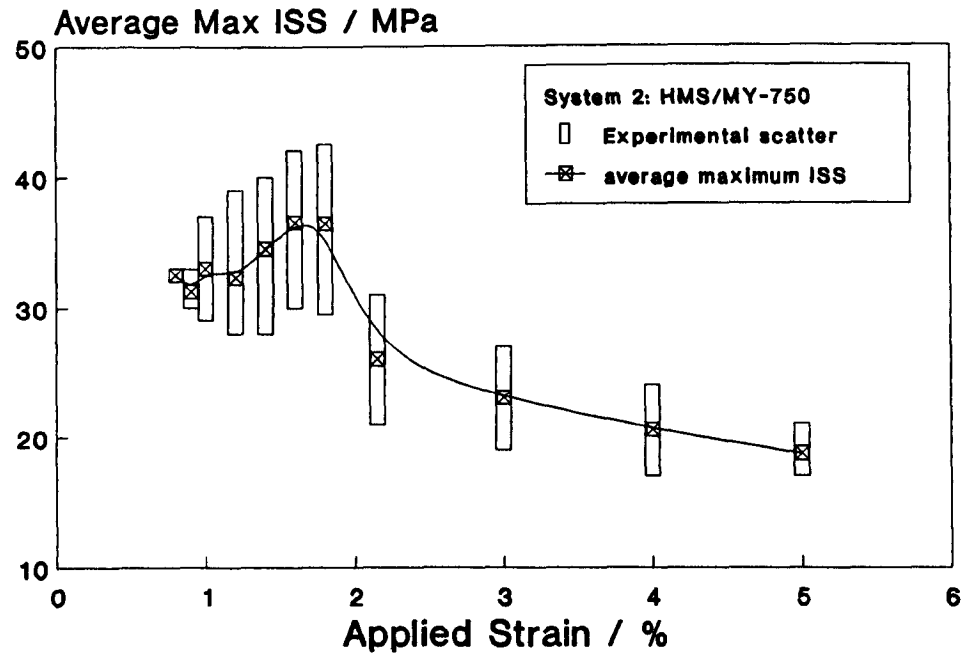

Fig.5.29 The average maximum ISS, calculated over all fragments tested, as a function of applied strain, for the HMS/MY-750 system. The experimental scatter is indicated by the bars, which correspond to the standard deviation of the averaged values.

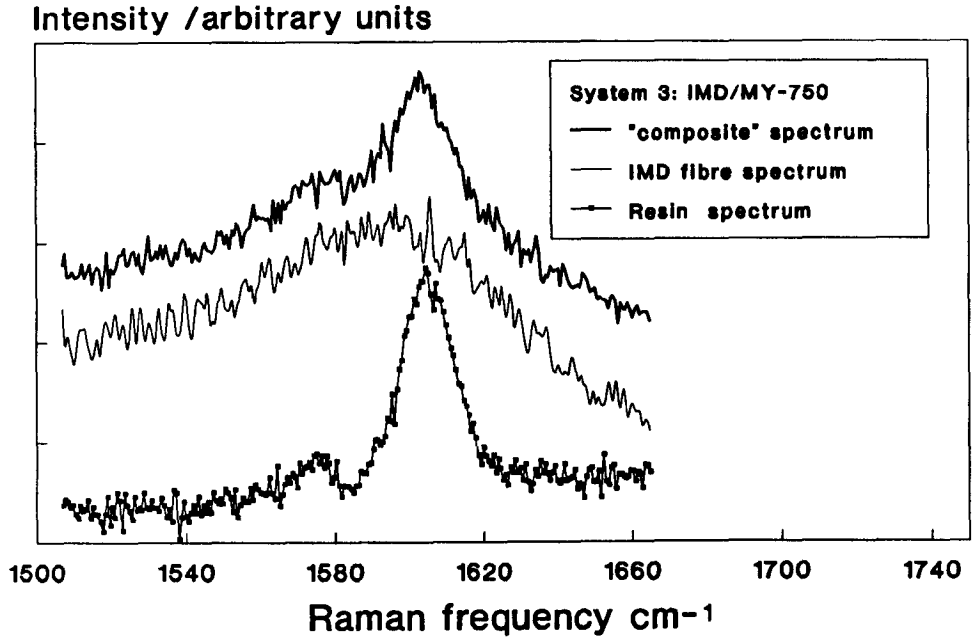

Fig.5.30 The Raman spectrum of the IMD fibre embedded in MY-750 epoxy resin. The fibre and resin signals are also displayed.

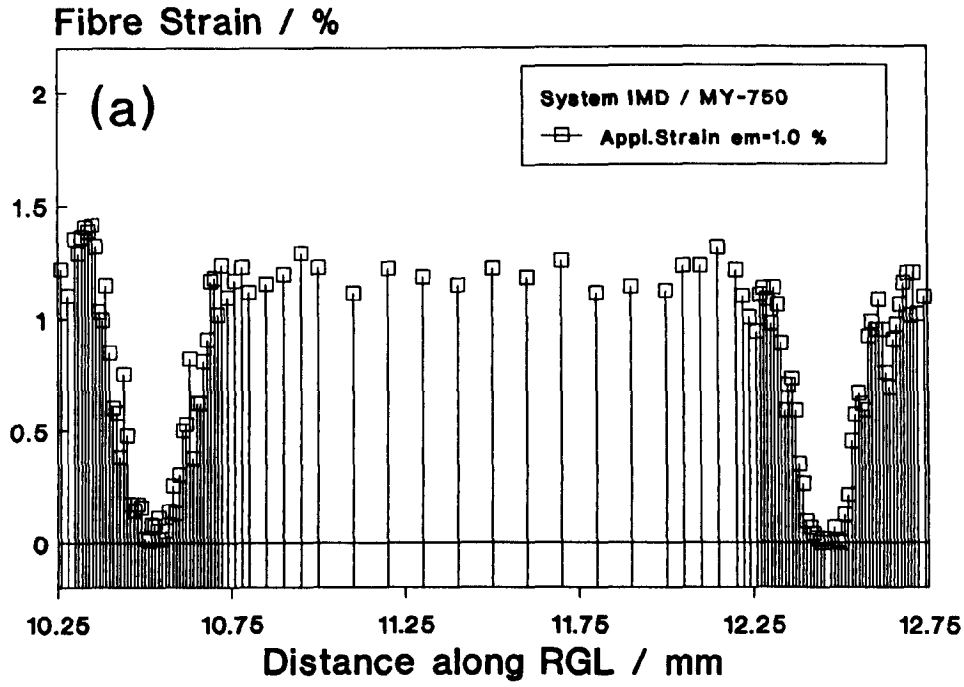

Fig.5.31 (a) The fibre strain distribution along the RGL for the IMD/MY-750 system at applied strain of 1.0%.

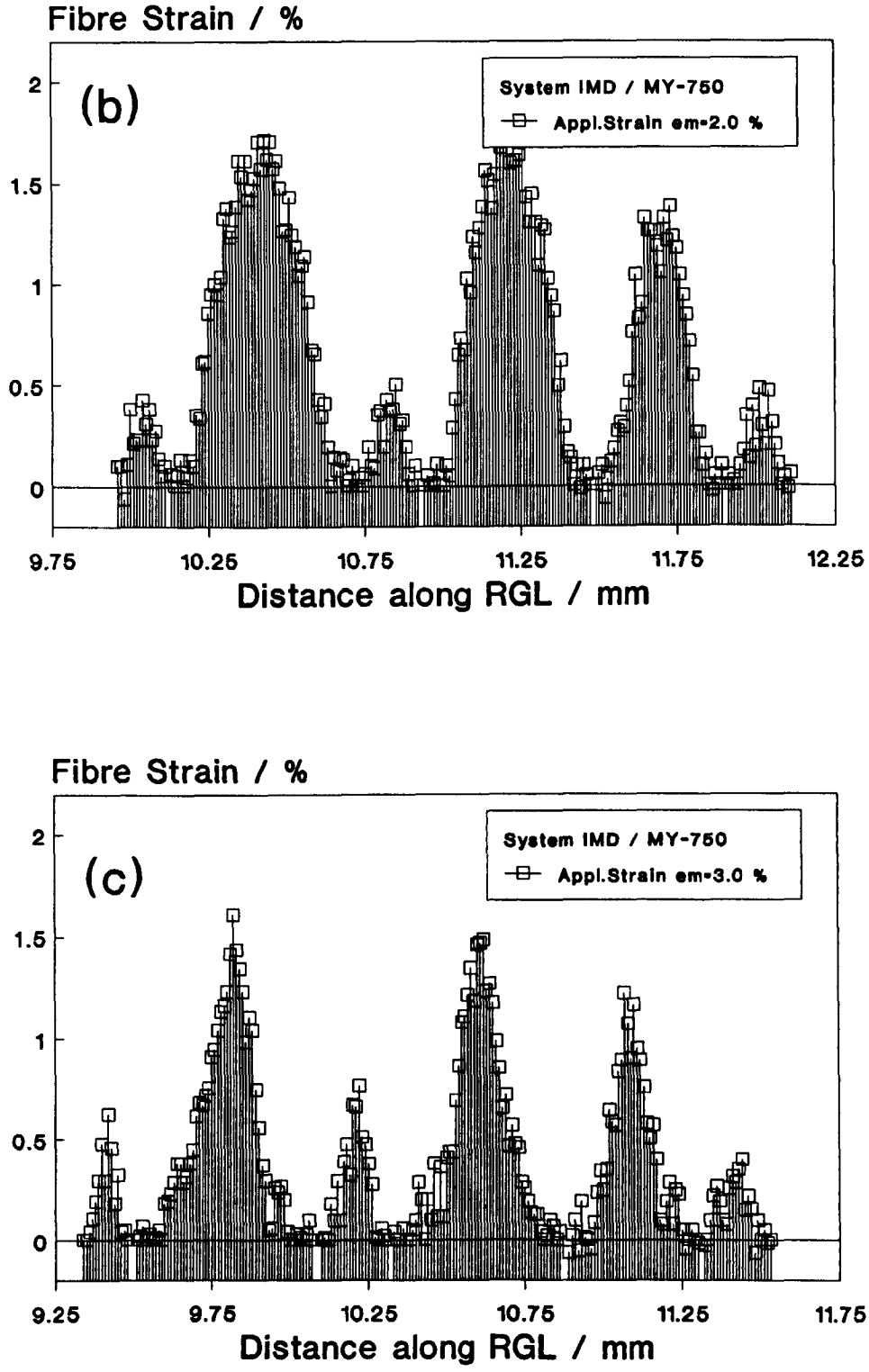

Fig.5.31 The fibre strain distribution along the RGL, for the IMD/MY-750 system at applied strain of **(b)** 2.0% and **(c)** 3.0%

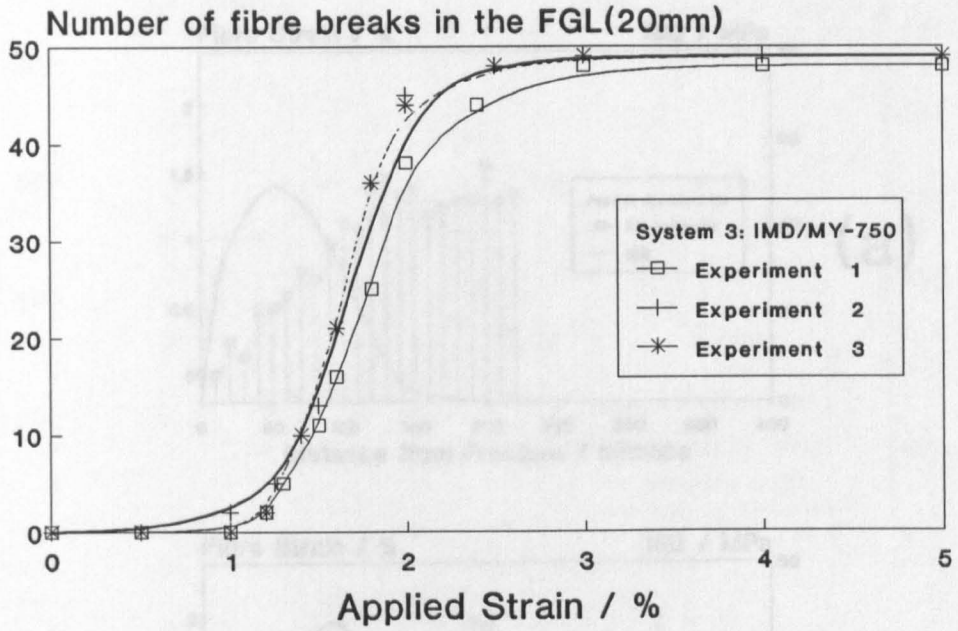

Fig.5.32 Number of fibre breaks as a function of applied strain, within a Fragmentation Gauge Length (FGL) of 20 mm, for the IMD/MY-750 system.

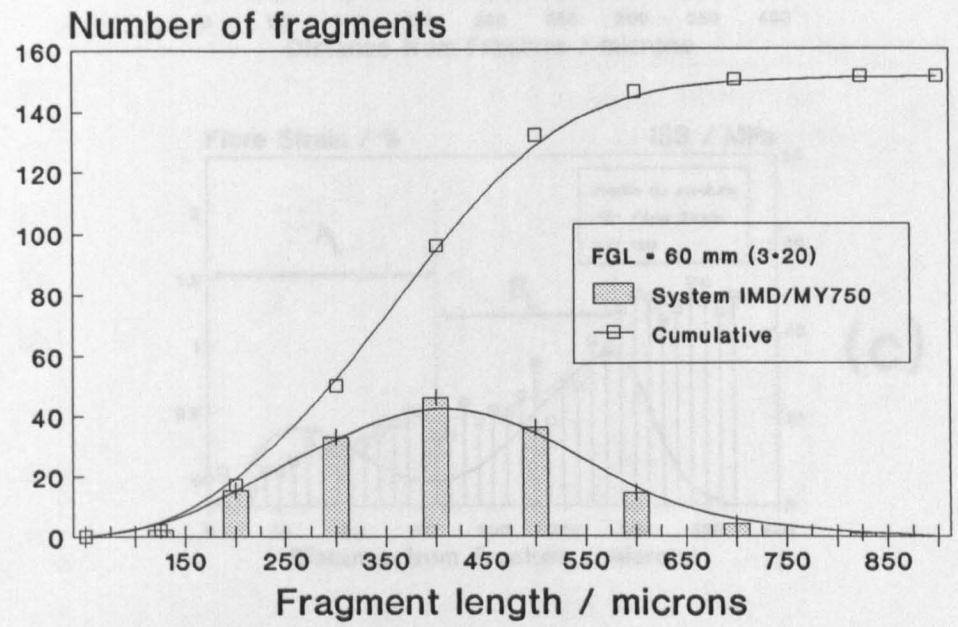

Fig.5.33 Histogram of the fragment length distribution at the end of the fragmentation process for the IMD/MY-750 system.

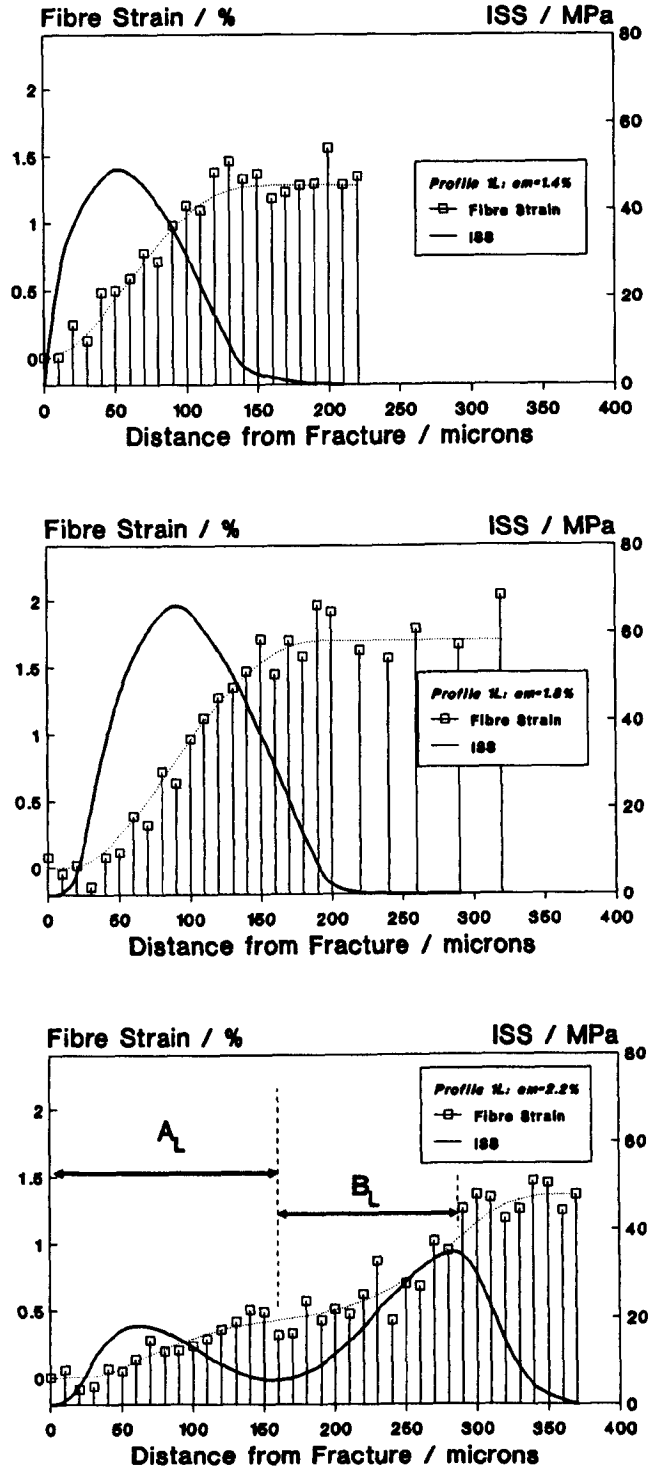

Fig.5.34 The fibre strain and the ISS distributions on the profile C1 of system 3 (Table 5.9), at three levels of applied strain : (a) 1.4%, (b) 1.8%, (c) 2.2%.

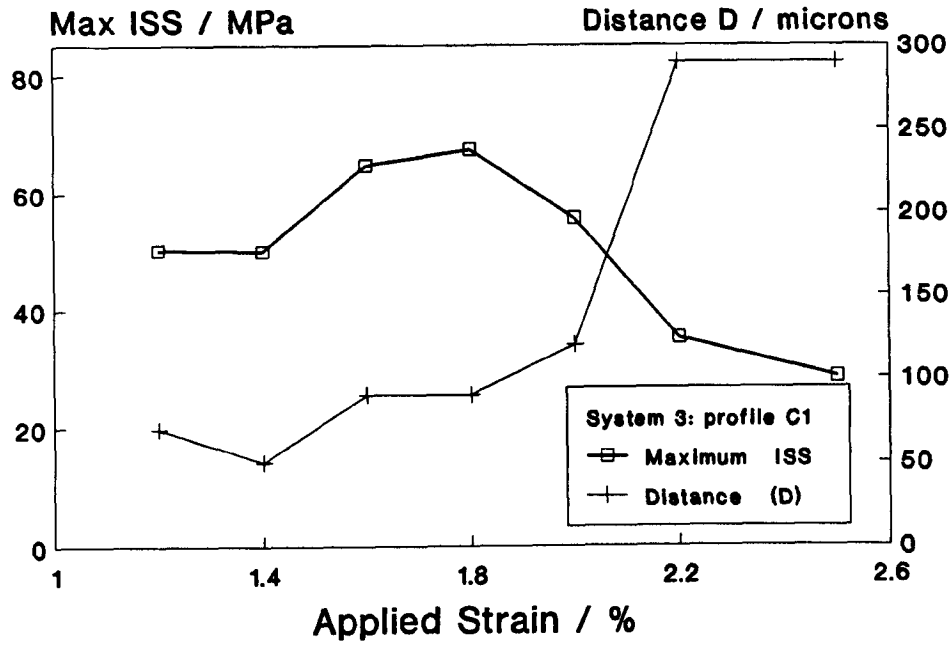

Fig.5.35 The maximum ISS on profile C1 of system 3 as a function of applied strain and the distance D from the distance fragment end where this maximum ISS appears.

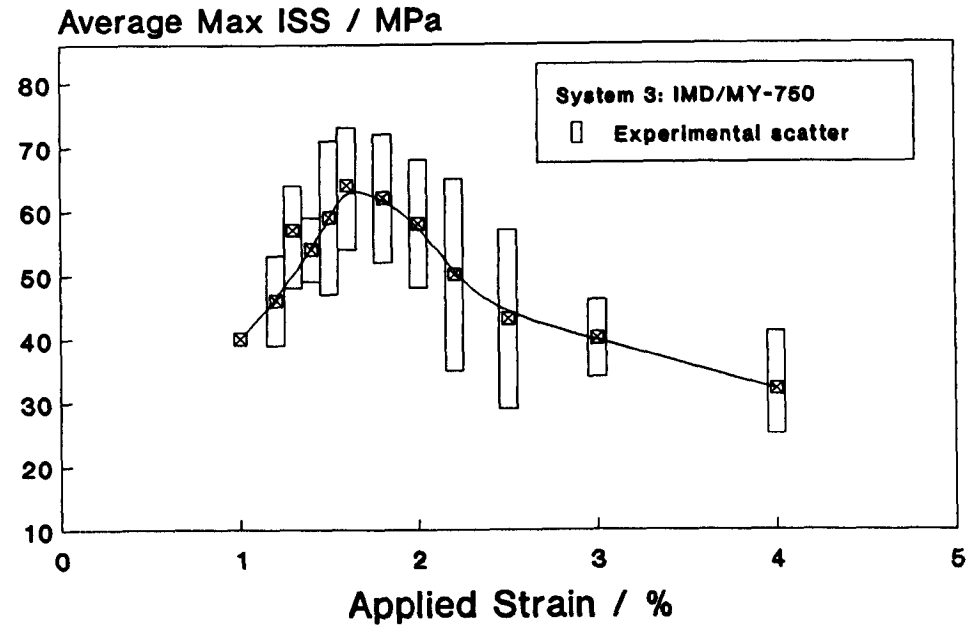

Fig.5.36 The average maximum ISS, calculated over all profiles examined in the three tests, as a function ofapplied strain, for the IMD/MY-750 system.

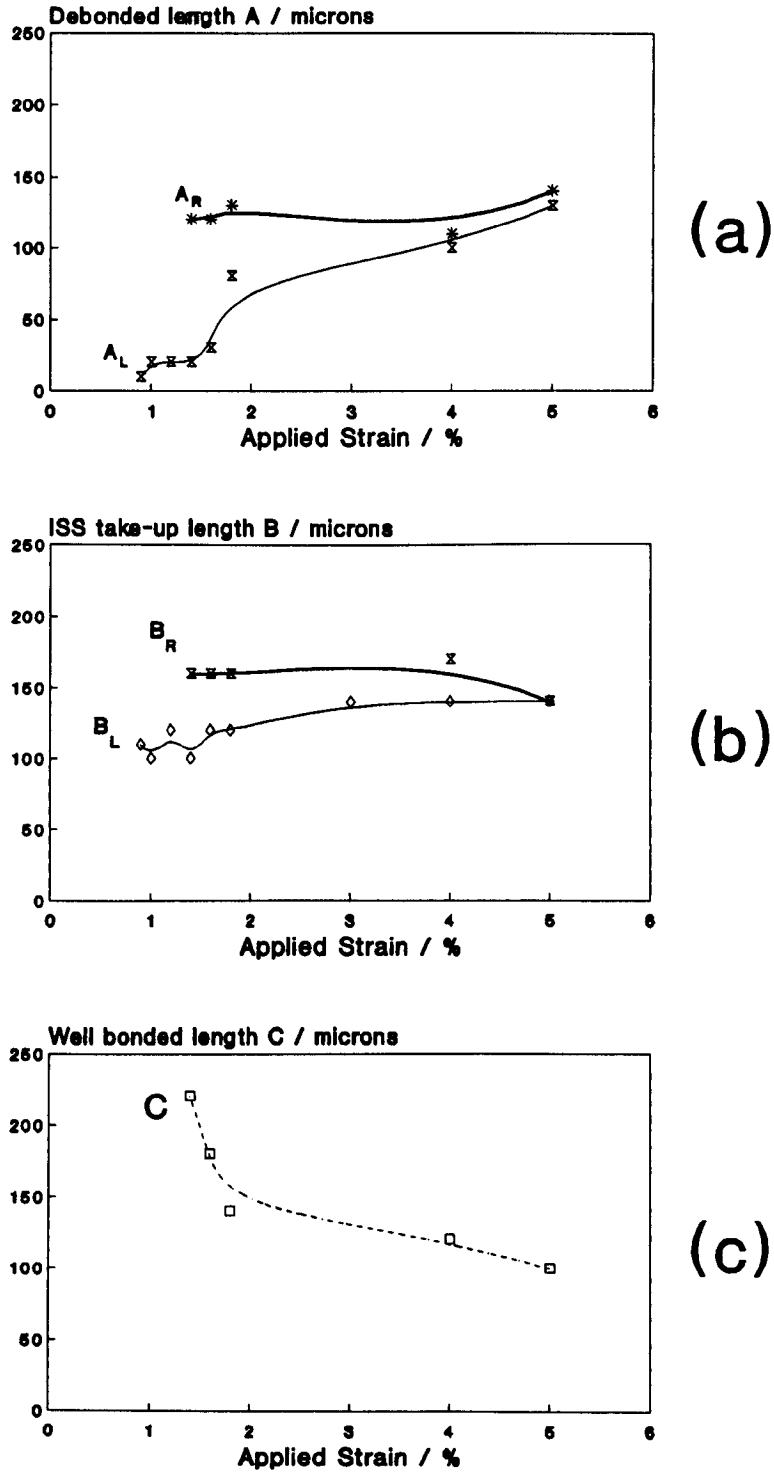

Fig.5.37 The characteristic lengths A (debonded length), B (ISS take-up length) and C (well-bonded length), as a function of the applied strain for the F1 fragment (figs.5.27 a to h) of the HMS/MY-750 system. The subscripts R, L denote the right and left- hand side of fragment F1.

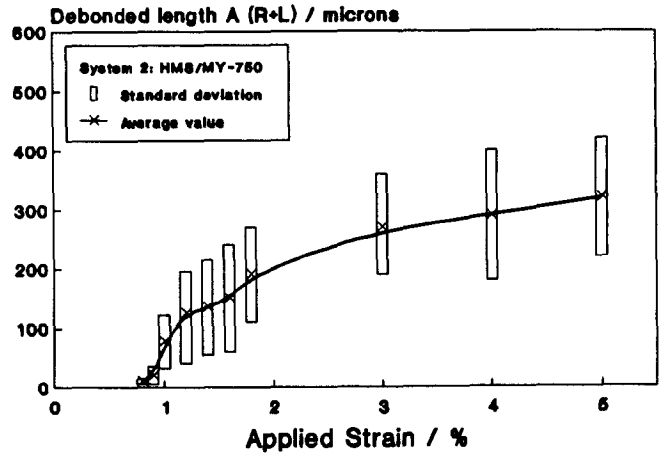

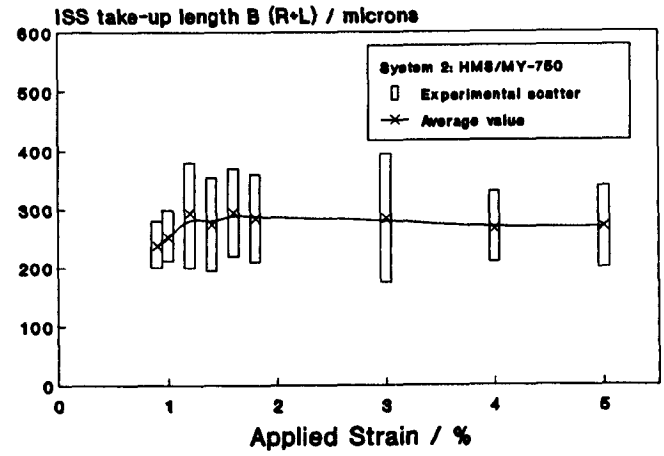

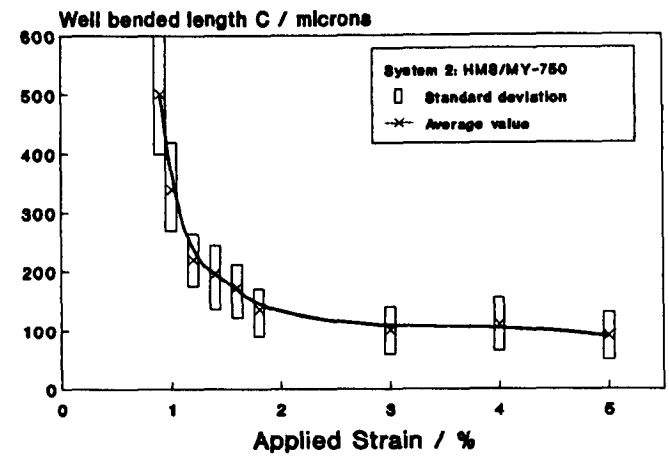

Fig.5.38, 39, 40 The average characteristic length A (debonded length), the average characteristic length B (ISS take-up length), and the average characteristic length C (well-bonded length) calculated over all fragments tested, for the HMS/MY-750 system.

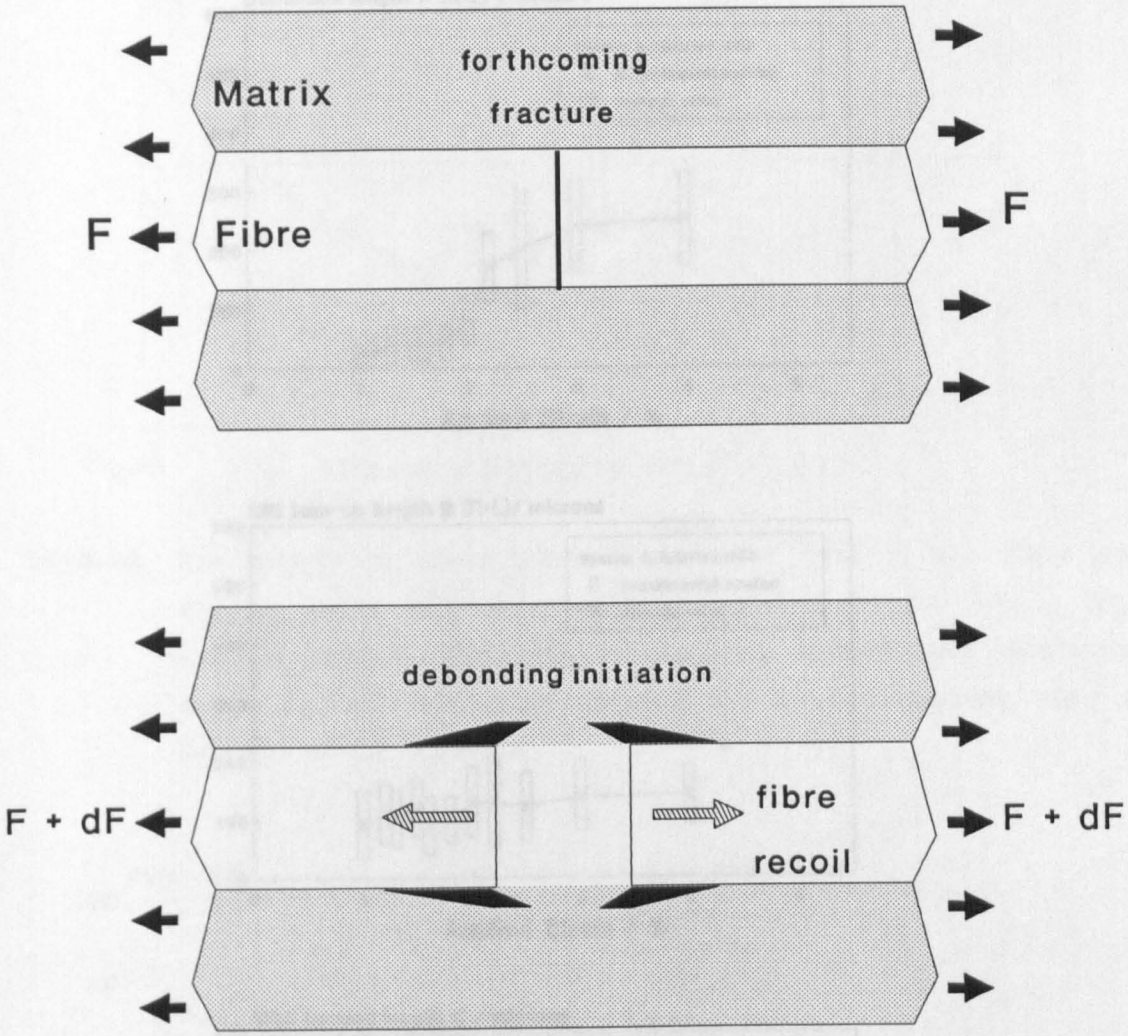

Fig.5.41 A schematic presentation of the recoiling mechanism activated by fibre fracture.

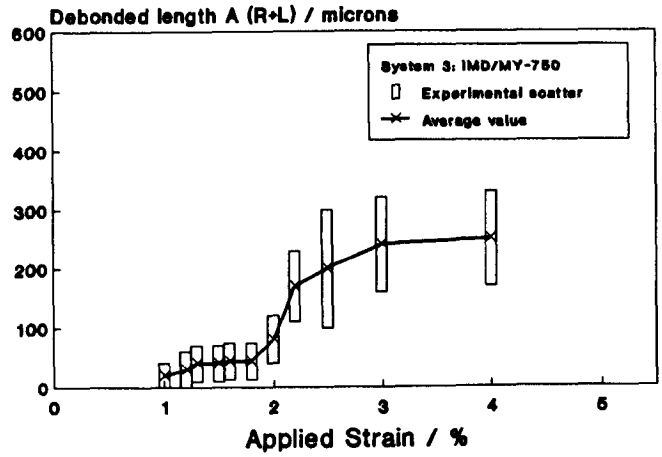

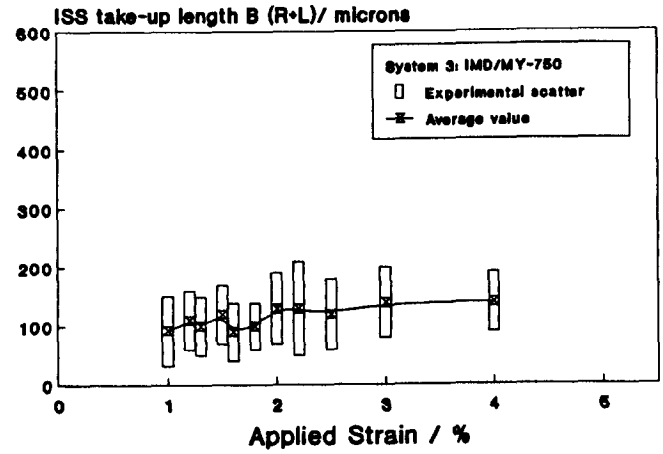

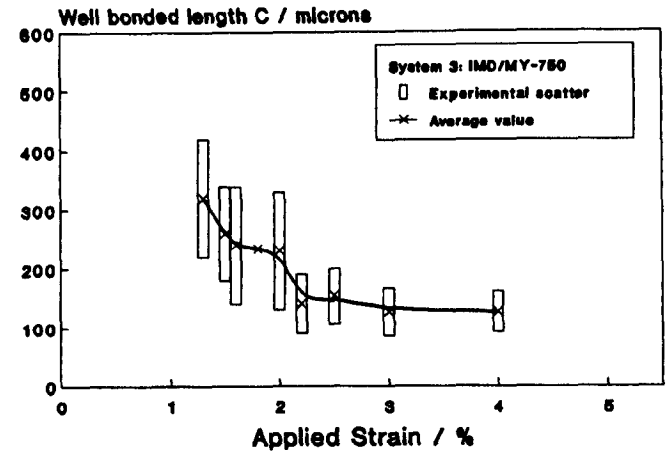

Fig.5.42, 43, 44 The average characteristic length A (debonded length), the average characteristic length B (ISS take-up length), and the average characteristic length C (well-bonded length) calculated over all fragments tested, for the IMD/MY-750 system.

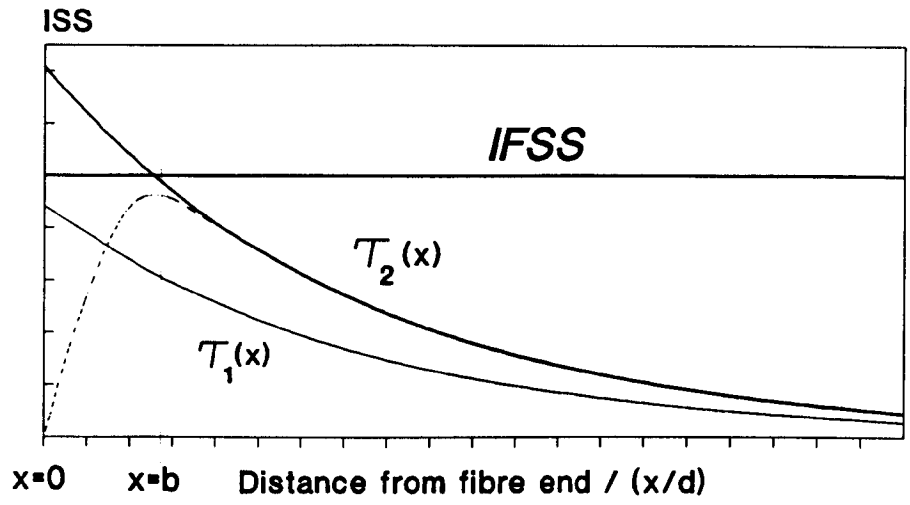

Fig.5.45. The interfacial shear stress distribution next to the fibre end at two levels of applied strain, according to the elastic load transfer models. When the shear stress exceeds the interfacial shear strength (IFSS) of system, the gradual yielding zone B develops at the interface.

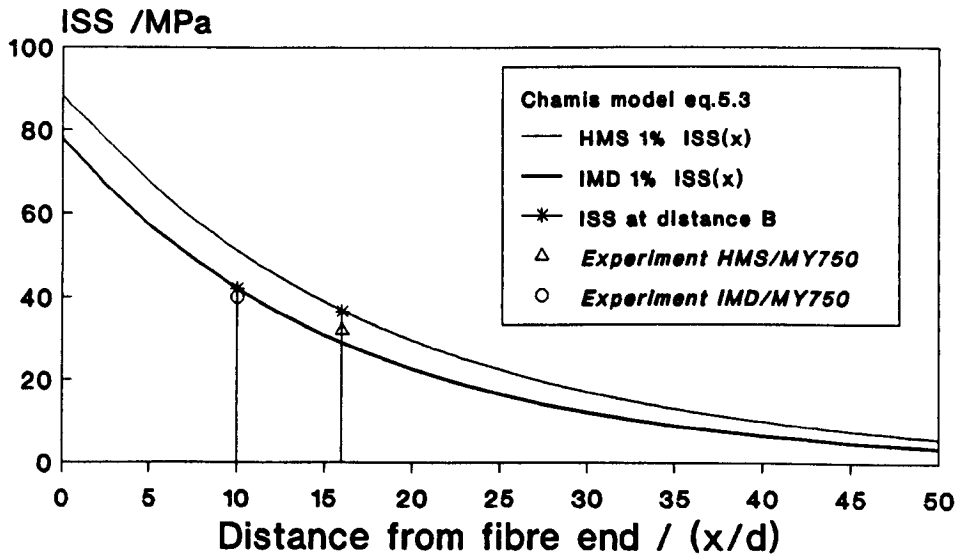

Fig.5.46 The ISS distribution for both systems 2 and 3, as a function of the distance from the fibre end, according to the Chamis model of elastic load transfer **[Chamis 1974]**, at 1.0% applied strain.

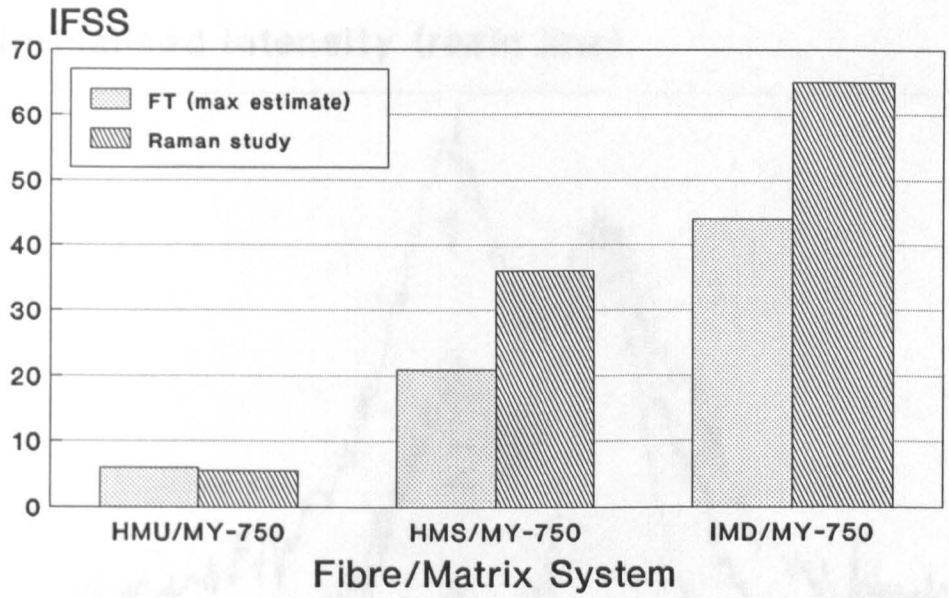

Fig.5.47 Comparative chart of the fibre/matrix IFSS estimates according to the fragmentation test and the Raman studies.

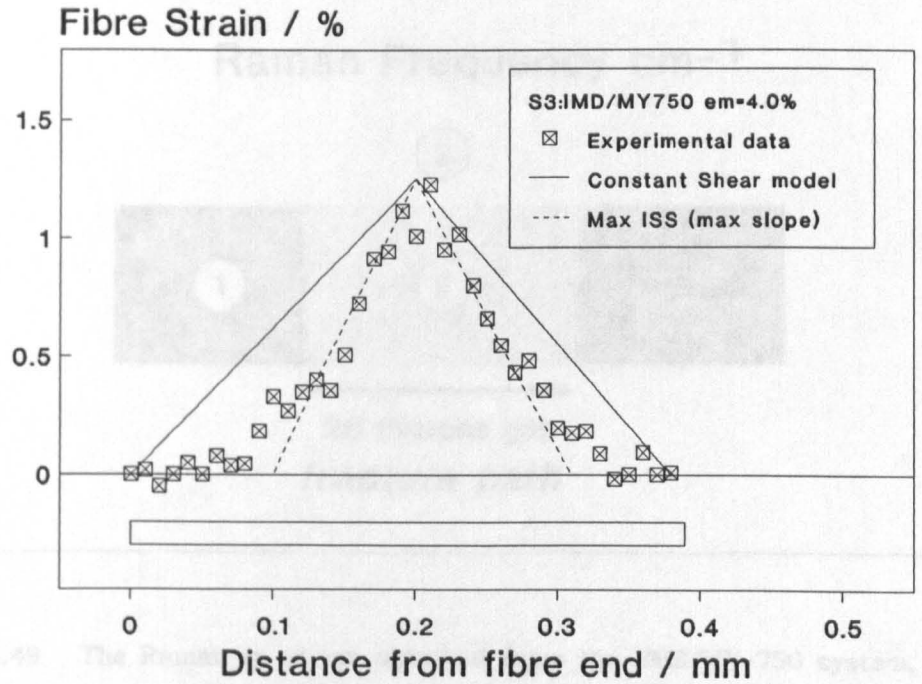

Fig.5.48 The fibre strain distribution on an IMD/MY-750 system fragments, at 4.0% applied strain. The derivative of the distribution is proportional to the ISS (equation 5.15).

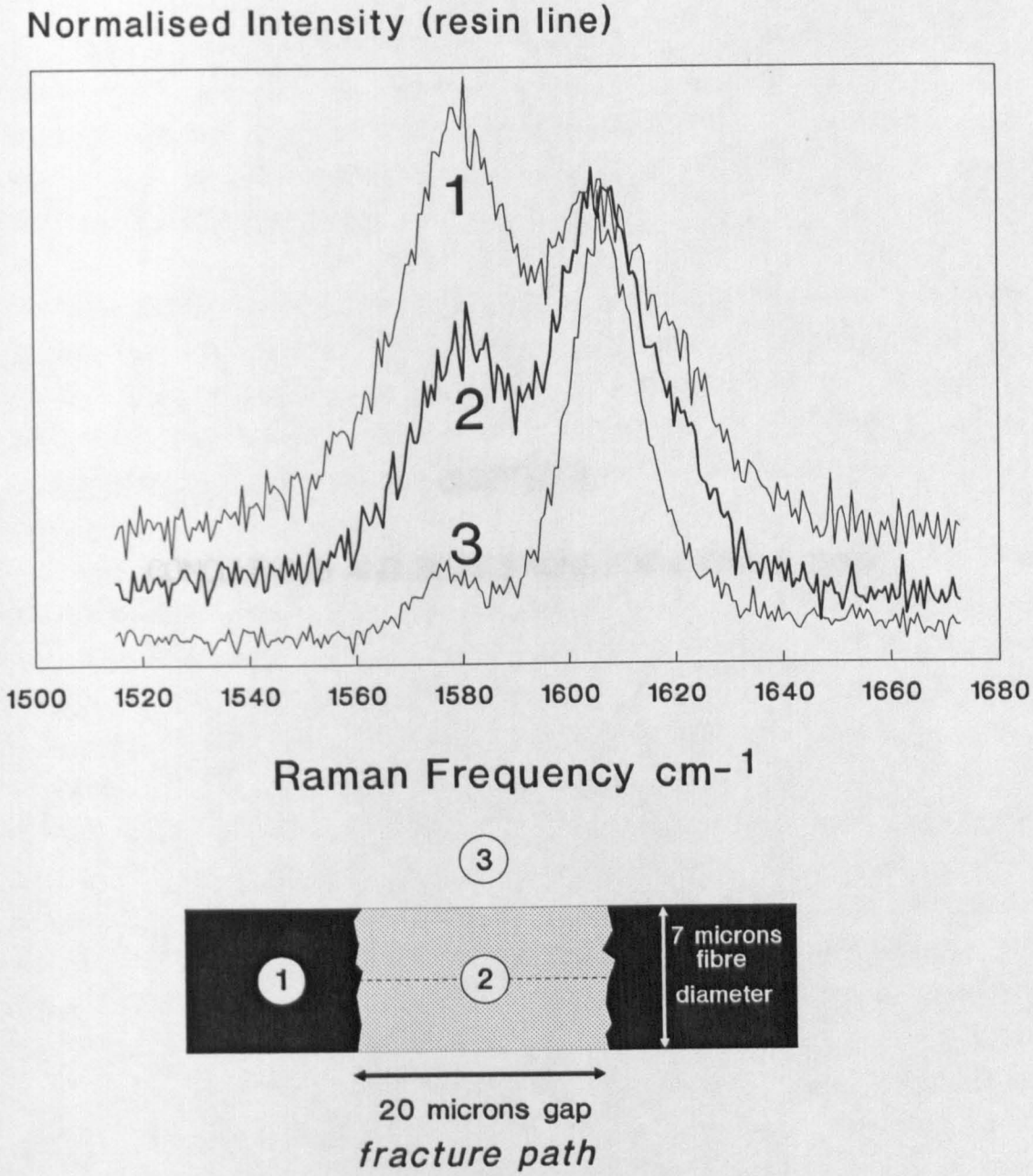

Fig.5.49 The Raman spectrum obtained from the HMS/MY-750 system, with the laser probe focused on: (1) the fibre next to the break, (2) the fracture path (gap) in between the fragments and (3) the resin material just outside the fracture path.

CHAPTER 6

CONCLUSIONS AND SUGGESTIONS FOR FURTHER WORK

6.1. Carbon fibre characterisation.

Laser Raman Spectroscopy has been employed in this thesis as the major experimental tool for the characterisation of carbon fibres the detection of the response of carbon fibre structure upon externally applied loads and, finally, the examination of the fibre/matrix interface in model carbon fibre/epoxy resin composites.

The Raman spectrum of carbon fibres comprises a number of frequency bands, each one assigned to a certain structural configuration. Only one Raman line is indisputably identified. This is the G-line, located at ~1580 cm^{-1}, and assigned to the E_{2g} vibrational mode of the graphite crystal [**Tuinstra 1970, Nemanich 1977, Chieu 1982**]. The appearance of other bands in the Raman spectrum of carbon fibres indicates the presence of "disordered" structure, particularly at carbonisation stages, or two and three-dimensional crystallinity, at graphitisation temperatures.

Fibres produced at low annealing temperatures (below 1300 $^{\circ}C$) exhibit broad Raman features and the so called "disorder" -induced lines D and D' (at ~1355 and ~1620 cm^{-1}, respectively) are dominant in the Raman spectrum, overshadowing the "graphitic" G-line (e.g. fibres IM43 and XAS, Chapter 2). These bands have been attributed to the presence of graphite edge planes perturbing the smoothly stratified crystallites of the fibre surface [**Katagiri 1988**], or to the increase in the amount of the crystallite boundaries due to smaller crystallite size [**Tuinstra 1970**], or even to the presence of non-graphitic structure that may exist in the fibre structure [**Nakamizo 1974, Fitzer 1988**].

The increase in the heat treatment temperature (firing temperature), yields a fibre product with highly oriented, larger crystallite units, resulting in a higher fibre Young's modulus [**Donnet 1984, Dresselhaus 1988**]. The Raman spectrum of such a fibre exhibits a pronounced, narrow and intense G-line, decaying "disorder" features and a growing high frequency band, denoted as G'-line at ~2700 cm^{-1} (Chapter 2). In terms of its Raman frequency value and its wavelength dependence, the G'-line appears as an overtone of the "disorder"-induced D-line; however, in terms of its other Raman characteristics (intensity, HHBW, RFGF) is closely associated with the G-line. A more appropriate assignment of this band seems to be the one that relates its presence and growth to the

development of a two and three-dimensional structuring of the crystallite units **[Lespade 1984]**.

Surface treatment of carbon fibres with highly crystalline surface results in an enhancement of the disorder bands of the Raman spectrum and a parallel decline of the graphitic features. On the contrary, the same treatment has no detectable effect in the Raman spectrum of low modulus and less crystalline fibres (Chapter 2). While the first indicates the existence of some sort of radial anisotropy in the high modulus (and highly crystalline surface) fibre **[Chen 1983]**, the latter rather confirms the turbostratic structure of lower modulus fibres.

A measure of the fibre surface crystallinity is given by the intensity ratio I_D/I_G of the D and the G-lines of the carbon fibre Raman spectrum. However, this ratio cannot be directly related to the fibre modulus, since control of the fibre morphology during manufacture can yield fibres with different intensity ratio, but similar Young's modulus (e.g. fibres LF-negative and LF-neutral, Chapter 2).

The "tailoring" of the fibre morphology can produce a fibre with less "graphitic" surface features, as revealed by its Raman spectrum, but of equal or even higher fibre modulus (e.g. fibres LF58, 405 GPa and HMS, 390 GPa). It is believed that as a result of this morphology alteration (the technical details of which have not been fully disclosed by the manufacturer), radial anisotropy phenomena are reduced. By eliminating skin-core effects, a fibre with higher *average* modulus can be produced, while still having a lower *surface* modulus than that of a radially anisotropic fibre. As a future undertaking, the radial anisotropy in the carbon fibre structure can be studied by trimming the fibre diameter (possibly using electrolytic etching **[Chen 1983]** to remove outer layers) and subsequently by examining the resulting fibre surface with the Laser Raman probe.

Tensile studies have been conducted on single filaments (Chapter 3). The load in the fibre has been applied by means of a microextensometer, while the Raman spectrum of the fibre has been obtained at every increment of applied strain. All Raman frequencies of carbon fibres are found to be sensitive to applied strain (Chapter 3). The negative shift of the Raman frequency with applied strain is attributed to the anharmonicity of the interatomic force constants in the crystallite units **[Bretzlaff 1983, Tashiro 1990]**. The Raman Frequency Gauge Factor (RFGF) expresses the rate

of frequency shift with strain and is found to be approximately constant for each type of fibre.

With respect to the graphitic G-line, the higher the fibre surface crystallinity, the greater the (absolute) value of the RFGF. This is due to the fact that, in fibres with highly oriented crystallites, the externally applied deformations along the fibre axis are almost fully delivered to the crystallite axis. In fibres with a lower degree of crystallinity, a significant amount of the external deformation is consumed into shearing and rotational deformations at the expense of bond stretching deformations. The RFGF is proportional to the fibre Young's modulus only for the series of fibres that have been produced via the same manufacturing route (Chapter 3).

Since in all carbon fibres the basic structural unit is the same [Guigon 1984], it should be expected that the stress dependence of the Raman frequency G is the same for all carbon fibres, irrespectively of the modulus or the manufacturing route. As the crystallites are more disturbed and misoriented in low modulus fibres [Donnet 1984, Dresselhaus 1988], they would simply require higher macroscopic strains, to develop the same levels of stress as in a high modulus fibre. The finding that the *apparent* stress dependence (α_σ=RFGF/E_f) is the same for all fibres of the same series (same manufacturing route) comes to justify the expectation of an equal stress dependence of all fibres irrespectively of the modulus (Chapter 3). On the other hand, the change in the *apparent* stress dependence coefficient with the altering of the manufacturing route (Chapter 3) is questionable since the exact values of surface moduli are not known.

In fact, the discrepancy between the *real* and the *apparent* stress dependence of a fibre's Raman frequency can be utilised, in the future, as an individual test to assess the degree of radial anisotropy in the fibre. The *real* stress dependence can be derived either from a stress - frequency experiment, or, from the strain dependence of a verified homogeneous fibre, divided by the constant-modulus of the material.

Compressive Raman studies on single carbon fibres have been conducted by bonding single filament on the compressible side of a cantilever beam (Chapter 4). This loading configuration has allowed the acquisition of the Raman spectrum of the compressed fibre and the derivation of the compressive strain dependence of the carbon fibre Raman frequencies (Chapter 4).

The advantages of the cantilever beam/ Raman technique for the study of the compressive properties of single filaments are the following:

(1) The "gauge length effect" is eliminated by subjecting the long fibre in a gradient of strain.

(2) Even if not optically detected, catastrophic fibre failure can be traced from the Raman frequency drop and the implied strain release.

(3) The fibre is "frozen" in position and can be scanned several times.

(4) The health hazard is prevented by encapsulating the fibre into a thin film.

(5) The fibre can be recovered from the soluble film for subsequent examination (e.g. SEM, fracture topography etc).

(6) The test can be easily conducted in tensile configuration by simply reversing the deflection direction of the cantilever beam.

The mode of failure in compression was found to be linked to the fibre radial anisotropy. A distinct compressive failure by "shear-like" fracture has only been detected on fibres with low intensity ratios ($I_D/I_G \leq 0.5$) and pronounced skin-core effects. As soon as these effects are eliminated by using a different manufacturing route, the mode of compressive failure changes from catastrophic to gradual yielding or "softening" of the material, as the accelerating reduction of the Raman frequency strain sensitivity indicates. Local collapse of the fibre contiguity in the form of "bulging", or, "ballooning" (Chapter 4) does not affect the fibre load carrying capability and, therefore, can not be characterised as clear compressive mode of failure. Such an improvement in the compressional behaviour of the radially "homogenised" fibres has been explained in terms of a two phase fibre structure. The highly oriented crystallites of the carbon fibre surface, weak in shear **[Dobb 1990]** and vulnerable to buckling instabilities **[Crasto 1990]** can be more constrained within the fibre structure if a second phase of "disordered" material is allowed to develop in the same region.

As the response of the carbon fibre Raman frequencies to the externally applied load was found to be a measure of the fibre stiffness, the reduction (in absolute values) of the rate at which the Raman frequency G changes with applied strain in compression, compared with the rate in tension, gives a strong indication of modulus softening in compression.

A non-linear regression of the experimental Raman frequency - (tensile and compressive) strain curves was found to yield a much more realistic description of the effect of applied load on the fibre structure, in

accordance with the reported non-linear elasticity of carbon fibres [**Hughes 1986, Arsenovic 1988**]. According to this approach the Raman Frequency Gauge Factor (RFGF), being now a strain dependent quantity, still characterises the slope of the Raman frequency - applied strain data, at every level of strain (compressive and tensile). It is, therefore, still a measure of the carbon fibre structure sensitivity to the externally applied load. This modelling allowed the correlation of the RFGF at a distinct level of strain with the fibre modulus at the same level of strain and eventually facilitated the derivation of a fibre modulus estimate at every level of strain, between the critical strains to failure, in tension and compression.

The final outcome of this analysis is focused on the finding that the only way to improve the compressive strength of carbon fibres is to prevent the catastrophic mode of failure in compression. Beyond that, any attempt to achieve higher critical compressive strains by employing lower modulus fibres does not appear to improve the compressive strength of the material (Chapter 4). This is due to the significant modulus softening in compression which eliminates any gains in the critical compressive strain of the fibre. However, the change of the compressive mode of failure from fibre fracture to yielding, without fibre splitting and detachment, will probably have beneficial results to the integrity of a fibre composite, since it eliminates the number of nucleation points for crack propagation along and across the composite.

The selection of a beam material with linear elastic properties extended over higher applied strain range will allow in the future the testing of single filaments at high compressive loads, particularly useful for fibres that do not exhibit a catastrophic mode of failure at low compressive strains.

6.2. Interfacial studies.

The significance of the fibre/resin interface in the design of composites has been recognised for both short fibre and unidirectional fibre composites. The stress-strain curve of short fibre composites can be strongly affected by the stress transfer mechanism [Piggott 1978].

In unidirectional fibre composites the interface must also serve to stop fibre initiated cracks from propagating through the solid. Thus, a localised impact may break a few filaments, but the crack should be stopped from propagating either by a ductile interface or by fibre/matrix debonding. Non catastrophic failure requires a balance between the tensile composite strength and the interfacial bond strength. Very low interfacial strength produces composites that behave poorly in shear and tension, but with low flaw sensitivity. Very high interfacial strength results in tough and brittle composites with high flaw sensitivity. The optimisation of the interfacial shear strength of a fibre/resin composite, depends on the requirements of the application in which the composite is to be employed at [Diefendorf 1985]. For example, for critical aircraft applications, the designing specifications for a wing box would require a fibre with at least 2.0% strain to failure and a composite with a 100 MPa shear strength [Diefendorf 1985]. To tailor the shear and the tensile strength of a unidirectional composite, good knowledge of the interfacial shear strength is vitally required [Shih 1987, Nairn 1988].

In the presented investigation (Chapter 5), interfacial studies on single carbon fibre model composites have been conducted by the combined use of the classical fragmentation test as the loading configuration and the Laser Raman Spectroscopy as the strain monitoring technique. The embedded carbon fibre is viewed as an internal strain gauge in tandem to its reinforcing role. The significantly different load transfer pattern produced by altering the surface treatment and/or the stiffness of the reinforcing fibre is characteristically demonstrated in figure 6.1, on three fragments of similar length, same type of resin, but different type of fibre.

Employing a simple balance of forces model, the experimentally measured fibre strain distribution can be converted to interfacial shear stress (ISS) distribution. No assumption has to be made with respect to the

nature of the shear stresses at the interface.

The application of this model to the experimental strain data yields almost constant shear stresses at the interface for the untreated fibre/epoxy system and variable ISS at the interface for the two treated fibre/epoxy systems, according to the elastic stress transfer theories. The resulting ISS distribution for the 3 fragments of figure 6.1, is displayed in figure 6.2.

The maximum ISS (averaged over all fragments per system) varies with applied strain. While for the untreated HM fibre/resin system the maximum ISS is almost constant throughout the fragmentation test, for both treated fibre systems, (a) it increases with applied strain, (b) it reaches an upper limit the point of saturation of the fragmentation process and (c) decays at higher applied strains. The maximum ISS (averaged over all fragments tested per system) is plotted as a function of applied strain in figure 6.3, for the three fibre/resin systems.

The upper limit of the average maximum ISS is considered to give a good estimate of the interfacial shear strength (IFSS) of the system. The scatter band about this value is thought to represent the distribution of the IFSS and the experimental error.

The frictional type of reinforcement in the untreated HMU fibre/system is verified by the almost constant value of the shear stresses at the interface of such a system. The surface treatment of the HM fibre improves dramatically the interfacial strength by mainly removing the less adherent, highly graphitic external surface layers of the fibre.

The debonding propagation depends on the applied strain and the strain energy release produced by the fibre recoiling that follows the fracture. The significantly higher IFSS of the IM fibre/resin system is a result of a stronger interfacial bond that resists successfully the debonding propagation up to the end of the fragmentation process.

The gradual yielding of the interface next to the fibre breaks is the reason for the shifting of the maximum ISS towards the middle of the fragment. The presence of this region of gradual interfacial yielding implies that the moment the fibre fracture occurs, the interfacial shear stresses, that develop instantaneously to diffuse the recoiling forces into the matrix, are higher than the interfacial shear strength (IFSS) of the system. As the force equilibrium is reestablished after the fracture, temporary relaxation of the fibre stresses and the reinforcing interfacial shear stresses is observed. Further loading of the specimen results in the

rebuild of the maximum ISS up to the IFSS levels, as long as no other fracture occurs in the region under examination. The moment the IFSS of the system has been reached, pronounced interfacial failure is observed in the form of a dramatic collapse of the fibre strain profiles and propagation of the debonded length. At higher applied strains the load transfer mechanism is purely controlled by the matrix material, which exhibits pronounced yielding at strains higher than 2.5%. Hence, the maximum ISS decays to values much closer to the bulk matrix yield strength.

To conclude, as a result of the nature of the fragmentation test, it is most probable that the interfacial shear strength is not detected at the strain level it is initially reached by the shear stresses. This is due to the local yielding near the fibre breaks, developed at the moment of fibre fracture. A complementary test which can clarify the above point is the Raman frequency mapping of a short carbon fibre embedded in epoxy resin. In such a configuration, the ISS can be measured from the well bonded fibre end, avoiding complications introduced by the fibre fracture and its consequences. In addition, other loading configurations, such as, pull-out and microindentation can also be employed to study the effect of the loading conditions upon the developing stress field at the interface.

Laser Raman Spectroscopy and its capability to sense the strain at microscopic level has offered the unique opportunity to measure *in situ* the strain in a fibre embedded into a resin matrix and to monitor closely the whole fragmentation process of a single fibre model composite. The enormous amount of information that was obtained by combining the Raman spectroscopic data with simple mechanics demonstrates the usefulness of the fragmentation test and points out its weaknesses as a technique for the study of the fibre/resin interface and the mechanisms of reinforcement in the heart of the composite. ▮

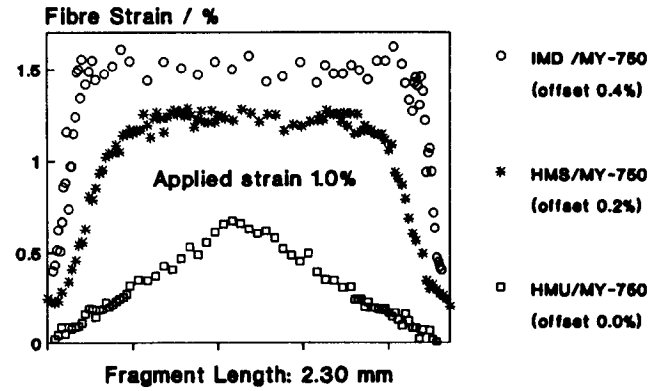

Fig.6.1 Comparison of the strain distribution on a similar length fragment for the three systems of the current study.

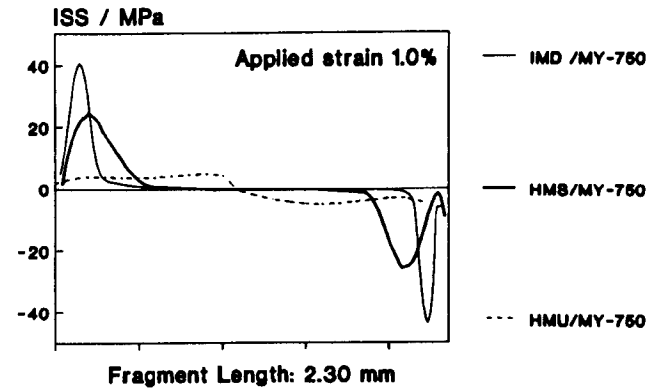

Fig.6.2 Comparison of the ISS distribution on a similar length fragment (of fig.6.1) for the three systems of the current investigation.

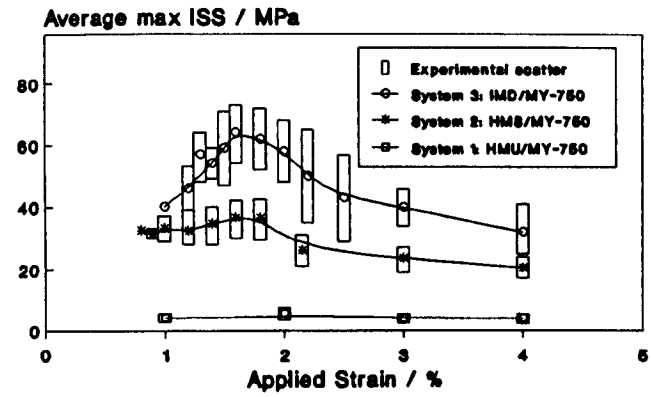

Fig.6.3 Comparison of the average maximum ISS as a function of the applied strain, for the three systems of the present study.

APPENDICES

APPENDIX A1. The equal stress model.

A two-phase model for the carbon fibre structure can be employed to explain the increased strain sensitivity (of the structure and the Raman spectrum) of fibres with higher surface crystallinity. According to such a model, a carbon fibre comprises of a perfectly crystalline phase, denoted as A, and inclusions of disordered (non-crystalline) structure, denoted as B (fig.3.11). The crystalline phase A has a Young's modulus E_A much higher than the modulus of the disordered phase E_B , so that:

$$E_A/E_B > 1 \qquad (A.1)$$

An equal stress situation requires the stress in region A to be equal to the stress in region B and also to the stress in the fibre cross-section:

$$\sigma_A = \sigma_B = \sigma_f \qquad (A.2)$$

The applied strain in the fibre, ε_f, is then related to the strain in the crystalline phase A and the strain in the disordered phase B, through the rule of mixtures equation:

$$\varepsilon_f = \varepsilon_A \cdot V_A + \varepsilon_B \cdot (1-V_A) \qquad (A.3)$$

where V_A is the "volume fraction" of the crystalline phase A in the fibre, ε_A is the strain in the crystalline phase and ε_B is the strain in the non-crystalline (disordered) phase. The greater the value of V_A the higher the degree of the fibre crystallinity. The equal stress model (equation 2) also requires:

$$\varepsilon_A \cdot E_A = \varepsilon_B \cdot E_B \quad \Leftrightarrow \qquad (A.4a)$$

$$\varepsilon_B = \varepsilon_A \cdot \frac{E_A}{E_B} \qquad (A.4b)$$

Substitution of equation 4b to equation 3 gives:

$$\varepsilon_f = \varepsilon_A \cdot V_A + \varepsilon_A \cdot \frac{E_A}{E_B} \cdot (1-V_A) \quad \Leftrightarrow \qquad \text{(A.5a)}$$

$$\varepsilon_f = \varepsilon_A \cdot \left(V_A + \frac{E_A}{E_B} \cdot (1-V_A) \right) \qquad \text{(A.5b)}$$

Let us assume that the same amount of external strain is applied to two fibres of different surface crystallinity. Fibre 1 exhibits higher surface crystallinity than fibre 2 and, therefore, $V_{A1} > V_{A2}$. Since $\varepsilon_{f1} = \varepsilon_{f2}$, then:

$$\varepsilon_{A1} \cdot \left(V_{A1} + \frac{E_A}{E_B} \cdot (1-V_{A1}) \right) = \varepsilon_{A2} \cdot \left(V_{A2} + \frac{E_A}{E_B} \cdot (1-V_{A2}) \right) \qquad \text{(A.6a)}$$

Rearranging equation 6a :

$$\frac{\varepsilon_{A1}}{\varepsilon_{A2}} = \frac{\left(V_{A2} + \frac{E_A}{E_B} \cdot (1-V_{A2}) \right)}{\left(V_{A1} + \frac{E_A}{E_B} \cdot (1-V_{A1}) \right)} \qquad \text{(A.6b)}$$

The term $"\left(V_A + \frac{E_A}{E_B} \cdot (1-V_A) \right)"$ of equation A.5b is inversely proportional to the volume fraction of the crystalline phase, V_A, as can be proven by the derivative of this term with respect to V_A. In fact, the value of this derivative is given:

$$\frac{d}{dV_A} \left(V_A + \frac{E_A}{E_B} \cdot (1-V_A) \right) = 1 - \frac{E_A}{E_B} < 0 \qquad \text{(A.7)}$$

since the modulus of the crystalline phase A is always higher than the modulus of the disordered phase B (equation A.1). As a result of this finding the numerator of equation A.6a is greater than the denominator, which consequently yields:

$$\frac{\varepsilon_{A1}}{\varepsilon_{A2}} > 1 \qquad (A.8)$$

Thus, following this model, it can be proved that under the same amount of externally applied strain ε_f, the crystalline units of a fibre exhibiting a high degree of surface crystallinity are deformed more than the equivalent units in a fibre exhibiting a lower degree of surface crystallinity. Consequently, the Raman spectrum of a highly crystalline fibre should demonstrate an increased sensitivity (and hence RFGF) to a discrete amount of externally applied strain, compared with a less crystalline fibre. ▮

APPENDIX A2. Polynomial and spline interpolation of the fibre strain data.

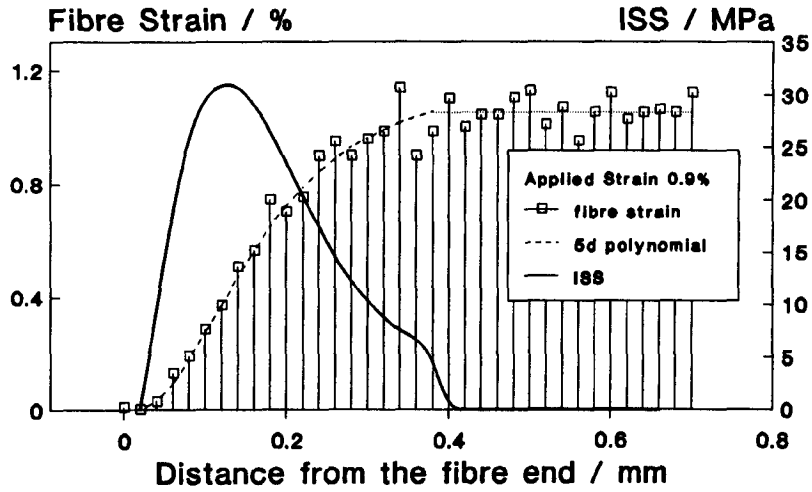

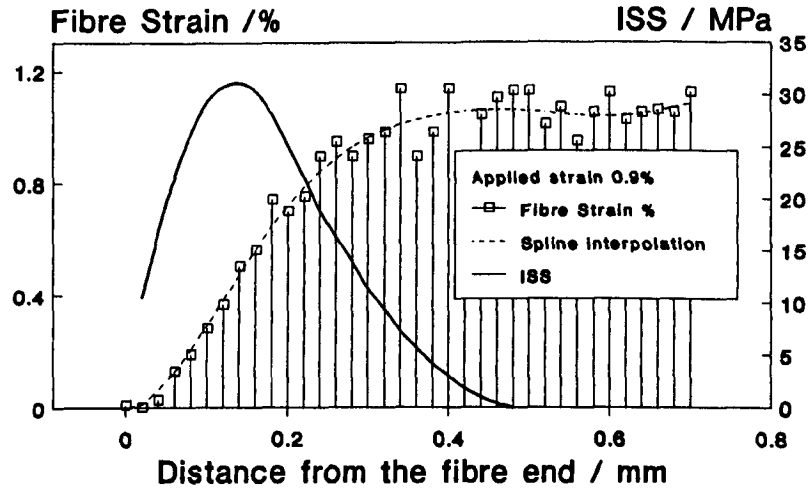

A fifth degree polynomial and a spline interpolation function have been fitted to the same set of data. The 5th degree polynomial is defined only within 0.4 mm from the fibre end, distance equal to the transfer length of the specific profile. The resulting ISS distributions (through the balance of forces model and equation 5.15) are similar and, what is most important, the maximum ISS is about 31 GPa, developing at about 0.14 mm from the fibre end, for both regressions. ▮

REFERENCES

Agarwal 1979

Agarwal B.D., Bansal R.K., (1979), *Fibre Science and Technology*, 12, p.149.

Agarwal 1980

Agarwal B.D., Broutman L.J., (1980), **Analysis and Performance of Fibre Composites**, Wiley-Interscience, New York.

Ager 1990

Ager III J.W., Veirs D.K., Shamir J., Rosenblatt G.M., (1990), *Journal of Applied Physics*, 68, No7, p.3598.

Al-Jishi 1982

Al-Jishi R., Dresselhaus G., (1982), *Physical Review B*, 26, No8, p.4514.

Allen 1988

Allen S.R., (1988), *Polymer*, 29, p.1091.

Allen 1989

Allen S.R., Roche E.J., (1989), *Polymer*, 30, p.996.

Amon 1948

Amon F.H., (1948), US Pat. 2,439,442.

Anastassakis 1970

Anastassakis E., Pinczuk A., Burnstein E., Pollak F.H., Cardona M., (1970), *Solid State Communications*, 8, p.133.

Arsenovic 1988

Arsenovic P., Jiang H., Eby R.K., A. and J.M.Liu, (1988), Conference proceedings, p.485, **CARBON '88**, Newcastle upon Tyne, Institute of Physics.

Ashbee 1988

Ashbee K.H.G., Ashbee E., (1988), *Journal of Composite Materials*, 22, p.602.

Bahl 1984

Bahl O.P., Mathur R.B., Dhami T.L., (1984), *Polymer Engineering and Science*, 24, No7, p.455.

Barnet 1974

Barnet F.R., Norr M.K., (1974), **Carbon Fibres - Their Place in Modern Technology**, The Plastics Institute, London.

Banwell 1983

Banwell C.N., (1983), **Fundumentals of Molecular Spectroscopy**, McGraw - Hill (U.K), London.

Bascom 1986

Bascom W.D., Jensen R.M., (1986), *Journal of Adhesion*, 19, p.219.

Beesley 1971

Beesley M.J., (1971), **Lasers and their Applications**, M.J.Beesley, London.

Bennet 1976

Bennet S.C., (1976), PhD thesis, University of Leeds.

Bennet 1978

Bennet S.C., Johnson D.J., (1978) Proceedings of the 5th London Carbon and Graphite Conference, v1, p.377.

Bikerman 1968

Bikerman J.J., (1968), **The Science of Adhesive Joints**, (2nd edition), Academic Press, New York.

Boll 1990

Boll D.J., Jensen R.M., Cordner L, Bascom W.D., (1990), *Journal of Composite Materials*, **24**, No2, p.208.

Bretzlaff 1983

Bretzlaff R.S., Wool R.P., (1983), *Macromolecules*, 16, p.1907.

Briscoe 1978

Briscoe B.J., Tabor D., (1978), *Journal of Adhesion*, v9, p.45.

Broutman 1969

Broutman L.J., (1969), **Interfaces in Composites**, ASTM STP 452, p.27.

Broutman 1970

Broutman L.J., (1970), 25th Annual Tech.Conference, Reinforced Plastics/ Composites Division, The Society of Plastics Industry, section 13-B, p.1.

Broutman 1974

Broutman L.J., Agarwal B.D., *Polymer Engineering and Science*, **14**, No8, p.581.

Burns 1977

Burns C, (1977), **Introduction to Group Theory with Applications**, Academic Press, London.

Caldwell 1989

Caldwell D.L., Babbington D.A., Johnson K.F., (1989), Conference Proceedings, **Interfacial Phenomena in Composite Materials '89**, p.44, Ed.F.R.Jones, Sheffield.

Carrara 1968

Carrara A.S., McGarry F.J., (1968), *Journal of Composite Materials*, **2**,

No2, p.222.

Cerdeira 1972

Cerdeira F., Buchenauer C.J., Pollak F.H., Cardona M., (1972), *Physical Review B*, 5, No2, p.580.

Chamis 1974

Chamis C.C., (1974), *Composite Materials*, v6, p31, Academic Press, New York.

Chen 1983

Chen K.J., Diefendorf R.J., (1983), Proceedings of the 16th Biennial Conference on Carbon, p.490.

Cherepanov 1979

Cherepanov G.P., (1979), **Mechanics of brittle fracture**, Chapter 9, McGraw-Hill, N.York.

Chieu 1982

Chieu T.C., Dresselhaus M.S., Endo M., (1982), *The American Physical Society*, 26, No10, p.5867.

Chieu 1983

Chieu T.C., Timp .G., Dresselhaus M.S., Endo M., Moore A.W., (1983), *Physical Review B*, 27, No6, p. 3686

Cooper 1971

Cooper G.A., Mayor R.M., (1971), *Journal of Material Science*, 6, p.60.

Cox 1952

Cox H.L., (1952), *The British Journal of Applied Physics*, 3, p.72.

Crasto 1990

Crasto A.S., Anderson D,P. (1990), Conference proceedings of ASC'90, American Society of Composites, p.809.

Curtis 1968

Curtis G.J., Milne J.M., Reynolds W.N., (1968), *Nature*, 220, p.1024.

DeTeresa 1982

DeTeresa S.J., Richard J.F., (1982), *Polymer Composites*, 3, No2, p.57.

DeTeresa 1984

DeTeresa S.J., Allen S.R., Farris R.J., Porter R.S., (1984), *Journal of Material Science*, 19, p.57.

DeTeresa 1985

DeTeresa S.J., Porter R.S., Farris R.J., (1985), *Journal of Material Science*, 20, p.1645.

DeTeresa 1988

DeTeresa S.J., Porter R.S., Farris R.J., (1988), *Journal of Material*

Science, 23, p.1886.

DiBenedetto 1978

DiBenedetto A.T., Nicolais L., (1978), **Advances in Composite Materials**, ed.G.Piatti, p.153,

Diefendorf 1985

Diefendorf R.J., (1985), **Carbon fibres and the composites**, p.46, ed. E.Fitzer, Spinger-Verlag, Berlin.

Dobb 1981

Dobb M.G., Johnson D.J., Saville B.P., (1981), *Polymer*, 22, p.960.

Dobb 1990

Dobb M.G.,Johnson D.J., Park C.R., (1990), *Journal of Material Science*, 25, p829.

Dollish 1974

Dollish F.R., Fateley W.G., Bentley F.F., (1974), **Characteristic Raman Frequencies of Organic Compounds**, Wiley-Interscience, New York.

Donnet 1973

Donnet J.B., Dauksch H., (1973), Proceedings of the 1st International Conference on **Carbon Fibres, their Composites and Applications**, p.49, Plastics Institute, London.

Donnet 1984

Donnet J.B., Bansal R.P., (1984) **Carbon Fibres**, Marcel Dekker, Inc., New York.

Dow 1963

Dow N.F., (1963), Report R63SD61, Space Sciences Laboratory, General Electric.

Dresselhaus 1977

Dresselhaus M.S., Dresselhaus G., Eclund P.C., Chung D.D.L., (1977), *Materials Science and Engineering*, 31, p.141.

Dresselhaus 1988

Dresselhaus M.S., Dresselhaus G., Sugihara K., Spain I.L., Goldberg H.A., (1988), **Graphite Fibres and Filaments**, Springer-Verlag, Berlin.

Drzal 1983a

Drzal L.T., Rich M.J., Lloyd P.F., (1983), *The Journal of Adhesion*, 16, p.1

Drzal 1983b

Drzal L.T., (1983), Proceedings of the 28th International SAMPE Symposium, p.1057.

Ebril 1981

Ebril A., Postman M., Dresselhaus G., Dresselhaus M.S., (1981), Extended Abstracts and Program, 15th Biennial Conference on Carbon, Univ.of Pennsylvania, p.48.

Favre 1990

Favre J.P., Jacques D., (1990), *Journal of Material Science*, **25**, p.1373.

Fischbach 1986

Fischbach D.B., Couzi M., (1984), *Carbon*, **24**, No3, p.365.

Fitzer 1985

Fitzer E., (1985), **Carbon fibres and the composites**, p.3, ed. E.Fitzer, Spinger-Verlag, Berlin.

Fitzer 1987

Fitzer E., Gantner E., Rozploch F., Steinert D. (1987), *High Temperatures - High Pressures*, **19**, No5, p.537.

Fitzer 1988a

Fitzer E., Frohs W., (1988), Conference proceedings, p.295, **CARBON '88**, Newcastle upon Tyne, Institute of Physics.

Fitzer 1988b

Fitzer E., Künkele F., (1988), Conference proceedings, p.488, **CARBON '88**, Newcastle upon Tyne, Institute of Physics.

Fitzer 1988c

Fitzer E., Rozploch F., Künkele F., (1988), Conference proceedings, p.248, **CARBON '88**, Newcastle upon Tyne, Institute of Physics.

Fitzer 1988d

Fitzer E., Rozploch F., (1988), *High Temperatures - High Pressures*, **20**, p.449

FitzGerald 1988

FitzGerald J.D., Taylor G.H., (1988), Conference proceedings, p.386, **CARBON '88**, Newcastle upon Tyne, Institute of Physics.

Fourdeux 1973

Fourdeux A., Perret R., Ruland W., (1973), Proceedings of the 1st International Conference on **Carbon Fibres their Composites and Applications**, p.57, Plastics Institute, London.

Fraser 1975

Fraser W.A., Ancker F.H., DiBenedetto A.T., (1975), Conference Proceedings, 30th Annual Technical Conference on Reinforced Plastics, The Society of Plastics Ind., section 22-A, p.1.

Galiotis 1985

Galiotis C., Robinson I.M., Young R.J., Smith B.J.E., Batchelder D,N., (1985), *Polymer Communications*, **26**, p.354.

Galiotis 1988a

Galiotis C., Batchelder D.N., (1898), Journal of Material Science - Letters, **7**, p.545.

Galiotis 1988b

Galiotis .C, Melanitis N., Batchelder D.N., Robinson I.M., Peacock J.A., (1988), Composites, **4**, p.321.

Galiotis 1991

Galiotis C., (1991), *Composites Science and Technology*, in press.

Ganesan 1970

Ganesan S. Maradudin A.A., Oitmaa J., (1970), *Annals of Physics*, **56**, p.556.

Gill 1972

Gill R.M., (1972), **Carbon Fibres in Composite Materials**, The Plastics Instutue, London.

Gray 1984

Gray F.J. (1984), *Journal of Material Science*, **19**, p.861.

Greenwood 1974

Greenwood J.H., Rose P.G., (1974), *Journal of Material Science*, **9**, p.1809.

Greszczuk 1969

Greszcsuk L.B., (1969), **Interfaces in Composites**, ASTM STP 452, p.42.

Greszczuk 1981

Greszcsuk L.B., (1981), Proceedings of the 2nd USA-USSR Symposium on **Fracture of Composite Materials**, ed. G.C.Shih, p. 231, The Hague.

Guigon 1984

Guigon M., Oberlin A., Desarmot G., (1984), *Fibre Science and Technology*, **20**, p.177.

Guillory 1977

Guillory W.A., (1977), **Introduction to Molecular Structure and Spectroscopy**, Allyn and Bacon, Inc., Boston.

Haeberle 1990

Haeberle J., Matthews F.L., (1990), Proceedings of ECCM-4, **Developments in the Science and Technology of Composite Materials**, p.517, Elsevier, Stuttgart.

Hahn 1986

Hahn H.T., Sohi M.M., (1986), *Composites Science and Technology*, **27**, p.25.

Hawthorne 1974

Hawthorne H.M. Teghtsoonial E., (1974), *Journal of Adhesion*, **6**, p.85.

Hawthorne 1975

Hawthorne H.M.,Teghtsoonian E., (1975), *Journal of Material Science*, **10**, p.41.

Hancox 1975

Hancox N.L., (1975), *Journal of Material Science*, **10**, p.234.

Henrat 1987

Henrat P. (1987), in **Looking Ahead in Materials and Processes**, p.389, Elsevier, Amsterdam.

Herinckx 1968

Heninckx C., Perret R., Ruland W., (1968), *Nature*, **220**, p.63

Hughes 1986

Hughes J.D.H.,(1986), *Carbon*, **24**, p.551

Hull 1981

Hull,D. (1981) **An introduction to composite materials**, Cambridge University Press, Cambrigde.

Ishida 1986

Ishida H., Fukuda H., Katagiri G., Ishitani A., *Applied Spectroscopy*, **40**, No3, p322.

Ishitani 1985

Ishitani A., (1985), *Polymer Science and Technology*, **27**, p.321.

Jacques 1987

Jacques D., Favre J.P., (1987), Proceedings of the 6th ICCM (ECCM-2), v5. p.471, Elsevier Applied Science.

Jahankhani 1991a

Jahankhani H., Galiotis C. *Journal of Composite Materials*, in press,

Jahankhani 1991b

Jahankhani H. (1991), PhD thesis, University of London.

Jaffe 1981

Jaffe H., (1981), **Thermal Characterisation of Polymer Materials**, ed. E.A.Turi, Academic Press, New York.

Janssen 1973

Janssen T., (1973), **Crystallographic Groups**, North Holland Publishers, Amsterdam.

Jenkins 1976

Jenkins G.M., Kawamura K., (1976), **Polymeric Carbons**, Cambridge University Press, Cambridge.

Johnson 1969

Johnson D.J., Tyson C.N., (1969), *Journal of Physics D: Applied Physics*, **2**, p.787.

Johnson 1973

Johnson D.J., Crawford D., Jones B.F., (1973), *Journal of Material Science - Letters*, **8**, p.286.

Johnson 1988

Johnson D.J., Dyson H.M., (1988), Conference proceedings, p.383, **CARBON '88**, Newcastle upon Tyne, Institute of Physics.

Jones 1971

Jones W.R., Johnson J.W., (1971), *Carbon*, **9**, p.645.

Kalnin 1985

Kalnin I.L, Jäger H.,(1985), **Carbon Fibres and their Composites**, p.62, ed. E.Fitzer, Spinger-Verlag, Berlin.

Katagiri 1984

Katagiri G., Ishida H., Ishitani A., (1984), Proceedings of the 9th Conference on Raman Spectroscopy, p.256, Tokyo.

Katagiri 1988

Katagiri G., Ishida H., Ishitani A., (1988), *Carbon*, **26**, No4, p.565.

Kelly 1966

Kelly A. (1966), **Strong Solids**, Clarendon Press, Oxford.

Kelly 1981

Kelly B.T., (1981), **Physics of Graphite**, Applied Science, London.

Kinloch 1983

Kinloch A.J., Young R.J., (1983), **Fracture behavour of polymers**, Applied Scienes, London.

Lespade 1982a

Lespade P.,Al-Jishi R., Dresselhaus M.S., (1982), *Carbon*, **20**, No5, p.427.

Lespade 1982b

Lespade P., (1982), PhD thesis, University of Bourdeaux.

Lespade 1984

Lespade P., Marchand A., Couzi M., Cruege F., (1984), *Carbon*, **22**, No4/5, p.375.

Loudon 1964

Loudon R., (1964), **Advances in Physics**, The Raman effect on Crystals, p.423,

Long 1977

Long D.A., (1977), **Raman Spectroscopy**, McGraw-Hill, New York.

Madhukar 1990

Madhukar M.S., Drzal L.T., (1990), Proceedings of ASC'90, p.849, Michigan.

Maeda 1979

Maeda M., Kuramoto Y., Horie C., (1979), *Journal of the Physical Society of Japan*, **47**, No1, p.337.

Mandell 1980

Mandell J.F., Chen J.H., McGarry F.J., (1980), *International Journal of Adhesion and Adhesives*, **1**, No1, p.40.

Mandell 1986

Mandell J.F., Grande D.H., Tsiang T.H., McGarry F.J., (1986), Proceedings of the 7th Conference on Composite Materials, **Testing and Design**, ASTM STP 893, p.87, ed.J.M.Whitney, Philadelphia.

McCartney 1988

McCartney L.N., (1988), NPL Report DMA(A)168.

McLaughlin 1966

MacLaughlin T.F., (1966), *Experimental Mechanics*, October, p.481.

Megerdigian 1987

Megerdigian C., Robinson R., Lehmann S., (1987), Proceedings of the 32nd International SAMPE Symposium, p.1126.

Menarch 1984

Menarch T.P., Cooney R.P., Johnson, R.A., (1984), *Carbon*, **22**, No1, p.39.

Miller 1987

Miller B., Muri .P., Rebenfeld L., (1987), *Composites Science and Technology*, **28**, p.17.

Nairn 1985

Nairn J.A., (1985), *Polymer Composites*, **6**, No2, p.123.

Nairn 1988

Nairn J., (1988), *Journal of Composite Materials*, **22**, p.561.

Nakamizo 1974

Nakamizo M., Kammereck R., Walker P.L., (1974), *Carbon*, **12**, p.259.

Narisawa 1985

Narisawa N., Oba T., (1985), *Journal of Material Science*, 20, p.4527.

Narkis 1988

Narkis M., Chen J.H., Pipes R.B., (1988), *Polymer Composites*, 9, No4, p.245.

Nemanich 1977a

Nemanich R.J., Lukovsky G., Solin S.A., (1977), *Solid State Communications*, 23, p.117.

Nemanich 1977b

Nemanich R.J., Solin S.A., Gúerard D., (1977), *Physical Review B*, 16, No6, p.2965.

Nemanich 1979

Nemanich R.J., Solin S.A., (1979), *Physical Review B*, 20, No2, p.392.

Netravali 1989a

Netravali A.N., Henstenburg R.B., Phoenix S.L., Swhwartz P.,(1989), *Polymer Composites*, 10, No4, p.226.

Netravali 1989b

Netravali A.N., Topoleski L.T.T., Sachse W.H., Phoenix S.L., (1989), *Composites Science and Technology*, 35, p.13.

Nicholson 1977

Nicholson A.P.P., Bacon D.J., (1977), *Journal of Physics C: Solid State*, 10, p.2295.

Ohsawa 1978

Ohsawa T., Nakayama A., Miwa M., Hasegawa A. (1978), *Journal of Applied Polymer Science*, 22, p.6203.

Ohsawa 1990

Ohsawa T., Miwa M., Kawade M., Tsushima E., (1990), *Journal of Applied Polymer Science*, 39, p.1733.

Outwater 1956

Outwater J.O., (1956), *Modern Plastics*, March 1956, p.156.

Piggott 1978

Piggott M.R., (1978), *Journal of Composite Materials*, 13, p.1709.

Piggott 1980

Piggott M.R., (1980), **Load Bearing Fibre Composites**, Pergamom Press, Oxford.

Piggott 1981

Piggott M.R., (1981), *Journal of Material Science*, 16, p.2837.

Piggott 1987

Piggott M.R., (1987), *Polymer Composites*, **v8**, No5, p.291.

Pitkethly 1989

Pitkethly M.J., Doble J.B., (1989), Conference Proceedings, **Interfacial Phenomena in Composite Materials '89**, p.35, Ed.F.R.Jones, Sheffield.

Raman 1928

Raman C.V., Krishnan K.S., (1928), *Nature*, **121**, p.501.

Rand 1977

Rand B., Robinson R., (1977), *Carbon*, **15**, p.257.

Robinson 1986

Robinson I.M., Yeung P.H.J., Galiotis C., Young R.J., Batchelder D.N., (1986), *Journal of Material Science*, **21**, p.3440.

Robinson 1987

Robinson I.M., Zakikhani M., Day R.J., Young R.J., Galiotis C., (1987), *Journal of Material Science - Letters*, **6**, p.1212.

Rosen 1964

Rosen B.W., (1964), *AIAA Journal*, **v2**, No11.

Rosen 1965

Rosen B.W., (1965), **Fibre Composite Materials**, ASM, Ohio.

Ruland 1967

Ruland W., (1967), *Journal of Applied Physics*, **38**, p.3585.

Sakata 1987

Sakata H., Dresselhaus G., Endo M., (1987), MIT Report - AFOSR-TR-880234.

Sasaki 1984

Sasaki Y., Nishina Y., (1984), Proceedings of the 9th International Conference on Raman Spectroscopy, p.463, Tokyo.

Schuster 1964

Schuster D.M., Scala E., (1964), Transactions of the Metallurgical Society of AIME, **230**, December, p.1637.

Sharp 1973

Sharp J.V., Burnay S.G., (1973), Proceedings of the 1st International Conference on **Carbon Fibres their Composites and Applications**, p.68, Plastics Institute, London.

Sharpe 1972

Sharpe L.H., (1972), *The Journal of Adhesion*, **4**, p.55.

Shih 1987

Shih G.C., Ebert L.J., (1987), *Journal of Composite Materials*, **21**,

p.207.

Sinclair 1950

Sinclair D., (1950), *Journal of Applied Physics*, **21**, p.380.

Siesler 1980

Siesler H.W., Holland-Moritz K., (1980), **Infrared and Raman Spectroscopy of Polymers**, Marcel Dekker, New York.

Smith 1970

Smith G.E., Spencer A.G.M., (1970), *Journal of Mech.Physics, Solids*, **18**, p.81.

Sokolnikoff 1956

Sokolnikoff I.S., (1956), **Mathematical Theory of Elasticity**, McGraw-Hill, New York.

Summerscales 1987

Summerscales J., (1987), Structural Mechanics Section Research Publication , p.1321

Szymanski 1967

Szymanski H.A., (1967), **Raman Spectroscopy**, Plenum, New York.

Tashiro 1990

Tashiro K., Wu G., Kobayashi M., (1990), *Journal of Polymer Science B: Polymer Physics*, **28**, p.2527.

Tetlow 1990

Tetlow P.L., (1989), Queen Mary and Westfield College, private communication.

Termonia 1987

Termonia Y., (1987), *Journal of Material Science*, **22**, p.504.

Tidjani 1986

Tidjani M., Lachter J., Kabre T.S., Bragg R.H., (1986), *Carbon*, **24**, No4, p.447.

Timoshenko 1961

Timoshenko S.P., Gere J.M., (1961), **Theory of Elastic Stability**, McGraw-Hill, New York.

Tse 1985

Tse M.K., (1985), SAMPE Journal, September, p.11.

Tsu 1978

Tsu R., Gonzalez J.H., Hernandez C.I., (1978), *Solid State Communucations*, **27**, p.507.

Tuinstra 1970a

Tuinstra F., Koenig J., (1970), *The Journal of Chemical Physics*, **53**,

No3, p.1126.

Tuinstra 1970b

Tuinstra F., Koenig J., (1970), *Journal of Composite Materials*, **4**, p.492.

Turrell 1972

Turrell G., (1972), **Infrared and Raman Spectra of Crystals**, Academic Press Inc., London.

Tyson 1965

Tyson W.R., Davies G.J., (1965), *British Journal of Applied Physics*, **16**, p.199.

Vidano 1981

Vidano R.P., Fischbach D.B., Willis L.J., Loehr T.M. (1981), *Solid State Communications*, **39**, p.341.

Waterbury 1990

Waterbury M.C., Drzal L.T., (1990) *Journal of Composites Technology and Research*, in press.

Watt 1971

Watt W., (1973), Proceedings of the 1st International Conference on **Carbon Fibres, their Composites and Applications**, p.45, Institute of Plastics, London.

Whitney 1987

Whitney W., Drzal L.T., (1987), in **Toughened Composites**, ASTM STP 937, p.179, ed. N.Johnston, Philadelphia.

Woodward 1972

Woodward L.A., (1972), **Introduction to molecular vibrations**, Clarendon Press, Oxford.

Wool 1986

Wool R.P., Bretzlaff R.S., (1986), *Journal of Polymer Science B*, **24**, p.1039.

Wright 1976

Wright R.B., Varma R., Gruem D.M., *Journal of Nuclear Materials*, **63**, p.415.

Yoshimori 1956

Yoshimori A.,Kitano Y., (1956), *Journal of the Physical Society of Japan*, **11**, No4, p.352.

Zhang 1983

Zhang Z.Y., (1983), SAMPE Quarterly, **v15**, part 1, p.51.

Zwaag 1988a

Zwaag S., Picken S.J., Sluijs C.P., (1988), Proceedings of **The integration of fundamental polymer science and technology**, The Netherlands.

Zwaag 1988b

Zwaag S., Kampschoer G., (1988), Proceedings of **The integration of fundamental polymer science and technology**, The Netherlands. ▮